
Doped Indium Oxide: Surface Potentials, Electronic and Optical Properties

Dotiertes Indium Oxid: Oberflächenpotentiale, elektronische und optische Eigenschaften

Zur Erlangung des akademischen Grades Doktor-Ingenieur (Dr.-Ing.)

genehmigte Dissertation von Andreas Hilarius Hubmann aus Frankfurt am Main

Tag der Einreichung: 23.03.2021, Tag der Prüfung: 15.06.2021

Darmstadt – D 17

1. Gutachten: Prof. Dr. Andreas Klein

2. Gutachten: Prof. Dr. Karsten Albe



TECHNISCHE
UNIVERSITÄT
DARMSTADT

Fachbereich Materialwissenschaften
Fachgebiet Elektronenstruktur von Ma-
terialien

Doped Indium Oxide: Surface Potentials, Electronic and Optical Properties
Dotiertes Indium Oxid: Oberflächenpotentiale, elektronische und optische Eigenschaften

Genehmigte Dissertation von Andreas Hilarius Hubmann aus Frankfurt am Main

1. Gutachten: Prof. Dr. Andreas Klein
2. Gutachten: Prof. Dr. Karsten Albe

Dissertationsort: Darmstadt, Technische Universität Darmstadt

Tag der Einreichung: 23.03.2021

Tag der Prüfung: 15.06.2021

Jahr der Veröffentlichung der Dissertation auf TUprints: 2022

Bitte zitieren Sie dieses Dokument als:

URN: urn:nbn:de:tuda-tuprints-177628

URL: <https://tuprints.ulb.tu-darmstadt.de/17762>

Dieses Dokument wird bereitgestellt von tuprints,

E-Publishing-Service der TU Darmstadt

<http://tuprints.ulb.tu-darmstadt.de>

tuprints@ulb.tu-darmstadt.de

Die Veröffentlichung steht unter folgender Creative Commons Lizenz:

CC BY-SA 4.0 International

<https://creativecommons.org/licenses/by-sa/4.0/>

Erklärung laut Promotionsordnung

§8 Abs. 1 lit. c PromO

Ich versichere hiermit, dass die elektronische Version meiner Dissertation mit der schriftlichen Version übereinstimmt.

§8 Abs. 1 lit. d PromO

Ich versichere hiermit, dass zu einem vorherigen Zeitpunkt noch keine Promotion versucht wurde. In diesem Fall sind nähere Angaben über Zeitpunkt, Hochschule, Dissertationsthema und Ergebnis dieses Versuchs mitzuteilen.

§9 Abs. 1 PromO

Ich versichere hiermit, dass die vorliegende Dissertation selbstständig und nur unter Verwendung der angegebenen Quellen verfasst wurde.

§9 Abs. 2 PromO

Die Arbeit hat bisher noch nicht zu Prüfungszwecken gedient.

Darmstadt, den

(A.H. Hubmann)

Contents

1	Motivation	3
2	Indium Oxide	7
2.1	Crystal Structure	7
2.2	Electronic Structure	8
2.3	Intrinsic Defects	10
2.4	Doped Indiumoxide	10
2.4.1	Defect Structure in ITO	12
2.4.2	Electronic Properties	14
2.4.3	Surface Potentials	17
3	Methodology	19
3.1	Optical Characterization of Thin Films	19
3.1.1	Light and its Interaction with Matter	19
3.1.2	Spectrophotometry	25
3.1.3	Spectroscopic Ellipsometry	25
3.1.4	Modeling of Optical Spectra	26
3.1.5	Dielectric Model for doped In_2O_3	27
3.1.6	Optical Band Gap Determination from the Spectral Absorption Coefficient	30
3.1.7	Sample Spectra	32
3.2	Photoelectron Spectroscopy	33
3.3	Electronic Characterization: Conductivity and Hall-Effect	34
3.4	Magnetron Sputter Deposition	36
4	Experimental Procedures	39
4.1	Optical Spectroscopy	39
4.2	X-Ray Diffraction	40
4.3	Photoelectron Spectroscopy	40
4.4	Electronic Characterization: Conductivity and Hall-Effect	42
4.5	Thin Film Deposition	42
5	Molybdenum Doped Indium Oxide	45
5.1	Structural Analysis	45
5.1.1	Effect of Dopant and of Stress on Reflection Angles	46
5.2	Electronic Properties, Conductivity and Hall-Effect Measurements	49
5.3	Optical Analysis	53
5.3.1	Influence of Dopant Concentration onto the Optical Properties	57
5.3.2	Comparison of Electronic properties obtained from Conductivity-Hall-Effect and Optical Measurements	58
5.4	Photoelectron Spectroscopy	59
5.4.1	X-Ray Photoelectron Spectroscopy	59

5.4.2	Oxidation state and Segregation	66
5.4.3	Sputter depth profiles	72
5.4.4	Ultraviolet Photoelectron Spectroscopy and Surface Potentials	76
5.5	Summary	79
6	Titanium Doped Indium Oxide	83
6.1	Structural Analysis	83
6.2	Electronic Properties, Conductivity and Hall-Effect Measurements	84
6.3	Optical Analysis	86
6.4	Photoelectron Spectroscopy	90
6.4.1	X-Ray Photoelectron Spectroscopy	90
6.4.2	Ultraviolet Photoelectron Spectroscopy and Surface Potentials	96
6.4.3	Titanium Band Gap State	99
6.5	Summary	101
7	Doped Indium Oxide - A Comparison	103
7.1	Optical Properties	103
7.2	Surface Potentials	107
7.2.1	Summary of Observations	107
7.2.2	Influence of Dopant Segregation	111
7.2.3	Summary	115
7.3	Carrier Concentration	115
7.3.1	Doping Limit by Intrinsic Defects: Self-Compensation	117
7.3.2	Doping Limit by Charge Transfer Points	119
7.3.3	Doping Limit by Dopant Segregation	122
7.3.4	Summary	124
7.4	Carrier Mobility	125
7.4.1	Grain Boundary Barriers	126
7.4.2	Mobility Limit	127
8	Conclusion And Future Outlook	131
	References	137
9	Appendix	153



1 Motivation

Transparent conductive oxides (TCOs) are crucial for modern optoelectronic applications [1, 2]. They combine transparency in the visible range of light (VIS) and a high conductivity due to a large optical band gap and the Fermi level being positioned in the conduction band, respectively [3]. Transparent electrodes for displays and solar cells, heating or anti-static layers [4, 5] as well as gas sensors [6, 7] are examples for their utilization. Increasing device size and field of application demand for ongoing research and optimization of the already known materials [8].

In₂O₃ based thin films are of major technological relevance [8]. The addition of tetravalent doping elements as Sn, Zr, Ge, Ti and Mo is used to improve its electronic properties [5, 9–11]. Sn doped In₂O₃, for example, is the most commonly used TCO in the flat panel and organic light emitting diode industry [12]. High Sn concentrations, generating up to 10²¹ cm⁻³ free carriers, are necessary to achieve the highest conductivities [13]. On the other hand a high carrier concentration n leads to strong reflectivity in the near infra-red (NIR), being disadvantageous for the application in e.g. solar cells [14]. Films with similar electronic properties as Sn:In₂O₃ but a plasmon absorption shifted to higher wavelength require high mobilities μ [15]. This demand can be met by In₂O₃ doped with e.g. Zr, Mo or Ti [5, 14, 16]. The correlation between optical and electronic properties of a high- n and a high- μ , i.e. Sn:In₂O₃ and Ti:In₂O₃ thin film is shown in Fig. 1.1. Transmission and reflection spectra are shown on the left, Hall mobility μ_{Hall} and Hall carrier concentration n_{Hall} on the right. Both films have a similar conductivity of $\sigma = 5 \times 10^3 \text{ Scm}^{-3}$ but significantly differ in the transparency window.

As for other semiconducting materials, the concentration of free carriers in In₂O₃ depends on intrinsic and extrinsic donor or acceptor defects [3, 19, 20]. Defect chemistry therefore is essential for its electronic and optical properties. Oxygen vacancies $V_O^{\bullet\bullet}$, oxygen interstitials O_i'' , indium vacancies V_{In}''' and substitutional defects as Sn_{In}^{\bullet} are commonly considered [3, 21–23]. The formation energy of latter defects, being dependent on the chemical potential of the constituents and electrons is decisive for the equilibrium defect concentration and the electronic and optical transition energies [19, 22, 24]. The physical properties of In₂O₃ thin films hence are strongly affected by the dopant element, its concentration and the deposition conditions.

In contrast to the carrier concentration, the carrier mobility is not directly connected to the defect chemistry. It therefore was assumed a constant which, however, recently was shown to be a misbelief [15, 17, 25]. μ is affected by scattering at ionized impurities, polar optical phonons and grain boundaries. Since each mechanism is dominant over a specific range in carrier concentration, the mobility is a function of n . A model describing $\mu(n)$ for single crystalline In₂O₃ and Sn:In₂O₃ fits well to experimental results except for carrier concentrations close to $2 \times 10^{20} \text{ cm}^{-3}$ [17]. Depending on the dopant element the model significantly underestimates experimentally obtained mobilities [15]. The reasons for the latter observation are not known yet. Similarly doping efficiency as well as the impact of the dopant on the mobility are still subject of ongoing research [14, 16, 26]. Segregation of the dopant to the surface and grain boundaries is expected to be decisive [15].

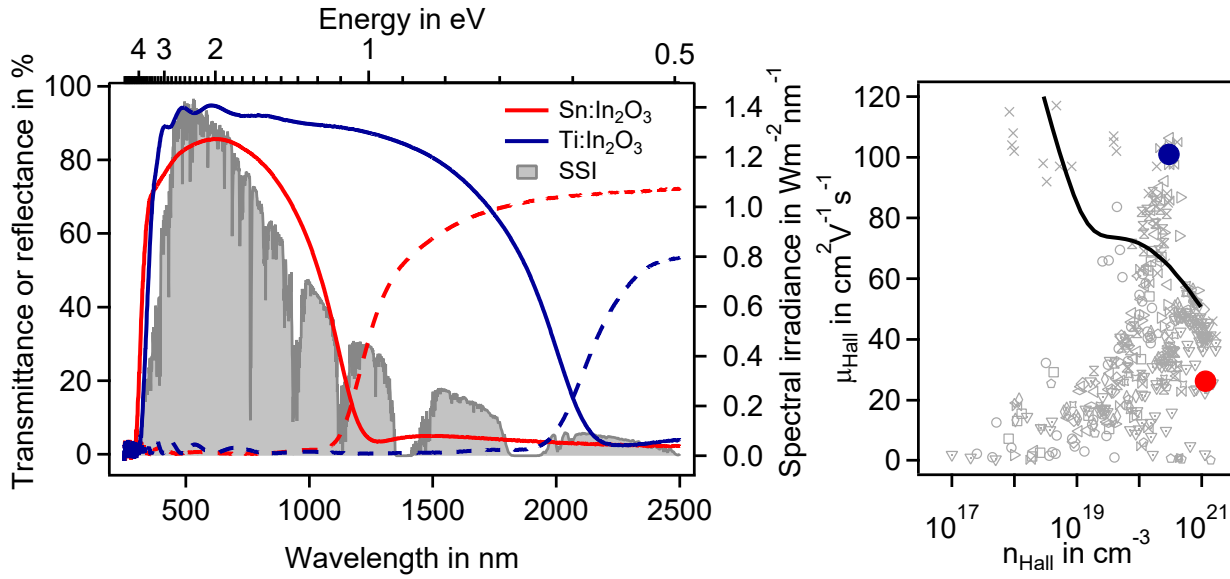


Figure 1.1: Comparison of optical and electronic properties of Sn:In₂O₃ and Ti:In₂O₃ thin films with a dopant concentration of either 10 wt% or 2 mol% respectively. Transmission (solid lines) and reflection (dashed lines) are presented on the left while Hall mobility is plotted over Hall carrier concentration on the right. The gray markers represent other doped and undoped In₂O₃ samples. The solid black line indicates the theoretical mobility limit, calculated for Sn:In₂O₃ single crystals [17]. In addition to the optical measurements a spectrum of the solar spectral irradiance is shown (SSI) [18]. Both films have a similar conductivity of about 5000 Scm⁻¹, either due to a very high mobility or carrier concentration. The latter two significantly affect the transmittance window of the films.

Besides the demands on conductivity and transparency, carrier injection and extraction are essential for device performance [27]. Latter are determined by the surface potentials as work function ϕ and ionization potential I_p [28–31]. Deposition condition, surface treatment and dopants are known to affect those properties [32, 33].

For polar materials as In₂O₃ a correlation between surface potentials and the surface orientation or termination is expected [7, 34]. A relationship between latter properties was recently reported for epitaxial In₂O₃ and textured Sn:In₂O₃ films [29, 33]. Besides surface termination and structure a significant dopant dependence is found [7, 32, 35]. Dopant segregation and potentially even the formation of a dopant oxide layer at the surface is assumed to be an important factor [35].

It becomes clear that most of the relevant properties of doped and undoped In₂O₃ are strongly intertwined and defect chemistry is crucial in this context. There are a number of articles correlating theoretical approaches to the defect chemistry and experimental results [7, 19, 22, 24, 26, 36]. A number of questions, concerning e.g. the mobility limit, doping limit and segregation behavior of different dopants, nevertheless remain unanswered. Objective of this work is to extend the experimental data base for doped In₂O₃ to provide a better understanding of this material and especially the effect of different dopant elements.

This work queues in a series of PhD thesis related to doped and undoped In_2O_3 , carried out in the electronic structure of materials group, Technische Universität Darmstadt [37–40]. The surface electronic structure and potentials of sputtered In_2O_3 and $\text{Sn}:\text{In}_2\text{O}_3$ thin films, in dependence on deposition conditions, surface treatment and crystallographic orientation were intensively studied. Investigations on oxygen exchange, defect chemistry and the correlation between carrier concentration and mobility were carried out. Besides unintentionally and Sn doped In_2O_3 thin films, Zr and H were analyzed as dopants.

A correlation between Fermi energy and the surface dopant concentration could be shown for $\text{Sn}:\text{In}_2\text{O}_3$ [15, 41]. The determination of grain boundary barrier heights of doped and undoped In_2O_3 showed highest values for $\text{Sn}:\text{In}_2\text{O}_3$. Tin segregation to surfaces and grain boundaries as well as the crystallographic orientation of the latter was made responsible for those observation. Several open questions concerning the influence of the dopant element remain open which are the starting point for this work. Previous research is pursued by investigating $\text{Sn}:\text{In}_2\text{O}_3$, $\text{Ge}:\text{In}_2\text{O}_3$, $\text{Mo}:\text{In}_2\text{O}_3$ and $\text{Ti}:\text{In}_2\text{O}_3$ thin films.

The influence of the film texture on $\text{Sn}:\text{In}_2\text{O}_3$ surface potentials and the Hall mobility was analyzed by growing epitaxial and highly textured films. In an attempt to tailor ϕ and I_p , self assembling monolayers (SAMs) of organic molecules were grown on differently treated $\text{Sn}:\text{In}_2\text{O}_3$ surfaces. The effect on surface potentials and the stability of the molecules was investigated. Even though, $\text{Sn}:\text{In}_2\text{O}_3$ films of different orientation or texture could be grown, no systematic correlation between orientation and mobility or surface potentials was found. Latter observation on the surface potentials is mainly related to the fact that (100) oriented films show (111) facets. Dopant segregation is expected to play an important role as well. Adsorption of thermally evaporated 4-(Dimethylamino)benzoic acid proved to be a self-limiting process as expected for the formation of a SAM. After adsorption a significant reduction in the work function down to 2.82 eV could be measured. Latter results can be found in [27].

To establish a broader base for understanding the fundamental properties of doped In_2O_3 , the influence of other donor dopants is investigated by systematically analyzing $\text{Ge}:\text{In}_2\text{O}_3$, $\text{Mo}:\text{In}_2\text{O}_3$ and $\text{Ti}:\text{In}_2\text{O}_3$. Thin films were grown by radio frequency magnetron sputtering. Multiple target compositions and deposition conditions, i.e. substrate temperature and oxygen content of the process atmosphere, were used. Transmission, reflection and spectroscopic ellipsometry measurements were carried out to distinguish optical properties. By simulation of those spectra optical carrier concentration and mobility could be compared to values obtained by conductivity and Hall-effect measurements. Photoelectron spectroscopy was used to access the surface electronic structure and its chemical composition. To correlate the crystal structure to former features selected samples were analyzed by X-ray diffraction.

Independent on the dopant element a decreasing carrier concentration is found with increasing oxygen chemical potential. This indicates interstitial oxygen to act as compensating defect. The conductivity tends to increase with temperature. Depending on the dopant and its concentration a complete loss of the carrier mobility may be found at high deposition temperatures. The carrier mobility and overall doping efficiency, going with the

maximum carrier concentration, is highly dopant specific. The mobility is determined by the grain boundary barrier height, which is mainly influenced by dopant segregation. Several effects, possibly limiting the carrier concentration are discussed. Dopant segregation at the surface is found for almost all investigated materials. Depending on the element either oxidizing or reducing conditions lead to enhanced segregation. While Ti behaves similar to Sn, increasing Ge and Mo surface concentrations are measured for oxidizing conditions. No correlation to the Fermi level is found in those two cases. Possible reasons for the contrasting conditions based on defect chemistry, oxide stability and ionic radii are discussed. Surface potentials were found to be subject to the doping elements. The wide variety in surface dipole is expected to be due to the formation of dopant oxide layers. A correlation to the surface termination and orientation as seen for In_2O_3 cannot be confirmed for any dopant element.

This thesis is structured into eight chapters. This general motivation is followed by establishing a scientific basis. Fundamental properties of doped and undoped In_2O_3 , as well as the methodology and experimental procedures employed here are introduced. The experimental data for $\text{Mo:In}_2\text{O}_3$ and $\text{Ti:In}_2\text{O}_3$ thin films is presented afterwards. Details on $\text{Ge:In}_2\text{O}_3$ will not be reproduced here, since it was studied by Hoyer in the framework of a master thesis and already published [35]. Before concluding and giving a future outlook, observations made for $\text{Mo:In}_2\text{O}_3$, $\text{Ti:In}_2\text{O}_3$ and $\text{Mo:In}_2\text{O}_3$ will be discussed by setting them into context with previously obtained results on other dopants.

2 Indium Oxide

2.1 Crystal Structure

In_2O_3 exhibits three different crystal structures, two body centered cubic and one orthorhombic structure depending on temperature and pressure [23, 42]. It is present in the bixbyite structure, i.e. in a body centered cubic lattice described by the space group $I3\bar{a}$ under normal conditions. The bixbyite structure is isostructural to the C-type rare earth structure and closely related to the fluorite structure. This means it is composed of a distorted fluorite lattice with only three quarters of all anion sites occupied [23, 42, 43]. One unit cell contains 80 atoms and has a lattice parameter of 1.0117 nm [20, 43, 44].

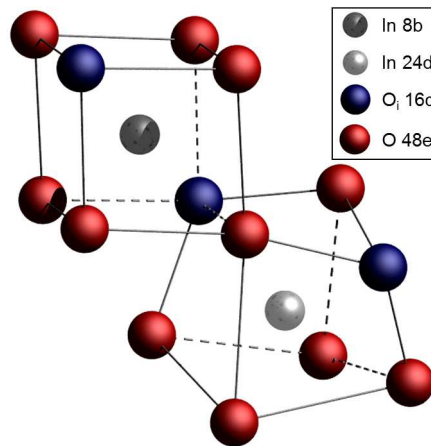


Figure 2.1: Excerpt of an In_2O_3 unit cell showing both Indium sites (light and dark gray) and their coordination to the nearest oxygen atoms (red). Structural oxygen vacancies, i.e. oxygen sites, which would be occupied in the fluorite structure but are not occupied in the bixbyite structure are shown in blue. Black lines emphasize the distorted cubes made of anion and anion vacancies surrounding each cation.

A section of the In_2O_3 structure is shown in Fig. 2.1. The cations are distributed on the $8b$ and on the $24d$ Wyckoff positions, which are structurally different cation sites [20]. The 48 oxygen anions are found on the e positions. Structural oxygen vacancies on the $16c$ positions, i.e. anion sites which would be occupied in a fluorite lattice, are indicated as well. Indium atoms are positioned in the centers of distorted octahedra made of oxygen ions or distorted cubes when occupied and unoccupied oxygen sites are considered. Two nonequivalent sites for the Indium atoms exist due to different oxygen vacancy locations. One with the two structural oxygen vacancies lying on the opposite corners of the bodydiagonal and the other with them on the facediagonal of the coordination cube [20, 43]. All oxygen ions are fourfold coordinated by Indium.

The $16c$ positions which are not occupied by oxygen atoms, i.e. the structural oxygen vacancies, are locations for oxygen interstitials and therefore important for the defect chemistry in doped In_2O_3 [20].

2.2 Electronic Structure

The requirements on the band gap of a transparent conductive material are conflicting. A high transparency in the visible range demands a large band gap (> 3 eV) while a high carrier concentration, as necessary for a good conductivity, asks for a low band gap [45]. Doped and undoped In_2O_3 combine a high transparency and good conductivity. Regardless on the scientific interest and its technological importance, the nature of its band gap has been resolved only recently [46]. Early investigations on In_2O_3 reported the onset of a strong optical absorption around 3.75 eV and a much weaker one at about 2.6 eV [47]. This implies, that the valence band maximum and conduction band minimum are not positioned at the same k and In_2O_3 is an indirect semiconductor [43, 48]. The latter explanation was accepted for a long time but is under revision in more recent articles.

Several publications combining density functional theory calculations and different experimental methods, refrain from the earlier hypothesis but fail to give a non-ambiguous explanation for optical transitions starting from two significantly different photon energies. Consent is that the conduction band minimum is positioned at the Γ point in the Brillouin zone and the next conduction band state occurs at a significantly higher energy due to the strong ionic character of In_2O_3 [6, 42, 45, 46, 49, 50]. No unison answer is given considering the position of the valence band maximum. Some authors propose the VBM to be positioned slightly above (≈ 50 meV) the highest valence band at the Γ point and therefore refer to an indirect fundamental band gap [6, 42, 49, 51]. This small energetic difference, however, fails to explain the approximately 1 eV offset in optical absorption onsets. A strong upward dispersion at the Γ point would be required [52] which is clearly in contrast to the latter observations.

Other authors report a direct band gap [45, 46, 50, 53]. It is suggested that direct optical transitions from the valence band maximum to the conduction band minimum at the Γ point are parity (selection rule) forbidden. The first strong optical transition can occur only from 0.81 eV below the valence band maximum, leading to a significant difference between the fundamental and the optical band gap of this films. Details of this model will be discussed in the following.

A band diagram for In_2O_3 , based on density functional calculations carried out by Walsh *et al.* [46], is shown in Fig. 2.2 on the left. A direct band gap with the VBM and CBM positioned at the Γ point is found. The state at the Γ point of the conduction band minimum is made up of In 5s and O 2s orbitals, while the valence band maximum is derived from In 4d and O 2p. Both have an even parity [45, 46, 54]. Since the bixbyite structure contains an inversion center it possesses an uneven electric-dipole operator. Optical transitions between two states of even parity and therefore between the valence band maximum and conduction band minimum are forbidden. The first band of odd parity and with a non-negligible matrix element at Γ (Γ_8) is positioned 0.81 eV [46] or 0.71 eV [45] below the valence band maximum. A discrepancy of the optical and fundamental band gap by the latter value is therefore expected. Local symmetry breaking can result in weak transitions below the optical band gap though [54]. These transitions are observable for In_2O_3 single crystals [47, 49] but not for thin films due to the low transition probability [51].

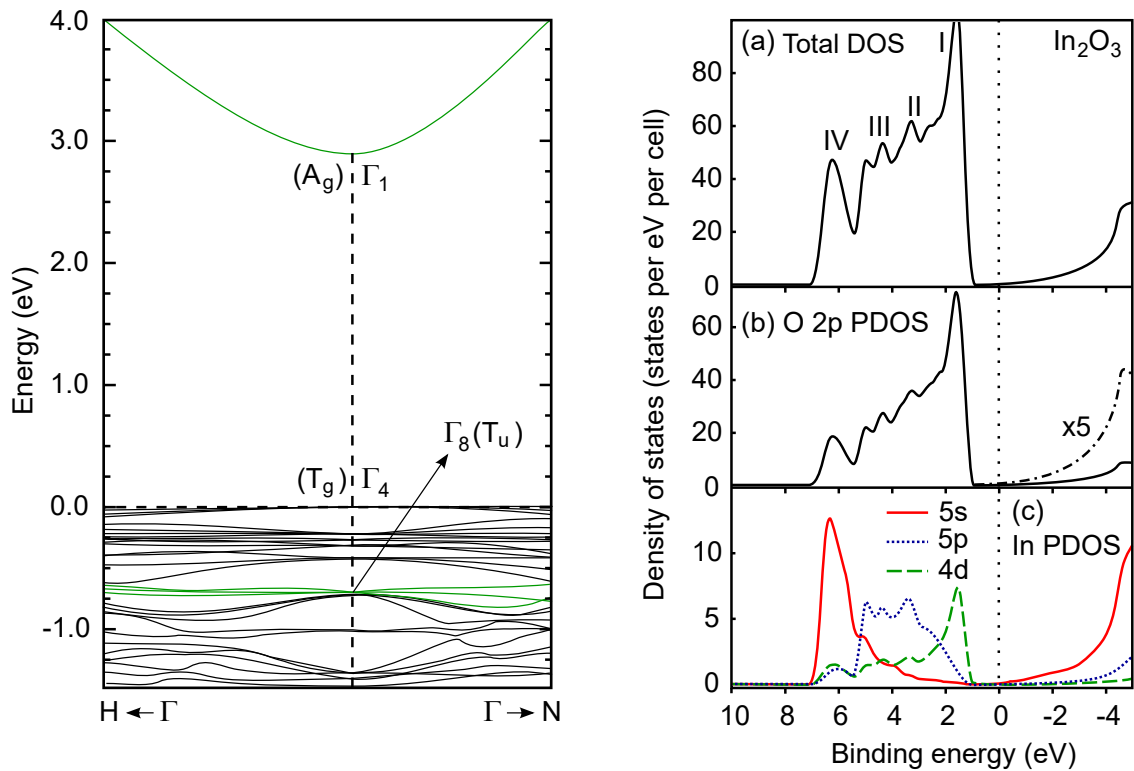


Figure 2.2: Band structure (left) and density of states of In_2O_3 based on DFT calculations (right) [46, 52]. Conduction band minimum and highest valence band allowing for direct optical transitions are indicated in green.

DFT calculations using the local density approximation (LDA) or general gradient approximation (GGA) usually significantly underestimate band gaps [6, 22, 42, 45, 46, 52]. Walsh *et al.* [46] therefore corrected their calculations by matching the empirically and computationally found optical band gaps, i.e. by shifting the conduction band minimum to higher values. This results in a reasonable agreement between the calculated fundamental band gap of 2.89 eV and the experimentally found upper limit for In_2O_3 of 2.9 eV. A corresponding value of 2.93 ± 0.15 eV is reported elsewhere [51].

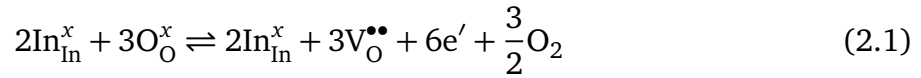
Experimental studies using photoelectron spectroscopy (PES), X-ray emission and X-ray absorption were employed to give prove for the calculated electronic structure [51–53]. PES measurements probe the whole Brillouin zone and therefore provide information about the total valence band density of states [51, 52]. By utilizing different photon energies a variation in the photoionization cross-sections allows to distinguish the orbitals which are involved in the formation of the valence band. X-ray absorption and oxygen K-shell X-ray emission have proven to be suitable tools to investigate the O 2p partial density of states [53].

The total and partial density of states for In_2O_3 are shown on the right of Fig. 2.2 [46, 51–53, 55]. The top of the valence band is dominated by O 2p orbitals with little intermixing of In 4d, while the bottom is dominated by O 2p and In 5s orbitals. The features in the center of the valence band are mostly derived from O 2p and In 5p states. While in the given figure a mixture of In 5s and O 2p gives rise to the conduction band minimum others report O 2s and In 5s interaction to be dominating [45, 56].

2.3 Intrinsic Defects

Already the earliest studies found that electronic and optical properties of unintentionally doped In_2O_3 are strongly influenced by the oxygen partial pressure of the surrounding atmosphere at elevated temperatures [47, 57, 58]. In_2O_3 is indeed a non stoichiometric compound with a ratio of In/O larger than 2/3 under various conditions [59]. As a result it is an n-type semiconductor [9, 21, 57–59].

oxygen vacancies $V_{\text{O}}^{\bullet\bullet}$ are the majority defects in In_2O_3 . The defect chemistry for its generation can be described by the following equation [23, 59]:



From the latter equation it can be seen that by the formation of one oxygen vacancy two free electrons are required to account for the charge neutrality. The free energy for the formation of oxygen vacancies in post-transition metal oxides is rather small [56]. This can explain the high oxygen vacancy concentrations even under equilibrium growth conditions, which make high carrier concentrations of $10^{17} - 10^{19} \text{ cm}^{-3}$ possible [56].

The Mott criterion can be used to distinguish between non-degenerate and degenerate electron concentrations [17].

$$n_{\text{non-degenerate}} < \left(\frac{0.26a_B m^*}{m_e \epsilon_r} \right)^3 < n_{\text{degenerate}} \quad (2.2)$$

With a_B is the hydrogen Bohr radius, m^* the effective electron mass and ϵ_r the low frequency dielectric permittivity. For doped and undoped In_2O_3 , i.e. $\epsilon_r = 9$ and $m^* = 0.3m_e$ the Mott transition is found to be at $5.5 \times 10^{18} \text{ cm}^{-3}$ [17]. This shows that In_2O_3 is for most preparation conditions degenerate considering common carrier concentrations.

2.4 Doped Indiumoxide

Extensive research on improving the electronic and optical properties of In_2O_3 by doping with various elements was carried out. Mainly tetravalent elements were investigated. While a high carrier concentration commonly is beneficial for a high conductivity it as well affects the optical properties.

The carrier concentration depends on the nominal dopant concentration as well as on the dopant element itself. Maximum carrier concentrations n_{max} obtained for differently doped In_2O_3 thin films plotted over the nominal carrier concentration n_{nom} , i.e. n calculated for a doping efficiency of 100%, are shown in Fig. 2.3. n_{max} was taken from conductivity and Hall-effect measurements carried out by members of the surface science or electronic structure of materials group at Technische Universität Darmstadt. The nominal carrier concentration was determined based on the dopant concentration in the sputter

target as specified by the manufacturer. Values for the nominal doping and resulting carrier concentrations are given in Tab. 9.2.

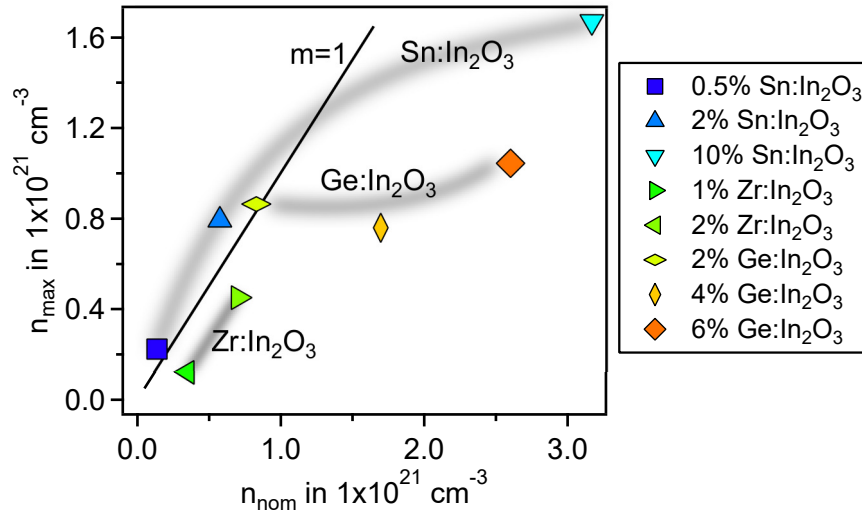


Figure 2.3: Maximum Hall carrier concentration n_{\max} of differently doped In_2O_3 thin films plotted over the nominal carrier concentration n_{nom} . Latter was calculated based on the dopant concentration in the sputter targets.

The black line in Fig. 2.3 passes through the origin and has a slope of one. It therefore represents a doping efficiency of 100%, i.e. each donor leads to one free electron. For low doping concentrations a high doping efficiency is found independent on the dopant element. Increasing dopant concentration leads to an increasing deviation. Unmatched carrier concentrations and overall highest conductivities are obtained for 10% $\text{Sn}:\text{In}_2\text{O}_3$, which is the reason for it being the TCO of highest technological importance.

The influence of doping and its limitations for In_2O_3 will be presented in the following section. Even if $\text{Sn}:\text{In}_2\text{O}_3$ is not the material of main concern in this work, an extensive analysis of its properties will be carried out. It is taken as model TCO due to the broad abundance of literature and research articles.

Doped In_2O_3 still exhibits a bixbyite structure independent on the dopant element [5, 16, 43, 60–65]. Mössbauer spectroscopy on $\text{Sn}:\text{In}_2\text{O}_3$ indicates that the Sn ions occupy the b , i.e. the less distorted octahedra sites [61]. Combined neutron and x-ray diffraction measurements confirm that Sn can be found on indium sites [20]. Dopant ions will be mainly incorporated as substitutional defects below a critical concentration. Due to dissimilar effective ionic radii $r_{i,eff}$ of the native and dopant cation, a variation of the lattice constant is plausible. The effective ionic radii of cations relevant in this work are listed in Tab. 2.1. It can be seen that the potential dopant ions are smaller in size as In^{3+} . According to Vegard’s law, a decreasing lattice parameters should be expected [61, 66]. The majority of publications, however, find an increasing lattice constant with dopant concentration. The incorporation of dopant cations as interstitials, being a possible explanation for increasing lattice constants, can be neglected. Frank *et al.* [21] proposed stronger repulsive forces between the Sn^{4+} ions as possible explanation. Later it will be shown that an increasing donor concentration results in an increasing oxygen interstitial concentration [67], which will also contribute to larger lattice constants.

Table 2.1: Effective radii of sixfold coordinated ions [68].

Ion	$r_{i,eff}$ in nm
In ³⁺	0.08
Sn ⁴⁺	0.069
Zr ⁴⁺	0.078
Ge ⁴⁺	0.053
Mo ⁴⁺	0.065
Mo ⁶⁺	0.059
Ti ⁴⁺	0.061

While oxygen vacancies are the majority defects in undoped In₂O₃, substitutional dopant ions take over in doped In₂O₃ [21]. In an ideal case one free charge carrier is generated for each tetravalent atom on an indium site [43]. The doping efficiency of Sn in Sn:In₂O₃ was found to depend on its concentration. Up to 4 – 6 at% each Sn atom is positioned on an indium site forming Sn_{In}[•]. One free electron is generated per dopant atom [21, 69]. The oxygen vacancy concentration can be neglected, since the majority of free electrons are generated by Sn doping [21]. A lower doping efficiency is observed for higher Sn contents, indicating the formation of compensating defects [48]. A more detailed discussion concerning the defect chemistry will be carried out later.

The carrier concentration of Sn:In₂O₃ thin films deposited by sputter deposition can be varied between 10¹⁸ cm⁻³ to 10²¹ cm⁻³ by adjusting the oxygen partial pressure during deposition [13]. Conductivities of 10⁴ Scm⁻¹ and carrier concentrations of 1.5 × 10²¹ cm⁻³ can be achieved [21, 69].

2.4.1 Defect Structure in ITO

The defect structure of a semiconducting material is ultimately responsible for its carrier concentration and mobility. Having a look how external parameters influence the latter features can therefore help to identify possible defects. The carrier concentration in Sn:In₂O₃ initially increases with increasing dopant concentration [61]. Oxidizing conditions lead to a decreasing carrier concentration independent on the Sn content [13, 21, 61, 69]. Defects due to the dopant itself, as well as oxygen related ones therefore are decisive in the case of Sn:In₂O₃.

As discussed in Sec. 2.4, Sn is found on the *b* cation sites. Since Sn is stable in both the 2+ and the 4+ oxidation state, it could hypothetically act as donor or as acceptor. Mössbauer spectroscopy could show, however, that the oxidation state of Sn is 4+ independent on its concentration [20, 48, 61, 70, 71]. Therefore it is always a donor.

V_O^{••} being the majority defect and donor in In₂O₃, usually is of minor importance in Sn:In₂O₃ except for very low Sn concentrations or oxygen partial pressures. Compensating defects could either be In vacancies or oxygen interstitials. X-ray diffraction studies showed that the formation of V_{In}^{'''} is rather unlikely and O_i^{''} are the most probable charge compensating defects [21]. The oxygen interstitials will be found on the "structural oxygen vacancies", i.e. the *c* lattice sites.

Frank *et al.* [21] carried out an in depth analysis of the defect chemistry in Sn:In₂O₃ depending on oxidation state and dopant concentration. The following defects were proposed to dominate in Sn:In₂O₃: (1) Sn_{In}[•] singly charged donors; (2) V_O^{••} doubly charged donors; (3) (2Sn_{In}[•]O_i'')^x loosely bound, neutral defect associates consisting of one interstitial oxygen on the c site and two Sn_{In}[•], which are not nearest neighbors; (4) (Sn₂O₄)^x and (5) ((2Sn_{In}[•]O_i''))(Sn₂O₄)^x strongly bound neutral defect associates.

Brouwer diagrams are used to display the logarithm of the defect concentration versus the logarithm of the oxygen partial pressure or dopant concentration. Fig. 2.4 shows such diagrams for Sn:In₂O₃ based on a simplified model, i.e. neglecting the defects (4) and (5) [67], as compared to the one proposed by Frank *et al.* [21]. Three regions are found in which different defects dominate the carrier concentration.

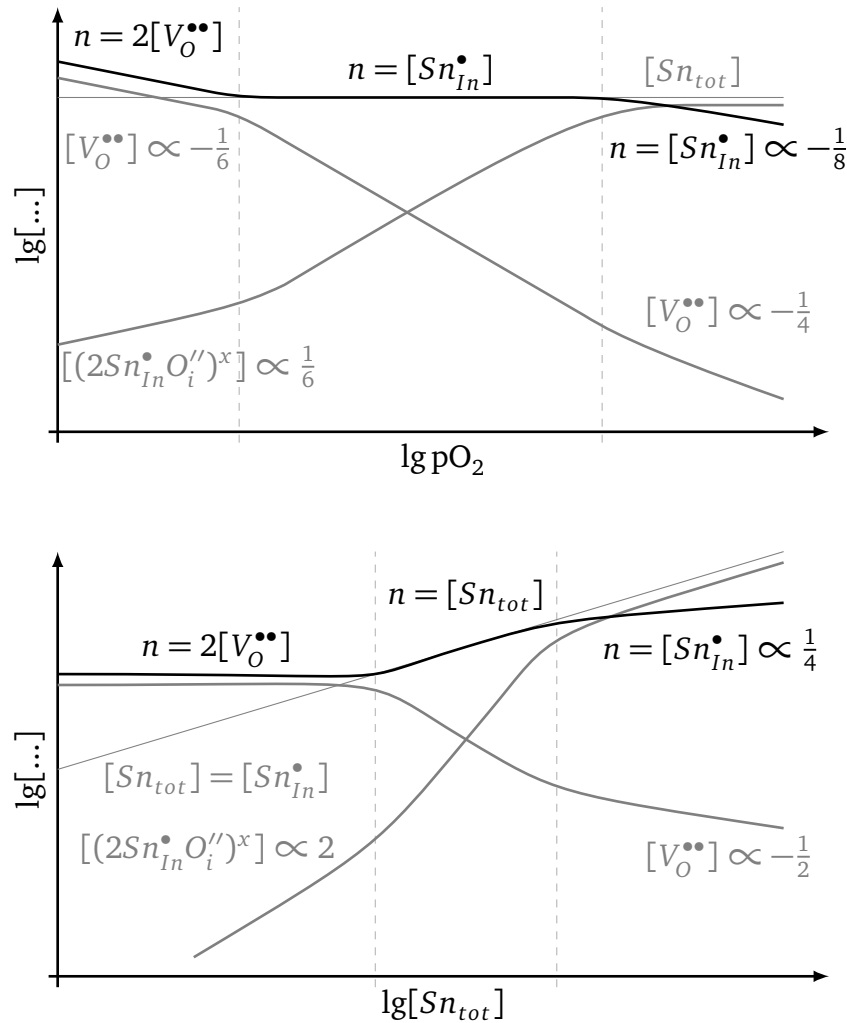


Figure 2.4: Brouwer-diagrams for Sn:In₂O₃ (according to [67]). The logarithm of carrier and defect concentration plotted over the logarithm of either the oxygen partial pressure (top) or Sn concentration (bottom).

At low oxygen pressures and tin contents, n is defined by the oxygen vacancy concentration: $n = 2[V_O^{\bullet\bullet}] \propto pO_2^{-1/6}$. At intermediate oxygen partial pressures and tin concentrations, $V_O^{\bullet\bullet}$ and neutral defect associates are minority species and n is proportional to the dopant concentration: $n = [Sn_{In}^{\bullet}] \propto pO_2^0 [Sn]^1$. For high oxygen partial pressures and

Sn concentrations, $(2\text{Sn}_{\text{In}}^{\bullet}\text{O}_i^{\prime\prime})^x$ defect associates are majority species and n is determined by the concentration of the unassociated Sn atoms: $n = [\text{Sn}_{\text{In}}^{\bullet}] \propto p\text{O}_2^{-1/8}$, $n \propto [\text{Sn}]^{1/4}$. The proportionality factors, i.e. the slopes in the Brouwer diagrams, are based on defect equations and charge neutrality considerations and supported by experimental results [20, 21, 67].

Films can be overreduced. This means annealing at too high temperatures, for long times, under reducing conditions leads to a full loss of conductivity and dark films. This is the only exception when the carrier concentration in Sn:In₂O₃ is determined by the oxygen vacancy concentration. Since more free charge carriers are generated by the formation of oxygen vacancies the mobility decreases, resulting in the loss of conductivity. Surpassing a critical value leads to decomposition of the crystal structure and the formation of metallic In precipitates. Doping shifts the oxygen partial pressure at which decomposition occurs to lower values [21].

Even though the latter model is widely accepted, some of the experimental validation is under criticism since it assumes a constant carrier mobility [20, 67]. In the following section it will be shown that this is an unreasonable precondition. Irrespective of this error, the outlined defect model is suitable to describe the effects of varying oxygen or Sn concentration in Sn:In₂O₃.

2.4.2 Electronic Properties

The electronic conductivity of a material is determined by the concentration, mobility and charge q of the free carriers as described by Eq. 2.3 [72]:

$$\sigma = qn\mu \quad (2.3)$$

The carrier concentration is significantly affected by doping as was discussed in the previous section. The highest conductivity for In₂O₃ based TCOs is achieved when doped with Sn. While huge carrier concentrations extending up to $1.5 \times 10^{21} \text{ cm}^{-3}$ [21, 69] are responsible for the high conductivity in this case, it is a high mobility for other dopants. Mobilities up to $120 \text{ cm}^2(\text{Vs})^{-1}$ are reported for titanium doped In₂O₃ but are still exceeded by zirconium doped In₂O₃ [9].

The electronic film properties are strongly influenced by the deposition conditions [60]. Annealing at different oxygen partial pressures has a similar effect [21]. As discussed in Sec. 2.4.1, an enhanced oxygen incorporation leads to a decreasing carrier concentration. For Sn:In₂O₃, neutral $(2\text{Sn}_{\text{In}}^{\bullet}\text{O}_i^{\prime\prime})^x$ defect complexes were found to decrease the effective dopant concentration. The mobility shows a more complex behavior [13, 60]. Depending on n_{Hall} , a maximum in the mobility is visible [9, 48].

The solubility limit of Sn in In₂O₃ depends on the sample type. While $\approx 6 \text{ at\%}$ Sn is found for sintered powders [21, 69], higher values are reported for thin films or nanocrystalline samples [20]. Highest Sn concentrations are obtained by preparation techniques as sputtering or other non-equilibrium methods, which result in metastable phases [20].

Frank *et al.* [21] report a monotonically decreasing mobility with increasing doping concentration. A maximum in conductivity and carrier concentration is seen around the solubility limit.

The correlation between carrier mobility and concentration for a variety of dopants in polycrystalline films is shown in Fig. 2.5. Beside dopant element and concentration, the deposition conditions are crucial for the electronic film properties which explains the large variation. The black solid line represents a calculated mobility limit for doped In_2O_3 single crystals [17]. For some dopants, a rather good agreement between theoretical calculation and experimental data is found, when only the maximum mobility values above a certain carrier concentration are considered. This means that for the undoped, Sn and Ge doped films the mobility limit at highest carrier concentrations is indeed given by the mobility in In_2O_3 single crystals. All films show a strong deviation from the single crystal model for lower carrier concentrations. Polycrystalline Zr and Ti as well as epitaxial Sn doped In_2O_3 thin films show mobilities exceeding the theoretical values around a carrier concentration of 10^{20} cm^{-3} .

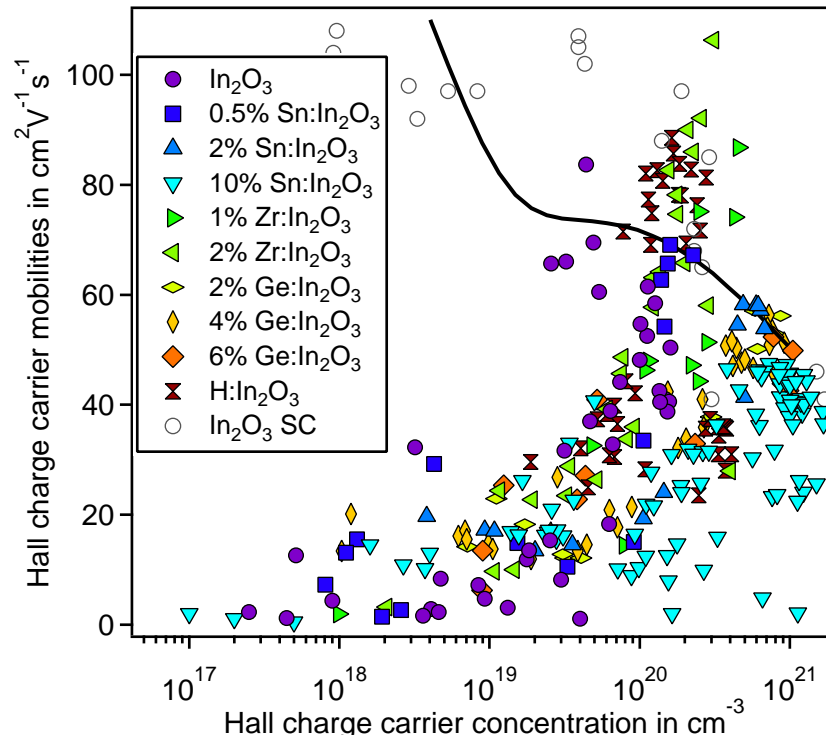


Figure 2.5: Hall carrier mobility plotted over the logarithm of the Hall carrier concentration of doped In_2O_3 thin films. Colored markers represent samples prepared and measured by members of the OF and ESM groups, open circles data for epitaxial In_2O_3 or $\text{Sn:In}_2\text{O}_3$ films [17]. Variation of the deposition conditions, i.e. deposition temperature and oxygen content, leads to the diversity of electronic properties for a single dopant type and concentration. The solid black line indicates the theoretical mobility limit for In_2O_3 single crystals [17].

One key aspect is the influence of different scattering mechanisms on the carrier mobility. Electron-defect, electron-lattice (phonon) and electron-electron interaction can lead to scattering. Following defects are possible scattering centers: ionized and neutral impu-

rities, external surfaces, grain boundaries and dislocations [4, 13, 43]. A differentiation between the mechanisms and scattering centers is not straightforward [13]. For TCOs, mostly grain boundary and ionized impurity scattering are to be expected [13, 15]. The coexistence of different phases can also not be neglected due to their generally high dopant concentration [13].

Starting the investigations on single crystalline material allows to neglect scattering at grain boundaries and focus on other mechanisms. Preissler *et al.* [17] therefore examine the electrical transport in single crystalline In_2O_3 and $\text{Sn}:\text{In}_2\text{O}_3$. A comparison between experimental data and a theoretical model, considering ionized impurity and phonon scattering, was carried out. Their calculations for ionized impurity scattering are based on doubly charged oxygen vacancies and singly ionized $\text{Sn}_{\text{In}}^\bullet$. Oxygen interstitials, being known as defects in $\text{Sn}:\text{In}_2\text{O}_3$, are not considered. Due to the low ionization energy of donor atoms in TCOs (< 50 meV) and therefore the negligible concentration of neutral impurities, scattering at the latter can also be neglected [4]. Polar optical phonons are found to be dominating scattering centers over a wide range of electron concentrations. A change to ionized impurity scattering occurs for highest concentrations. Acoustic phonon scattering is always negligible. Simulation and experimental data match reasonably well for high and low carrier concentrations. However, the simulations underestimate mobilities around $n \approx 10^{20} \text{ cm}^{-3}$ [17]. The origin for those high mobilities is still unclear [15].

Carrier transport in polycrystalline TCO thin films was discussed controversially. Grain boundaries have to be considered going from single crystals to polycrystalline thin films. They constitute imperfections in the crystal structure and therefore electronic defects [4]. Several of the earlier articles report an increasing mobility up to a critical carrier concentration, which was explained by the presence of electron barriers at the grain boundaries due to depletion layers. As soon as this n is exceeded the barriers will not contribute to scattering anymore and ionized impurity scattering will dominate [73–75]. Others report ionized impurity scattering as the mobility determining mechanism independent on the carrier concentration [2, 43, 71, 76, 77]. No differences should therefore be expected for single crystalline samples and polycrystalline thin films.

More recent articles nonetheless prove the dominance of grain boundaries under certain conditions in polycrystalline TCO thin films [2, 4, 15]. Minami *et al.* [2] showed that, depending on the carrier concentration, the Hall mobility in doped and undoped ZnO is either well described by scattering at grain boundaries (low n_{Hall}) or at ionized impurities (high n_{Hall}). Similar observations were later as well made for $\text{Sn}:\text{In}_2\text{O}_3$ [4]. Mobility values match calculations for single crystal data when a carrier concentration of 10^{20} cm^{-3} is exceeded. Grain boundary barriers vanish completely due to the high carrier concentrations and do not act as scattering centers anymore [4].

Scattering at grain barriers was first described on the example of polycrystalline silicon by Seto [78]. Charging of the defects, introduced by breaking the crystal symmetry, with carriers from the grains may result in depletion zones and electrostatic potential barriers between them. The latter model is not suited for degenerately doped semiconductors since it presumes the depletion approximation. The Kazmerski model expresses the mobility in

polycrystalline materials as the product of a mobility in the grain, i.e. the mobility in a single crystal and the thermionic emissions across the grain barriers [15]:

$$\mu_{\text{poly}} = \mu_g(T, n) \exp\left(\frac{E_B}{k_B T}\right) \quad (2.4)$$

with $\mu_g(T, n)$ the temperature and carrier concentration dependent single crystal mobility.

Temperature dependent Hall-effect measurements on differently doped In_2O_3 thin films lead to the result that grain boundary scattering can influence the carrier mobility up to carrier concentrations of 10^{21} cm^{-3} [15]. Dopant species and especially segregation at the grain boundaries influence the mobilities. Simulation of the grain boundary barrier height directly show a decreasing energy barrier with increasing carrier concentration. This behavior can be explained by a decreasing barrier height with increasing Fermi energy due to a better screening of the charged defects at the grain boundaries. Typical barrier heights amount up to 100 meV. Comparing the barriers obtained for various dopants at an electron concentration of 10^{20} cm^{-3} a clear dependence on concentration and species is found. The high barriers found for $\text{Sn}:\text{In}_2\text{O}_3$ are likely related to Sn segregation at the grain boundaries.

To conclude this section the main points describing the transport properties in doped In_2O_3 , relevant for this work, are summarized in the following list.

- (i) decreasing mobility for very high carrier concentrations is explained by ionized impurity scattering
- (ii) decreasing mobility with decreasing carrier concentration in polycrystalline films is related to scattering at grain boundaries, i.e. an increasing grain boundary barrier height
- (iii) different barrier heights at similar carrier concentrations are obtained depending on dopant species, dopant segregation may be determining
- (iv) poly and single crystalline samples may exceed the theoretical mobility limit at $n \approx 10^{20} - 10^{21} \text{ cm}^{-3}$

2.4.3 Surface Potentials

TCOs are used as electrodes in a variety of applications. Besides the necessity of a high conductivity, an efficient carrier injection or extraction into the TCO is crucial. The efficiency is determined by the work function $\phi = E_{\text{vac}} - E_F$. The latter parameter is affected by a variation of either the distance between Fermi energy and valence band maximum $E_F - E_{\text{VBM}}$ or the surface dipole [27, 28]. Isolated values for the work function therefore do not allow a distinction of both effects. It is necessary to know $E_F - E_{\text{VBM}}$ and ϕ or the ionization potential $I_p = E_{\text{vac}} - E_{\text{VBM}}$, which is directly correlated to the surface dipole.

The influence of the deposition and post-deposition treatment on the surface potential of In_2O_3 and $\text{Sn}:\text{In}_2\text{O}_3$ were already extensively studied [27, 28, 32]. Different carrier

concentrations result, for example, in a variation of $E_F - E_{\text{VBM}}$, which in turn affects the work function. The atomic arrangement at the surface decides about the surface potential. Termination, i.e. by oxygen ions or cations as well as polar adsorbates are important factors. A larger surface dipole is generally obtained for a more negative surface charge. It has also been shown that the chemical potentials of the elements forming a compound influence its surface potential. This means that for example the oxygen partial pressure affects the I_p of an oxide [32].

In the case of ionic or partially ionic materials, the surface dipole is also expected to depend on the crystallographic orientation [28, 29]. Tasker *et al.* [34] classified the surfaces of fluorite-type crystals into three categories. Type I, stoichiometric ratio of anions and cations forming neutral surfaces; type II, charged surfaces with no perpendicular dipole moment; type III, polar surfaces exhibiting a dipole moment perpendicular to the surface. For the fluorite or bixbyte structure, a (110) oriented surface corresponds to Tasker type I, a (111) surface to a Tasker type II and a (100) surface to a Tasker type III surface. Agoston *et al.* [7] calculated the surface tension γ for In_2O_3 . It was shown that the stability of stoichiometric surfaces follows $\gamma(111) < \gamma(110) < \gamma(100)$. A variation in surface energy in dependence of the oxygen chemical potential was found as well. While the stoichiometric (111) surface is the most stable one over a large range of oxygen chemical potentials, (100) surfaces are either for very high or low values more stable. Hohmann *et al.* [29] demonstrated that the ionization potentials of epitaxial In_2O_3 thin films grown on yttria stabilized zirconia (YSZ) single crystals are indeed orientation dependent. They may differ between 7.7 eV and 7.0 eV for (100) and (111) oriented films, if grown under strongly reducing or oxidizing conditions, respectively. Similar experiments were as well carried out for 10 wt% Sn: In_2O_3 leading to the formation of facets with (111) orientation on the nominally (100) oriented thin film [27].

The ionization potentials and work functions of polycrystalline In_2O_3 thin films were found to depend on the dopant [32]. A rather constant I_p of the as deposited films was found for each dopant. A variation of the work function is therefore exclusively related to changing Fermi level positions. Ionization potentials around 7.0 eV are found for undoped In_2O_3 , while values of 7.7 eV are found for Sn: In_2O_3 . As previously discussed, dopant segregation is a present phenomenon in Sn: In_2O_3 thin films. A SnO or SnO₂ layer at the surface therefore may set I_p in Sn: In_2O_3 .

Post deposition treatments are known to influence the surface potentials [27, 28, 32]. Highly oxidizing procedures, such as annealing in oxygen containing atmospheres, ozone or oxygen plasma treatments, significantly affect both the surface dipole and the Fermi level position. While these lead to an increasing surface dipole and further to a decreasing Fermi energy, other treatments have an opposite effect. Ar-ion etching or exposure to H₂O vapor, for example, lead to a reduction of the surface and therefore to a decreasing I_p and increasing $E_F - E_{\text{VBM}}$.

In summary, deposition conditions affect work functions mostly due to a variation of $E_F - E_{\text{VBM}}$. Different dopant elements can influence the surface dipole, probably via surface segregation. Post deposition treatments may affect both.

3 Methodology

The characterization and preparation methods, most important for this thesis, will be introduced in the following. Most of the applied methods were thoroughly discussed in previous Ph.D. theses of this group [37–39, 79]. Only a brief summary about X-ray diffraction (XRD), photoelectron spectroscopy, conductivity and Hall-effect measurements as well as magnetron sputtering will therefore be given here. Even though the optical characterization of thin films is of likewise importance as other methods, special attention will be paid in this chapter. The primary reason is a limited abundance of concerning information in previously written theses.

3.1 Optical Characterization of Thin Films

Optical characterization of thin films can be used to obtain a variety of information. Film thickness, refractive index and extinction coefficient are among the most common investigated parameters [80]. While there are several different methods for the optical characterization of thin films, only the two relevant in the context of this work will be introduced here.

Spectrophotometry can be used to acquire intensity transmission and reflection data while changes of polarization upon reflection can be investigated with spectroscopic ellipsometry (SE). The latter is often considered as the method of choice regarding the determination of dielectric functions of thin films [81]. Due to the different information provided by intensity and polarization data, however, more insight into the interaction of electromagnetic radiation with a material is obtained by using both methods [82]. The high surface sensitivity of ellipsometry is combined with the more bulk sensitive spectrophotometry data [83, 84].

Before an introduction into the optical characterization of thin films is given, a brief discussion about the interaction of electromagnetic radiation and matter, neglecting non-linear effects will be carried out. Non magnetic, isotropic media are assumed. For more detailed information see references [80, 85–87].

3.1.1 Light and its Interaction with Matter

Light is defined as a transversal electromagnetic wave in a wavelength region of roughly 10^6 nm to 10 nm [86]. Neglecting the magnetic component of the wave, light may be described only by the real part of the electric field vector $\vec{E}(z, t)$. Assuming a monochromatic plane wave propagating along the z-direction, $\vec{E}(z, t)$ can be described as a combination of two waves with the complex amplitudes E_x and E_y pointing either in x or y direction. A formula for this case is given by Eq. 3.1 [86].

$$\vec{E}(z, t) = \text{Re} \left\{ \begin{pmatrix} E_x \\ E_y \end{pmatrix} e^{i(k_z z - \omega t)} \right\} \quad (3.1)$$

k_z is the non vanishing component of the propagation vector and ω the angular frequency. The trajectory, which is described by the projection of \vec{E} onto a plane normal to the propagation direction at any z , can be used to distinguish between different polarization states of the light.

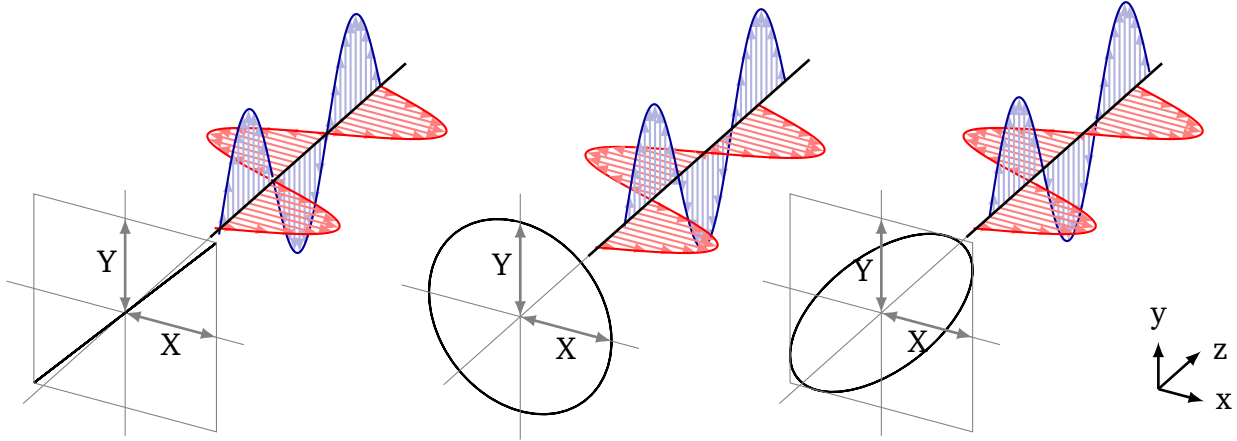


Figure 3.1: From left to right: x and y components of a monochromatic wave propagating along the z-direction with $X=Y$ for different relative phase shifts Δ resulting in linear, circular or elliptic polarized light.

Examples for the three different kinds of polarization, i.e. linear, circular and elliptic are given in Fig. 3.1 from left to right. The amplitudes X and Y in the corresponding direction are kept constant while the phase difference Δ between $\vec{E}_x(z, t)$, displayed in red, and $\vec{E}_y(z, t)$, displayed in blue is varied. The projected trajectory of $\vec{E}(t)$ onto a plane normal to the propagation direction is shown for all three cases. Elliptic polarization is the most general case. Under certain conditions the ellipse collapses either to a line or forms a circle, resulting in linear or circular polarized light. Linear polarized light is obtained for $\Delta = 0$ or $\Delta = \pi$ independent on the ratio X/Y . Circular polarized light requires a ratio $X/Y = 1$ and $\Delta = \pm\pi/2$.

On the left hand side of Fig. 3.2 light incident on a parallel film on a substrate is shown. It is assumed that the structure is in vacuum and all media possess different complex refractive indexes \tilde{n}_v , \tilde{n}_f and \tilde{n}_s . The complex refractive index \tilde{n} is defined as:

$$\tilde{n} = n + ik \tag{3.2}$$

The real part n is called refractive index and the imaginary part k extinction coefficient. For non absorbing media k is zero. As can be seen in Fig. 3.2, when light passes from one media into another, a part of it is reflected at the interface, a part transmitted and a part absorbed. The light will be reflected many times at the top and bottom interface of each layer, even though only a single reflection in the thin film is shown. Light may be absorbed in the substrate as well. Due to energy conservation, the intensity of reflected, transmitted and absorbed light, I_R , I_T and I_A , is required to add up to I_0 , the intensity of the incident light.

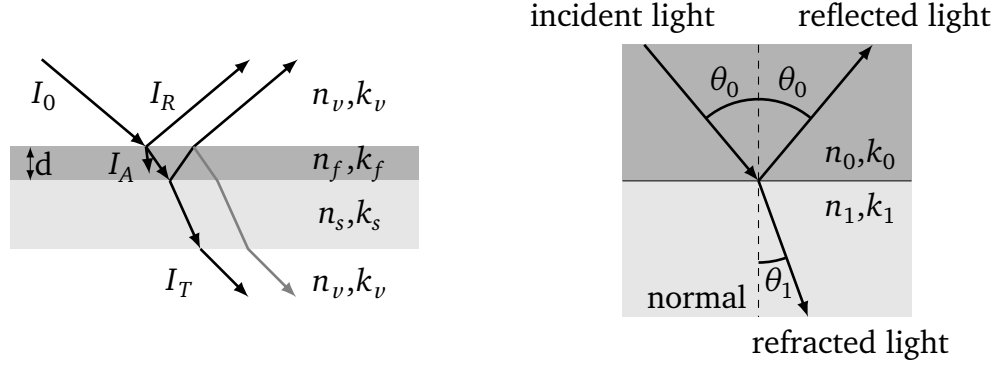


Figure 3.2: Transmission and reflection of a thin film on a thick substrate on the left. Angular correlation between incident, reflected and refracted light at the interface of two half spaces is shown on the right.

$$I_0 = I_R + I_T + I_A \quad \text{or} \quad 1 = \frac{I_R}{I_0} + \frac{I_T}{I_0} + \frac{I_A}{I_0} = R + T + A \quad (3.3)$$

The ratios of reflected, transmitted and absorbed intensity relative to the incident intensity are called reflectance R , transmittance T and absorptance A , respectively. For the example discussed here, diffuse scattering is neglected.

Angular correlations between incident, reflected and refracted light are shown in Fig. 3.2 on the right. For specular (regular) reflection the angle between surface normal and wave vector of the reflected light, is equal to the angle of incidence θ_0 , defined as the angle between wave vector of incident light and surface normal. The angle between the wave vector of transmitted light and the surface normal θ_1 is related to the angle of incidence via the ratio of refractive indexes of the adjacent media as described by Snell's law given in Eq. 3.4.

$$\frac{n_0}{n_1} = \frac{\sin \theta_1}{\sin \theta_0} \quad (3.4)$$

In Fig. 3.3 the electronic components of linear polarized light, with two different polarization directions, are sketched as they are reflected and transmitted at a single interface between two media, possessing refractive indexes n_0 and n_1 ($k_0 = k_1 = 0$). In this configuration it is common to distinguish between s- and p- polarized light. Depending on the orientation of the electric field vector of the incoming light relative to the plane of incidence, which is spanned by the surface normal of the plane of reflection and the wave vector of the light, the differentiation is carried out. The electric field vector of s-polarized light is oriented perpendicular to the plane of incidence while it is parallel for p-polarized light. The letters s and p stem from the German words "Senkrecht" and "Parallel". As can be seen, the amplitude of reflected and transmitted light directly depends on whether s- or p-polarized light is incident. Based on Maxwell's equations, the amplitude coefficients for

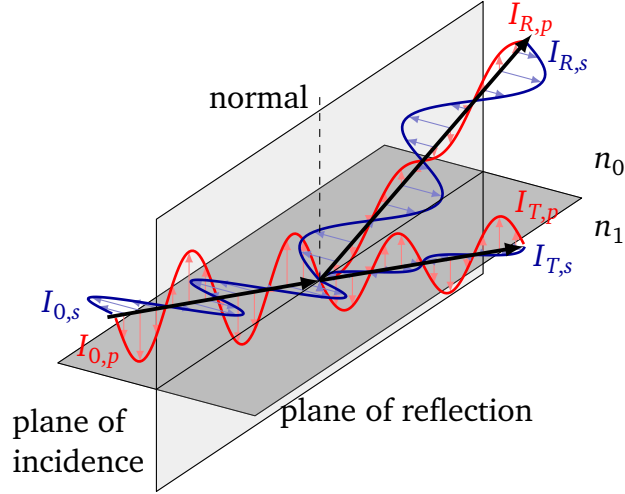


Figure 3.3: Amplitude change of p-polarized (red) and s-polarized (blue) light upon reflection and transmission at a surface. Only the electric component of the electromagnetic radiation is displayed.

reflection r_s and r_p and transmission t_s and t_p at a single boundary between two materials can be calculated and are represented by the Fresnel equations:

$$r_s = \frac{n_0 \cos \theta_0 - n_1 \cos \theta_1}{n_0 \cos \theta_0 + n_1 \cos \theta_1} \quad (3.5)$$

$$r_p = \frac{n_1 \cos \theta_0 - n_0 \cos \theta_1}{n_1 \cos \theta_0 + n_0 \cos \theta_1} \quad (3.6)$$

$$t_s = \frac{2n_0 \cos \theta_0}{n_0 \cos \theta_0 + n_1 \cos \theta_1} \quad (3.7)$$

$$t_p = \frac{2n_0 \cos \theta_0}{n_1 \cos \theta_0 + n_0 \cos \theta_1} \quad (3.8)$$

Combining the Fresnel equations and Snell's law, intensity reflection coefficients R_s and R_p , being the square of r_s and r_p and intensity transmission T_s and T_p coefficients can be calculated as function of incident angle and refractive indexes. R_s and R_p are displayed in Fig. 3.4 as function of the incident angle. Extinction coefficients of zero, $n_0 = 1$ and $n_1 = 1.7$ were chosen to simulate conditions as for visible light being reflected at an air/glass boundary.

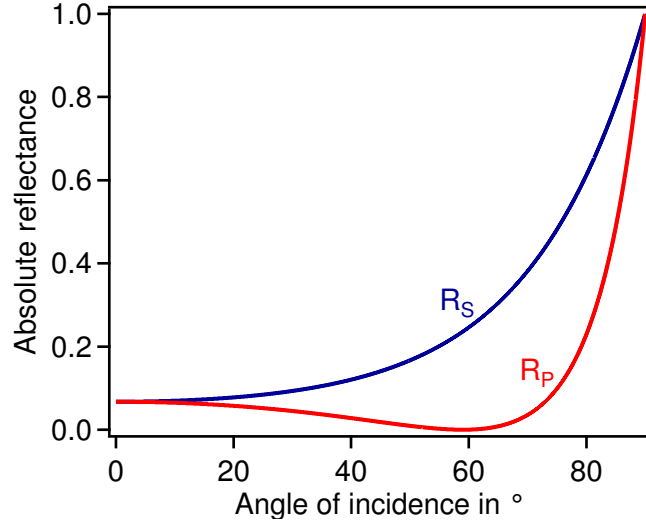


Figure 3.4: R_s and R_p as function of the angle of incidence calculated using Fresnel's equations and Snell's law. Non absorbing media, i.e. $k_{1,2}=0$, with refractive indexes of $n_0=1$ and $n_1=1.7$ are assumed. The given conditions represent the case of light in the visible range being reflected at the boundary between two half spaces of air and glass.

R_s is monotonically increasing while R_p first decreases reaching 0 at approximately 60° before increasing as well. When $n_0 < n_1$ the intensity reflection coefficient R_p equals zero at a certain angle of incidence, which is called Brewster or polarizing angle θ_B :

$$\tan \theta_B = \frac{n_1}{n_0} \quad (3.9)$$

At normal incidence both intensity reflection coefficients are equal.

Going from a single interface to reflection/transmission at two or more interfaces, interference phenomena have to be considered. They will occur when the coherence length of the light is comparable to the film thickness d and when the following equation is valid:

$$\Delta\lambda \ll \frac{\lambda^2}{2\pi nd} \quad (3.10)$$

with $\Delta\lambda$ the spectral bandwidth and λ the wavelength. Interference patterns will be present in both T and R spectra as periodic modulation, where magnitude and period length depend on film thickness and complex refractive index.

Maxwell's equations can be used to exactly describe the interaction of light with matter in a classical approach [87, 88]. Qualitatively, it can be said that an electric polarization P is induced in matter when exposed to electromagnetic radiation E as described by Eq. 3.11 [89].

$$P = \epsilon_0 \chi E \quad (3.11)$$

ϵ_0 is the permittivity of free space and χ the dielectric susceptibility of the material. The dielectric susceptibility is the sum over all individual susceptibilities χ_i based on different physical polarization mechanisms. The complex dielectric function ϵ is then given by:

$$\epsilon = 1 + \sum_i \chi_i \quad (3.12)$$

As the ability of a material to be polarized can be described by its complex dielectric function ϵ , a correlation between the latter and the complex refractive index \tilde{n} is evident. Since ϵ is a function of frequency, the complex refractive index will be as well. In case of non magnetic materials, optical properties are fully described by their dielectric function as shown by the following equations:

$$\epsilon(\omega) = \tilde{n}^2 \quad (3.13)$$

$$\epsilon' + i\epsilon'' = (n + ik)^2 \quad (3.14)$$

ϵ' and ϵ'' represent the real and the imaginary component of the dielectric function. Several phenomena contribute to the polarization and therefore to the dielectric function depending on the frequency of electric field as shown schematically in Fig. 3.5. Different mathematical expressions can be used to describe the features. Orientation polarization of permanent dipoles by the Debye equation, free electrons by the Drude formula and absorption or dispersion processes by an oscillator model e.g. the Lorentz model.

Different phenomena are dominant over certain frequency ranges, therefore it is possible to describe the dispersion relation of the dielectric function as a sum with one term for each contribution.

Several articles, concerned with the determination of the refractive index and extinction coefficient, discuss the angular sensitivity of the measurements [90–94]. Even though the proposed methods differ from the simulations applied here, the findings are expected to still hold true. Depending on n and k different optimum angles of incident are found. The tendency of an increasing accuracy with larger angles is nonetheless true independent on the latter parameters.

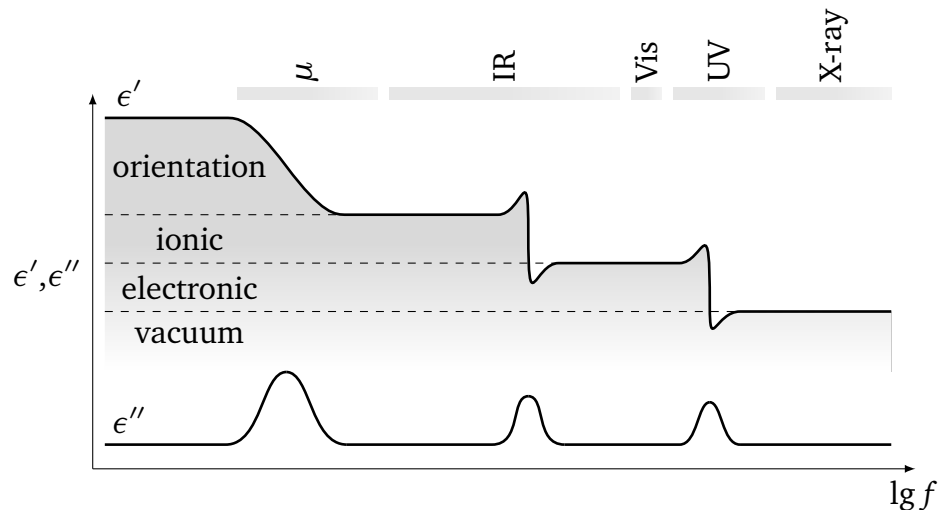


Figure 3.5: Real and imaginary part of the dielectric function of a polar crystal as a function of the frequency.

3.1.2 Spectrophotometry

Spectrophotometry is a method for which reflected and/or transmitted intensity are measured in a certain wavelength range. Several techniques and setups exist for measuring e.g. specular or diffuse transmission and reflection, some with the necessity of well defined standards. Sample and desired information hereby dictate, which technique is suitable. For the samples being of concern in this thesis, only a minor fraction of the light is reflected or transmitted diffusely. Therefore a dual beam spectrophotometer capable of measuring specular reflection and transmission at variable incident angles is suited. In a double beam spectrophotometer, the sample and the reference beam intensities are constantly compared to obtain information about attenuation of the sample beam. The advantage of this procedure is that a fluctuation in light intensity during a measurement does not alter the resulting spectra.

3.1.3 Spectroscopic Ellipsometry

Phase and amplitude changes of the s and p components of light, most commonly after reflection, are investigated with ellipsometry. In the case of spectroscopic ellipsometry the measurement is carried out over a certain range instead of a single wavelength. As schematically shown in Fig. 3.6 a sample will be exposed to linear polarized light of known polarization angle and a phase shift. The change in polarization state upon reflection is then analyzed and evaluated.

The polarizer is used to obtain linearly polarized light of known polarization angle and the retarder to adjust the phase shift between the s and p component. The retarder is optional, depending on which parameters shall be obtained. In case of a rotating analyzer ellipsometer, the polarizer remains fixed during a measurement while the analyzer is rotated and therefore used to determine the polarization state of the reflected light.

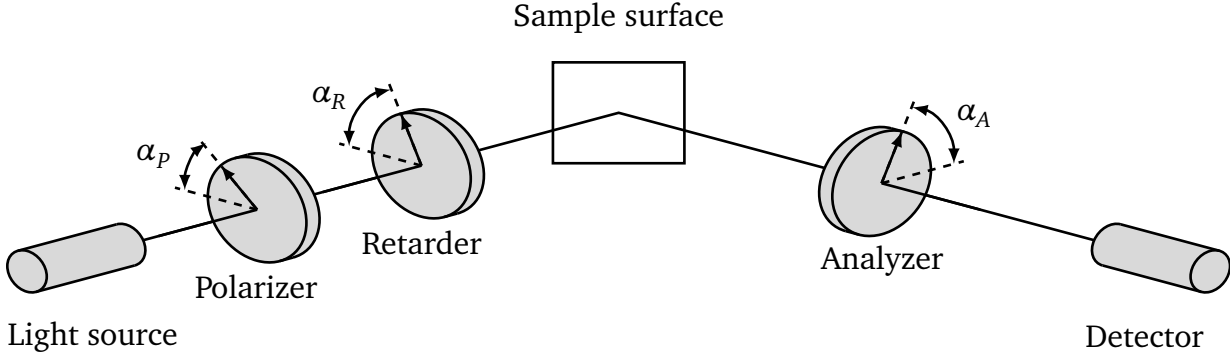


Figure 3.6: Schematic setup of the used spectroscopic ellipsometer.

In Sec. 3.1.1 it was shown that the reflectance of s and p polarized light differ depending on incident angle and complex refractive index of adjacent media. Further a phase difference upon reflection between r_s and r_p can occur for anisotropic media or thin films. Thus when linear polarized light is reflected, its polarization will change. The angle and/or the phase may be influenced resulting in an elliptic polarization. The fundamental parameters of spectroscopic ellipsometry are Ψ and Δ , the first being correlated to the intensity ratio and the second to the phase difference. They are defined as:

$$\frac{r_s}{r_p} = \tan \Psi e^{i\Delta} \quad (3.15)$$

$$\tan \Psi = \frac{|r_s|}{|r_p|} \quad \text{and} \quad \Delta = \delta_s - \delta_p \quad (3.16)$$

with δ_s and δ_p being the absolute phase of the s and p component.

Measurements over a spectral range covering UV-Vis and NIR are commonly realized by combining a photometric ellipsometer with a Fourier transform spectrometer, i.e. an interferometer is introduced into the setup shown in Fig. 3.6. Performing measurements at least at three different polarization angles, i.e. $\alpha_p = 0^\circ, 45^\circ, 90^\circ$, either Ψ and Δ or $S_1 = \frac{s_1}{s_0} = -\cos 2\Psi$ and $S_2 = \frac{s_2}{s_0} = \sin 2\Psi \cos \Delta$ can be calculated. To obtain the first pair of parameters, a retarder is required. S_1 and S_2 are called Fourier coefficients, s_0 to s_2 Stokes parameters.

3.1.4 Modeling of Optical Spectra

Explicit equations to calculate transmittance and absorptance spectra for a single interface scenario were given in Sec. 3.1.1. Similar equations can be formulated for ellipsometry parameters. This is possible even for thin films on thick substrates or multilayer systems. One prerequisite is that the complex refractive index of all materials is known. Furthermore, the film thickness d has a significant influence on the results. In most scenarios, how-

ever, the complex refractive index and film thickness are not known and it is of interest to determine them from optical spectra.

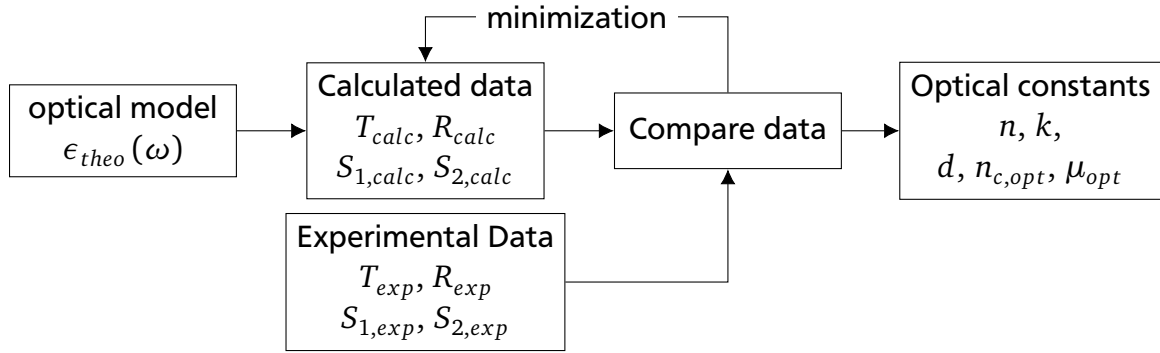


Figure 3.7: Flow chart visualizing the basic process to model optical spectra

While there are several different approaches, only the method of solving a minimization problem will be discussed here. The basic procedure is visualized in the flow chart in Fig. 3.7. The starting point is a model describing the dielectric function over the wavelength range of interest. Choosing appropriate starting conditions, spectra for all quantities of interest are calculated. These are compared to the experimentally obtained spectra and a minimization problem, as exemplarily shown in Eq. 3.17 for transmittance and reflectance data, is solved.

$$J = \frac{1}{j} \sum_j \{ [T_{calc}(v_j) - T_{exp}(v_j)]^2 + [R_{calc}(v_j) - R_{exp}(v_j)]^2 \} \quad (3.17)$$

Where $T_{calc}(v_j)$ and $R_{calc}(v_j)$ are the calculated values and $T_{exp}(v_j)$ and $R_{exp}(v_j)$ the measured values. The mean squared deviation J is minimized by varying the parameters of the complex refractive index model. When an appropriate model and starting conditions were chosen, this fitting procedure will lead to the desired parameters.

Physically reasonable parameters and a high fit quality do not necessarily go together. A physically inadequate model may lead to a good fit but will result in parameters, which are completely unreasonable. Furthermore, great care has to be taken when choosing the starting conditions. A downhill simplex method may not end up in the global minimum when the starting conditions were too close to a local minimum.

3.1.5 Dielectric Model for doped In_2O_3

The model used in this work to describe the optical properties of doped and undoped In_2O_3 is also discussed by other authors [81, 89]. It consists of four parts and is given by

$$\chi(\omega) = \epsilon_B + \chi_{BG}(\omega) + \chi_{UV}(\omega) + \chi_D(\omega) \quad (3.18)$$

ϵ_B is not frequency dependent and is required to model the dielectric background.

Based on the model introduced by O'Leary et al. [95], called O'Leary-Johnson-Lim model (OJL), the band-gap absorption is described by $\chi_{BG}(\omega)$. It was proposed to model the band gap of amorphous silicon but leads to qualitatively acceptable results for degenerately doped TCOs [81, 89, 96]. It assumes completely filled or empty, parabolic valence or conduction bands respectively and exponentially decaying tail states. Since this is not true for degenerately doped TCOs it is questionable whether the band gap values obtained in this way are correct [81]. The combined density of states based on the assumptions made here is proportional to the imaginary part of the dielectric function, which in turn can be used to obtain the real part by using the Kramers-Kronig-Relation [89].

An empirical term required for a good fit of the UV region is represented by $\chi_{UV}(\omega)$. A harmonic oscillator with an extension, allowing to shift from a Gaussian to a Lorentzian line shape, as suggested by Kim et al. [97] is used. The necessity of this part may be due to the inaccuracy of the OJL model [81]. The dielectric spectrum of a semiconductor in the UV region contains several critical points and lines. Since only the low energy tail (below 5 eV or 40000 cm^{-1}) is of interest here, it has been suggested that it is sufficient to use a single oscillator [89].

The susceptibility of free electrons χ_{Drude} is modeled by the Drude formula [43, 89]. Amongst others, charge carrier concentration, mobility and conductivity can be obtained from the parameters of this part.

$$\chi_{Drude}(\omega) = -\frac{\Omega_{Drude}^2}{\omega^2 + i\omega\Gamma_{Drude}} \quad (3.19)$$

The real and imaginary part of the dielectric function are given by

$$\epsilon_1^{Drude}(\omega) = \epsilon_\infty - \frac{\Omega_{Drude}^2}{\omega^2 + \Gamma_{Drude}^2} \quad (3.20)$$

$$\epsilon_2^{Drude}(\omega) = \frac{\Gamma_{Drude}}{\omega} \left[\frac{\Omega_{Drude}^2}{\omega^2 + \Gamma_{Drude}^2} \right] \quad (3.21)$$

The description of all variables and constants used in Eq. 3.19 - Eq. 3.23 is given in Tab. 3.1. It has to be pointed out that angular frequencies are used in the latter equations.

A frequency dependence of the damping coefficient Γ_{Drude} was first mentioned by Köstlin et al. [48]. Hamberg et al. [43] discuss this frequency dependence of the damping term as required to account for ionized impurity scattering. In the extended Drude model (EDM), Γ_{Drude} is replaced by the frequency dependent damping coefficient $\Gamma_{EDM}(\omega)$ [89]:

$$\Gamma_{EDM}(\omega) = \Gamma_L - \frac{\Gamma_L - \Gamma_H}{\pi} \left[\arctan\left(\frac{\omega - \Gamma_X}{\Gamma_W}\right) + \frac{\pi}{2} \right] \quad (3.22)$$

Γ_L and Γ_H are damping frequencies for low and high ω respectively, Γ_X the cross over frequency between high and low and Γ_W the width of the transition region.

The Drude frequency Ω_{Drude} is often called plasma frequency, which is only correct for materials with a high frequency dielectric constant ϵ_∞ of 1. The plasma frequency is generally defined as the frequency where the real part of the dielectric constant is zero [43, 48, 89, 98]. According to Eq. 3.20, this yields the following expression for ω_p :

$$\omega_p = \sqrt{\frac{\Omega_{Drude}^2}{\epsilon_\infty} - \Gamma_{Drude}^2} \quad (3.23)$$

Table 3.1: Constant and Variables used in the Drude and extended Drude model (EDM)

Constant or Variable	Description
	Angular frequencies in cm^{-1}, s^{-1} or eV
ω	angular frequency of light
Ω_{Drude}	Drude frequency
ω_p	Plasma frequency; $\epsilon_1^{Drude}(\omega_p) = 0$
Γ_{Drude}	Damping of Drude oscillations
Γ_L	Damping constant EDM low frequencies
Γ_H	Damping constant EDM high frequencies
Γ_X	EDM crossover frequencies
Γ_W	EDM width of transition region
	other constants
ϵ_∞	high frequency dielectric constant

Since $\Gamma_{Drude} \ll \Omega_{Drude}$ usually holds true [43], the high frequency dielectric constant in combination with the Drude frequency is sufficient to determine the plasma frequency. To obtain ϵ_∞ the real part of the dielectric function is plotted over $(\hbar\omega)^{-2}$ and linearly extrapolated towards zero. This procedure is shown for different samples studied in this work in Fig. 3.8. In accordance with literature [43, 48, 99], $\epsilon_\infty \approx 4$ is obtained in this work for doped and undoped In_2O_3 .

Based on ω_{Drude} and the damping coefficients, charge carrier concentrations n_{opt} and mobilities μ_{opt} can be calculated [89]:

$$n_{opt} = \frac{\Omega_{Drude}^2 \epsilon_0 m_{eff}}{e^2} \quad (3.24)$$

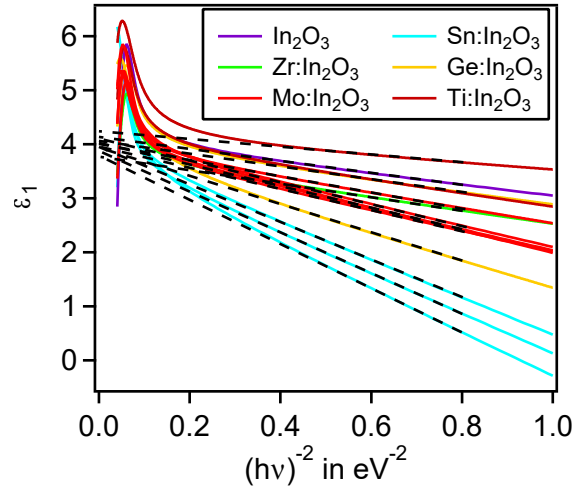


Figure 3.8: ϵ_1 of doped and undoped In_2O_3 plotted over the reciprocal square of the energy. ϵ_1 was obtained by simultaneously modeling transmission, reflection and ellipsometry spectra. Values for ϵ_∞ can be approximated by extrapolating the linear parts towards zero.

$$\mu_{opt} = \frac{e}{m_{eff}\Gamma} \quad (3.25)$$

with e elementary charge and m_{eff} the effective electron mass. In the case of the basic Drude model Γ_{Drude} is used in Eq. 3.25. When the extended Drude model is applied, i.e. the damping coefficient Γ_{EDM} is frequency dependent, Γ_L is used to calculate the optical mobility.

3.1.6 Optical Band Gap Determination from the Spectral Absorption Coefficient

Tauc *et al.* [100] proposed a method to determine optical band gaps based on the relation between the spectral absorption coefficient $\alpha(h\nu)$ and the photon energy $h\nu$ given in Eq. 3.26:

$$\alpha(h\nu) \propto (h\nu - E_g)^n \quad (3.26)$$

The exponent n has to be chosen depending on the type of band gap [101, 102]. In the case of doped In_2O_3 , i.e. a direct optical band gap with dipole forbidden transitions, $1/2$ is set as n . To determine the band gap, $\alpha(h\nu)^2$ is plotted vs. $h\nu$ and the high absorption regime is extrapolated linearly to $\alpha(h\nu)^2 = 0$. Hamberg *et al.* [43] refer to this as commonly used, however, still being object of criticism. They mention explicitly that this method is not suitable for degenerately doped semiconductors. Dolgonos *et al.* [103] propose a method similar to a Tauc plot, which is applicable to the latter materials. Even though absolute band gap values obtained from either method have to be interpreted with care, they are still acceptable for a qualitative evaluation of e.g. band gap widening.

The spectral absorption coefficient can be determined in different ways. It is often calculated from transmittance and reflectance data, as those measurements are easily carried out. Depending on the sample type, different equations have to be used. In case of a single slab of material, i.e. light impinging on the surface of a homogeneous double-sided polished sample, the spectral absorption coefficient $\alpha(h\nu)_{slab}$ can be approximated by the following equation [104]:

$$\alpha(h\nu)_{slab} = \frac{1}{d} \ln \left(\frac{(1-R)^2}{T} \right) \quad (3.27)$$

For thin films on a thick substrate, the following equation is commonly used [83, 102, 105, 106]:

$$\alpha(h\nu)_{film} = \frac{1}{d} \ln \left(\frac{1-R}{T} \right) \quad (3.28)$$

This approximation is based on equations given by Heavens *et al.* [107]. Tomlin [92], Denton [108] and Wu [109] showed that it is suitable for a thin film on a substrate, given the substrate refractive index is in the range of 1.5 to 1.7. Eq. 3.28 is often further simplified by neglecting reflectance, thereby allowing to estimate the absorption coefficient from the transmittance alone [101, 110].

Another possibility is to determine the complex refractive index and to use the extinction coefficient for its calculation [85, 111]:

$$\alpha(h\nu) = \frac{4\pi k}{\lambda} \quad (3.29)$$

A shift of the absorption onset is related to a variation of the optical band gap $E_{G,opt}$ of the films [112]. The fundamental energy gap is defined as the energy difference between the valence band maximum and the conduction band minimum. In contrast to this, the optical band gap is determined by the energy difference between the highest occupied state in the valence band and the lowest unoccupied state in the conduction band as indicated in Fig. 3.9. For degenerate n-type semiconductors, such as donor-doped In_2O_3 , the valence band is fully occupied and the conduction band is partially occupied ($E_F > E_{CBM}$). At higher charge carrier concentration, a higher Fermi level and therefore a larger optical band gap will be found. Burstein [112] and Moss [113] were the first to give an explanation for the dependence of absorption onset in InSb on the impurity level, which subsequently was transferred to other semiconducting materials. Hence a variation of the absorption onset due to a variation of the carrier concentration is called Burstein-Moss shift. An expression for the measured band gap $E_{G,opt}$ Eq. 3.30 can be used according to this model [114]

$$E_{G,opt} = E_{G,0} + \frac{\hbar}{2m_{cv}^*} (3\pi^2 n_e)^{2/3} \quad (3.30)$$

with $E_{G,0}$ being the intrinsic band gap, m_{cv}^* the reduced mass and n_e the carrier density.

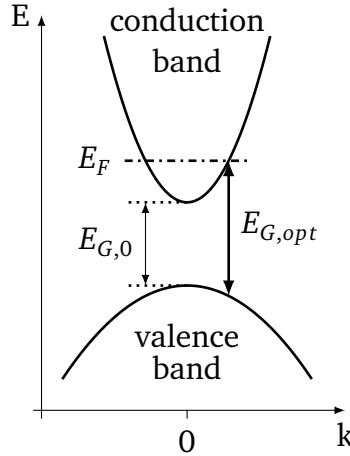


Figure 3.9: Schematic dispersion relation for a degenerately doped, direct band gap semiconductor. The Fermi level is positioned inside the conduction band. The optical band gap therefore differs from the fundamental one.

3.1.7 Sample Spectra

Hamberg *et al.* [43] thoroughly investigated the optical properties of Sn:In₂O₃ thin films. Deposition conditions and post deposition treatments strongly affect the optical spectra of the films. In the UV region, the dielectric function is dominated by interband absorption while it is phonon absorption in the far infrared. In between, the optical spectra were found to be consistent with the Drude theory, pointing out that free electrons are critical for the optical properties. The widening of the optical band gap is often explained solely assuming the Burstein-Moss shift. Although the latter phenomenon has the largest effect on the optical band gap, electron interaction and impurity scattering contribute as well.

Transmission and reflection spectra of an In₂O₃ thin film doped with 10 wt% Sn are shown in Fig. 3.10. The spectra were measured at an incident angle of 60° using either s or p polarized light.

The differences in transmission and reflection can be explained based on Fresnel's equations Eq. 3.5 - Eq. 3.8, describing their angular dependence for s and p polarized light. The influence of the polarization is especially pronounced since the angle of incidence is close to the Brewster angle of Sn:In₂O₃ on glass. The periodic modulations of the transmission and reflection signals at low wavelength are called interference fringes. While this effect is very prominent in the measurements using s polarized light, hardly any influence can be seen for p polarized light, as the reflectance in the visible region is very low in this case.

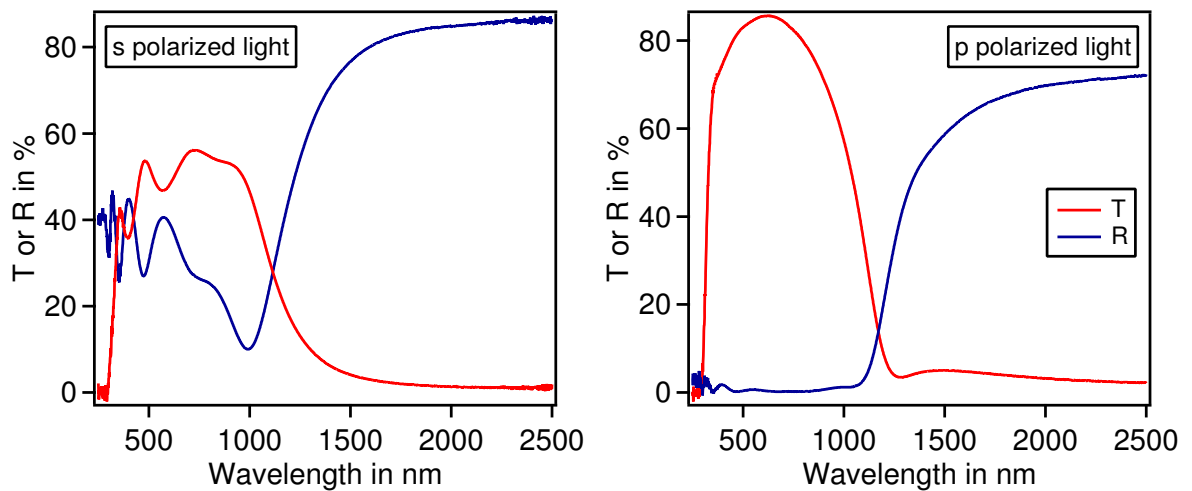


Figure 3.10: Reflectance (grey) and transmittance (black) spectra of a 10 wt% Sn-doped In_2O_3 thin film are shown. Measurements were done at an incidence angle of 60° using s or p polarized light.

Three different regions can be observed independent on the polarization. Up to roughly 300 nm, the transmittance is zero. Surpassing this limit, a rapid increase of the transmittance is observed, while the reflectance remains at the same average value but becomes affected by interference effects. Highest transmittance is observed in the visible range, followed by a decreasing transmittance and increasing reflectance at longer wavelengths.

The low T at short wavelength is explained by the absorption of light at the semiconductor band gap [43]. Above a certain wavelength the energy of the incoming light is not sufficient to excite carriers from the valence to the conduction band and absorption decreases. In the visible region, reaching into the near infrared, the films show high transparency similar to a dielectric [48]. The opposing behavior of transmittance and reflectance in the near infrared region are explained by free carrier absorption [5, 115], i.e. plasma oscillations of the free electron gas [48].

3.2 Photoelectron Spectroscopy

A basic introduction into photoelectron spectroscopy will be given here. More detailed information can be found elsewhere [116–118].

Photoelectron spectroscopy is a very surface sensitive characterization technique. Common applications are chemical analysis of surfaces and investigation of their electronic structure. The method is based on the external photoelectric effect, i.e. the emission of electrons by absorption of a photon. By measuring the kinetic energy of the emitted electrons, it is possible to conclude the initial binding energy E_{bind} , given the photon energy $h\nu$ and the sample work function ϕ are known. Since the sample has to be electronically conductive and grounded via the spectrometer, the following equation is valid for the calculation of E_{bind} :

$$E_{\text{bind}} = h\nu - E_{\text{kin}} - \phi_{\text{spec}} \quad (3.31)$$

with ϕ_{spec} the spectrometer work function.

Based on the excitation sources, PES may be categorized into X-ray photoelectron spectroscopy or Ultra-Violet photoelectron spectroscopy. By illuminating samples with photons of various energies, different information of a sample can be obtained. Increasing excitation energies lead to a higher information depth and allow to probe states of higher E_{bind} . A much higher surface sensitivity is obtained for lower photon energies, as it is the case for UPS.

Core level binding energies are element specific and influenced by the chemical environment. PES can therefore be used to identify the surface chemical composition and oxidation states of its constituents by exciting core level electrons. The energy region close to the Fermi energy, i.e. $E_{\text{bind}} = 0$ eV, provides information about the valence band structure at the surface. In the case of semiconductors, it is possible to extract the difference between the valence band maximum and the Fermi energy $E_F - E_{\text{VBM}}$ from latter measurements. The sample work function can be determined by the energetic position of the secondary electron cut-off. The latter feature is caused by electrons, which were inelastically scattered and leave the sample with a kinetic energy of 0 eV.

Photoelectron spectroscopy can be used to estimate atom fractions C_x in a homogeneous sample as shown in Eq. 3.32. The most common way for a quantitative analysis is based on the determination of the peak areas I_i and correlating them to atomic sensitivity factors (ASF). The ASFs depend on the element, the excitation energy and instrument specific parameters. A set provided by the spectrometer manufacturer is ideally used.

$$C_x = \frac{I_x / \text{ASF}_x}{\sum I_i / \text{ASF}_i} \quad (3.32)$$

The atomic subshell photoionization cross section is specific for each element and orbital of interest. The photon energy can change the photoionization cross section by several orders of magnitude [119]. The application of multiple photon sources can therefore be used to identify the contribution of different orbitals to, for example, the valence band density of states.

In this work, photoelectron spectroscopy will be mainly used to ensure uncontaminated surfaces, to determine the dopant surface concentration and the surface potentials of the as deposited films.

3.3 Electronic Characterization: Conductivity and Hall-Effect

The conductivity is generally defined by the charge of the free carriers, their concentration and mobility. In the case of n-type semiconductors, electrons as majority carriers are used for its calculation.

A common measurement technique to determine the conductivity and Hall coefficients of arbitrarily shaped samples is the van der Pauw method. A four-point probe configuration is used, which is not affected by the contact resistance of the probes. It is applicable

when the following conditions are fulfilled: contacts are positioned at the circumference of the sample, sufficiently small contacts are used, a uniform sample thickness is provided and its surface does not contain any isolating defects.

The sample structure and measurement geometry used in this work, i.e. an electronically conductive thin film on an insulating substrate with Pt contact pads in the corners, is shown in Fig. 3.11.

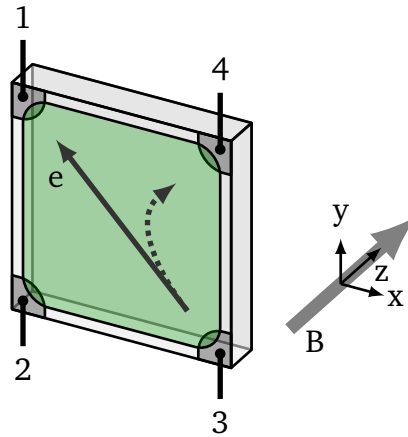


Figure 3.11: Sample structure as used for conductivity and Hall-effect measurements. Isolating substrate, platinum contacts in the corners and In_2O_3 based thin film are shown. The paths of electrons during a Hall-effect measurement is indicated by gray arrows. In this permutation, a current is fed in between contacts 1 and 3 while the Hall voltage is measured between contacts 2 and 4. The magnetic field is pointing in direction of the z-axis.

The conductivity is determined by imposing a current between two neighboring contacts and measuring the voltage drop between the remaining ones. In the case of a symmetrically shaped sample, the van der Pauw correction factor is equal to one and σ can be calculated when the sample thickness t is known:

$$\sigma = \frac{\ln(2)}{\pi \cdot t \cdot R_{12,34}} \quad (3.33)$$

$R_{12,34} = V_{34}/I_{12}$ is the resistance based on the voltage drop between contacts 3 and 4 while driving the current through contacts 1 and 2.

The so-called Hall effect can be used to determine the carrier concentration. It is based on charge separation by the Lorentz force, i.e. a force which affects moving charge carriers in the presence of an external magnetic field. On the right hand side of Fig. 3.11, the schematic electron path is shown if a current I_{13} is applied. The Hall voltage V_{24} , induced by the separation of carriers with opposing charge, is perpendicular to the initial current and correlated to the Hall coefficient R_H . The latter parameter is further defined as $-1/(n_{Hall} \cdot e)$ in the case of n-type semiconductors, leading to the following equation:

$$R_H = \frac{t \cdot R_{13,24}}{B} = -\frac{1}{n_{Hall} \cdot e} \quad (3.34)$$

When the conductivity and Hall carrier concentration are known, the Hall mobility μ_{Hall} can be calculated using Eq. 2.3. It should be noted here that possible errors due to the uncertainty of the film thickness affect only σ and n_{Hall} while it has no effect on μ_{Hall} .

Mobilities and carrier concentrations from Hall effect measurements generally have to be corrected by the Hall scattering Factor r_{Hall} :

$$\mu = \frac{\mu_{Hall}}{r_{Hall}} ; \quad n = \frac{n_{Hall}}{r_{Hall}} \quad (3.35)$$

Since the Hall scattering factor is close to unity for degenerate semiconductors, it can be neglected for most of the doped and undoped In_2O_3 thin films [17].

3.4 Magnetron Sputter Deposition

The majority of all thin films prepared in this work were deposited by radio frequency (rf), reactive magnetron sputtering from planar targets. Basics of this method will be outlined in the following section. If not explicitly specified, the given information is taken from [120, 121].

Sputtering in general describes the process of ejecting atoms etc. from a surface by bombarding with highly energetic ions. It is therefore not only limited to thin film deposition but may also be used for other applications. Sputter deposition belongs to the physical vapor deposition (PVD) methods. PVD comprises several vacuum based techniques involving material being transferred from a solid state to a vapor phase and then being allowed to condense on a substrate forming a thin film. Methods basically differ in the way how the energy, which is required to transfer a material to the vapor phase, is brought into the initial solid. The term for the initial solid is target when talking about sputtering.

A sketch of the basic setup for a sputter chamber is shown Fig. 3.12. A high voltage is applied between the target and remaining deposition chamber, sustaining a plasma close to the target surface. Pressures in the range of 10^{-3} mbar are required. The most common gas used for sputtering is argon. It is a comparably low cost inert gas with a sufficient sputter efficiency. Positively charged Ar ions are accelerated towards the target, which is used as cathode. Amongst other processes, atoms, secondary electrons and other species are ejected from its surface by momentum transfer. By placing either an electrically floating or grounded substrate close to the cathode, part of the vaporized species condense and form a thin film.

A variety of techniques are available for plasma excitation. Using rf power allows to extend the range of possible target materials from conductors to insulating dielectrics.

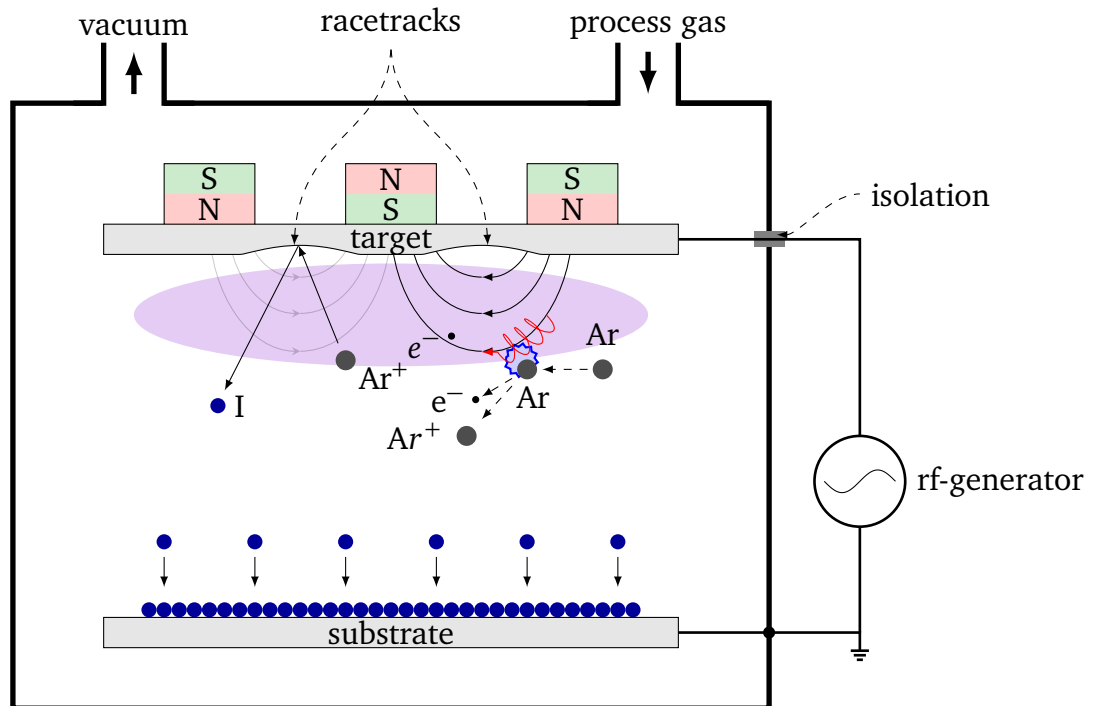


Figure 3.12: Schematic of a vacuum chamber as used for rf magnetron sputtering.

Generally, lower deposition rates and particles of lower energy are obtained, which may increase deposition time but film quality as well.

Placing permanent magnets in the cathode assembly behind the target confines the plasma closer to its surface. The magnetic field forces the moving electrons on cycloidal paths, which increases the electron concentration nearby. The ionization probability of the process gas is higher and a lower pressure is required to sustain a plasma. One downside of using magnetron cathodes is the inhomogeneous target erosion. The formation of so-called racetracks significantly reduces the effective material utilization.

Other gaseous species may be added to the process atmosphere. If reactive gases are added, it is termed reactive sputtering. Oxygen or nitrogen are commonly added to obtain oxide or nitride films from metallic targets. In the case of In_2O_3 and related materials, which are usually deposited from fully oxidized ceramic targets, supplementing oxygen was found to be a suitable tool to tune the film properties. Deposition under such more oxidizing conditions leads to oxygen-enriched films due to the bombardment of the substrate with highly energetic oxygen ions [32, 122].



4 Experimental Procedures

4.1 Optical Spectroscopy

The optical properties of the thin films were analyzed by means of spectrophotometry and spectrometric ellipsometry.

Transmittance and reflectance measurements were carried out using an Agilent Cary 7000 Universal Measurement Spectrophotometer (UMS), which combines a Cary 7000 UV-Vis-NIR spectrophotometer with a Cary Universal Measurement Accessory (UMA). A halogen and a deuterium lamp are used as light source for the Vis-NIR and the UV region respectively. Monochromatization of light is obtained utilizing rotatable diffraction gratings with different line densities for the UV-Vis and NIR regime. The full width at half maximum intensity of light, i.e. the spectral band width $\Delta\lambda$ can be defined by setting the exit slit width of the monochromator. A chopper, i.e. a spinning disc consisting of thirds of reflecting, black and "cut-out" surface, "splits" the monochromatized beam into a reference and a measurement beam. Two Si/InGaAs detectors are used. One to measure the intensity of the reference beam and a second one to measure in the sample compartment. The reference beam is directed via mirrors through two static apertures to the reference detector, while the sample beam passes adjustable apertures and a polarizer before entering the measurement compartment. Two vertical apertures allow to set the beam collimation and one horizontal aperture to set the beam height. By adjusting the variable angle polarizer, the polarization of the measurement beam can be chosen. In the center of the measurement compartment is a rotatable sample stage, which is revolved by the measurement detector. Angles of the sample stage and the measurement detector can be set independently to allow for different measurement modes. The measurement angle is defined as the angle between the direction of incident light and the surface normal of the sample while the detector angle as the central angle between direction of incident light and detector position. For transmission measurements a detector angle of 180° is maintained while the sample angle may be freely adjusted. Specular reflection is measured by setting the detector angle to two times the sample angle.

The range between 2500 nm and 250 nm, at a step width of 1 nm and an integration time of 0.5 s was investigated. The apertures were selected as 3° vertical and 1° horizontal leading to the best general photometric accuracy according to the instrument documentation. Latter specifications ask for a constant spectral band width of 4 nm. Adjusting the measurement patch to the sample dimensions, it was necessary to reduce this value to 3 nm. A sample angle of 60° , close to the Brewster angle of In_2O_3 , was chosen for increased sensitivity. Transmittance and specular reflectance were measured with s and p polarized light. A baseline was measured each day, meaning a measurement without sample and at an detector angle of 180° . Those spectra were then used to reference all consecutive measurements to 100% transmission or reflection.

Spectroscopic ellipsometry was measured on a Sentech SE 850 spectroscopic ellipsometer. The schematic in Fig. 3.6 shows its basic components. Utilization of the retarder is optional. It is a rotating analyzer ellipsometer with a wavelength range of 250 nm to

1700 nm. Two light sources and two detectors are employed depending on the wavelength regime. A Xenon lamp in combination with a diffraction grating and Si photodiode array is used in the UV/Vis region while a halogen lamp in combination with an interferometer modulated Si/InGaAs sandwich photo-detector is used in the IR range. A motorized goniometer allows to measure in an angular range from 40° to 90° without changing the sample position. The height and tilt of the sample can be manually adjusted by moving or tilting the sample stage. Correct alignment can be verified by an optical microscope.

An incident angle of 60° was chosen similar to the other optical measurements. The polarizer angle was set to 45° . The Fourier coefficients S_1 and S_2 were measured over the wavelength range from 250 nm to 1700 nm. By selecting the high accuracy mode in the spectrometer software Spectrarray II, the best signal to noise ratio was provided. It was resolved to measure the Fourier coefficients since the usage of the retarder is not required here. This gives access to wavelengths above 1540 nm. Prior to each measurement, Scotch Magic Tape was applied to the back of each sample to avoid reflections from the backside of the transparent substrates. The tape serves as index matching material, which significantly reduces reflections at this interface [123].

4.2 X-Ray Diffraction

XRD measurements were carried out by courtesy of Ali Nowroozi, Fachgebiet Materialdesign durch Synthese, TU Darmstadt. Diffraction patterns were recorded using a Bruker D8 Advance (Bruker-AXS) diffractometer in Bragg-Brentano geometry. A ceramic Cu X-ray tube in combination with a Ni filter, providing Cu K_α radiation with only a minor fraction of K_β , was used for the measurements. The step size in 2θ was set to 0.0075° at a scanning speed of 0.1 s per step.

4.3 Photoelectron Spectroscopy

Photoelectron spectroscopy using either X-ray or UV radiation was measured routinely on the thin films. The as deposited thin films were directly transferred into the analysis chamber without breaking the vacuum to avoid surface contamination. XPS measurements were usually carried out first but no strict sequence was followed.

A Phi 5700 photoelectron spectrometer equipped with a monochromatic Al K_α X-ray source and a Helium gas discharge lamp was used. XPS was measured at pressures below 5×10^{-9} Torr. Since a differentially pumped He glow discharge lamp, mounted on the analysis chamber itself, was used for UPS measurements the latter experiments had to be carried out at a higher chamber pressure. At a pressure of 7.5×10^{-8} Torr in the analysis chamber, the He I line is dominating. The latter configuration provides photons of mainly 21.2 eV.

A constant pass energy, depending on the measurement method, was chosen. XPS survey measurements were carried out to identify elements present in the samples and to exclude contaminations. When a clean sample was confirmed by a survey measurement high resolution spectra of the relevant core levels and valence band region were recorded. UPS measurements over the accessible energy range were carried out to obtain the sam-

Table 4.1: Parameters for PS measurements. Pass energy E_{Pass} is given in eV, spot size in μm .

Method	E_{Pass}	eV/step	ms/step	Spot size
Survey XPS	187.85	0.8	50	800×2000
High Resolution XPS	5.85	0.05	100	800×2000
UPS	2.95	0.025	50	$\varnothing 400$

ple ionization potential. The relevant settings for each method are given in Tab. 4.1. By carefully adjusting the measured energy range for each core level, the measurement time could be significantly reduced. The number of sweeps, i.e. of repetitions each region is measured, was individually set to obtain an adequate signal-to-noise ratio. Settings for both of the last steps were chosen by judging binding energy and peak intensity from survey spectra.

XPS and UPS measurements were done at takeoff angles of either 45° or 90° . The alignment of the sample z-height relative to the focus point was done by maximizing the intensity of the $\text{In}3d_{5/2}$ emission for XPS. The alignment for UPS required a rotation of the sample to 90° relative to the analyzer entrance. A similar procedure as for XPS was carried out while step-wise rotating until reaching 89° . Since no signal from the X-ray source can be measured for a sample angle of 90° the shape and intensity of the secondary electron edge was checked using He I radiation. No major adjustment in position or height were done at this point. To allow the He lamp to stabilize, at least 5 min passed between ignition and measurement. A bias of -4V was applied between sample and analyzer during the UPS measurements to extract electrons leaving the sample with a kinetic energy of 0 eV.

To account for the daily variation of the spectrometer work function, silver reference spectra were recorded on each measurement day. A purpose-built sample was used consisting of a $5 \times 5 \times 1.5 \text{ mm}^3$ piece of solid silver mounted on a sample holder. The silver reference was cleaned by argon ion etching to remove any kind of contamination. This sputter procedure was done after aligning for XPS to guarantee that the sample is in the focus point of the ion gun. The sample was bombarded by Ar ions for 5 min while rotating around the z-axis at one revolution per minute. An acceleration voltage of 1 keV and an etching area of $6 \times 6 \text{ mm}^2$ were chosen. Survey and high-resolution spectra of the Ag 3d core level were measured only by XPS and while the Fermi edge was recorded for both methods. All subsequently measured spectra were shifted according to the daily silver Fermi energy calibration.

Routine services, e.g. replacement of the X-ray anode and other factors had a tremendous impact on the signal intensity over the course of this work. To compare the core levels of different samples, a normalization procedure to the overall weighted peak area was therefore sometimes necessary. This was done using a procedure programmed in the IGOR Pro analysis software, which references the measured peaks to the area calculated by Eq. 4.1, where A_{all} is the overall weighted peak area and A_j and ASF_j the peak area and atomic sensitivity factor of the core level emission j .

$$A_{all} = \sum_j \frac{A_j}{ASF_j} \quad (4.1)$$

Following equations were employed to determine the work function and ionization potential based on the $E_F - E_{VBM}$ for XPS and UPS and the energy of the secondary electron cutoff in UPS. Since UPS is more prone to charging effects, among others due to a higher photon intensity, work functions were always referenced to the XPS Fermi energy. This procedure is based on the assumption of a parallel shift of the secondary electron edge and $E_F - E_{VBM}$ for slightly charging samples. As a consequence, the I_p determined by UPS is still valid and by subtraction of $E_F - E_{VBM}$ obtained from XPS, a more reliable value for the work function ϕ_{XPS} can be calculated.

$$\phi_{UPS} = h\nu - E_{SEC} \quad (4.2)$$

$$IP = \phi_{UPS} + E_{VBM,UPS} \quad (4.3)$$

$$\phi_{XPS} = IP - E_{VBM,XPS} \quad (4.4)$$

4.4 Electronic Characterization: Conductivity and Hall-Effect

A homemade conductivity and Hall-effect measurement setup, described in detail elsewhere [38, 39], was used to investigate the electrical properties of most of the films.

All measurements were carried out in van-der-Pauw geometry at room temperature. The measurement current was usually set to 1 mA or 5 mA for conductivity and Hall-effect measurements respectively. The latter values had to be decreased for films with a low conductivity to avoid running into the compliance of the current source. Delay times of 1 s and 3 s were used. A magnetic field of 1.3 T was applied for the Hall-effect measurement. To obtain conductivity, carrier concentration and mobility data the film thickness of each sample was set in the labview routine. The film thickness was determined by means of a profilometer. The average of at least three measurements was taken. One precondition was to have no variation of the three significant digits between those measurements for each sample.

4.5 Thin Film Deposition

Sample preparation, i.e. thin film deposition, was carried out at the Darmstadt Integrated System for Materials Research (DaisyMat). All films were deposited by reactive or non-reactive radio frequency magnetron sputtering. Cathodes of the type IX2U 9100, supplied

by Thin Film Consulting, in combination with a PFG 300 RF rf-generator and match box by Hüttinger were used. The films were deposited from 2" targets with a purity of 99.99%. The Sn:In₂O₃ targets were obtained from Kurt J. Lesker Company, all other materials from Alineason Materials Technology GmbH. All films in this work were deposited in a chamber exclusively for TCOs. Different cathodes were used for different materials.

The total pressure of the process atmosphere p , the total gas flow $flux_{tot}$, the target to substrate distance d_{ts} and the power P were kept constant over all depositions. Standard conditions are defined as $p = 5 \times 10^{-3}$ mbar, $flux_{tot} = 6.6$ SCCM, $d_{ts} = 6.9$ cm and $P = 25$ W. A mixture of argon and oxygen was used with the oxygen content ranging from 0 vol% to 10 vol%. A conditioning of the target prior to each deposition was carried out. This was done by setting the process atmosphere and running a plasma with closed shutter for 30 min.

The substrate temperature during the deposition could be adjusted by a radiative heater, i.e. a halogen lamp positioned below the sample holder. A proportional–integral–derivative (PID) controller (Eurotherm model 2416) was used to measure a temperature at a reference point close to the sample holder and adjust the power output of a DC power supply to keep the temperature during deposition at a constant value. Films were deposited on either unintentionally heated substrates or at temperatures up to 600 °C. The sample holder was kept at the desired deposition temperature for 1 h before starting the deposition. The maximum possible rate was used while heating up to the deposition temperature and a cooling rate of ≤ 10 Kmin⁻¹ was used. The process atmosphere was kept during the cooling period until reaching a substrate temperature below 60 °C.

Soda lime glass or fused silica glass were used as substrate. The dimensions of the latter are $10 \times 10 \times 0.5$ cm³. Soda lime glass was used for depositions carried out at substrate temperatures up to 400 °C, for higher temperatures fused silica was chosen. All substrates underwent the same cleaning procedure. First they were immersed in acetone and treated in an ultrasonic bath for 15 min. Followed by rinsing with fresh acetone, isopropyl alcohol, denatured ethanol and de-ionized water before drying in a stream of nitrogen gas.

Platinum contact pads were deposited on the corners of the substrates after cleaning. A Quorum Q300T D bench top sputter coater was used. The thickness amounts to roughly 100 nm. The platinum pads fulfill two purposes. They serve as contacts for the conductivity and Hall-effect measurement on the one hand. On the other hand, a more reliable electronic contact is established between the sample holder used for the TCO deposition and the film itself. The latter is important for the PES measurements, which require an electronic contact of the sample.

The substrates were mounted on sample holders using shadow masks covering roughly half of a millimeter around the edges. After reaching a stable substrate temperature and conditioning of the target, samples were placed concentric relative to the cathode to start the deposition. The final height adjustment was carried out while exposing the substrate to the plasma since the target to substrate distance during the deposition was closer than possible with a closed shutter.



5 Molybdenum Doped Indium Oxide

This chapter is concerned with the analysis of molybdenum doped In_2O_3 thin films deposited under varying conditions. Doping concentrations of 2 mol% and 5 mol% molybdenum were investigated with the focus on samples with higher dopant content. Oxygen content of the atmosphere and substrate temperature during deposition were chosen to adjust the film properties. Structural, electrical and optical film characteristics will be studied before addressing surface electronic features and chemical composition. Part of the results presented here have been obtained within the Bachelors thesis of M. Lederer [124].

5.1 Structural Analysis

To investigate the influence of the deposition conditions on the structure of $\text{Mo:In}_2\text{O}_3$ films, selected samples doped with 5 mol% were studied by XRD. $\theta/2\theta$ scans were measured of films deposited at different temperatures under reducing conditions or at 400°C with varying oxygen content in the deposition atmosphere. The results are shown in Fig. 5.1 and Fig. 5.2. Powder diffraction data were used to reference the reflections as indicated by the bars at the bottom of each graph.

All reflections, except for the ones at angles of 40° and 39° , are consistent with cubic In_2O_3 according to the International Centre for Diffraction Data (ICDD) pattern 00-006-0416. The reflection at an angle of 40° can be attributed to Pt (111) (PDF card 87-642), which was used as contact pads in the corners of each sample and is present depending on the position of the measurement spot. The additional reflection at 39° , which can only be observed for the sample deposited at 600°C , matches to MoO_3 (060) according to the American Mineralogist Crystal Structure Base (AMCSB) code 0017972. No other reflections of MoO_3 are observed, also outside the range shown in Fig. 5.1. The reason why only one MoO_3 reflection is detected is not clear.

The XRD measurements indicate that sputtered $\text{Mo:In}_2\text{O}_3$ films are polycrystalline and grow in the cubic bixbyite structure similar to In_2O_3 . Since all reflections for samples deposited below 600°C match with In_2O_3 or platinum, films consisting of a single phase can be assumed. A second phase seems to be present for the sample deposited at highest temperature, which most likely can be explained by $\alpha\text{-MoO}_3$ having an orthorhombic crystal structure with the symmetry $Pbnm$ [125, 126]. Structural characterization of $\text{Mo:In}_2\text{O}_3$ films in literature also exhibit the bixbyite structure [16, 26, 62–64, 127–130]. The thin films in most of those references were grown at substrate temperatures below 600°C . But even for the films grown by PLD at or above 600°C [128] no evidence for the presence of a molybdenum oxide phase has been reported.

To evaluate the crystallinity of the shown samples, overall peak intensity can be set in relation to the intensity of the broad feature at 23° , which is assigned to the amorphous quartz glass substrate. Since this feature hardly shows any variation for the different measurements due to comparable In_2O_3 film thickness, a direct comparison of the reflection intensities can be carried out. Looking at the diffraction patterns shown in Fig. 5.1 no

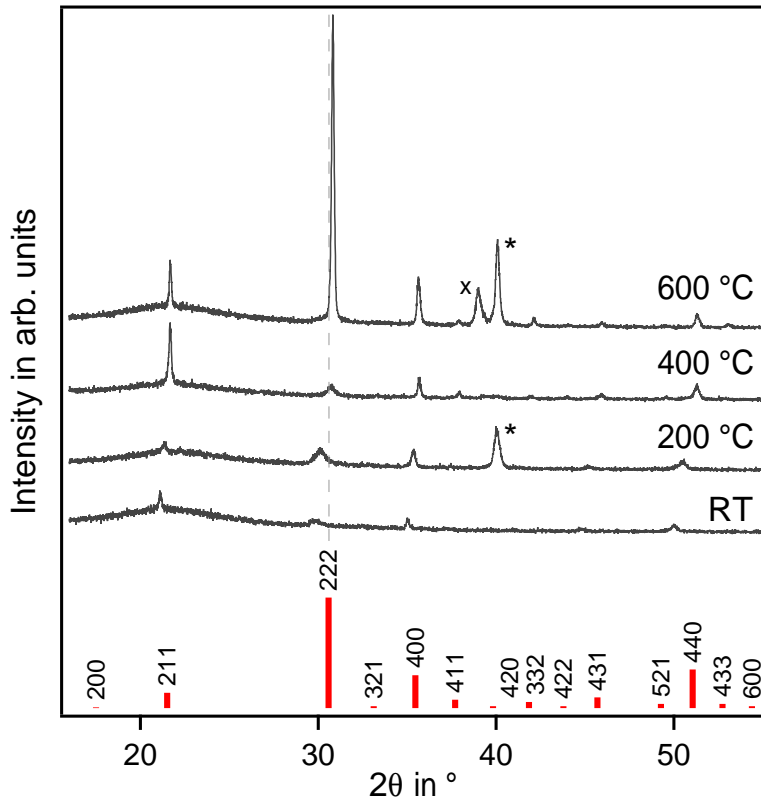


Figure 5.1: XRD $\theta/2\theta$ diffraction patterns of 5 mol% doped Mo:In₂O₃ films. Deposition was carried out in argon and substrate temperature was increased from 20 °C to 600 °C. Red bars at the bottom indicate In₂O₃ reflection angles according to ICDD pattern 00-006-0416. Reflections due to Pt contacts are marked by a "*" while the reflection marked with an "x" is related to MoO₃.

significant changes can be observed up to temperatures of 400 °C. Slight variations of the (211), (222) and (400) reflection are observed, but only for the film deposited at 400 °C an increase of the (211) reflection is worth to mention. Further increasing the temperature or adding oxygen to the process gas leads a significant increase of the (222) reflection.

5.1.1 Effect of Dopant and of Stress on Reflection Angles

In both Fig. 5.1 and Fig. 5.2 the 2θ value of the In₂O₃ (222) reflection is shown by a dashed line to follow the reflection angle relative to the reference value. A shift between both can be observed for almost all cases. According to Bragg's equation [131] this indicates a mismatch in the lattice plane spacing of the films and the powder. Two of the possible explanations, namely influence of the dopant and of stress, will be discussed here.

The dopant is expected to affect the lattice parameters of the film since the ionic radii of In and Mo do not match perfectly [68]. Further, it is known, that thin films deposited by sputtering often contain significant mechanical stress [132, 133], which explains a variation of lattice parameters with deposition conditions. It is hardly possible to separate both effects in a qualitative X-Ray analysis as done here. Structural refinement of the diffraction patterns would be an option but is outside of the scope of this work. Nevertheless, some

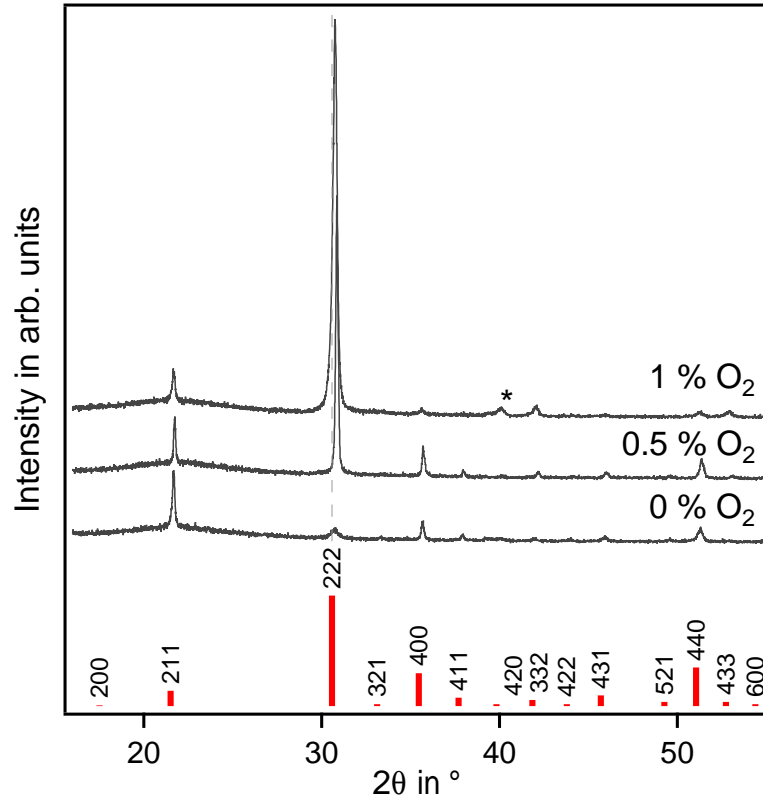


Figure 5.2: XRD $\theta/2\theta$ diffraction patterns of 5 mol% doped Mo:In₂O₃ films. Deposition was carried out at 400° C substrate temperature and different oxygen contents. Red bars at the bottom indicate In₂O₃ reflection angle according to ICDD pattern 00-006-0416. Reflections due to Pt contacts are marked by a "*".

conclusions can still be drawn. Therefore, first the influence of the dopant on the lattice constant of powders and second general effects of stress in thin films will be discussed before concluding what can be learned in the present case.

To investigate the influence of the dopant onto the lattice parameters, a comparison of latter values obtained from powder diffraction measurements is reasonable since less distortion can be expected here [61]. Due to the lack of powder diffraction data for Mo:In₂O₃, lattice parameters of Sn:In₂O₃ and In₂O₃ are compared. As seen in Tab. 2.1 the ionic radius of Sn⁴⁺ is smaller than the one of In³⁺, which is analogous to molybdenum and independent of its oxidation state [68]. Shin *et al.* [63] claim this to be the reason for reduced lattice constants for doped In₂O₃ thin films. The structural characterization of Sn:In₂O₃ powder, however, results in a lattice constant larger than for undoped In₂O₃ [61, 134]. The unit cell expansion is explained by repulsion of the positively charged Sn atoms due to incomplete charge compensation of Sn[•] by O_i^{''}. Based on this, a larger lattice constant should be expected for Mo:In₂O₃ powders as well.

Stress in thin films may be categorized into compressive or tensile stress and usually refers to a variation of lattice spacing along in-plane directions [133]. This means, in a compressive stress state, the spacing of lattice planes perpendicular to the surface is reduced and for tensile stress vice versa. The Poisson ratio then determines the elonga-

tion or shortening along out-of-plane directions. Furthermore, it is common to separate between extrinsic and intrinsic contributions. All stresses, which are not induced by mismatch of thermal expansion coefficient between film and substrate, are counted to the intrinsic while thermal expansion mismatch defines extrinsic stress [132].

To exclude an effect of the dopant on the lattice parameters, diffraction patterns of undoped In_2O_3 thin films will be analyzed for stresses induced during the deposition process. Figure 9.12 in the appendix shows $\theta/2\theta$ measurements of undoped In_2O_3 thin films deposited at different substrate temperatures. The samples were deposited under similar conditions as the ones shown in Fig. 5.1 except for a target to substrate distance of 10 cm and an argon flow of 10 sccm. It can clearly be seen, that the (222) reflection shifts to higher angles when the substrate temperature is increased. This indicates a reduction of the lattice parameters along out-of-plane direction. One reason for this may be extrinsic stress as discussed by Frischbier [39]. The thermal expansion coefficients of In_2O_3 ($6.7 \times 10^{-6} \text{ K}^{-1}$ [25]) and of fused silica glass ($0.5 \times 10^{-6} \text{ K}^{-1}$ [135]) differ by one order of magnitude. Higher temperatures lead to less expansion of the substrate as compared to the thin film during the deposition. After cooling down to room temperature this induces tensile stress in the film. An increasing lattice constant along in-plane direction and therefore decreasing value along out-of-plane directions, i.e. shift of reflections towards larger angles will be the result.

Comparing the positions of the (222) reflection of In_2O_3 thin films and the powder, temperatures below or equal to 200°C lead to a shift towards lower angles while temperatures above or equal to 400°C lead to a shift towards higher angles. Taking the powder diffraction data as a reference value for unstrained films, a transition from compressive to tensile stress at a certain substrate temperature is indicated. While the explanation for tensile stress is given above, a possible reason for compressive stress in sputtered films is the atomic peening effect [136]. Bombardment with ions as well as neutrals during the growth process leads to a displacement of the atoms from their equilibrium positions, which in turn causes compressive stress in the film [132].

For $\text{Mo}:\text{In}_2\text{O}_3$ thin films similar observations in dependence on the deposition temperature are made. Extrinsic stress in the films is sufficient to explain this evolution. It can therefore not be concluded whether doping with Mo leads to a larger lattice constant or not. Overall, a decreasing expansion along the out-of-plane direction with increasing substrate temperature during the deposition was observed for $\text{Sn}:\text{In}_2\text{O}_3$ [115, 137] as well.

The effect of oxygen content in the process atmosphere is not that straightforward. Increasing oxygen content leads only to a slight variation of the reflection angles. Upon closer inspection a shift to higher angles can be observed for 0.5 % oxygen content followed by a shift back to the initial position for 1 % oxygen content. In literature an increasing lattice constant is observed when the oxygen partial pressure is increased for both $\text{Sn}:\text{In}_2\text{O}_3$ and $\text{Mo}:\text{In}_2\text{O}_3$ [60, 128, 137]. Mergel *et al.* [137] suggest a lattice expansion with increasing oxygen content in the film. The additional oxygen is expected to be incorporated as interstitial oxygen, which induces lattice strain due to the large ionic radius. The insufficient amount of data shown here in combination with its inconsistency, however, allows no conclusion to be drawn.

From the structural analysis of Mo:In₂O₃ thin films it was seen, that, similar to Sn:In₂O₃ and In₂O₃, both deposition temperature and oxygen content of the process atmosphere influence crystallinity and reflection angles. Crystallinity and diffraction pattern of a sample deposited at room temperature do not significantly differ from films deposited at 200 °C or 400 °C. Under reducing conditions a temperature of 600 °C is required to induce serious change in the diffractogram, even a new phase was found, which most likely is MoO₃. Enhanced intensity of the (222) reflection is obtained when little amounts of oxygen are added to the deposition atmosphere. Based on a comparison to Sn:In₂O₃, it can be assumed that the lattice constant of stress-free Mo:In₂O₃ is larger than the one of undoped In₂O₃. It was observed that the (222) reflection shifts from smaller to larger angles as compared to In₂O₃ powder diffraction data when the substrate temperature is increased from room temperature to 600 °C. Similar observations were made for undoped In₂O₃ and explained by extrinsic stress caused by different thermal expansion coefficients between film and substrate. Whether the stress state is changing from a compressive to a tensile cannot be concluded.

5.2 Electronic Properties, Conductivity and Hall-Effect Measurements

The effect of the deposition conditions on the charge carrier concentration and mobilities as obtained from conductivity and Hall-effect measurements will be discussed in this section. All measurements were carried out at room temperature in a home-made Conductivity-Hall-Setup in Van der Pauw configuration as described by Wachau [38].

It is well known that the oxygen content in the atmosphere and substrate temperature during deposition significantly affect the electronic properties of doped and undoped In₂O₃ thin films. Several articles investigating Mo:In₂O₃, concerning variation of the latter parameters are available as well and will be used in the following to evaluate the data obtained in this thesis [10, 64, 128, 129, 138–140]. Carrier concentration, mobility and conductivity values of 5 mol% doped Mo:In₂O₃ films deposited at varying conditions are shown in Fig. 5.3. The top row presents samples at a constant substrate temperature of 400 °C and varying oxygen content in the process atmosphere. In the bottom row films prepared in pure argon at different substrate temperatures are shown.

An increasing oxygen content leads to an overall reduction of all values. While the carrier concentration is monotonically decreasing with increasing oxygen content in the process gas, both the mobility and the conductivity first increase for 0.5% and 1% O₂ and then decline. Temperature variation leads to a different picture. The carrier concentrations are constant and rather low for temperatures of 200 °C and below. When this temperature is exceeded, the carrier concentration abruptly increases by one order of magnitude and remains rather constant for higher temperatures. The mobility initially increases with temperature and reaches a maximum of 58.9 cm²(Vs)⁻¹ at 350 °C. Beyond this temperature lower mobilities are measured reaching almost 0 cm²(Vs)⁻¹ at 600 °C. As a consequence, the conductivity is low either for lowest or highest substrate temperatures and reaches a maximum around 400 °C.

A decreasing carrier concentration upon the addition of oxygen to the process atmosphere indicates that a rising oxygen content in the film leads to a lower number of

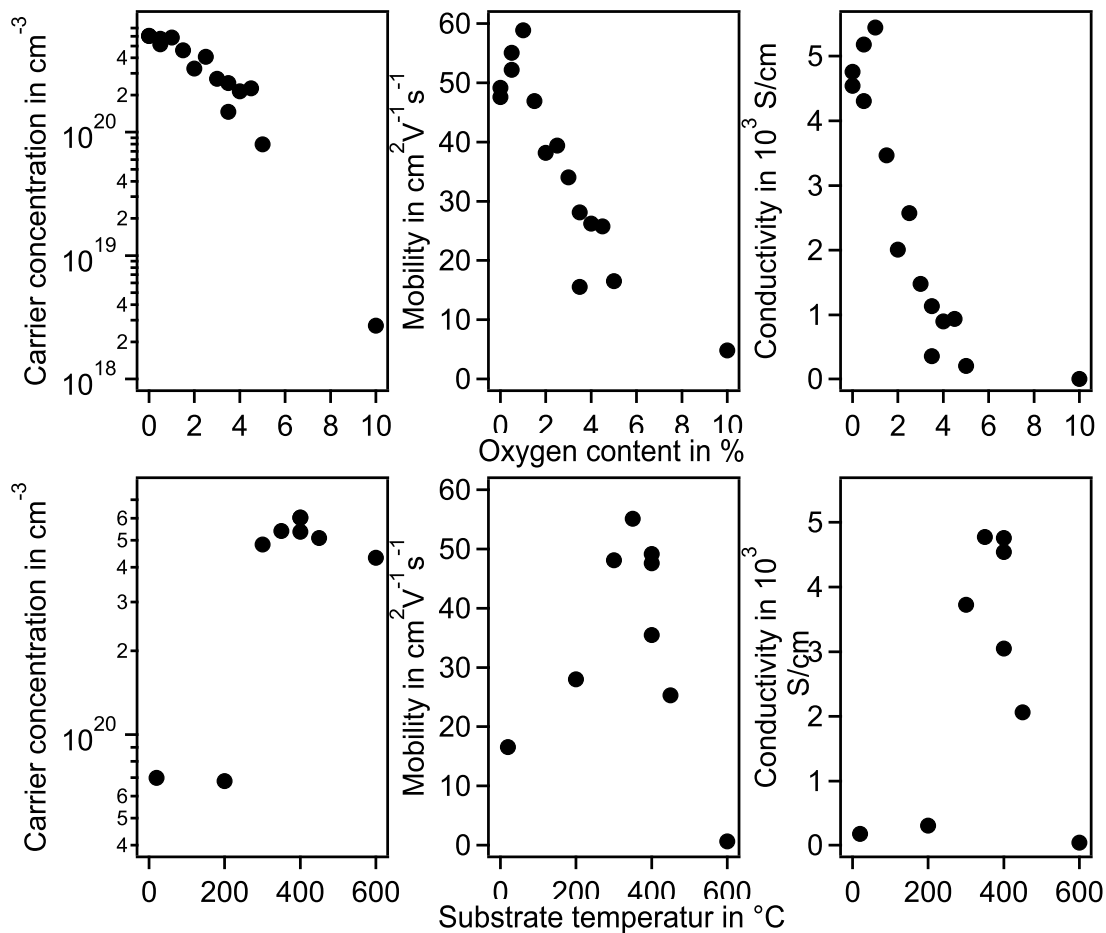


Figure 5.3: Electron mobility, carrier concentration and conductivity of 5 mol% doped Mo:In₂O₃ films deposited at a substrate temperature of 400° C and varying oxygen content in the process atmosphere (top) and at different substrate temperatures in pure Ar atmosphere (bottom). Conductivity and Hall-effect measurements were carried out for the determination of the presented values.

effective dopants. Discussion of this fact on the topic of Mo:In₂O₃ can be found in literature [10, 64, 128, 129, 138, 139]. Since those are based on what was published for In₂O₃ and Sn:In₂O₃, a brief summary will be given here. The concentration of oxygen vacancies determines the number of free charge carriers in In₂O₃ [59], while it is of minor importance for Sn:In₂O₃. In donor-doped In₂O₃ thin films, the carrier concentration due to the dopant will outweigh the ones due to oxygen vacancies except for overreduced samples [21]. Neutral defect associates, $(2\text{Sn}_{\text{In}}^{\bullet}\text{O}_{\text{i}}^{\prime\prime})^x$ in the case of Sn:In₂O₃, are made responsible for a stagnation in carrier concentration when the dopant concentration is increased beyond a certain value. Since those defect associates are composed of the dopant and interstitial oxygen, a correlation between oxygen content in the film and the carrier concentration is evident. Incorporation of $\text{O}_{\text{i}}^{\prime\prime}$, which will be more acute with increasing oxygen content in the process atmosphere, leads to the formation of neutral defect associates and causes a reduction of effective donors and thereby of the free carrier concentration.

The presence of defect associates is widely accepted in the case of Mo:In₂O₃ thin films and adequate to explain decreasing carrier concentrations with increasing oxygen content in the process atmosphere. Since uncertainties concerning the oxidation state of molybdenum are still present, no unison solution for the defect associate can be given. A detailed discussion of the Mo oxidation state in Mo:In₂O₃ will be carried out in Sec. 5.4.

The observation that a certain amount of oxygen is required to obtain the highest mobility is as well confirmed by several articles [10, 64, 128, 129, 138, 139]. Whether severe oxygen deficiency and thereby induced lattice structural disorder [139] is an explanation for the reduced conductivity under reducing conditions is questionable. One more plausible reason for the initially increasing mobility is the enhanced crystallinity of the thin films when little amounts of oxygen are added [128, 138]. This is consistent with the X-ray diffraction patterns shown in Fig. 5.2.

Increasing numbers of defect associates are expected when more oxygen is present during the deposition. This in turn boosts the number of neutral impurities functioning as scattering centers [64, 138]. In case of Sn:In₂O₃ these associates have a quite large scattering cross-section [21]. Since the loosely bound interstitial oxygen is made responsible for this, the assumption of a large scattering cross-section should be valid for Mo:In₂O₃ as well. In the case of polycrystalline films, scattering at grain boundaries has to be considered as mobility limiting factor for not too high carrier concentrations [15, 77, 78]. According to the Seto-model, these potential barriers at the grain boundaries are affected by the carrier concentration [78]. Frischbier *et al.* [15] recently showed, that these barriers vanish for differently doped In₂O₃ thin films if the carrier concentration reaches a certain level. A rising number of scattering centers and increasing grain boundary barriers are a plausible explanation for the reduction of the mobility when more oxygen is added to the process atmosphere.

A sudden jump in conductivity when a certain substrate temperature is exceeded was already reported by van Hest *et al.* [140]. The temperature regions for this differ between their work and what was found in this thesis, though. While temperatures above 400 °C were required in literature, here it is found that the transition already starts at 400 °C. The observed jump in charge carrier concentration may confirm the suggestion of a minimum substrate temperature required to activate the dopant [140]. Assuming that this process goes with dissociation of the defect associates [63, 141, 142] the jump in carrier concentration can be explained and, due to a reduction of very effectively scattering neutral impurities, the larger mobility as well. Increasing mobility due to enhanced crystallinity as a result of higher substrate temperature [128] cannot be confirmed when the XRD measurements shown in Fig. 5.1 are considered. In contrast to some articles [128, 140, 142] a decreasing mobility and therefore conductivity is observed at temperatures exceeding 400 °C. From the XRD pattern of the sample deposited at 600 °C shown in Fig. 5.1 the presence of a MoO₃ phase was concluded, which may be the reason for the very low mobility values.

Results of all conductivity and Hall-effect measurements performed on Mo:In₂O₃ thin films in this work are summarized in Fig. 5.4. The marker colors indicate the substrate temperature during the deposition while the marker size emphasizes the oxygen content

in the process atmosphere. Next to the previously discussed 5 mol% Mo containing films, data of 2 mol% doped Mo:In₂O₃ films are also included. Due to a smaller sample number, no detailed discussion about the latter will be given here. They shall mainly be used to point out the influence of dopant concentration onto the electronic properties. It must be noted that, some of the 2 mol% doped Mo:In₂O₃ thin films exhibit carrier concentrations above $3 \times 10^{20} \text{ cm}^{-3}$. This is higher than any value obtained with a dopant concentration of 5 mol% and might result from a measurement artifact. The samples will thus not be considered in the following. The solid line in Fig. 5.4 represents the calculated dependency of the mobility on the carrier concentration based on a model for In₂O₃ single crystals [17].

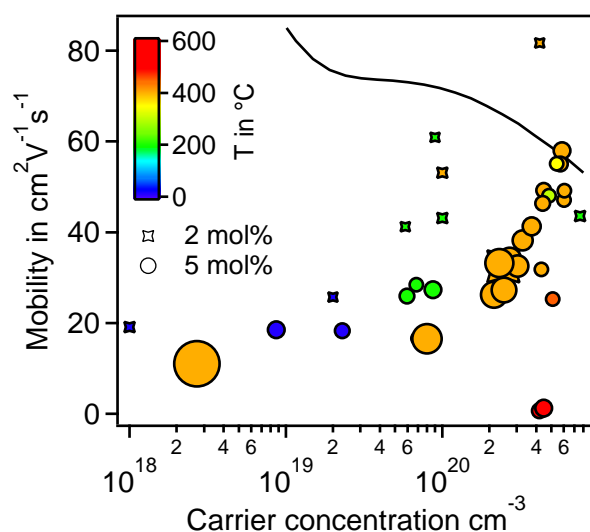


Figure 5.4: Electron mobility is plotted over the carrier concentration of 2 mol% and 5 mol% doped Mo:In₂O₃ films deposited at various substrate temperatures and oxygen contents in the process atmosphere. The solid line shows the calculated values $\mu(n)$ for In₂O₃ single crystals [17]. Conductivity and Hall-effect measurements were carried out for the determination of the presented values. Substrate temperatures are indicated by the marker color according to the given scale, while the marker size represents the oxygen content, which is varying between 0% and 10%.

Considering the data shown in Fig. 5.4, the influence of substrate temperature and oxygen content on the electronic properties of Mo:In₂O₃ thin films, as discussed before is valid even in context of a larger sample number. A substrate temperature of 400 °C leads to the highest carrier concentrations under most reducing conditions while the highest mobilities are obtained by adding some oxygen to the process atmosphere. Increasing oxygen content and lower deposition temperature result in lower carrier concentrations as well as mobilities. Films deposited at a temperature of 600 °C show a very low mobility whilst carrier concentrations remain quite high. At high carrier concentrations, the highest measured mobilities match the values expected for In₂O₃ single crystals, supporting the vanishing influence of grain boundary barriers [15].

Thin films doped with 2 mol% molybdenum show a temperature dependence comparable to the higher dopant concentration: mobilities and carrier concentrations increase with increasing substrate temperature up to 400 °C. It is pointed out that the lower dopant concentration leads to higher mobilities under similar deposition conditions. This leads

to the conclusion that a dopant concentration of 5 mol% molybdenum already results in over-doping and therefore worse electronic properties.

A number of articles in literature deal with the determination of the optimum molybdenum content [16, 130, 140, 142–144]. Over-doping is reported for molybdenum concentrations larger than 0.5 mol% [144] while others find best results for concentrations of 5 mol% [16]. Since the films in the mentioned articles were grown by different techniques and the determination of the dopant concentration is not the same as well, discrepancies for the doping limit may be related to the deposition technique. In Sec. 5.4.3 it will be shown that the bulk Mo content of the nominally 5 mol% doped films in this work is closer to 2.2 mol%. This is similar to the doping limit of 2 mol% molybdenum, obtained by van Hest *et al.* [140] who deposited their films by co-sputtering from In_2O_3 and MoO_3 targets.

5.3 Optical Analysis

In the following section transmission and reflection data of 5 mol% doped samples, deposited under varying oxygen content or substrate temperature, will be discussed. Afterwards a short comparison between different dopant concentrations will be given. The measurements were carried out with the Agilent Cary7000 spectrophotometer, over a wavelength region from 250 nm to 2500 nm, covering the UV, Vis and NIR region. It is pointed out that the presented spectra were measured using p polarized light, at an incident angle of 60° , which is close to the Brewster angle of In_2O_3 . The measurements therefore tremendously differ from spectra recorded at normal or near normal incidence and interference effects are only weakly pronounced.

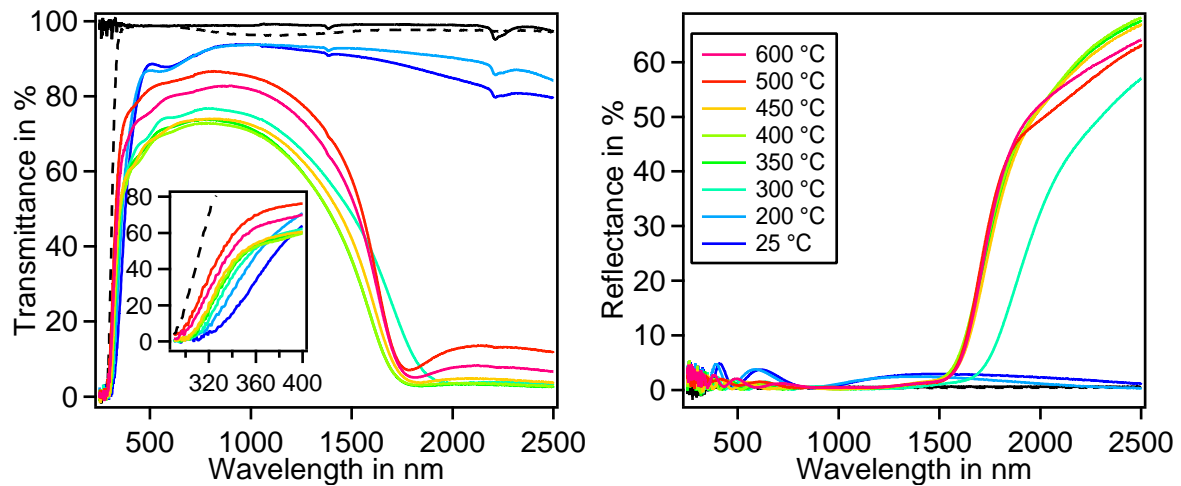


Figure 5.5: Transmittance (left) and reflectance (right) spectra of 5 mol% molybdenum doped In_2O_3 thin films on glass. The samples were deposited in argon atmosphere at different substrate temperatures. The solid and the dashed black lines indicate spectra of either quartz or soda lime glass. Measurements were done at an incident angle of 60° using p polarized light.

In Fig. 5.5 and Fig. 5.6 transmittance spectra are shown on the left while reflectance is shown on the right. Spectra for substrate temperature variation are shown in Fig. 5.5 and spectra for oxygen content variation at a substrate temperature of 400°C in Fig. 5.6. The

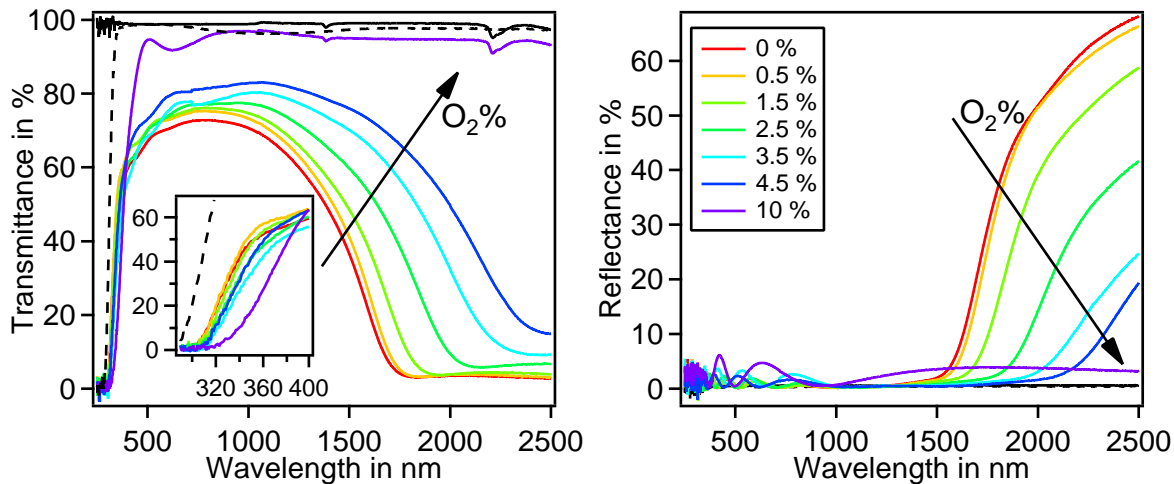


Figure 5.6: Transmittance (left) and reflectance (right) spectra of 5 mol% molybdenum doped In_2O_3 thin films on glass. The samples were deposited at a substrate temperature of 400°C . An Ar/O mixture with varying amount of oxygen was used as process atmosphere. The solid and the dashed black lines indicate spectra of either quartz or soda lime glass. Measurements were done at an incident angle of 60° using p polarized light.

corresponding spectroscopic ellipsometry measurements are shown in Fig. 9.5. Either soda lime glass or quartz glass are used as substrate. The spectra of the substrates are included in the graphs. Quartz glass is transparent over the entire wavelength region. Since the onset of transmission signal of each sample is at a longer wavelength as compared to soda lime glass the two different substrates hardly affect the resulting spectra. Subwindows in the transmittance graphs show the enlarged transmission onset for a more detailed discussion.

The deposition conditions are the major origin of the different optical properties of the presented films. Since the film thickness may differ between 200 nm and 400 nm it can not be completely neglected. Interference effects are rather low under the given experimental conditions. Therefore, a variation of film thickness will mainly affect the absolute transmission values.

There are several articles investigating the impact of dopant concentration, oxygen content and deposition temperature on the optical properties of doped and undoped In_2O_3 thin films [5, 10, 16, 43, 48, 63, 64, 115, 127–130, 136, 139, 140, 142, 145–147]. Independent on dopant, quite similar observations were made, which will be used to explain the features of the spectra in more detail. Both the onset of absorption below a certain wavelength and reflection above a certain wavelength strongly vary between samples. At the end it is mostly the free carrier concentration of the films, which is causing the different shapes of the spectra.

From the inset in Fig. 5.5 a clear blue-shift of the absorption onset for increasing substrate temperatures is visible. An opposite trend can be observed for increasing oxygen content. The absorption onset is shifting to longer wavelength when more oxygen is added to the process atmosphere. In the latter case, however, the shift is not as apparent as for

the temperature series. Values for the optical band gap, obtained from simultaneously fitting transmittance and reflectance spectra as well as ellipsometry data, are shown at the top in Fig. 5.7, either plotted versus substrate temperature or oxygen content in the process atmosphere. A more substantial number of samples is considered as compared to the ones shown in the above displayed spectra. The OJL model, described in Sec. 3.1.5, was used to model the band gap absorption. This model is based on assumptions, which are not valid for degenerately doped TCOs. Therefore, band gap values given in Fig. 5.7 are not expected to resemble the actual film properties but still to reflect the influence of the deposition conditions on the magnitude of the optical band gap.

A variation of the optical band gap in the range of 2.9 – 3.8 eV is observed. In literature values between 3.6 – 4.3 eV are reported for Mo:In₂O₃ [16, 64, 127, 138, 139, 144]. Considering that band gaps were determined in literature using Tauc plots or similar procedures, it can be confirmed that the OJL model leads to a significant underestimation when applied to doped In₂O₃, as also discussed by Mendelsberg *et al.* [81]. Using the extrapolation-based method described by Dolgonos *et al.* [103] to directly get the optical band gaps, values in the region between 3.6 – 4.2 eV are obtained in this work. Independent on how the optical band gap is determined, deposition conditions have a similar influence. Since a qualitative description is sufficient at this place, the effects of temperature and oxygen content will be discussed based on the values obtained from the optical simulation. For temperatures up to 400 °C a more or less linearly increasing optical band gap is found for each oxygen partial pressure, followed by a plateau at higher temperatures. Adding oxygen leads to a decreasing optical band gap. The deposition temperature is the dominant factor though.

The next feature that is strongly affected by the deposition conditions is the limit of the transparency window in the near infrared, i.e. where free carrier absorption starts and reflectance increases while transmittance decreases. In Fig. 5.5 it can be seen that this position, for samples deposited below 300 °C, is shifted so far into the infrared, that it cannot be measured with the used equipment. Substrate temperatures > 300 °C lead to transparency windows limited by roughly the same wavelength. The slope and maximum value differ for different temperatures. A rather monotonous variation of the transmittance window can be seen in Fig. 5.6 when the oxygen content in the deposition atmosphere is varied. More oxygen leads to a shift further into the infrared, reduction of the slope and increasing total transmittance.

A more quantitative way to define the limit of the transparency window in the near infrared is the plasma energy E_p . It can be derived from the simulations of the optical constants if the Drude model is used as described in Sec. 3.1.5. Or, if the optical constants were obtained differently, E_p may be taken as the energy where the real part of the dielectric function approaches zero [48]. According to the Drude model or free electron theory, the plasma energy increases with carrier concentration [48, 140]. Values for E_p of several samples are shown in the bottom graphs in Fig. 5.7, plotted against substrate temperature or oxygen content. The displayed data are in agreement with literature [75] and confirm what has been learned from the qualitative analysis of the transmittance and reflectance spectra. More oxygen leads always to lower values while the temperature hardly has an effect above 300 °C.

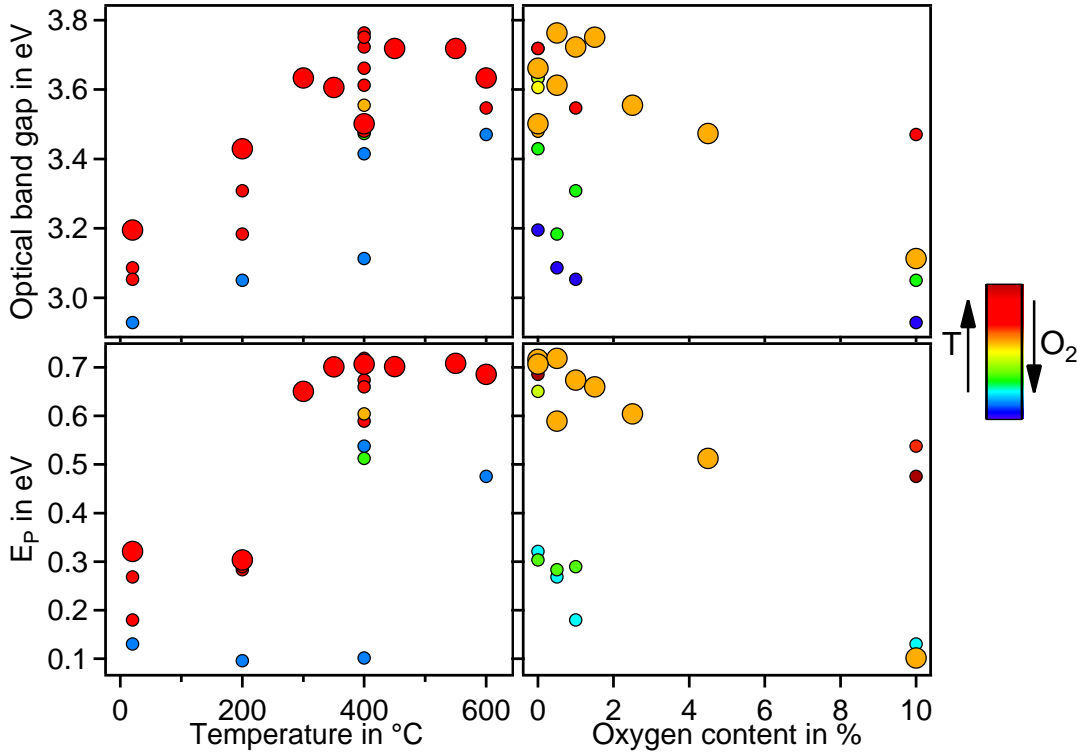


Figure 5.7: Optical band gap and plasma energy plotted versus substrate temperature or oxygen content of process atmosphere. Values obtained from simultaneously fitting transmission, reflection and ellipsometry spectra of 5 mol% molybdenum doped In_2O_3 thin films deposited on glass. The samples were deposited at varying substrate temperatures and oxygen partial pressures. Marker colors indicate oxygen content or substrate temperature respectively, as indicated by the color scale. The marker size of samples deposited either at 400°C or at 0% oxygen is increased.

So far, the observations allow a first comment on the effect of the deposition conditions onto the optical carrier concentration n_{opt} . It has to be pointed out that n_{opt} must not coincide with the carrier concentration obtained by other methods, as will be discussed later. Both, E_p and $E_{G,opt}$ increase with temperature, at least until 400°C , and decrease with addition of oxygen. According to Burstein [112] and Moss [113] and the Drude model [48] those results indicate an increase of n_{opt} up to the latter deposition temperature and a reduction by addition of oxygen.

A number of authors have observed a decreased transmittance in the wavelength region between approximately 350 nm to 600 nm for $\text{Mo:In}_2\text{O}_3$, related to the deposition conditions [10, 64, 127, 129]. Sun [64], Yoshida [10] and Li *et al.* [129] assume a second phase to be responsible while Elangovan *et al.* [127] excluded this explanation by XRD measurements and state that varying film stoichiometry is the reason, without providing a composition analysis. Having a look at the spectra shown in Fig. 5.5 and Fig. 5.6, no decreased transmittance can be seen. A variation of transmittance with the deposition conditions is indisputable but over the whole transparency window of each sample and not only for the above given specific wavelength range. From the oxygen series a simple relation is found: less oxygen leads to a lower overall transmittance, a blue shift of

the absorption edge and a decreasing E_p . For the temperature series, however, it is not that straightforward. While samples deposited either at the lowest or the highest temperatures show the highest transmittance, substrate temperatures around 400 °C lead to rather low values. A difference in carrier concentration therefore allows not always to draw conclusions about the film transmittance [64, 147].

In summary this section emphasizes the effect of deposition conditions on the optical properties of Mo:In₂O₃. The rather systematic Burstein-Moss shift and variation of the plasma frequency indicate different carrier concentrations, which fits to the results obtained from conductivity and Hall-effect measurements. A comparison between both methods will be carried out in Sec. 5.3.2. While some authors claim an overall dependence of transmittance on the carrier concentration [64, 147], the observations here are not fully coherent with the former mentioned indicators.

5.3.1 Influence of Dopant Concentration onto the Optical Properties

Looking at the VIS region in Fig. 5.5 and Fig. 5.6 it is apparent that films showing a high conductivity have a maximum transmittance of roughly 70%. This value is rather low and even falls below the maximum transmittance of Sn:In₂O₃ thin films with a dopant concentration of 10% and higher conductivities. In Sec. 5.2 lower mobilities of 5 mol% doped samples compared to lower dopant concentration and to literature was already suspected to be caused by over doping. Figure 5.8 shows transmission (dashed lines) and reflection (continuous lines) measurements of two Mo:In₂O₃ samples, deposited under similar conditions, i.e. 400 °C in 0% oxygen, but with different dopant concentration. The black and gray traces correspond to a dopant concentration of 5 mol% and 2 mol%, respectively. Electronic properties of the films are given in Tab. 5.1.

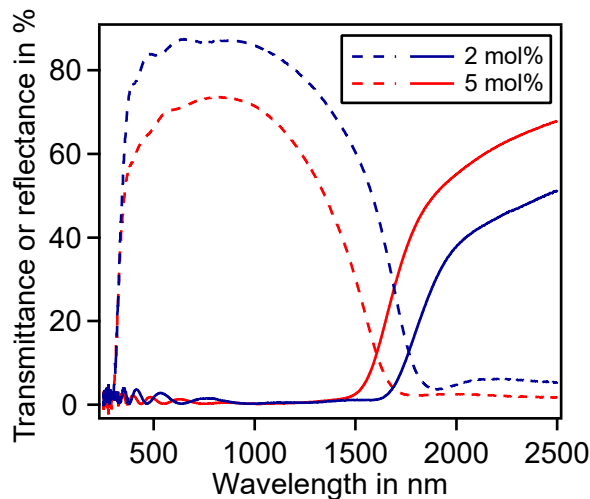


Figure 5.8: Transmittance and reflectance spectra of two Mo:In₂O₃ thin films deposited at 400 °C in 0% oxygen from a target with a concentration of either 2 mol% or 5 mol% molybdenum.

The 2 mol% Mo:In₂O₃ thin film has a significantly higher transparency in the visible region and a lower plasma frequency while exhibiting a higher conductivity as compared to the 5 mol% Mo:In₂O₃ sample. A slightly lower carrier concentration and a considerably

higher mobility of the 2 mol% doped sample can explain these observations. Similar optical band gaps can be estimated from the transmission onset, which is not expected based on the difference in carrier concentration. The enhanced transparency, reaching further into the infrared, and the increased conductivity of the 2 mol% doped film support the assumption that a dopant concentration of 5 mol% already leads to overdoping.

Table 5.1: Electronic properties of the two samples shown in Fig. 5.8. Conductivity, carrier concentration and mobility were determined by conductivity and Hall-effect measurements.

	σ_{el} in Scm^{-1}	μ_{Hall} in $\text{cm}^2\text{V}^{-1}\text{s}^{-1}$	n_{Hall} in cm^{-3}
2 mol%	5503	81.7	4.20×10^{20}
5 mol%	4540	47.1	6.02×10^{20}

5.3.2 Comparison of Electronic properties obtained from Conductivity-Hall-Effect and Optical Measurements

In Fig. 5.9 electrical properties determined by conductivity and Hall-effect measurements are compared to the results from simulation of the optical spectra. Only one data point is from a 2 mol% doped sample (open circle) while all others are from 5 mol% thin films (full circles). The optical band gap obtained from the OJL model plotted versus $n_{Hall}^{2/3}$ is shown in Fig. 5.9(a). The values based on the OJL model are significantly underestimating $E_{G,Opt}$ as discussed in Sec. 5.3. The linear behavior still indicates that the Burstein-Moss effect is responsible for the band gap widening. A correlation like $E_{G,Opt} \propto n^{2/3}$ is expected in this case, see Eq. 3.30.

Fig. 5.9(b) and Fig. 5.9(c) compare the optically and electrically determined carrier concentrations and mobilities respectively. Gray markers represent values obtained from optical simulations based on a constant effective mass of $0.3m^*$. Black markers indicate data points, which were calculated using Eq. 5.1 assuming a carrier concentration dependent effective mass according to Ref. [148].

$$m^*(\text{Sn} : \text{In}_2\text{O}_3) = (0.297 + 0.011 \times 10^{-20} n_{Hall}) m_0 \quad (5.1)$$

Only samples with n_{Hall} larger than 10^{20}cm^{-3} were considered, since otherwise free carrier absorption is shifted too far in the infrared and is not in the measurement region anymore. In this case a simulation using the extended Drude-model does not lead to reliable results.

For a non-constant effective mass a linear correlation between the carrier concentrations can be seen. Since the slope is unity, both methods yield similar values for this parameter. A rather poor agreement between optical and Hall mobilities is apparent from Fig. 5.9(c). It has to be pointed out that the determination of the mobility from optical measurements is based on the oscillation of free electrons excited by light. Since the actual extend of motion is much less as compared to DC Hall-effect measurements, where the carriers travel

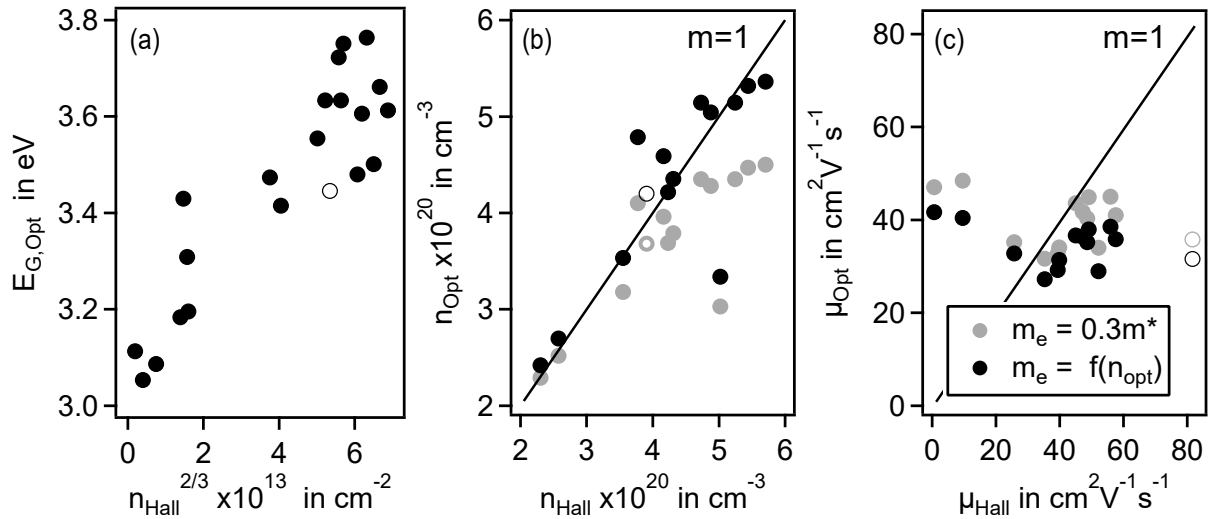


Figure 5.9: Comparison of optical band gap, with Hall carrier concentration (a), optical and Hall carrier concentration (b) and optical and Hall mobility (c). Data points of all measured samples are shown in (a). In (b) and (c) samples with a carrier concentration above $2 \times 10^{20} cm^{-3}$ are considered. Grey markers represent optical mobilities and carrier concentrations calculated for an effective electron mass of $0.3 m_e$ and black markers for an effective mass, which is a function of the carrier concentration.

through the whole sample, the optical mobility is said not to suffer from grain boundary scattering and therefore represent the mobility in a grain [89, 148]. An almost constant optical mobility can be seen. For the majority of data points $\mu_{Opt} < \mu_{Hall}$ is found. This is not expected if the last statement is correct as grain boundaries cannot lead to an enhancement of the mobility. In literature both a good agreement or an independent behavior of Hall and optical mobilities are reported [14, 81, 89, 137, 148, 149]. The reliability of the results seems to be increased if the measurements reach further into the infrared [14, 149]. No clear explanation for the unreasonable optical mobilities presented in Fig. 5.9 can be given so far.

5.4 Photoelectron Spectroscopy

5.4.1 X-Ray Photoelectron Spectroscopy

In Fig. 5.10 X-ray photoelectron spectra of a 5 mol% Mo: In_2O_3 film are displayed. Film deposition was carried out under standard conditions at $400^\circ C$ in a process atmosphere containing 0.5% O_2 . $O1s$, $In3d_{5/2}$, $Mo3d$ core level and the valence band region are shown. Additional to the measured $Mo3d$ signal the calculated background, a simulated spectrum and its components are displayed. The fit was done after background subtraction using three Gaussian doublets $Mo_I - Mo_{III}$. The simulated spectrum and background is shown as a gray solid line while the components can be identified according to the given legend.

Asymmetric shapes as observed for the O1s and In3d_{5/2} peaks are explained by plasmon screening of the core-hole [150]. High carrier concentrations are required for this effect to contribute to the asymmetry of the spectra.

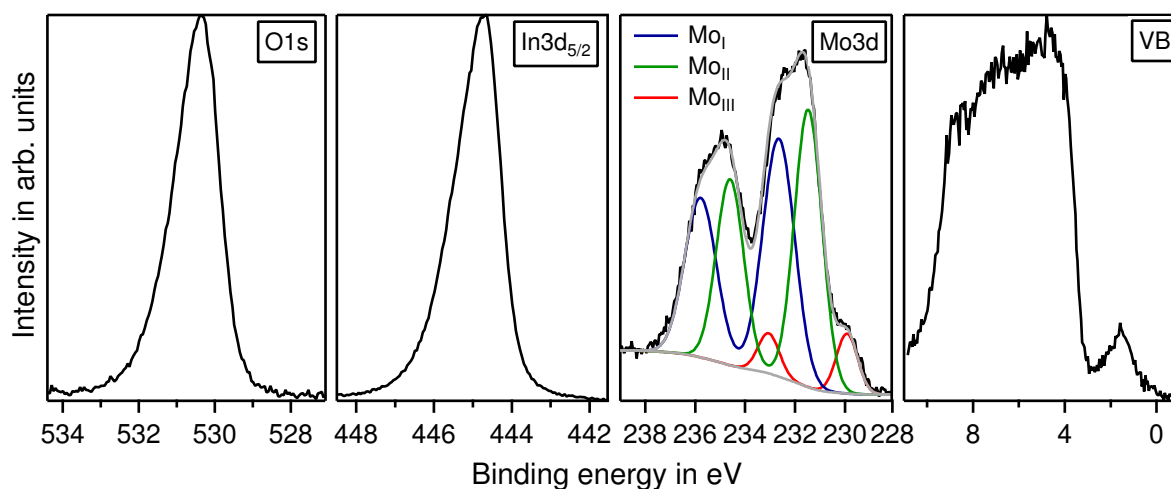


Figure 5.10: XPS O1s, In3d_{5/2}, Mo3d core level spectra and valence band region of a 5 mol% doped Mo:In₂O₃ film deposited at 400 °C in a process atmosphere containing 0.5 % O₂. Fit and background of the Mo3d emission, shown as solid gray lines, are included. Components Mo_I - Mo_{III} are shown as defined in the legend.

It is self-evident to explain the appearance of multiple components in the Mo3d spectrum with the presence of different oxidation states. Assignment of the latter to the visible components in Mo:In₂O₃ is often based on observations made on molybdenum oxide or other compounds [16, 62, 142]. Despite of more than 40 years of research and ESCA studies a controversial discussion about the oxidation states in molybdenum oxide is still ongoing [151–160]. A short summary will be given next.

Molybdenum possesses multiple oxidation states, i.e. Mo⁰, Mo²⁺, Mo³⁺, Mo⁴⁺, Mo⁵⁺ and Mo⁶⁺ [152, 153]. It is known to form MoO₃ and MoO₂ as stable oxides [151, 152, 161, 162]. Based on XPS measurements of oxide compounds, oxidation states from Mo⁴⁺ to Mo⁶⁺ were identified [151–160, 163]. Tab. 5.2 lists Mo3d_{5/2} binding energies and assigned oxidation states for molybdenum oxides and Mo:In₂O₃ as given in literature. The majority of publications account for three oxidation states while some explicitly exclude Mo⁵⁺.

Under the assumption that three oxidation states are present, the binding energy of Mo3d_{5/2} for Mo⁶⁺ is found between 232.4 eV – 232.7 eV, for Mo⁵⁺ between 231.0 eV – 231.6 eV and for Mo⁴⁺ between 229.1 eV – 229.6 eV [154–160, 163]. Subsequently Mo_I would be related to Mo⁶⁺, Mo_{II} to Mo⁵⁺ and Mo_{III} to Mo⁴⁺, assigning the components of the Mo3d_{5/2} emission displayed in Fig. 5.10.

Brox *et al.* [152] propose Mo⁴⁺ to show two components due to the screening of the core-hole. Accordingly Mo_{II} is assigned to unscreened and Mo_{III} to screened Mo⁴⁺ photoelectrons. This view is suggested by Scanlon *et al.* [151] who studied the electronic structure of different molybdenum oxides theoretically and experimentally. One corner-

Table 5.2: Literature values of Mo3d_{5/2} binding energies for different oxidation states, only considering molybdenum oxide, and Mo:In₂O₃. ^a two different Mo⁴⁺ components, at 229.6 eV and 230.2 eV, are mentioned here. ^b the value was estimated from a spectrum given in the reference. ^c a third, plasmon loss peak shifted by ≈0.6 eV is reported. Aerosol-Assisted Chemical Vapor Deposition AACVD. Atmospheric-Pressure Mist Chemical Vapor Deposition APMCVD. Magnetron Sputtering ms.

Ref.	Compound	Binding energy Mo3d _{5/2} in eV				
		Mo ⁶⁺	Mo ⁵⁺	Mo ⁴⁺	Mo ⁴⁺ _{screened}	Mo
[163]	MoO ₃ thin film	232.7	231.6			
[159]	MoO ₂ molybdenum foil					226.1
	MoO ₂ foil oxidized			230.4		
	MoO ₂ powder oxidized			230.6		
	MoO ₂ powder oxidized	232.5		230.9		
[158]	MoO ₃ /Co interface	232.7	231.1	229.6 ^a		
[157]	MoO ₃ /Co interface	232.7	231.1	229.6		
[156]	MoO ₃ thin films, reduced	232.4	231.0	229.3		228.0
[155]	nano powder		231.5			
[154]	MoO ₂			229.1		
	MoO ₃	232.6				
	Mo ₂ O ₅		231.6			
[152]	Mo oxidized	232.7		231.1	229.5	227.9
[151]	MoO ₃ single crystal	232.5				
	MoO ₂ powder			231.0	229.3	228.3
[62]	Mo:In ₂ O ₃ thermal evap.	232.8				
[10]	Mo:In ₂ O ₃ rf-ms	233.0		231.1 ^b		
[64]	Mo:In ₂ O ₃ plasma evap.	232.6				
[63]	Mo:In ₂ O ₃ rf/DC co-ms	232.6				
[16]	Mo:In ₂ O ₃ AACVD	232.5		231.3		
[142]	Mo:In ₂ O ₃ APMCVD, ms	232.5		231.5		
[26]	Mo:In ₂ O ₃ AACVD	232.5		231.2 ^c		

stone for the two latter articles is that MoO₃ and MoO₂ are the only stable molybdenum oxides.

Other authors acknowledge the instability of Mo₂O₅, as it would be required for Mo⁵⁺, but present certain conditions when Mo⁵⁺ supposedly is stable. For example Dhas *et al.* [155] report a stabilization upon incorporation of small atoms.

A recent article by Baltrusaitis *et al.* [153], establishing a new XPS data processing method on the example of molybdenum oxide, is aware of both positions but remain unclear about the existence of Mo^{5+} . White *et al.* [164] simply denotes the observed additional component as Mo^{x+} . Finally both camps agree that non-stoichiometric Magneli phases like $\text{Mo}_n\text{O}_{3n-1}$ will have mixed valence but do not explicitly appoint the resulting oxidation states. [151, 153, 163].

The discussion in literature differs in the case of $\text{Mo}:\text{In}_2\text{O}_3$. In photoelectron spectra for a variety of $\text{Mo}:\text{In}_2\text{O}_3$ films, deposited by several methods and with different doping concentrations only two doublets for Mo3d are discussed [10, 16, 62–64, 142]. As can be learned from Tab. 5.2 the high energy component appears at a binding energy which fits well to Mo^{6+} in molybdenum oxide. Meanwhile the binding energy of the low energy component matches either the Mo^{5+} or the unscreened Mo^{4+} state. All articles which observe the low binding energy component, address it to Mo^{4+} . Yoshida *et al.* [10] propose Mo^{4+} without discussing the assignment. This view is later adopted by others. Yamada *et al.* [142] make the decision based on references only assigning Mo^{4+} to components with a binding energy around 231.0 eV. It has to be noted that, upon closer inspection of the spectrum presented in the latter article a third component is present, which was ignored in the discussion. Bhachu *et al.* [16] explicitly ascribe the low binding energy component to unscreened Mo^{4+} states and base their decision on the article of Scanlon *et al.* [151]. Further indication for the presence of Mo^{4+} in the bulk is given by X-ray absorption spectra (XAS) comparing MoO_3 , MoO_2 and $\text{Mo}:\text{In}_2\text{O}_3$. Their explanation for the missing screened component in the XP spectra is that, due to the minimal contribution of Mo4d states to the valence band in $\text{Mo}:\text{In}_2\text{O}_3$, no local final state screening is to be expected. Reconsidering the spectrum shown in Ref. [151], however, another explanation may be the modest signal to noise ratio, which makes it hard to conclude over the presence of a third component.

Catalan *et al.* [141] investigated the oxidation state of molybdenum in $\text{Mo}:\text{In}_2\text{O}_3$ by extended X-ray absorption fine structure (EXAFS) measurements of amorphous films before and after annealing. Their conclusion is that after the deposition mainly Mo^{6+} is present, situated on In lattice sites, which changes to Mo^{4+} after annealing. Excess charge carriers due to the Mo^{6+} oxidation state are compensated by interstitial oxygen.

Wrapping up the literature review, the 6+ oxidation state can be pretty reliably assigned to Mo_I , while no final conclusion for the oxidation state of the other two components Mo_II and Mo_III can be drawn. For simplicity's sake, however, Mo_II will be addressed as Mo^{5+} and Mo_III as Mo^{4+} in the following.

The valence band structure of $\text{Mo}:\text{In}_2\text{O}_3$ is very similar to that of In_2O_3 in general. There are several studies based on computational calculations combined with different analytical techniques investigating the valence band region of those materials [16, 51, 165–167]. The In_2O_3 valence band maximum is dominated by O2p states. Hybridization with In4d at the top, In5p in the middle and In5s states at the bottom contribute to the final shape. Upon doping, characteristic features may appear. When doped with molybdenum no major changes occur to the shape of the valence band according to first principle calculation [16]. New states, however, appear in the band gap. For molybdenum oxides containing

other oxidation states than 6+ similar observations were made [156, 160, 162]. From calculations as well as from comparison to molybdenum oxide, these states can be attributed to emissions from Mo4d orbitals.

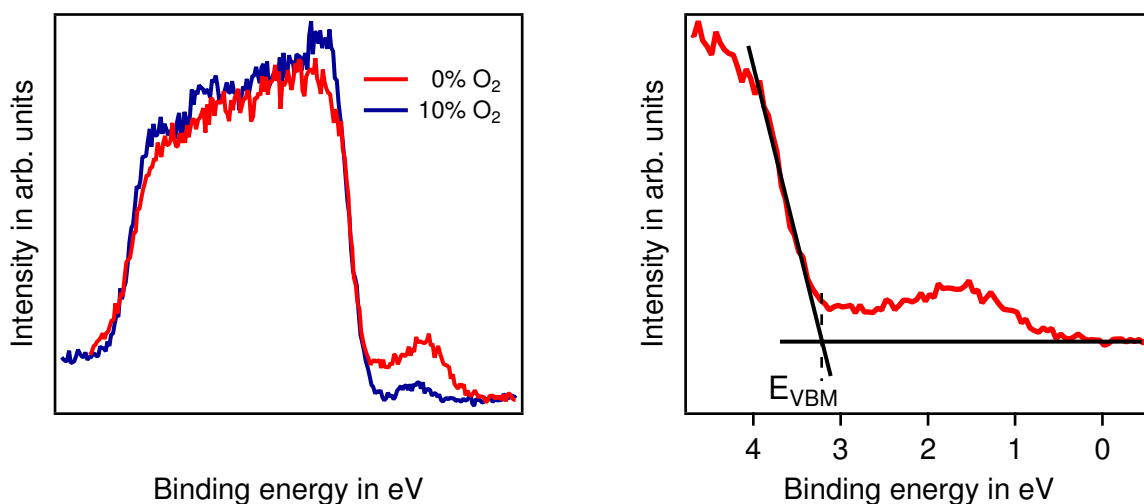


Figure 5.11: XPS valence region of two 5 mol% molybdenum doped In_2O_3 thin films on glass, deposited at 400°C either in pure argon or in 10% O_2/Ar mixture. The spectra on the left were shifted and scaled so valence band onsets and top slopes match. On the right only valence band onset with reference lines to determine the valence band maximum are shown.

XPS measurements of the valence band region for two different samples deposited at a substrate temperature of 400°C either in pure argon or in a 10% O_2 containing atmosphere are shown in Fig. 5.11 on the left. The spectra were shifted for similar valence band onsets and scaled to match in intensity. The valence band width is not affected by the deposition conditions. Under oxidizing conditions a larger initial increase and a sharper cutoff at low binding energies can be observed. Having a look at the $\text{O}2p$ partial density of states, two distinct features are present in those regions [16]. More oxygen during the deposition will result in an enhanced incorporation into the film giving rise to stronger oxygen signals, which in turn explains the latter observation.

A common way to determine the valence band maximum E_{VBM} from photoelectron measurements is to linearly extrapolate the leading edge and the background [168] as shown on the right side of Fig. 5.11. The energy of the intersection of both lines then represent E_{VBM} . It was shown before that this method leads to an underestimation of E_{VBM} of In_2O_3 and $\text{Mo}:\text{In}_2\text{O}_3$ [16, 51]. Calculated valence band density of states show an almost vertical onset. In combination with instrumental and life time broadening, however, a deviating slope will be measured, leading to an error. For $\text{Mo}:\text{In}_2\text{O}_3$ films the deposition temperature affects the slope of the onset up to 200°C , which can be explained by low temperature films being less crystalline as indicated by XRD measurements. This means not only a rigid shift of the valence band density of states but also a variation of the onset for different crystallinity leads to altered values of $E_F - E_{\text{VBM}}$.

For reduced In_2O_3 , $\text{Sn}:\text{In}_2\text{O}_3$ and SnO_2 samples emissions on the low binding energy side of the valence band could be observed [41, 169]. Those band gap states were at-

tributed to partially unsaturated cations [41]. Due to the presence of Mo4d states in the band gap of Mo:In₂O₃, however, a similar effect is difficult to observe.

In case of the Mo3d core level up to three components due to distinct oxidation states or screening could be clearly seen. A differentiation of the components contributing to the Mo4d emission in the band gap is hardly possible given its low intensity. Some notes can still be made. The occupation of s orbitals for transition metal elements in bound state is in general rather low. The electronic configuration of a bound molybdenum atom can be expressed by [Kr] 4d^{6-q}5s⁰, with q the oxidation state [170]. Based on this a maximum of two components can be expected for Mo4d, since no Mo4d valence electron remains for the Mo⁶⁺ state and therefore cannot be measured by XPS. This means, that Mo4d states are an indicator for the presence of molybdenum in an oxidation state less than 6+. It is hard to predict chemical shifts or hole screening for the Mo4d core level based on observations made on the Mo3d core level [116]. For various molybdenum oxides and Magneli phases two band gap states are reported in literature based on simulations and photoelectron spectroscopy measurements [151, 156, 171, 172]. A conclusive explanation is not given and it cannot be clarified whether one or two components contribute to the observed valence band state.

As shown in Fig. 5.11 more oxygen in the process atmosphere leads to a lower intensity of the band gap state and a variation of its energetic position. Binding energies of this state are plotted over In3d_{5/2} binding energies, which is shown in Fig. 5.12. The energetic position of the band gap state was determined by fitting a single Gaussian to the peak. For the In3d_{5/2} emission a single Gaussian was fitted to the data points close its maximum. Previously it was shown, that this procedure leads to approximately the binding energy of the screened component obtained from a more complex fitting procedure [41].

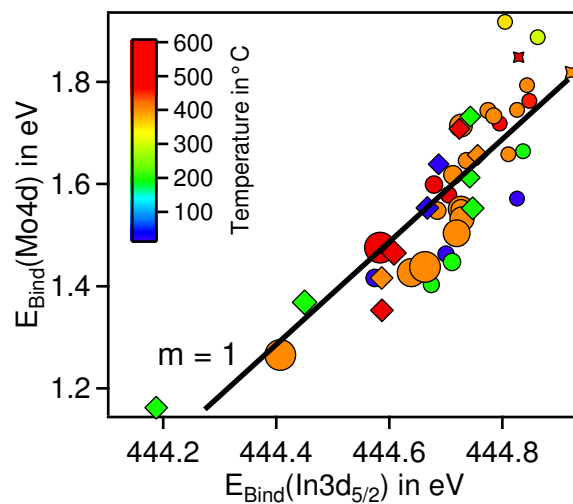


Figure 5.12: Mo4d plotted over In3d_{5/2} binding energies. The given color scale defines substrate temperature and marker size the oxygen content during deposition. Diamonds represent 2 mol% and circles 5 mol% doped samples, crosses samples after Ar-ion etching.

The binding energies of the band gap state and the In3d_{5/2} core level scale linearly with a slope of one. This indicates parallel shifting peaks as it is expected for two core levels

being affected by a variation of $E_F - E_{\text{VBM}}$. The latter observation emphasize the core level nature of the band gap states.

In Fig. 5.13 valence band regions of a 5 mol% Mo:In₂O₃ sample deposited in pure argon at 400 °C are shown, measured by XPS or UPS. The spectra were rescaled to match in maximum intensity of the valence band onset. The high intensity of the unmonochromatized Helium lamp compared to the monochromatic Al K α X-ray source provides a better statistics even after relatively short acquisition times, which explains the increased signal-to-noise ratio in the UP measurements. Both spectra show, in principle, the same features. The band gap state is visible and the valence band onset takes place at the same energy. Nevertheless does the overall shape differ significantly between both methods. Increasing intensity for binding energies above 9 eV in the UP spectra can be explained by inelastically scattered electrons. The number of those secondary electrons in this region is larger in UPS due to the high intensity of the unmonochromatized He-lamp. The photon energy is a further reason why the background is dominant at those binding energies. From first principle calculations it is known that the density of states show very abrupt onset for Mo:In₂O₃ [16]. The variation of the slope of the valence band onset therefore must be a result of varying instrumental broadening. Since the electron mean free path depends on the kinetic energy and therefore on the excitation energy as well [116], a variation of information depth has to be considered. This means that UPS measurements are even more surface sensitive than XPS. A gradient in the film, i.e. difference between surface and bulk composition, therefore may affect the measured valence band shape. Atomic subshell photoionization cross-sections depend as well on the excitation energy [119]. This implies varying contributions of the valence band states to the measured spectra between XPS and UPS. As a result of all the given factors individually shaped spectra are obtained.

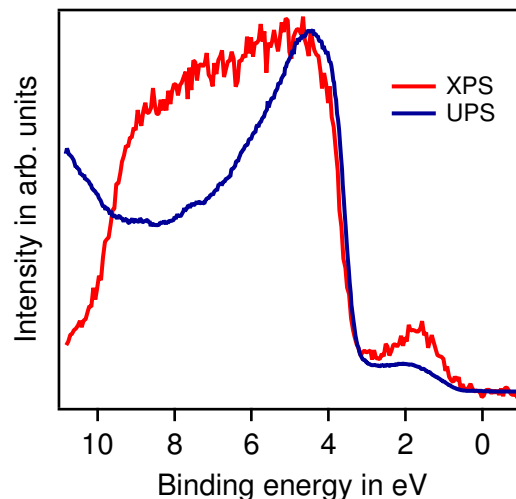


Figure 5.13: Comparison of the valence band region measured with XPS and UPS of a 5 mol% Mo:In₂O₃ sample deposited in pure argon at 400 °C. The spectra were scaled for matching maximum intensity of the valence band onset.

The band gap state in XPS was already attributed to the Mo4d emission, while in UPS an overlap between the Mo4d emission and a satellite feature, caused by the He- β line, has to be taken into account. Irfan *et al.* [173], who report a broad peak at a binding energy of

2.0 eV in the UP spectra after deposition of MoO₃ on ITO, attribute it exclusively to a satellite feature of the valence band maximum caused by the light of the unmonochromatized helium lamp. Since the band gap emission in UP spectra of Mo:In₂O₃ is much more pronounced as compared to In₂O₃, a second feature besides the valence band satellite must be present. Based on the results from XPS it is correlated to Mo4d states.

Comparing the intensity ratio of the band gap state, dominated by the Mo4d emission, and of the valence band maximum, a reduction can be observed from the XPS to the UPS measurement. This can be explained by the energy dependence of atomic subshell photoionization cross-sections, too. Yeh *et al.* [119] list the latter values for a variety of elements and photon energies. For the given material cross-sections for the O2p shell, which dominates the valence band region of doped In₂O₃, and of Mo4d have to be compared. The latter values as well as their ratio are given in Tab. 5.3 for the photon energies corresponding to He-I and Al-K α lines. From the cross-section ratios it is obvious, that a constant elemental ratio between molybdenum and oxygen will lead to a less pronounced Mo4d component compared to the valence band maximum intensity in UP over XP spectra.

Table 5.3: Atomic subshell photoionization cross-section of Mo4d and O2p and their ratio given for two different photon energies [119].

$h\nu$ in eV	σ_{Mo4d}	σ_{O2p}	$\frac{\sigma_{\text{Mo4d}}}{\sigma_{\text{O2p}}}$
21.2	26.27	10.67	2.46
1486.8	4.6×10^{-3}	2.4×10^{-4}	19.17

The basic features of the relevant core level and valence band region were discussed in this section. The Mo3d core level emission is composed of up to three different components. Based on literature, only the Mo⁶⁺ can be doubtlessly assigned to the Mo_I while the oxidation state or explanation for Mo_{II} and Mo_{III} remain unclear. The valence band region of Mo:In₂O₃ is comparable to other dopants except for a valence band state, which is correlated to occupied Mo4d states. This feature can therefore be used as indicator for oxidation states lower than Mo⁺⁶.

5.4.2 Oxidation state and Segregation

After introducing the general aspects of Mo:In₂O₃ photoelectron spectra, a closer look will be taken on the influence of substrate temperature and oxygen content in the process atmosphere. Films deposited under a variety of conditions will be discussed next.

In Fig. 5.14 and Fig. 5.15, XP spectra of 5 mol% molybdenum doped In₂O₃ films are shown. O1s, In3d_{5/2} and Mo3d core levels and valence band regions of samples deposited at different temperatures in argon or at a substrate temperature of 400 °C in a process atmosphere of varying oxygen content are shown. The spectra were normalized to the overall weighted peak area as described in Sec. 4.3.

A feature at higher binding energies can be seen in the O1s spectra of the samples deposited at 25 °C and 200 °C in pure argon. Independent on molybdenum content in the target this characteristic can be observed for films deposited at 200 °C or below, in a process atmosphere with maximum 0.5 % O₂ content. Similar to observations made on In₂O₃ films,

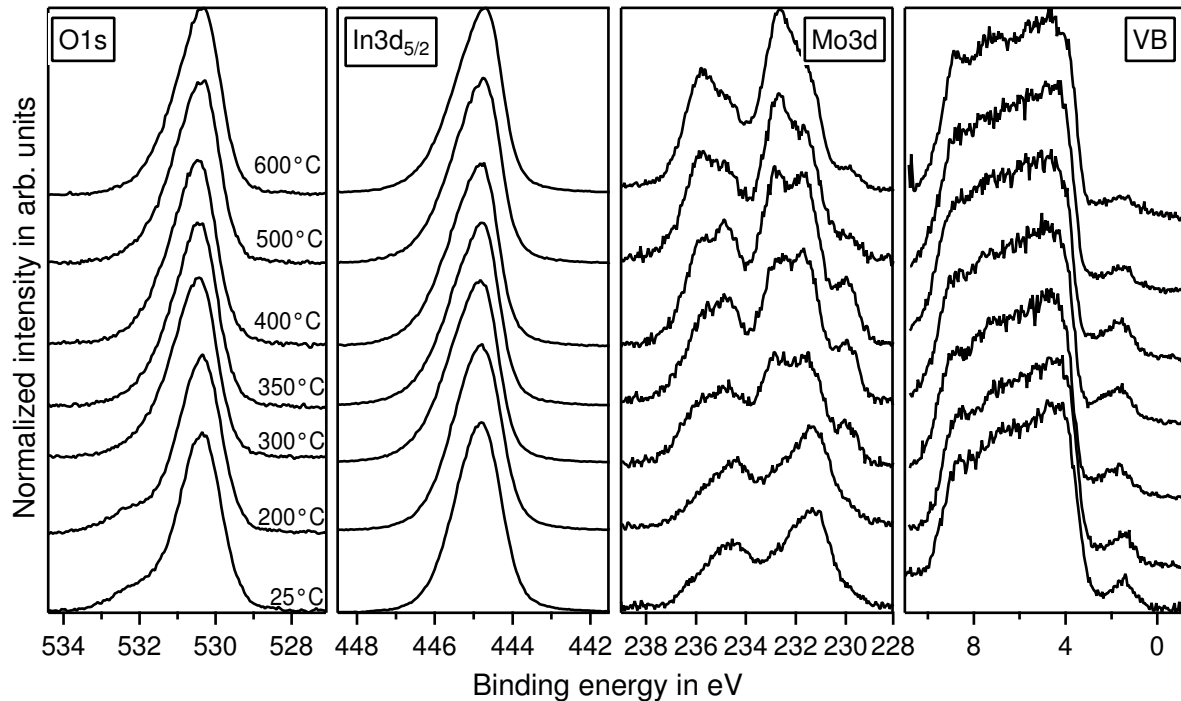


Figure 5.14: XPS core level spectra of the O1s, In3d_{5/2}, Mo3d emission and valence band region of 5 mol% molybdenum doped In₂O₃ thin films on glass. The samples were deposited in argon atmosphere at different substrate temperatures as indicated by labels in the O1s graph. All spectra are normalized to the overall weighted peak area. An offset in y-direction is introduced for clarity.

the additional feature can be explained by peroxide species at the surface [41]. In spite of increasing asymmetry, which is fully developed at 300 °C, no other major changes in peak shape or binding energy can be observed for the O1s and In3d_{5/2} emission when the temperature is varied. Analogously, a decreasing asymmetry can be seen when the oxygen content in the process atmosphere is increased. The different deposition conditions lead to slight changes of binding energies, which is especially pronounced for the sample deposited in 10% O₂ containing atmosphere and will be discussed later.

A significant variation of the components forming the Mo3d peak and the band gap feature in the valence band region can be identified for both temperature and oxygen series. The left-hand side of Fig. 5.16 and Fig. 5.17 show the Mo3d core levels without shift in y-direction. Peak areas of the three components, normalized to the corresponding In3d_{5/2} area, are shown on the right hand side of the graphs. Latter values were obtained by a fitting procedure as described in Sec. 5.4.

The molybdenum content at the surface increases with temperature up to 400 °C followed by a decrease for even higher temperatures. As apparent from the spectra as well as from fits, Mo⁶⁺, Mo⁵⁺ and Mo⁴⁺ states are present throughout the whole series although their ratios vary. For 25 °C and 200 °C Mo⁵⁺ is dominating. For higher temperatures the ratio changes in favor of Mo⁶⁺. Maximum content of Mo⁵⁺ and Mo⁴⁺ is achieved for 400 °C. Increase and decrease of the latter components occur in a similar manner.

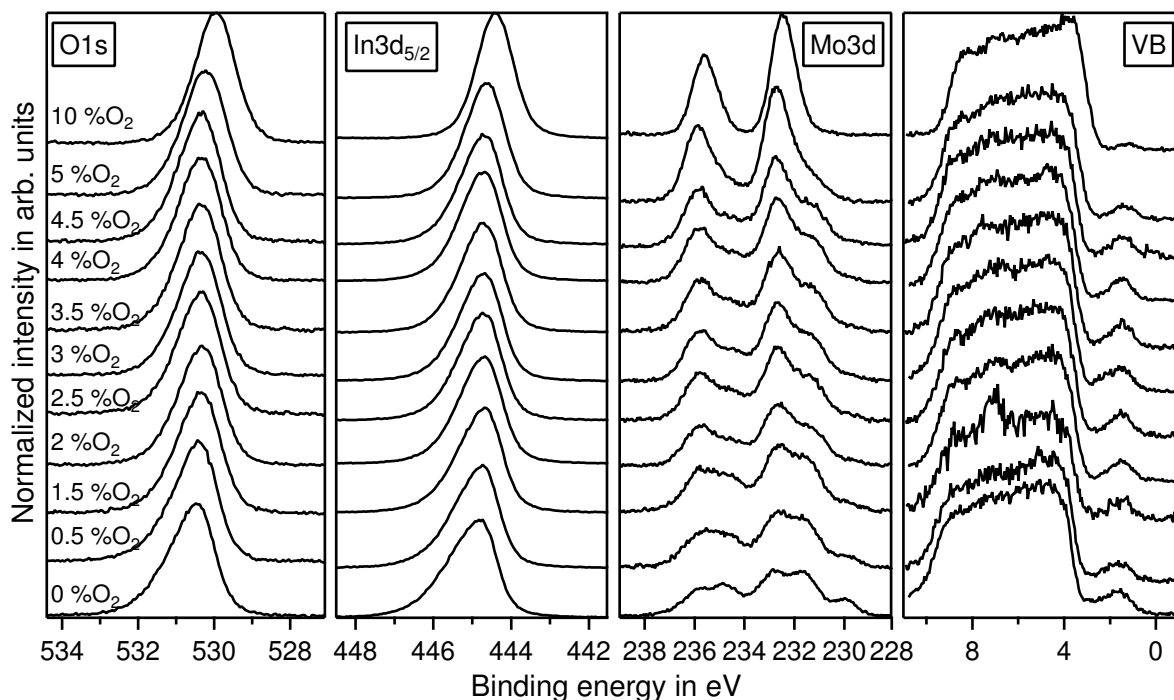


Figure 5.15: XPS core level spectra of the O1s, In3d_{5/2}, Mo3d emission and valence band region of 5 mol% molybdenum doped In₂O₃ thin films on glass. The samples were deposited at a substrate temperature of 400 °C. An argon/oxygen mixture was used as process atmosphere. Labels in the O1s graph indicate the oxygen content during deposition. All spectra are normalized to overall weighted peak area. An offset in y-direction is introduced for clarity.

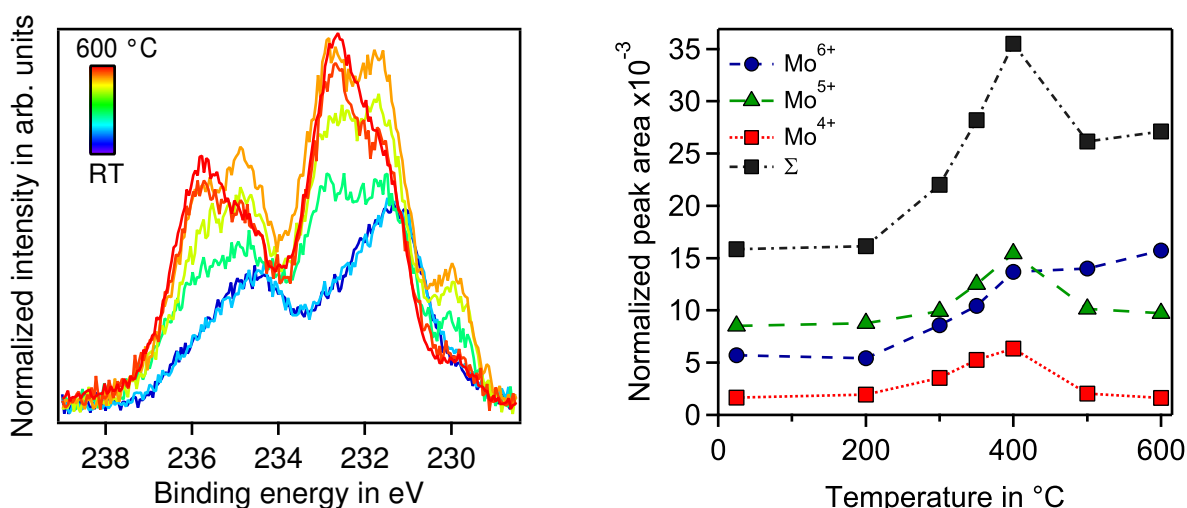


Figure 5.16: Mo3d core level emission for different temperatures deposited in argon on the left. Spectra are normalized to the corresponding In3d_{5/2} peak areas. Same data as shown in Fig. 5.14. Different levels of grey indicate temperature (light grey is low, black is high). Normalized peak areas of the three components and their sum, as obtained by a fitting procedure, are shown on the right.

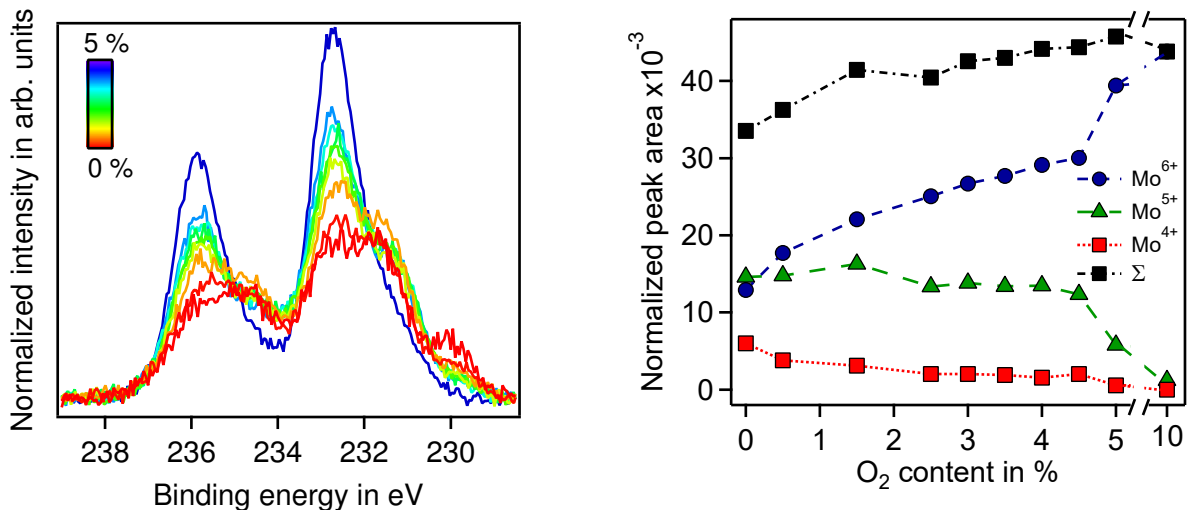


Figure 5.17: Mo3d core level emission for different oxygen partial pressures deposited at 400 °C are shown on the right. Spectra are normalized to the corresponding In3d_{5/2} peak areas. Same data is shown in Fig. 5.15. Different levels of gray indicate oxygen content in process atmosphere (light gray is low, black is high). Normalized peak areas of the three components and their sum, as obtained by a fitting procedure, are shown on the right.

The starting point for the oxygen series shown in Fig. 5.17 is the sample with highest molybdenum content at the surface as observed in the temperature series. Approximately equal amounts of Mo⁶⁺ and Mo⁵⁺ can be seen. Mo⁴⁺ clearly is present as well. By adding oxygen to the process atmosphere an increasing Mo⁶⁺ component can be observed. The amount of Mo⁵⁺ stays rather constant before significantly decreasing when 5% oxygen is added. The Mo⁴⁺ component initially decreases, then stays constant up to 4.5% and then drops again. At 10% O₂/Ar the latter components are almost completely gone. Compared to a thick MoO₃ film grown on Sn:In₂O₃, a shoulder on the low binding energy side is found. This indicates the presence of small amounts of Mo⁵⁺ and Mo⁴⁺. Given the uncertainty of the determined values, Mo⁵⁺ and Mo⁴⁺ are still correlated. The highest molybdenum content is obtained at 5% oxygen.

The overall molybdenum content in at.%, calculated from the O1s, In3d_{5/2} and Mo3d peak areas using Eq. 3.32, is shown in Fig. 5.18. Data points of all 2 mol% and 5 mol% doped Mo:In₂O₃ samples are displayed. Oxygen content and temperature affect the dopant concentration of the 2 mol% samples in a similar way as was observed for the 5 mol% samples. Higher temperatures and oxygen contents lead to increased molybdenum content at the surface. The only exception is the maximum at 400 °C, which cannot be found for the lower dopant concentration.

The Mo concentrations at the surface determined by XPS differ considerably from the nominal target concentrations. A total variation of 3.6 mol% and 2.6 mol% is found for the films deposited from the nominally 5 mol% and 2 mol% doped targets respectively. Based on sputter depth profiles discussed in Sec. 5.4.3 it can be shown that the bulk concentration in nominally 5 mol% doped films is closer to 2.2 mol%. Varying Mo content with deposition condition and distance from the surface, indicate segregation of molybdenum.

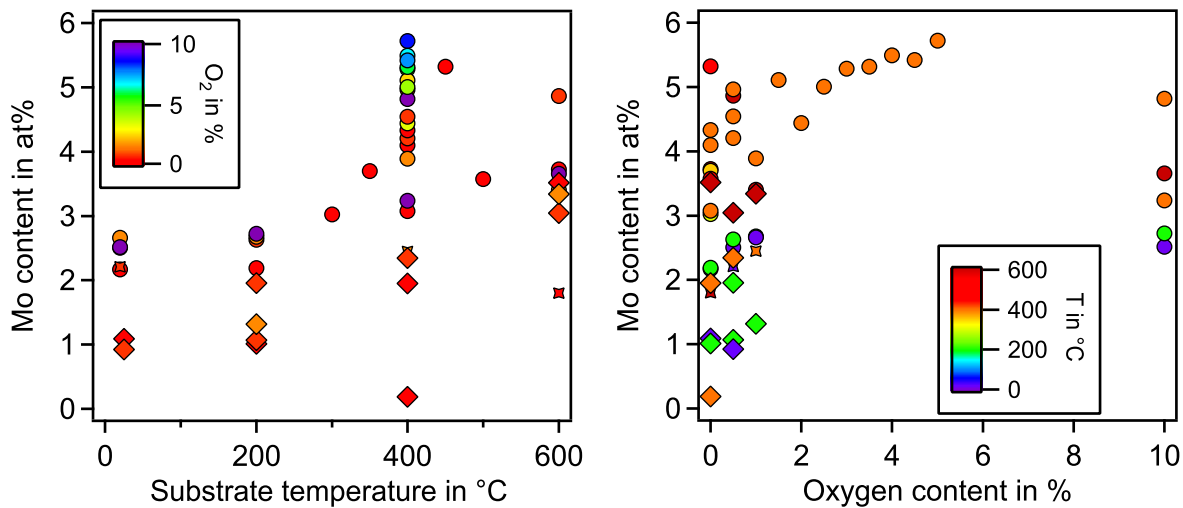


Figure 5.18: Molybdenum content in atom percent as obtained from XPS measurements plotted versus deposition temperature on the left and oxygen content on the right. Marker color indicates either oxygen content or substrate temperature according to the given color scales. Diamonds and circles indicate nominally 2 mol% and 5 mol% doped thin films respectively.

Hardly any difference in Mo surface concentration can be seen for films deposited at room temperature or 200 °C. Increasing the substrate temperature to 400 °C leads to a higher molybdenum content at the surface. Even higher temperatures lead to a reduced or respectively to an increased Molybdenum content for nominally 5 mol% and 2 mol% doped films. Overall a higher oxygen content in the process atmosphere leads to molybdenum enrichment at the surface. The samples deposited at 400 °C in 10% oxygen do not match this observation though.

For both, the oxygen and temperature series changing binding energy, intensity and shape of the Mo4d component is visible in Fig. 5.14 and Fig. 5.16. Its intensity follows the trend of the Mo⁵⁺ component. Due to the signal to noise ratio in this region, however, it is questionable whether a detailed discussion about the latter parameters from XPS measurements beyond what was done in Sec. 5.4 is reasonable.

Changes in the valence band region are similar to what was discussed in Sec. 5.4. A different slope of the valence band onset can be observed for samples deposited at 200 °C and below. Oxidizing conditions lead to a more defined shape of the valence band. Besides those observations no systematic variation of its form can be seen. Different values of $E_F - E_{VBM}$ as the result of varying deposition conditions are illustrated in Fig. 5.19. Valence band maximum for 2 mol% and 5 mol% doped Mo:In₂O₃ samples plotted over deposition temperature or oxygen content can be seen. A dopant concentration of 5 mol% leads, in general, to higher values of $E_F - E_{VBM}$. Low temperatures and high oxygen content yield low $E_F - E_{VBM}$ while the highest values are obtained around 400 °C under reducing conditions. Comparing the extreme values a difference of 1 eV is observed.

In Fig. 5.20, the In3d_{5/2} binding energy is plotted over $E_F - E_{VBM}$. A correlation between both energies can be seen. Samples deposited at 200 °C or below show a linear behavior with a slope of one, as indicated by the thick solid line, while samples deposited at higher

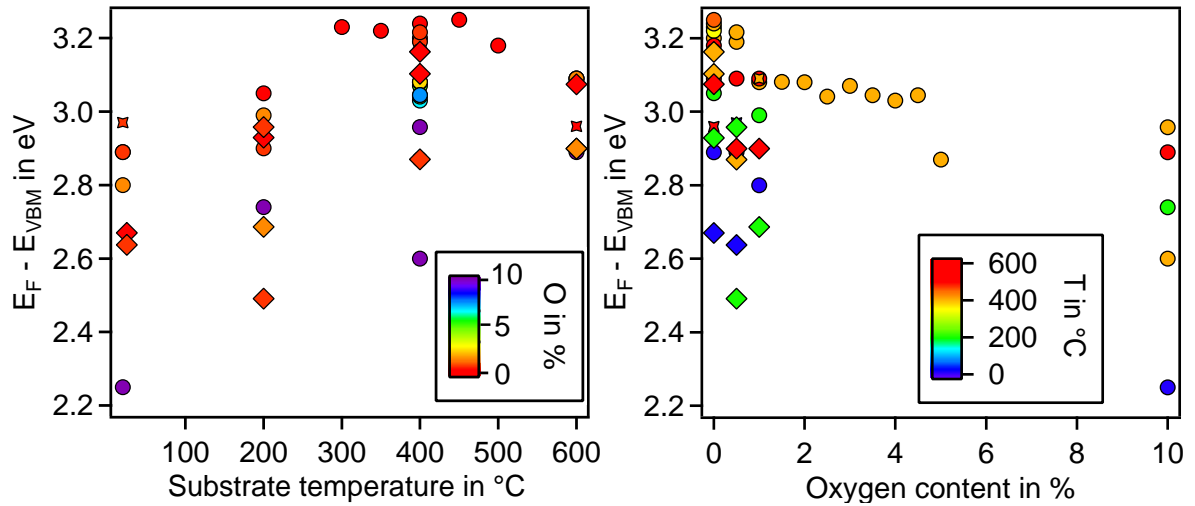


Figure 5.19: Valence band position plotted over substrate temperature (left) and oxygen content of process atmosphere (right) during deposition for 2 mol% (diamonds) and 5 mol% (circles) doped Mo:In₂O₃ films. Crosses are data points measured after Ar-ion sputtering. The colors indicate oxygen content of the process atmosphere or substrate temperature respectively.

temperatures coincide with a slope of 0.64. Distinct valence band onsets were observed for both temperature regions. This difference can explain an offset between the determined values. A slope deviating from one implies a variation of the distance between core level and valence band maximum, as previously reported for Sn:In₂O₃ [41]. Gassenbauer *et al.* [41] discuss screening of the core holes as explanation in this context.

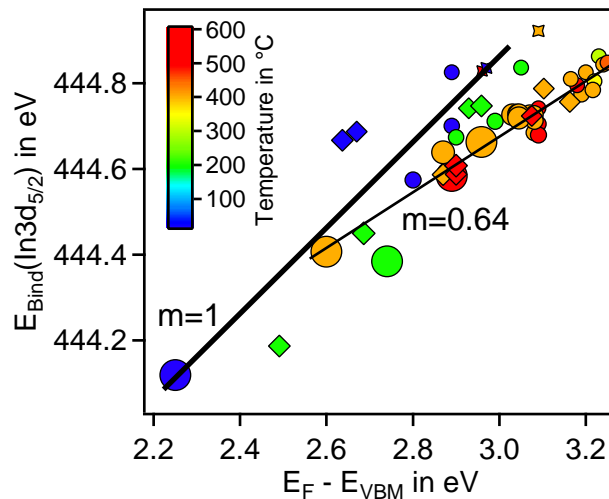


Figure 5.20: In3d_{5/2} binding energy plotted over valence band maximum for 2 mol% (diamonds) and 5 mol% (circles) doped Mo:In₂O₃ films. Crosses are data points measured after Ar-ion sputtering. The colors indicate the substrate temperature during deposition and marker size oxygen content of the process atmosphere. The solid line indicates a slope of one.

While kinetics in the film are mainly determined by the substrate temperature, the oxygen chemical potential is influenced both by temperature and oxygen content in the process atmosphere. Conditions at higher temperatures are more reducing, while adding oxygen obviously leads to more oxidizing conditions. Since hardly any difference in Mo core level spectra and surface concentration was seen for films deposited at room temperature or 200 °C it can be assumed that those temperatures are insufficient to enable diffusion of molybdenum. This observation is confirmed by X-ray diffraction patterns shown in Sec. 5.1 where no difference in crystallinity can be observed for films deposited at the latter temperatures. Changing molybdenum content at the surface and X-ray diffraction patterns indicate that both diffusion and recrystallization take place at temperatures above 200 °C. Deposition conditions significantly affect the Mo3d emission and therefore the molybdenum oxidation state as well. As expected, an increasing oxygen content leads to enhanced formation of Mo_I, which can be doubtlessly assigned to Mo⁶⁺, while both other components decrease. The total amount of Mo at the surface increases with oxygen in the process atmosphere. The effect of substrate temperature is not that clear. At temperatures above 400 °C the Mo⁶⁺ component is growing in favor of the other components. Further, the overall Mo surface concentration is decreasing. The vapor pressure of MoO₃ is the highest of all Molybdenum oxides and its mixtures [174–176]. As 600 °C are enough for PVD of MoO₃ thin films, evaporation of the latter might be a suitable explanation for the overall decreasing Mo concentration at the surface at 500 °C and 600 °C. Nevertheless, vanishing Mo⁵⁺ and Mo⁴⁺ for conditions being nominally more reducing cannot be explained this way. The position of $E_F - E_{\text{VBM}}$ is affected by the deposition conditions in a similar way as was reported for Sn:In₂O₃ and Ge:In₂O₃ [33, 35, 41]. Oxidizing conditions lead to lower values and reducing conditions vice versa. One difference is that for temperatures above 400 °C a decreasing $E_F - E_{\text{VBM}}$ is observed, independent on doping concentration or oxygen content. In the latter articles an effect of $E_F - E_{\text{VBM}}$ on Sn or Ge segregation at the surface was reported. No clear correlation between molybdenum content or a single Mo component and $E_F - E_{\text{VBM}}$ is found here as shown in Fig. 9.3 in the appendix.

5.4.3 Sputter depth profiles

To investigate the evident molybdenum enrichment at the surface, selected samples were Ar-ion etched in the XPS analysis chamber. This method was used before to give proof for Sn and Ge segregation in Sn:In₂O₃ and Ge:In₂O₃ [35, 41]. The acceleration voltage was set to 1 kV at a current of 0.7 μA. For most of the samples, an etching time of 5 min in combination with an erosion area of 4 × 4 mm² was chosen (Fig. 5.23) while a sample deposited in 10 % oxygen at 400 °C was etched for 25 min in total, in 1 min increments with an erosion area of 6 × 6 mm² (Fig. 5.21). The etching rate for the smaller erosion area is roughly 0.5 nm min⁻¹ while it is 0.2 nm min⁻¹ for the larger area. The discussion will be started with presenting the more detailed depth profile before concluding by comparing several samples.

In Fig. 5.21 different levels of gray are used to visualize the consecutive steps. On the right hand side of the figure, the molybdenum content is plotted over etching time. The same color scale is applied. In accordance to the above made observations, only Mo⁶⁺ can be identified in the Mo3d spectrum of the as deposited film under the given conditions.

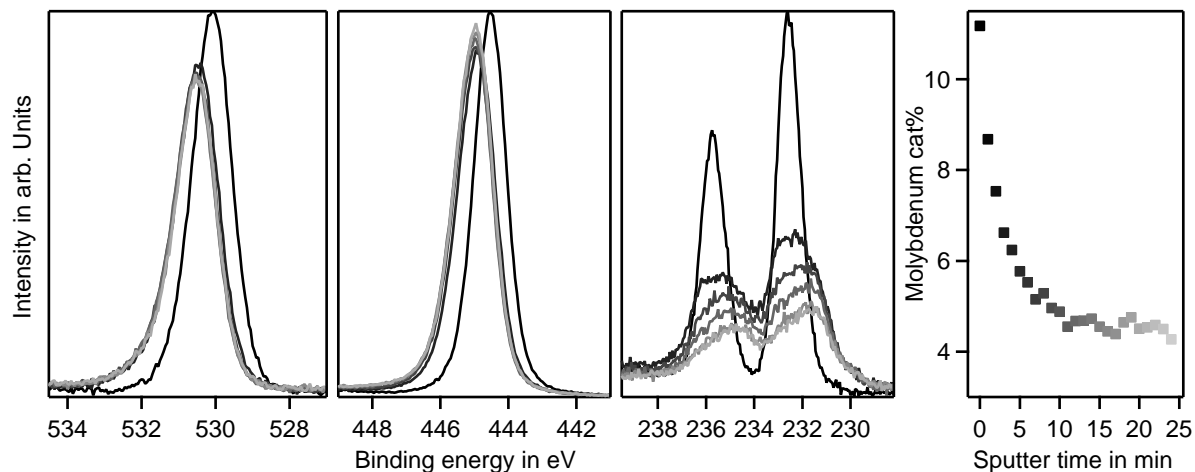


Figure 5.21: XPS sputter depth profile of a 5 mol% Mo:In₂O₃ sample deposited at 400 °C in a 10 % oxygen containing process atmosphere. The shown O1s, In3d_{5/2} and Mo3d spectra were measured after 0, 1, 2, 4, 14 and 24 min sputtering time. The molybdenum cat% over sputter time for all steps is displayed on the right side. The gray levels indicate sputter total time. The sputter rate is estimated to be 0.5 nm/min.

Further, a rather low Fermi level is indicated by the binding energies of the O1s and In3d_{5/2} core levels. After the first etching step a significant reduction of the Mo⁶⁺ component and appearance of Mo⁵⁺ and Mo⁴⁺ can be observed. O1s and In3d_{5/2} binding energies are shifted to higher values as can be expected for a reducing treatment as Ar-ion etching. Broadening and asymmetric peak shapes are a consequence of the etching procedure. An overall lower intensity after the first step has to be considered since all consecutive measurements were carried out at a higher chamber pressure as required for differential pumping of the ion gun. Up to a total etching time of 14 min, the ratios of the molybdenum components as well as the In3d_{5/2} intensity are changing while the O1s peak reaches its final shape earlier. In its final state Mo⁵⁺ is dominating while the other two components are still present.

To follow the development of surface composition the normalized peak areas of the three core levels are shown in Fig. 5.22 over sputter time. The latter values were obtained from integration of the background subtracted spectra and using Eq. 3.32. A decrease can be observed for molybdenum and oxygen while indium increases. During the first 5 min O1s and Mo3d peak areas decrease at the same rate, followed by further lowering of the Mo3d while the O1s area stays constant. The In3d_{5/2} area is gaining what is lost by the other two components.

The first conclusion, which can be drawn, is that a significant segregation of molybdenum at the surface is present for the given deposition conditions as the overall Mo3d area drastically decreases. Furthermore, the oxidation state of molybdenum changes upon Ar ion bombardment. Possible explanations for this observation are different Mo oxidation states at the surface compared to the bulk or a change due to the treatment itself. The inelastic mean free path of Mo3d photoelectrons can be estimated to be 2 nm using the NIST Electron Inelastic-Mean-Free-Path database with the TPP-2M equation [177]. The

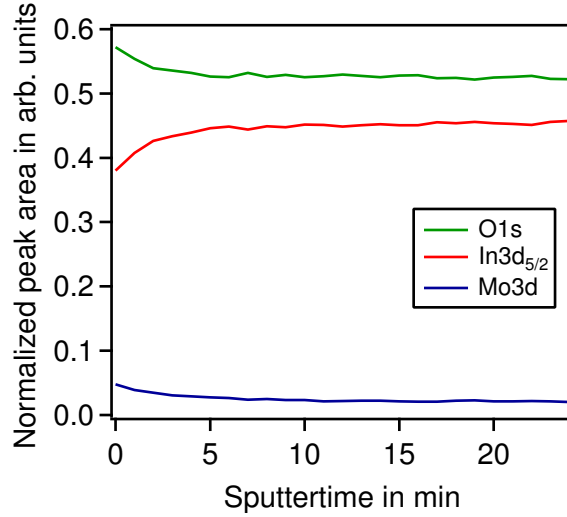


Figure 5.22: Normalized peak areas of O1s, In3d_{5/2} and Mo3d core levels during sputter depth profile.

information depth in XPS is usually a multiple of the electron inelastic mean free path. Based on the spectra of the as deposited film, the Mo⁶⁺ is the only component present over the whole information depth, which is larger than 2 nm. After the first etching step, which resembles a depth of about 0.2 nm, all three molybdenum components are already present. The abrupt appearance of the new states indicates that Mo⁵⁺ and Mo⁴⁺ are induced by ion bombardment. Therefore no conclusion can be drawn whether different Mo oxidation states are present at the surface and in the bulk.

Spectra of four samples deposited under different conditions are shown in Fig. 5.23 as is (black) and after etching about 2.5 nm deep (grey). At the bottom, spectra of the etched samples are compared. Deposition conditions, molybdenum content and Hall charge carrier mobility and concentration of the shown samples are given in Tab. 5.4.

Table 5.4: Molybdenum content before and after sputtering of samples presented in Fig. 5.23. Order of sample is similar. Hall charge carrier mobility and concentration after sputtering are given as well.

#	T _{Substrate} in °C	% O ₂	Mo at% _{before}	Mo at% _{after}	μ in $\frac{\text{cm}^2}{\text{Vs}}$	n in $\frac{\text{S}}{\text{cm}}$
1	400	10	4.8	2.2	11.0	2.70×10^{18}
2	600	0	3.7	1.7	0.78	4.33×10^{20}
3	400	0.5	4.2	2.5	55.1	5.71×10^{20}
4	20	0.5	2.5	2.2	18.3	2.30×10^{19}

As expected from the temperature and oxygen series, different Mo3d emissions can be observed for the as deposited films. Significantly different charge carrier concentrations and mobilities of the studied films emphasize contrasting bulk properties. Except for the room temperature sample, a significant reduction of the Mo3d signal can be seen after sputtering. All spectra are almost identical after the treatment. The only outlier is the sample deposited at 600 °C in 0% oxygen, having a lower molybdenum content. It seems

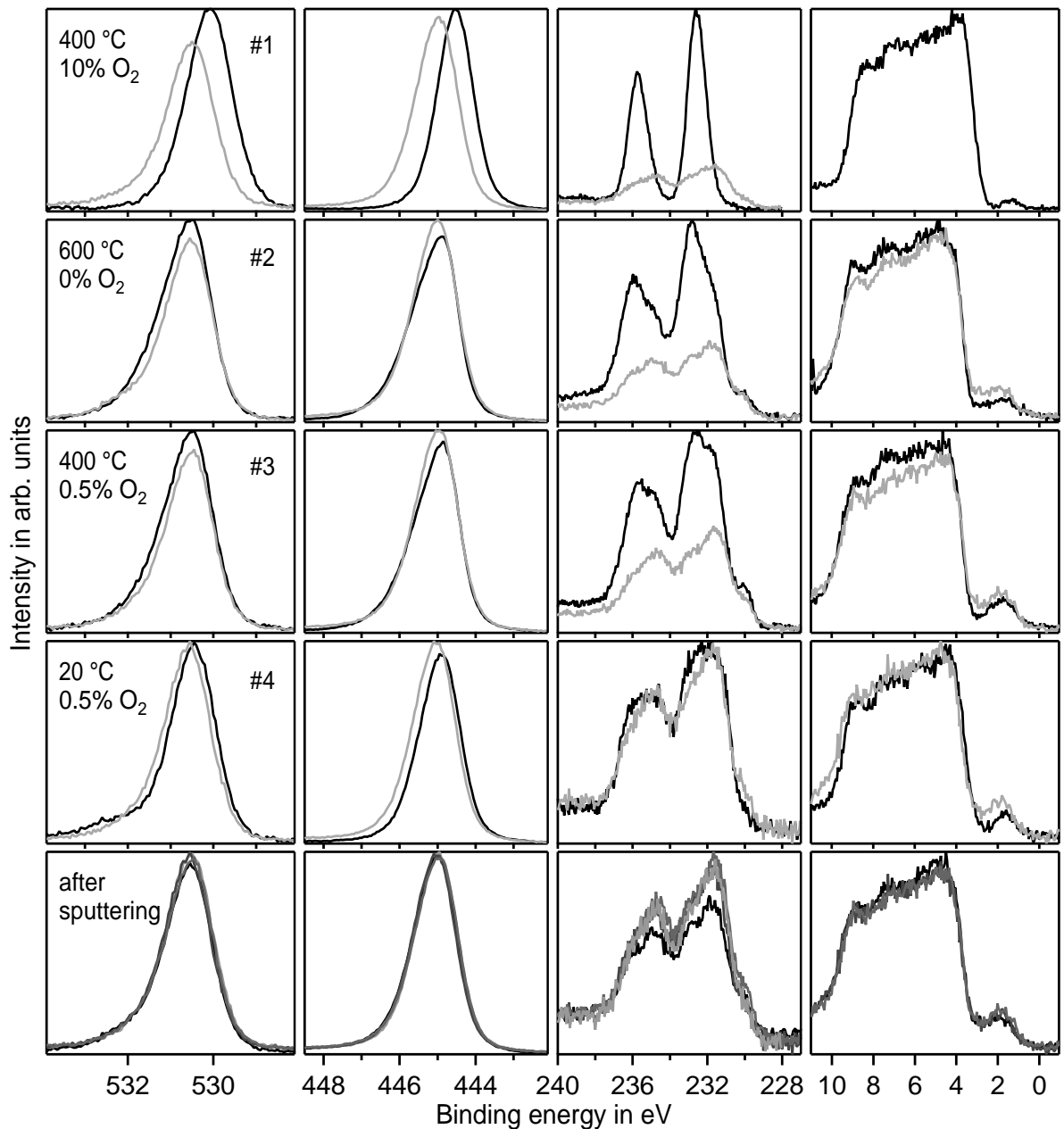


Figure 5.23: XPS sputter depth profile of four different 5 mol% Mo:In₂O₃ samples from top to bottom. O1s, In3d_{5/2} and Mo3d core level and valence band regions are shown (left to right). Deposition conditions are similar except for temperature and atmosphere as noted in the graphs. The shown spectra were measured of the as deposited film (black) and in a depth of roughly 2.5 nm (gray). The bottom row compares the above shown spectra of the sputtered samples.

that only the top layers of the films are affected by changes of the deposition conditions while the bulk is unchanged.

Ar-ion bombardment has a significant impact on the local order of the material by e.g. breaking of atomic bonds and intermixing. Preferential sputtering of certain species may as well influence the results. In the case of MoO₃, oxygen is preferentially sputtered [156].

Keeping this in mind, the measurements of a sputtered sample does very likely not represent how the spectrum in an unaffected bulk would look like. Above it was discussed that minimal Ar ion etching already leads to significant changes of the Mo3d emission, which most likely is a result of the treatment itself. Identical Mo3d emissions, of significantly different films, after 2.5 nm etching suggest a similar conclusion. This treatment is not suitable to compare oxidation states at the film surface and in larger depth. Still it can be used to investigate the composition when selective sputtering is excluded.

The amount of molybdenum at the surface is strongly affected by the deposition conditions, while the content in the film obtained after Ar ion etching is rather similar. No molybdenum segregation is found for the film deposited at room temperature. Higher deposition temperatures lead to considerably more molybdenum at the surface as compared to the bulk of the films. In context of the previous temperature series, where no difference between the room temperature and 200 °C sample could be observed, it seems probable that temperatures above 200 °C are required to allow for diffusion of molybdenum.

The oxygen content of the process atmosphere seems to have an influence on segregation as well. More oxygen leads to a higher molybdenum content at the surface. Due to the little number of samples a clear tendency can not be given, though.

5.4.4 Ultraviolet Photoelectron Spectroscopy and Surface Potentials

UP spectra of 5 mol% Mo:In₂O₃ samples deposited either at varying temperatures in pure argon atmosphere or at a substrate temperature of 400 °C in varying oxygen content are shown in Fig. 5.24 and Fig. 5.25. The high binding energy part is chosen to give a detailed look on the secondary electron cutoff while the low binding energy part gives an overview on the valence band onset. The spectra in each section were scaled for matching intensities of secondary electron cutoff or maximum of the valence band onset. The Mo4d emission and Fermi edge are shown enlarged in the insets. A scale from light gray to black is used to indicate increasing temperature or oxygen content. Arrows additionally illustrate the course of each parameter.

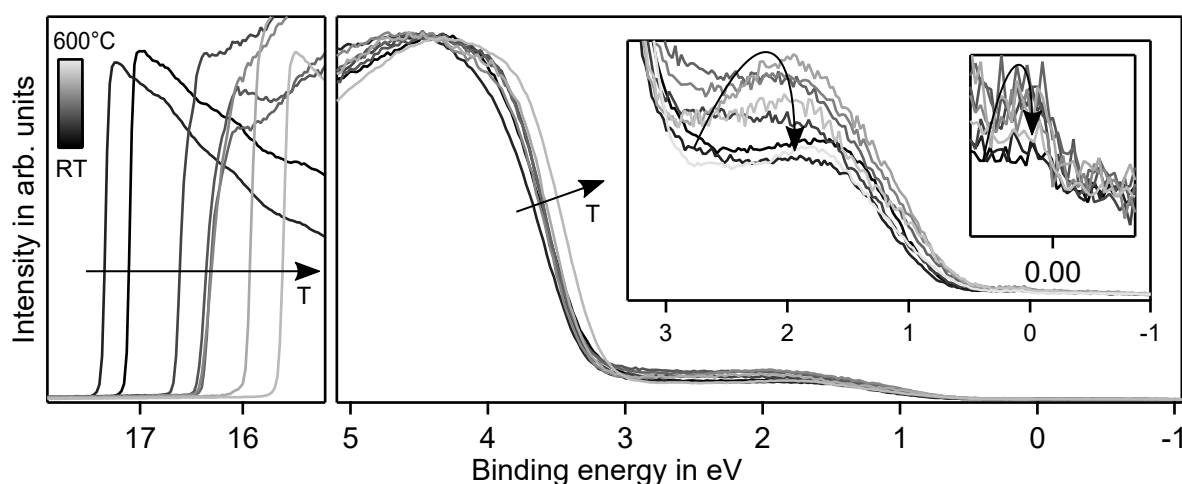


Figure 5.24: UPS spectra of 5 mol% Mo:In₂O₃ samples deposited in argon at varying temperatures. Different levels of gray indicate the deposition temperature.

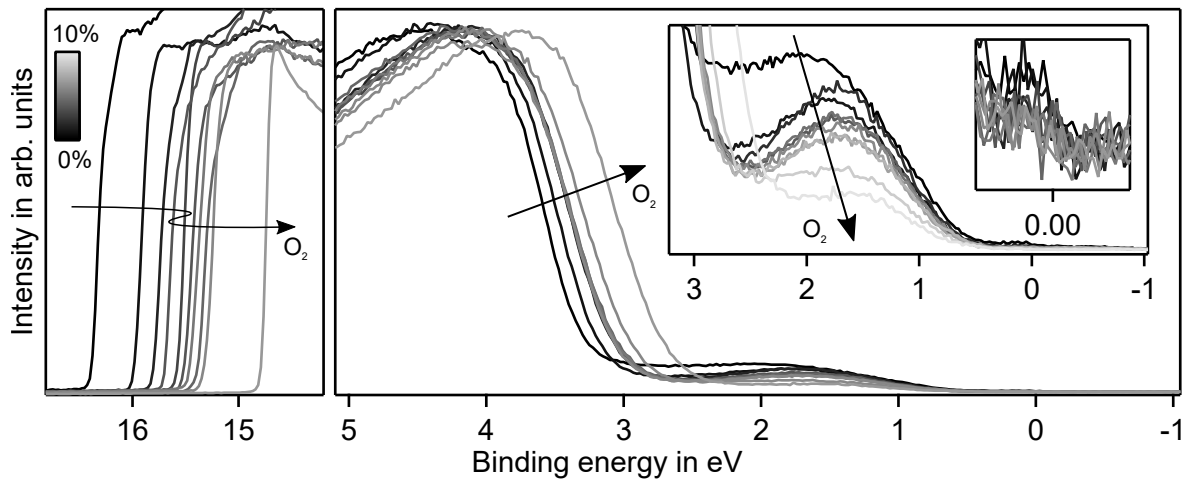


Figure 5.25: UPS spectra of 5 mol% Mo:In₂O₃ samples deposited at 400 °C in varying oxygen content. Different levels of gray indicate the amount of oxygen in process atmosphere.

Looking at the temperature series a variation of the slope of the onset can be observed for samples deposited at temperatures up to 200 °C in the UPS measurements. Above this temperature no changes in slope of valence band onset can be seen. Even the energetic position is almost identical except for the 600 °C sample which is shifted to lower binding energies. For the oxygen series a slight decrease of the slope can be seen as well as a shift towards lower binding energies with increasing oxygen content. Essentially constant energetic positions can be noted for samples deposited in 1.5%–4.0% oxygen containing atmospheres. Overall agreement with the valence band region from XPS can be found.

Due to a better statistics of the valence band region for UPS measurements, it is possible to follow the evolution of the Mo4d component quite well. Under the assumption of a constant satellite feature, the Mo4d intensities fit quite well to what was seen from XPS measurements and coincide with the intensities of the Mo⁵⁺ and Mo⁵⁺ components as shown in Fig. 5.16 and Fig. 5.17.

Using Eq. 4.3 and Eq. 4.4, the work function and ionization potentials of the films can be determined from UPS and XPS valence band spectra. While a large variation in secondary electron cutoff of about 2 eV can be seen, the valence band maximum changes only by roughly 0.6 eV. Since the two values do not change in a similar way it becomes obvious that different deposition conditions do not only affect the Fermi level position but also the surface dipole [32]. Termination and orientation of the surface, as well as adsorbates or dopant segregation were previously mentioned to influence the surface potentials of doped and undoped In₂O₃ [29, 32, 41].

Ionization potentials and work functions over substrate temperature and oxygen content in the process atmosphere are shown in Fig. 5.26. The colors indicate either oxygen content or temperature. Increasing either parameter leads to larger values of IP or ϕ . Ionization potentials and work functions in the range of 7 – 8 eV and 4 – 5 eV are reasonable for doped and undoped In₂O₃ [29, 32, 41]. In this work values of up to 9 eV and 6.5 eV were measured for Mo-doped films. While 10% oxygen always leads to the highest

work function, a temperature above 400 °C in combination with oxygen is required for maximum ionization potential.

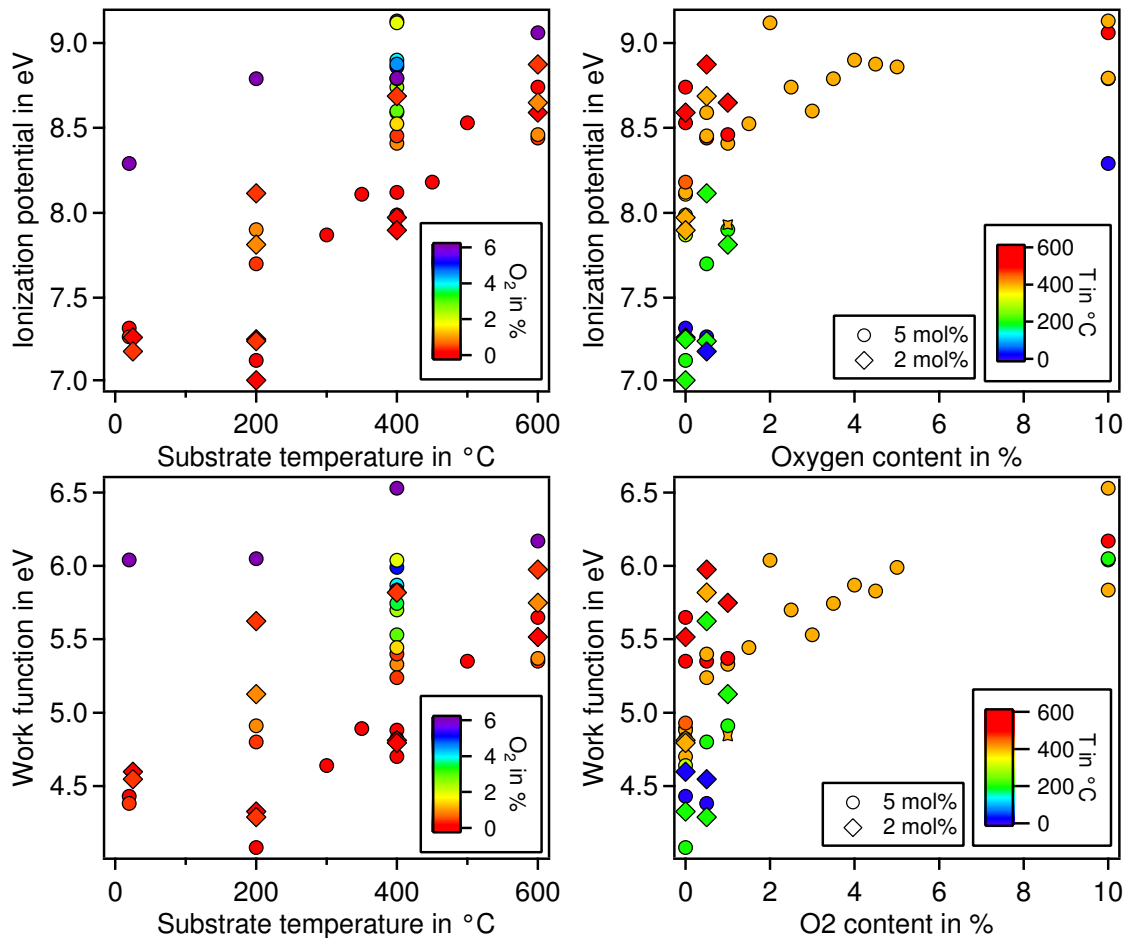


Figure 5.26: Ionization potential (top) or work function (bottom) plotted over substrate temperature and oxygen content of process atmosphere for 2 mol% and 5 mol% doped Mo:In₂O₃ films. The colors indicate oxygen content of the process atmosphere or substrate temperature respectively.

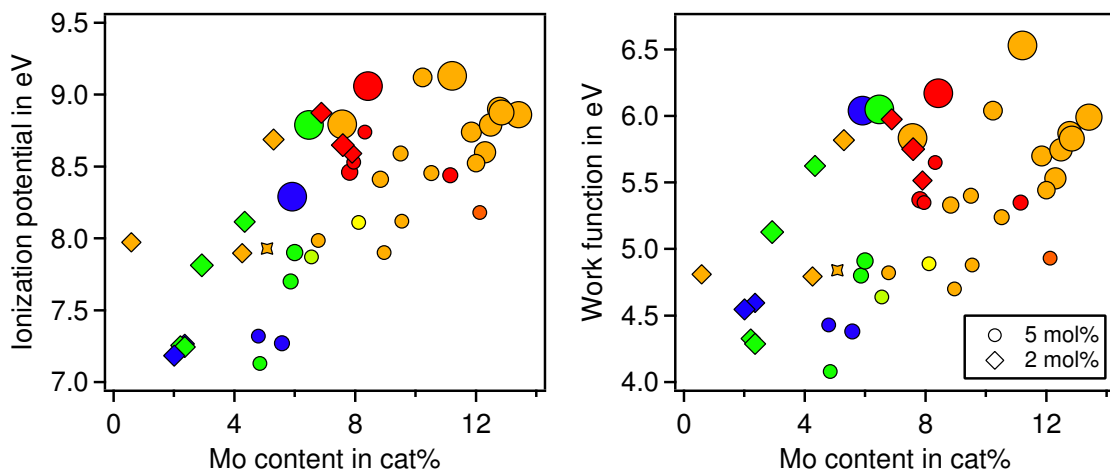


Figure 5.27: Ionization potential and work function plotted over the surface molybdenum concentration for 2 mol% and 5 mol% doped Mo:In₂O₃ films. The marker color indicates substrate temperature and marker size the oxygen content.

Ionization potential and work function plotted over the Mo content as determined by XPS are shown in Fig. 5.27. Even though the data points are scattered rather broadly, both parameters are found to increase with increasing molybdenum surface concentration. The highest values are obtained for samples deposited in oxygen containing atmospheres at temperatures of 400 °C or above.

From an interface experiment of thermally evaporated MoO₃ on Sn:In₂O₃ shown in Fig. 9.4 in the appendix and also from literature [156, 172, 173] ionization potentials of 9.6 eV and work functions between 7 eV and 6.1 eV were found for MoO₃. These are close to the maximum values measured for Mo:In₂O₃ thin films. XPS measurements indicate a larger fraction of the Mo⁶⁺ for latter samples. The formation of a MoO₃ surface layer, determining the surface potentials, is therefore plausible.

5.5 Summary

A brief outline of the findings for Mo:In₂O₃ thin films will be given here. The fundamental results will be discussed in comparison to other dopants in Sec. 7.

- Transparent conductive Mo:In₂O₃ thin films were grown by rf magnetron sputtering on glass. Ceramic targets with a dopant concentration of 2 mol% and 5 mol% were used in this work. The influence of substrate temperature and oxygen content of the deposition atmosphere, on structure, optical and electronic properties was investigated.
- According to XRD measurements most of the films consist of a single phase, possessing a bixbyite structure. One sample, deposited at 600 °C, shows a second phase which is most likely related to the formation of MoO₃. No clear correlation between preferential orientation and deposition conditions was found. Films with significant crystallinity tend to show a (111) texture. Deposition conditions affect the lattice constant. The effect of substrate temperature can be explained by extrinsic stress

due to differences in thermal expansion coefficients of film and substrate. The influence of oxygen in the deposition atmosphere and of the dopant itself could not be revealed.

- Electronic properties were investigated by Hall-effect and conductivity measurements. The deposition conditions influence the latter in a similar manner as compared to Sn:In₂O₃. Highest conductivities are obtained under reducing conditions and substrate temperatures close to 400 °C. Higher substrate temperatures tend to improve film crystallinity, having a positive effect on the carrier mobility. For films deposited at 600 °C μ_{Hall} drops to almost zero, which may be related to the formation of MoO₃ at the grain boundaries. The addition of oxygen is expected to decrease the concentration of effective dopants by the formation of neutral defect associates. A lower number of effective dopants and larger number of neutral impurities functioning as scattering centers explain decreasing carrier concentration and mobility with increasing oxygen content. Highest carrier concentrations are measured for 5 mol% Mo:In₂O₃ thin films. 2 mol% Mo:In₂O₃ films show highest mobilities. Latter are obtained at carrier concentrations where exceptionally high mobilities were measured for Zr and H doped In₂O₃. Similar values should be accessible by further varying the deposition parameters or at lower dopant concentrations.
- Optical characterization of the films was carried out by transmission and reflection measurements as well as spectrometric ellipsometry. A blue shift of the absorption onset with increasing carrier concentration can be explained by the Burstein-Moss effect. High carrier concentrations go with lower plasma wavelengths. 2 mol% Mo:In₂O₃ films show the highest transmission. The optical spectra were simulated to determine the optical band gap and plasma wavelength as well as the optical carrier concentration and mobility. The applied model results in a good agreement between measured and simulated spectra, the plausibility of the obtained parameters is questionable though. Similar trends of n_{Hall} and n_{Opt} were observed while μ_{Hall} and μ_{Opt} agree poorly. A very low Hall mobility, measured for high temperature samples, is not apparent from the optical spectra. Although a difference is to be expected, lower μ_{Opt} as compared to μ_{Hall} is physically not reasonable.
- Reviewing the electronic structure by photoelectron spectroscopy verifies a close relation to other doped and undoped In₂O₃ as well. The Mo3d emission consists of up to three components. Deposition temperature and oxygen content in the process gas determine the ratios between them. While the high energy component can be assigned to Mo⁶⁺ and increases with increasing temperature and oxygen content, it was not possible to doubtlessly ascribe specific oxidation states to the other two. Literature reports are not conclusive whether Mo⁵⁺ and Mo⁴⁺ or a screened and unscreened Mo⁴⁺ component are responsible. No distinct evidence was found for either in this work. An emission in the band gap close to $E_F - E_{VBM}$ is specific for Mo:In₂O₃. Latter feature is related to the presence of molybdenum in an oxidation state below Mo⁶⁺.
- The Mo surface concentration is affected by the deposition conditions. Sputter depth profiles indicate constant Mo concentration in the bulk of the films. Temperatures above 200 °C are required to allow for significant dopant diffusion. The surface

concentration scales with the oxygen content in the process atmosphere. Dopant surface segregation being favored at oxidizing conditions was previously observed for Ge:In₂O₃. The ionization potential and therefore the surface dipole is correlated to the Mo surface concentration. Exceptionally high work functions and ionization potentials are found. While the lower limits fit well to undoped In₂O₃, ionization potentials of up to 9.1 eV get close to measurements done on MoO₃.



6 Titanium Doped Indium Oxide

Results concerning Ti:In₂O₃ thin films will be presented in this chapter. Samples with a doping concentration of 2 mol% and 5 mol% were prepared under varying deposition conditions. The characterization was carried out analogously, as done for the Mo:In₂O₃ thin films.

6.1 Structural Analysis

Two X-ray diffraction patterns of 2 mol% doped Ti:In₂O₃ films are shown in Fig. 6.1. The deposition was carried out at a substrate temperature of 400 °C either in pure argon or in a 1% oxygen containing atmosphere. Similar to the XRD measurements of the previously shown Mo:In₂O₃ thin films, all reflections match the powder diffraction data of In₂O₃ or Pt. Platinum, which was used as contact material for Hall-effect and conductivity measurements, may be present depending on the position of the measurement spot.

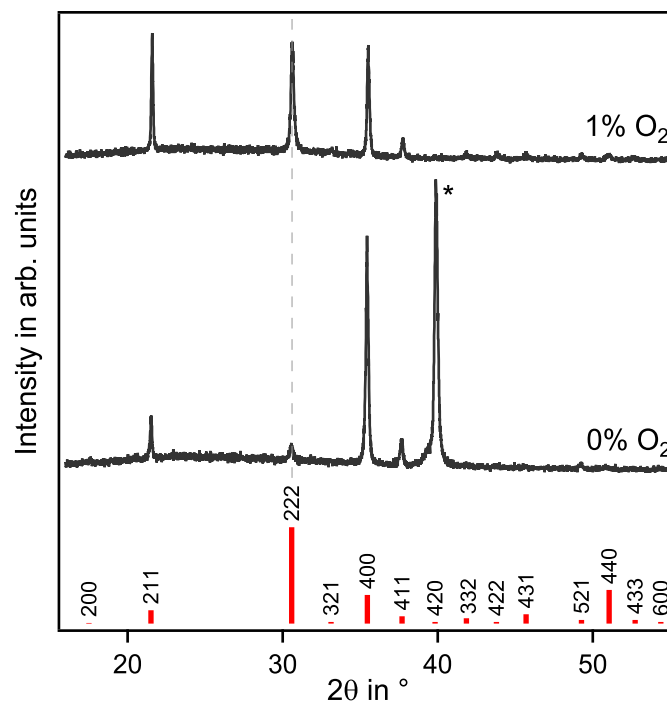


Figure 6.1: $\theta/2\theta$ diffraction patterns of 2 mol% doped Ti:In₂O₃ thin films deposited at a substrate temperature of 400 °C in either 0% or 1% oxygen containing atmosphere. Red bars at the bottom indicate In₂O₃ reflection positions according to ICDD pattern 00-006-0416. Reflections due to Pt contacts are marked by a "*".

Since all reflections, which are not related to Pt, can be assigned to In₂O₃ ICDD pattern 00-006-0416, the Ti:In₂O₃ thin films grown here consist of a single phase and have a cubic bixbyite structure, which is in accordance with literature [5, 65, 178–183]. Reflex positions match perfectly. As discussed in Sec. 5.1 lattice constants of a thin film do not necessarily coincide with the ones of powders due to stress in the films. Due to the limited

data it is not possible to discuss the influence of the deposition conditions on the lattice parameters. Nevertheless similar effects as observed for Mo:In₂O₃ are expected.

Looking at the relative intensities of the (211), (222) and (400) reflections a significant influence of the oxygen content in the process atmosphere on the film texture is evident. The film deposited under reducing conditions shows a pronounced (100) texture. Adding 1% oxygen during the deposition leads to a diffraction pattern in which all three (211), (222) and (400) reflections show roughly the same intensity. Compared to the intensities found for In₂O₃ powder this indicates a (211) texture. Inconsistent trends are reported in literature. A (222) texture is found either for pure argon or 1% oxygen containing atmosphere under otherwise similar deposition conditions. Wachau [38] could show that the deposition of In₂O₃ thin films grown under exactly the same conditions but not in the same deposition chamber led to differently textured films. A comparison between literature and the data shown here is therefore not reasonable.

Based on the X-ray diffraction patterns shown in this chapter, it can be confirmed that the investigated Ti:In₂O₃ thin films have a cubic bixbyite structure with similar lattice parameters as In₂O₃. They consist of a single phase and addition of oxygen to the deposition atmosphere leads to a significant variation of the film texture.

6.2 Electronic Properties, Conductivity and Hall-Effect Measurements

The effect of the deposition conditions on the electrical properties of 2 mol% and 5 mol% Ti:In₂O₃ thin films will be discussed in this section. Conductivity, charge carrier concentration and mobility as obtained from conductivity and Hall-effect measurements are shown in Fig. 6.2 for different deposition conditions. Triangles and circles indicate 2 mol% and 5 mol% dopant concentrations, respectively. Data for films grown at a substrate temperature of 400 °C and varying oxygen content are shown at the top while the values at the bottom represent films grown in pure argon and different temperatures.

A decreasing carrier concentration and mobility can be observed when oxygen is added to the process atmosphere during film growth. The carrier concentration of the 2 mol% doped sample deposited without oxygen is the only outlier in this series. Films deposited at the same oxygen partial pressure show similar carrier concentrations despite different doping levels. Carrier mobilities of the 2 mol% doped samples are approximately twice as high as of the 5 mol% ones. The lower dopant concentration therefore leads to a higher conductivity.

Increasing substrate temperature has essentially an opposite effect to adding oxygen. Carrier concentrations of the 5 mol% doped samples increase up to 400 °C and then remain rather stable. Hardly any difference can be observed between room temperature and 200 °C for the lower dopant concentration. Above this temperature, *n* increases for the 2 mol% doped films as well. The mobility instantly rises for both dopant concentrations with the substrate temperature. No significant variation can be observed between 200 °C and 400 °C for the 5 mol% doped samples while it drops to almost zero at 600 °C. Increasing mobilities up to 400 °C followed by a plateau are observed for a dopant concentration of 2 mol%.

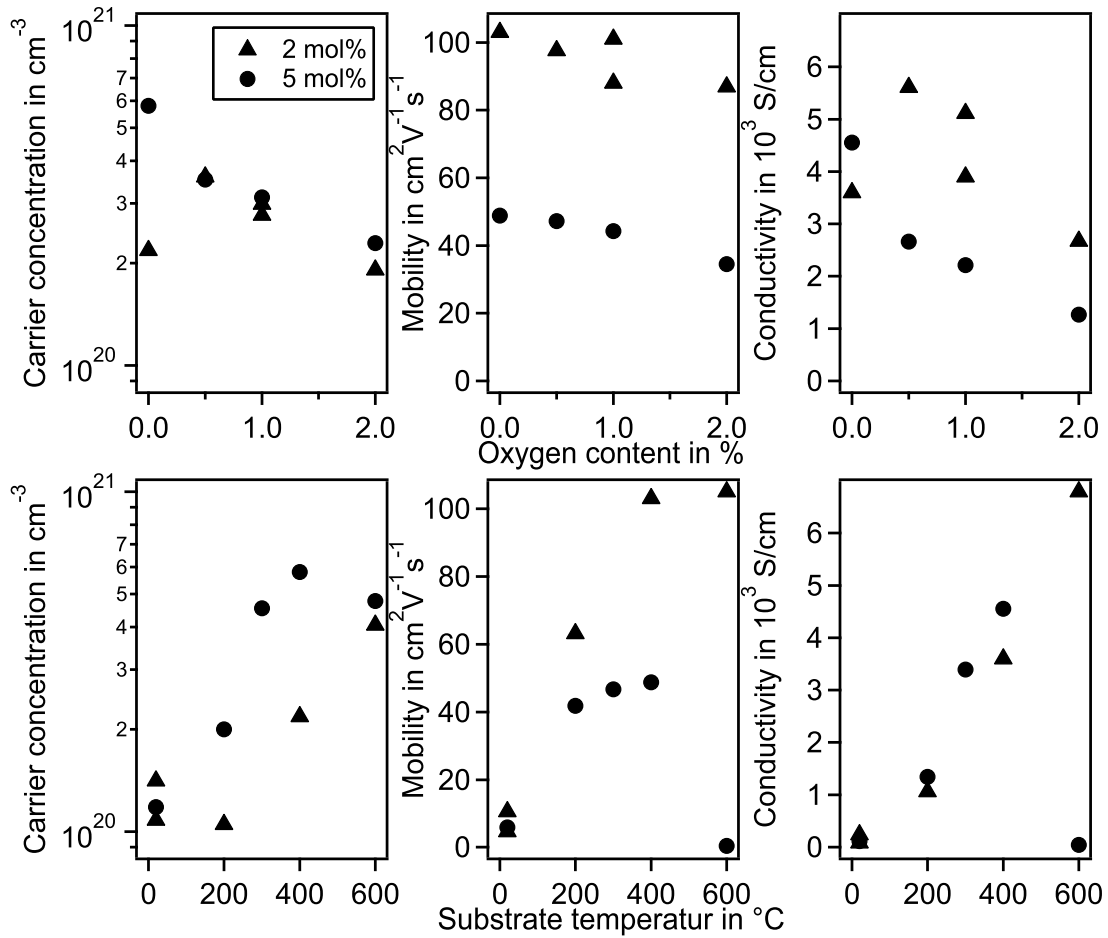


Figure 6.2: Carrier mobility, concentration and conductivity of 2 mol% (triangles) and 5 mol% (circles) doped Ti:In₂O₃ films deposited at a substrate temperature of 400 °C and varying oxygen content in the process atmosphere (top) and at different substrate temperatures in pure Ar atmosphere (bottom) are shown. Conductivity and Hall-effect measurements were carried out for the determination of the presented values.

The carrier mobility is plotted over the logarithm of the charge carrier concentration in Fig. 6.3. Marker type indicates dopant concentration, size the oxygen content during deposition and color substrate temperature according to the given scale. More samples are considered as compared to the ones shown in Fig. 6.2. In the context of a larger sample number, previously observed trends can be confirmed. Adding oxygen leads to a decreasing carrier concentration and mobility. Increasing the substrate temperature up to 400 °C is beneficial for both properties. Even higher temperatures hardly affect 2 mol% Ti:In₂O₃ films while the mobilities of 5 mol% samples drop down to almost zero at a comparable carrier concentration.

No systematic effect of the dopant concentration on n can be found. Otherwise identical deposition conditions lead to comparable carrier concentrations independent on the used target. The mobility, however, is strongly affected by dopant concentration. Mobilities of 2 mol% Ti:In₂O₃ films deposited above 200 °C are tremendously higher as compared to 5 mol% films.

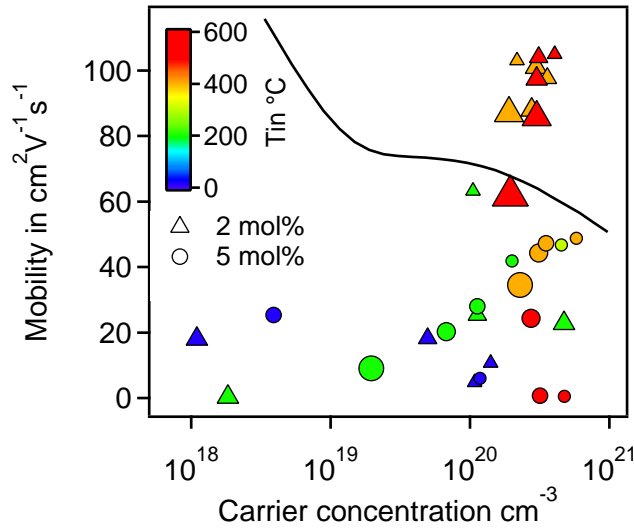


Figure 6.3: Electron mobility is plotted over the carrier concentration of 2 mol% and 5 mol% doped Ti:In₂O₃ films deposited at various substrate temperatures and oxygen contents in the process atmosphere. The solid line shows the calculated values $\mu(n)$ for In₂O₃ single crystals [17]. Conductivity and Hall-effect measurements were carried out for the determination of the presented values. Substrate temperatures are indicated by the marker color according to the given scale, while the marker size represents the oxygen content.

More information about the films with the best electronic properties is given in Tab. 6.1. A sample with a dopant concentration of 2 mol% shows both, highest conductivity as well as mobility. The highest carrier concentration was observed for 5 mol%. While a large difference is found in μ_{Hall} , carrier concentrations are similar.

Table 6.1: Deposition conditions and electronic properties of the two films showing both the highest conductivity and mobility or carrier concentration. Conductivity, carrier concentration and mobility were determined by conductivity and Hall-effect measurements.

	T in °C	O in %	σ in Scm ⁻¹	μ in cm ² V ⁻¹ s ⁻¹	n in cm ⁻³
2 mol%	600	0	6790	105	4.05×10^{20}
5 mol%	400	0	4550	48.8	5.80×10^{20}

The variation of the deposition conditions affects the electronic properties of Ti:In₂O₃ thin films as would be expected based on observations made for other dopants. More than 80% of all films show carrier concentrations between 1×10^{20} cm⁻³ and 6×10^{20} cm⁻³. Rather small differences in carrier concentration but a significant drop in mobility going from a dopant concentration of 2 mol% to 5 mol% are the most remarkable observations. Latter findings indicate over-doping and dopant segregation to play an important role in Ti:In₂O₃ thin films as well.

6.3 Optical Analysis

UV-Vis-NIR transmission and reflection spectra of Ti:In₂O₃ thin films with a dopant concentration of either 2 mol% or 5 mol% will be discussed in this section. Measurements

were carried out as described in Sec. 5.3. Only spectra recorded using p-polarized light are shown.

Spectra of 5 mol% Ti:In₂O₃ films are shown in Fig. 6.4 and Fig. 6.5. The samples were either deposited at 400 °C and varying oxygen content in the process atmosphere or under reducing conditions and varying substrate temperature respectively. The evolution of the spectra with deposition conditions can be explained based on what was learned in Sec. 5.3.

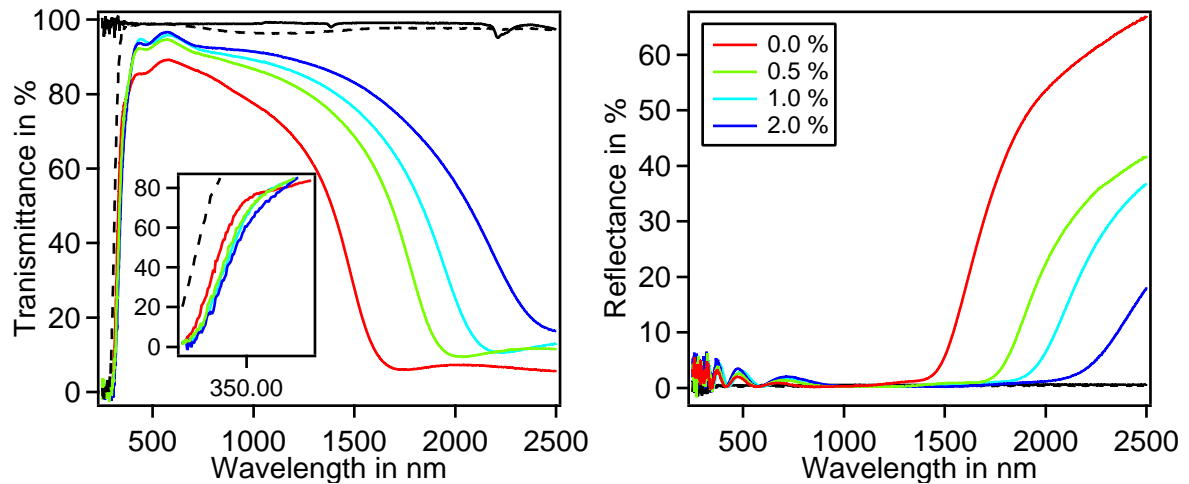


Figure 6.4: Transmittance (left) and Reflectance (right) spectra of 5 mol% Ti doped In₂O₃ thin films on glass. The samples were deposited at a substrate temperature of 400 °C and various oxygen contents in the process atmosphere. Measurements were done at an incident angle of 60° using p polarized light.

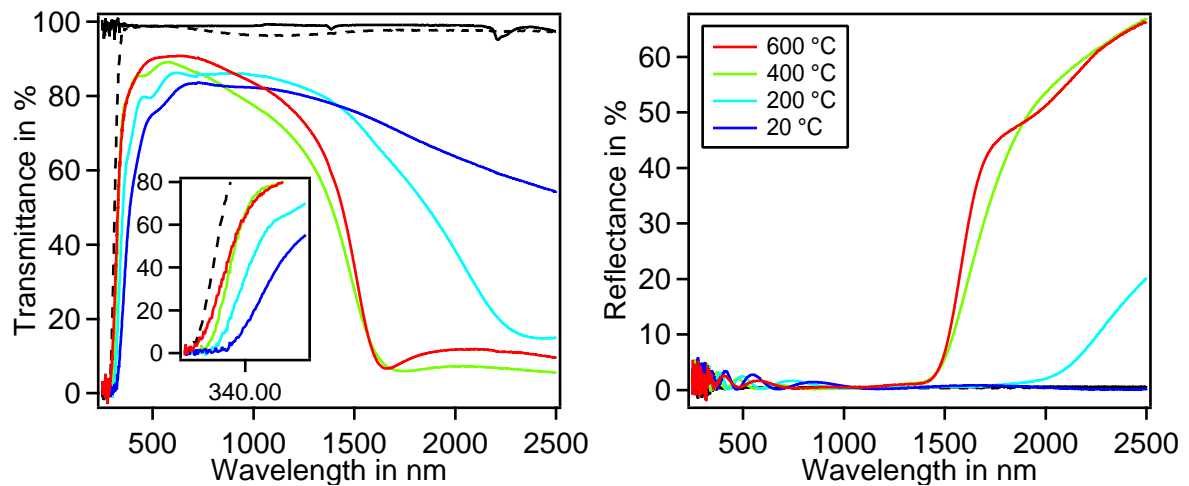


Figure 6.5: Transmittance (left) and Reflectance (right) spectra of 5 mol% Ti doped In₂O₃ thin films on glass. The samples were deposited in pure argon atmosphere. Substrate temperature of 20 °C, 200 °C, 400 °C and 600 °C were used. Measurements were done at an incident angle of 60° using p polarized light. Spectra of the bare substrates, for either fused silica (black solid line) or soda-lime glass (black dashed line), are included as well.

From Sec. 6.2 it is known that adding oxygen to the deposition leads to a decreasing carrier concentration and mobility. Lower n is expressed as a shift of the free carrier

and band gap absorption towards longer wavelength. A changing slope of the almost linearly declining part in the NIR range indicates a variation in mobility. Lower mobilities correspond to less steep slopes.

The temperature series leads to more significant changes in both carrier concentration and mobility. A stronger variation in the optical spectra can therefore be observed. As before, an increasing carrier concentration with substrate temperatures up to 400 °C is expressed by higher plasma energies and optical band gaps. Significantly enhanced mobilities lead to a much steeper slope in the NIR region. No major difference in n could be observed when the temperature was increased from 400 °C to 600 °C while the Hall mobility dropped down to almost zero. Comparing the red and green trace in Fig. 6.5, an essentially unchanged transparency window and overall shape of the spectra can be seen. This, on the one hand, confirms a similar carrier concentration but, on the other, does not give evidence for a strong variation in carrier mobility.

In Sec. 5.3.2 it was pointed out that the path electrons travel in both measurement techniques is very different. One possible explanation for the lower impact of the substrate temperature on the optical properties is therefore that at 600 °C, defects are formed which mainly influence the electrons moving through the whole sample. Oscillations on a scale as induced by light do not seem to be hindered.

Spectra of Ti:In₂O₃ thin films with a dopant concentration of either 2 mol% or 5 mol%, deposited in argon at a substrate temperature of 600 °C, are compared in Fig. 6.6. Their electrical properties determined from conductivity and Hall-effect measurements are given in Tab. 6.2. A lower plasma wavelength of the 5 mol% doped film can be explained by its higher carrier concentration. All samples with the higher Ti content exhibit a slightly lower transmittance. Otherwise no dopant concentration specific influence on the optical spectra can be observed.

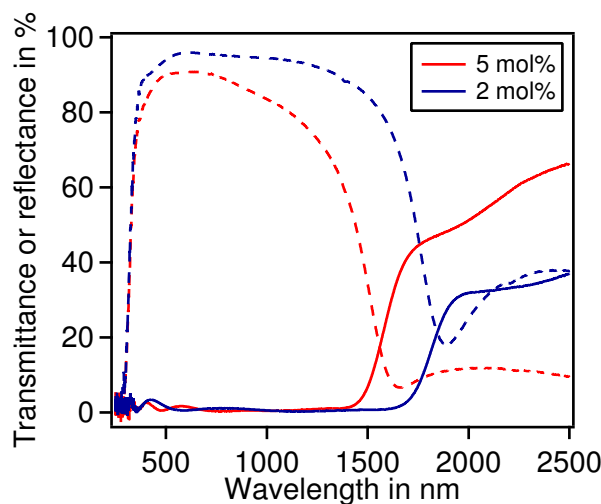


Figure 6.6: Transmittance and reflectance spectra of Ti:In₂O₃ thin films with a doping concentration of 2 mol% or 5 mol%. The thin films were deposited at a substrate temperature of 600 °C. Argon was used as process gas. Measurements were done at an incident angle of 60° using p polarized light.

The huge difference in Hall mobility between both samples at rather unaffected optical spectra is remarkable. This again suggests a process taking place in the higher doped films deposited at 600 °C, which leads to defects hindering the DC mobility but having little effect on the optical one.

Table 6.2: Electronic properties of the samples shown in Fig. 6.6. The films were deposited at 600 °C in 0% oxygen from a target with a concentration of either 2 mol% or 5 mol% titanium. Conductivity, carrier concentration and mobility were determined by conductivity and Hall-effect measurements.

	σ_{el} in Scm^{-1}	μ_{Hall} in $\text{cm}^2\text{V}^{-1}\text{s}^{-1}$	n_{Hall} in cm^{-3}
2 mol%	6790	105	4.05×10^{20}
5 mol%	42.5	0.56	4.77×10^{20}

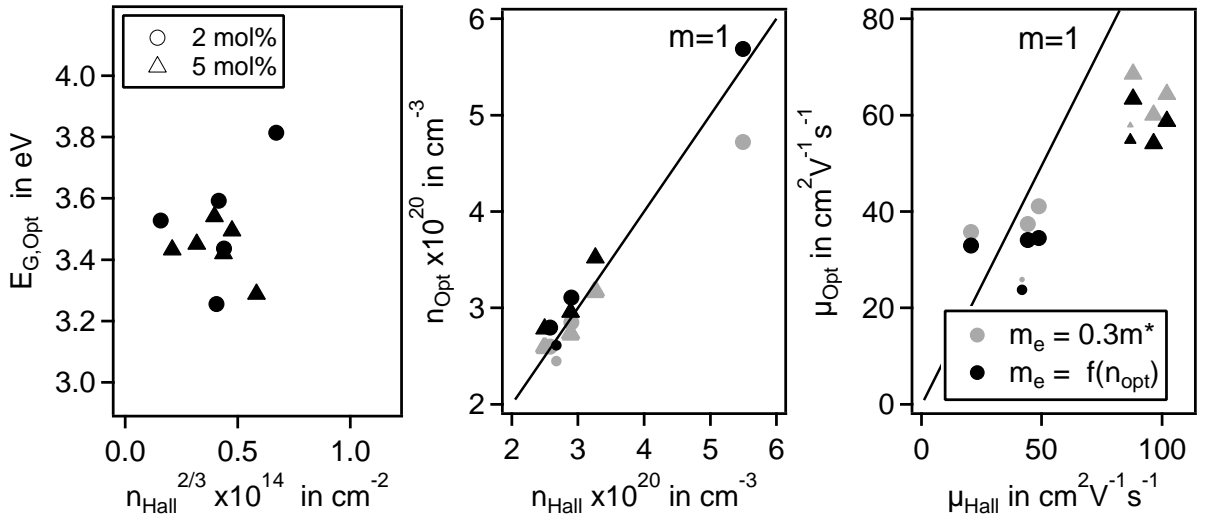


Figure 6.7: Comparison of $E_{G,Opt}$, optically and electrically determined carrier concentration and mobility of 2 mol% and 5 mol% doped $\text{Ti}:\text{In}_2\text{O}_3$ thin films. Different marker types indicate the dopant concentration. Optical mobility and carrier concentration calculated assuming either $m_e = \text{const.}$ or $m_e = f(n_{opt})$ are displayed in gray and black respectively.

The correlation between the optical band gap $E_{G,Opt}$ and the carrier concentration and mobility determined from electrical measurements and simulations of optical spectra are shown in Fig. 6.7. While a linear dependence between optical band gap and $n_{Hall}^{2/3}$ was found for the $\text{Mo}:\text{In}_2\text{O}_3$ thin films, no such tendency can be seen here. The selection of samples, i.e. $n_{Hall} > 2 \times 10^{20} \text{ cm}^{-3}$, and a small variation of n may be the reason why a trend can not be confirmed here. Similar to the other dopant, a linear correlation between optical and Hall carrier concentration is found when the effective electron mass is adjusted to n_{opt} . The optical mobility shows a distinct difference between 2 mol% and 5 mol% doped samples as would be expected based on the Hall-effect measurements. Compared to μ_{Hall} a significantly lower variation is found though. Overall lower optical mobilities are found, which was observed for $\text{Mo}:\text{In}_2\text{O}_3$ films as well.

Transmission and reflection measurements of $\text{Ti}:\text{In}_2\text{O}_3$ thin films mostly confirm the expected influence of deposition conditions on the optical properties. The variation of

the onset in band gap and free carrier absorption is in accordance with the Hall carrier concentration. Matching optically and electrically determined carrier concentrations are found. The optical spectra are not significantly affected by the variation of μ_{Hall} . Optically determined mobilities show decreasing values going from 2 mol% to 5 mol%. Even though this is similar to μ_{Hall} absolute values do still not match.

6.4 Photoelectron Spectroscopy

6.4.1 X-Ray Photoelectron Spectroscopy

Photoelectron spectra of 2 mol% and 5 mol% doped $\text{Ti:In}_2\text{O}_3$ thin films will be discussed in this section. The influence of substrate temperature and deposition atmosphere on the electronic structure and surface potentials will be the main focus. A quantitative analysis of the titanium surface concentration is carried out for the 5 mol% doped samples. Evaluation of the $\text{Ti}2p$ peak area could not be carried out for samples with a lower dopant concentration due to the low intensity and overlap with $\text{In}3d$ satellites. Since there is not a lot of literature available for photoelectron spectroscopy on $\text{Ti:In}_2\text{O}_3$, the following discussion is based on knowledge of other dopant elements.

XP spectra of a 5 mol% doped $\text{Ti:In}_2\text{O}_3$ thin film deposited on glass at 400°C in argon are shown in Fig. 6.8. $\text{O}1s$, $\text{Ti}2p$, $\text{In}3d_{5/2}$ core levels and the valence band region are displayed. Asymmetric peak shapes of the oxygen and indium emission are caused by screening effects due to the high electron concentration in the film.

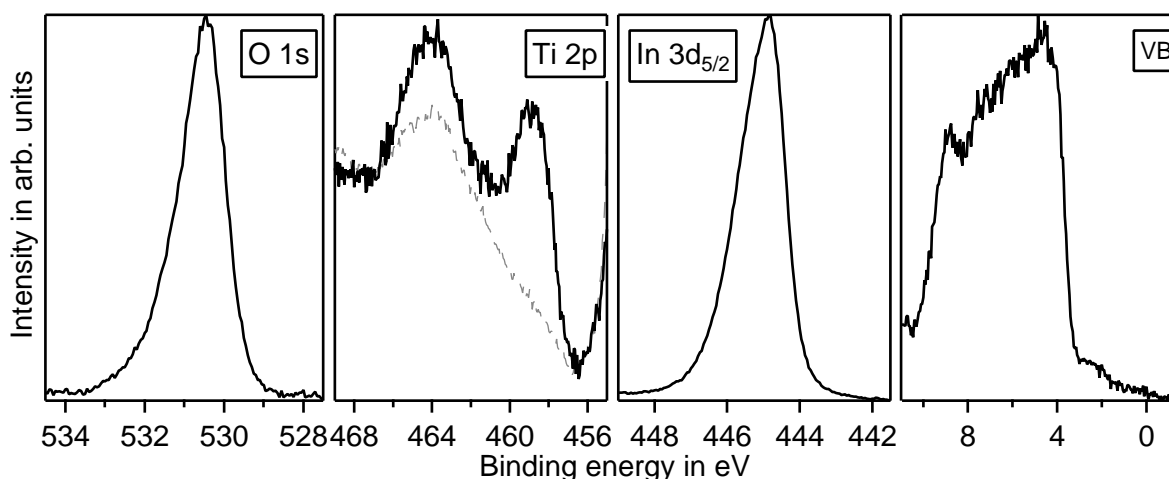


Figure 6.8: XP spectra of a $\text{Ti:In}_2\text{O}_3$ 5 mol% thin film deposited at 400°C in pure argon. $\text{O}1s$, $\text{Ti}2p$, $\text{In}3d_{5/2}$ core level and valence band region are shown. Data of a measurement done on an undoped In_2O_3 thin film, deposited under similar condition, is shown additionally in the energy region of the $\text{Ti}2p$ emission. Spectra are normalized to the overall peak area, no background correction was carried out.

The $\text{Ti}2p$ core level is positioned close to the $\text{In}3d$ emission. This region is therefore strongly influenced by Indium satellites. Data of an undoped In_2O_3 thin film deposited under similar conditions is shown in gray to demonstrate this effect. Considering this

background, a Ti2p doublet can be estimated. With a Ti2p_{3/2} binding energy of 458.8 eV, good agreement with Ti in TiO₂ is found [118]. It therefore can be concluded that Ti is in the 4+ oxidation state. Similar results were reported in literature [5, 99, 180]. The valence band structure basically resembles the one of undoped or doped In₂O₃. Slight dopant specific effects have to be considered. A state close to the valence band maximum can be seen.

Core level spectra recorded for films deposited at different substrate temperature for both dopant concentrations are shown in Fig. 6.9 and Fig. 6.10. Spectra of 5 mol% Ti:In₂O₃ films deposited at 400 °C in process atmospheres containing various amounts of oxygen are shown in Fig. 6.11.

The spectra shown in Fig. 6.9 illustrate the effect of the substrate temperature on 5 mol% Ti:In₂O₃ films. For both the O1s and In3d_{5/2} emission increasing asymmetry can be observed when the substrate temperature is increased. While the Ti2p core level gains intensity the feature close to the valence band maximum decreases. A component at lower binding energy indicating the presence of Ti³⁺ can be seen in the Ti2p spectra. The intensity of the latter scales with the intensity of the state close to the valence band. Both core level binding energy and valence band maximum tend to shift towards higher binding energies with increasing deposition temperature. A higher Hall carrier concentration fits to a more pronounced peak asymmetry and the shift of valence band maxima and core level binding energies.

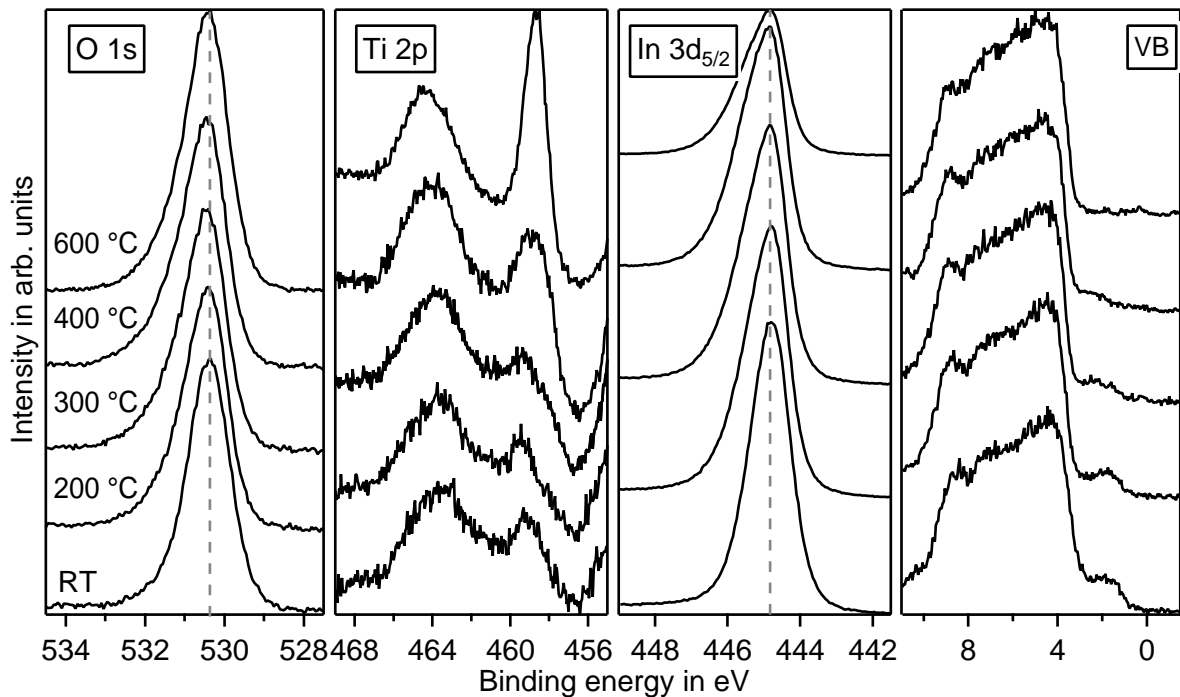


Figure 6.9: XP spectra of Ti:In₂O₃ 5 mol% thin films deposited in pure argon at substrate temperature of 20 °C, 200 °C, 300 °C, 400 °C and 600 °C. Spectra are normalized to the overall peak area, no background correction was carried out.

Hardly any Ti2p emission can be made out in the spectra of the 2 mol% doped Ti:In₂O₃ thin films shown in Fig. 6.10. A slight Ti2p_{3/2} emission appears for substrate tempera-

tures of 400 °C and 600 °C. Increasing Ti at the surface with increasing temperature can therefore be confirmed. Only for the room temperature deposition, a feature close to the valence band maximum is visible. Its shape differs from what was observed for higher dopant concentration though. The increased intensity close to 0 eV binding energy was thus likely caused by a spike. Higher temperatures lead to a more pronounced asymmetry of the O1s and In3d_{5/2} peaks. A high binding energy shoulder is found for O1s which decreases with increasing substrate temperature. A similar features was seen for Sn:In₂O₃ or Mo:In₂O₃ and can be explained by peroxide species at the surface [41]. A slight shift of both the O1s and In3d_{5/2} binding energies towards lower values can be seen. While the slope of the valence band onset is identical for samples deposited at 200 °C or higher, a difference can be seen for the room temperature film. The shift towards higher binding energy is expected to be caused by charging of the sample. For the high temperature films no variation in $E_F - E_{\text{VBM}}$ is found.

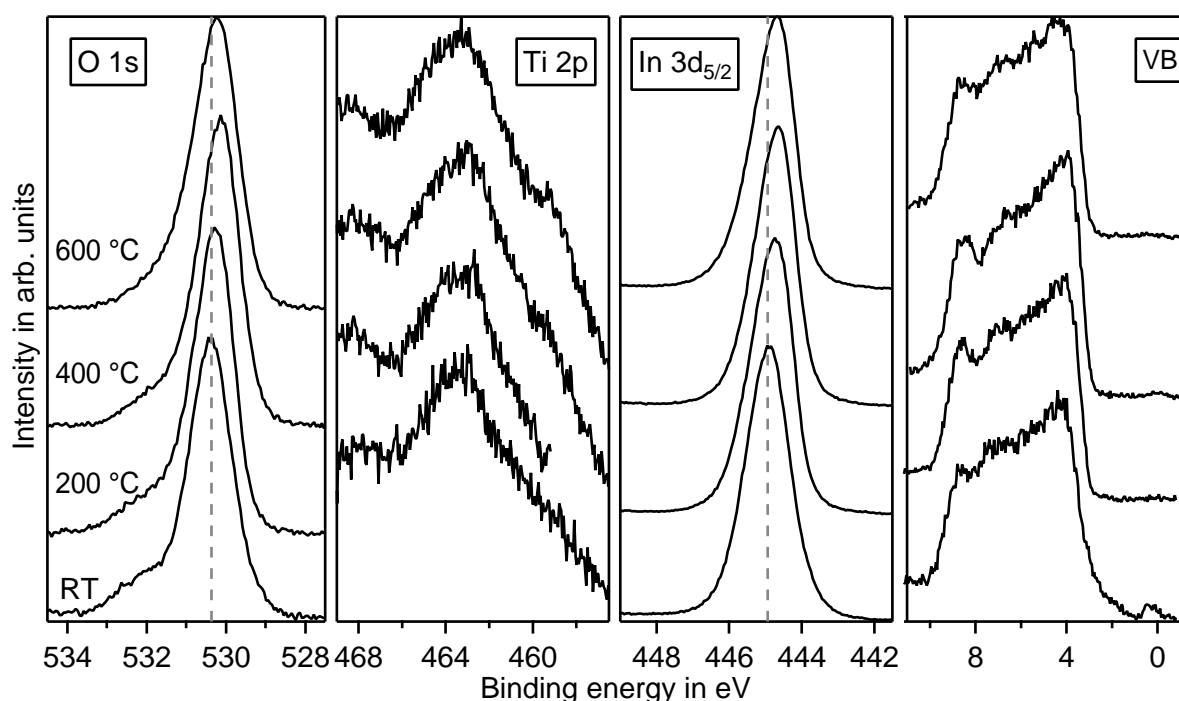


Figure 6.10: XPS spectra of Ti:In₂O₃ 2 mol% thin films deposited in pure argon at substrate temperature of 20 °C, 200 °C, 400 °C and 600 °C. Spectra are normalized to the overall peak area, no background correction was carried out.

Adding oxygen to the deposition of 5 mol% Ti:In₂O₃ thin films at a substrate temperature of 400 °C, leads to less asymmetric O1s and In3d_{5/2} emissions (Fig. 6.11). Furthermore, core level binding energies as well as valence band position shift to lower energies. The bandgap feature, only visible for the film deposited at 400 °C in argon, is immediately suppressed. Slight changes in the shape of the valence band, i.e. increasing intensity at its maximum and tail, can be observed. The Ti2p intensity is slightly affected. Adding 0.5% O₂ leads to a decreasing Ti concentration at the surface and the peak gets sharper. More oxygen has no effect.

The observation of a band gap feature in Fig. 6.9 and Fig. 6.11 goes with broadening of the Ti2p_{3/2} emission. An additional component at a slightly lower binding energy can

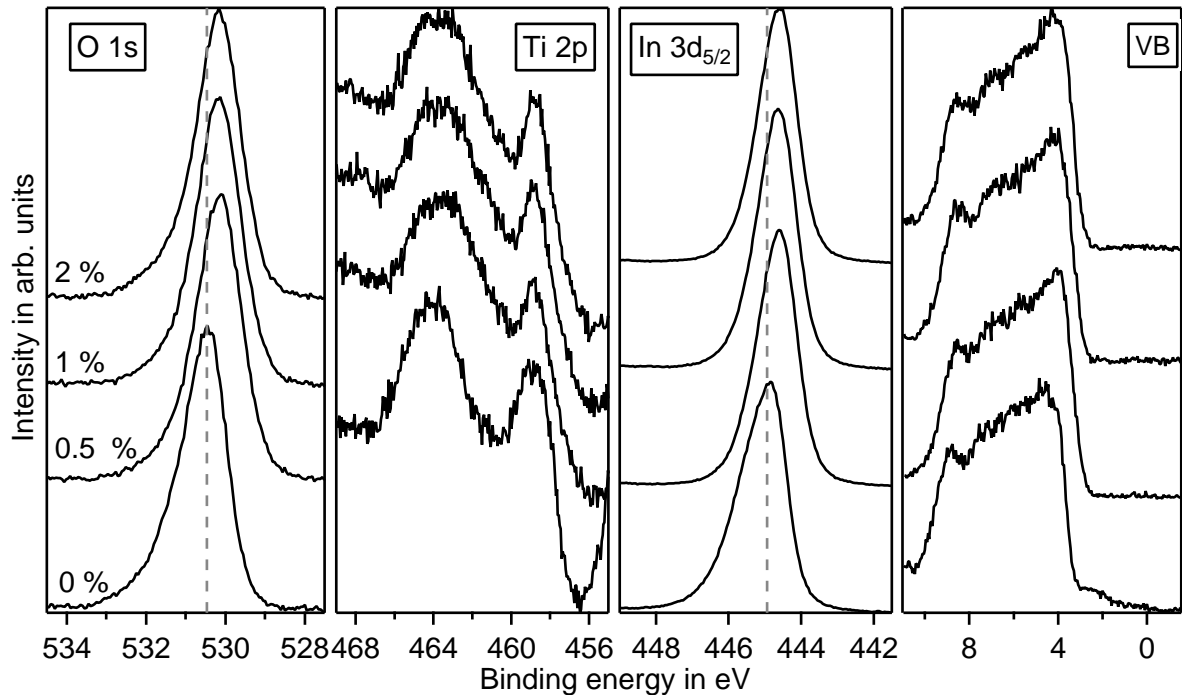


Figure 6.11: XPS spectra of Ti:In₂O₃ 5 mol% films deposited under various oxygen partial pressures at substrate temperature of 400 °C. Spectra are normalized to the overall peak area, no background correction was carried out.

be seen in the Ti2p spectrum. Occupied Ti3d states, i.e. Ti in a 3+ oxidation state, are considered to be responsible for the presence of band gap states in TiO₂ [184, 185] and could explain the second emission in the Ti2p spectrum as well. The correlation between the band gap state and broadening of the Ti2p emission will be discussed in Sec. 6.4.3.

It could be seen that the deposition conditions affect the titanium concentration at the film surface. A correct quantification of its content is rather complicated due to the overlap of the Ti2p emission and the In3d satellite. This makes a background correction questionable. To approximate the Ti concentration the intensity of the Ti2p_{3/2} emission, being positioned on an almost linearly increasing part of the In3d satellite, was determined. The way how the background estimation was carried out is shown in Fig. 9.6 in the appendix. A spline was used to model the almost linear part beneath the Ti2p_{3/2} emission. This procedure will not yield the real Ti2p intensity and unavoidably lead to rather large uncertainties, but it should suffice for a rough quantification of the titanium surface concentration. 2 mol% doped thin films were excluded from this analysis due to their low Ti2p intensity.

The titanium surface concentration in cat% as a function of temperature and oxygen content is shown in Fig. 6.12. While almost no variation can be seen up to 300 °C, higher temperatures lead to a significant increase in Ti at the surface. Variation of the oxygen content in the process atmosphere does not lead to a clear trend. No effect is found for samples deposited below 400 °C. For even higher temperatures a decreasing Ti concentration at the surface can be seen with increasing oxygen content even though the data points shows a rather large scattering. Overall, a variation between 1.5 cat% and 19 cat%

Ti at the surface is found. The values obtained for low temperatures fit quite well to the 2.56 cat%, which are expected based on the target composition according to the manufacturer specifications. Tremendously enhanced concentrations at temperatures of 400 °C and above indicate a significant Ti segregation at the surface for the given conditions.

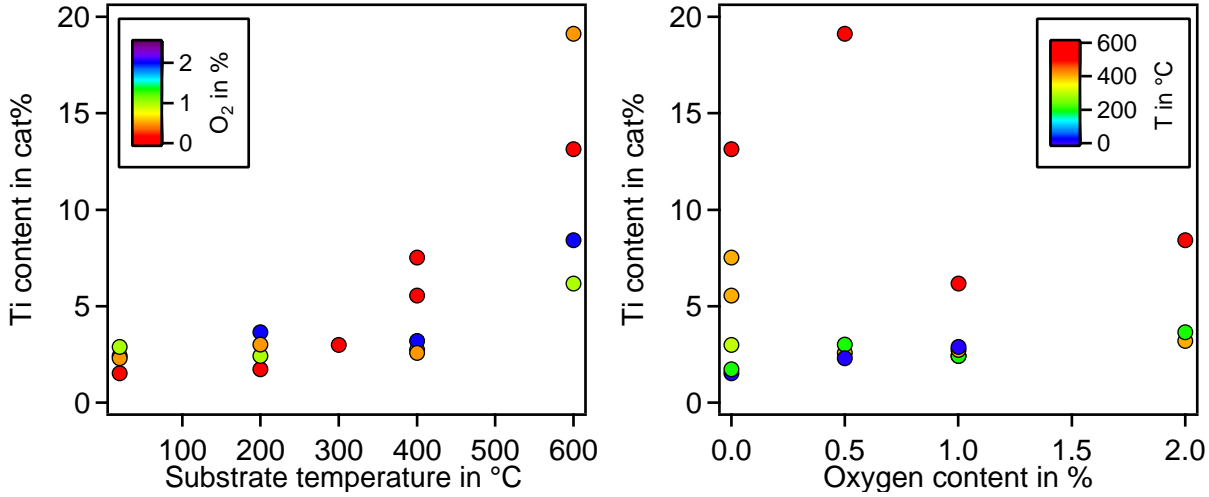


Figure 6.12: Titanium content in cat% plotted over substrate temperature or oxygen content. Only Ti:In₂O₃ thin films with a doping concentration of 5 mol% were considered. Marker colors indicate the other parameter respectively.

Fig. 6.13 shows $E_F - E_{VBM}$ plotted over either the substrate temperature or the oxygen content for a more detailed look on the effect of the deposition conditions on the position of the valence band maximum. All Ti:In₂O₃ films prepared in this work are shown. Colors indicate the oxygen content or the temperature according to the given scales. Values between 2.0 eV and 3.2 eV were measured. The highest and lowest valence band maximum was obtained for doping concentrations of 5 mol% and 2 mol% titanium, respectively. Except for those extreme values no distinct difference can be seen between both dopant concentrations. Samples deposited at room temperature show the largest scattering. As reported before, the onset of the valence band changes when intentionally heating the substrates. The reliability of the $E_F - E_{VBM}$ of room temperature films is therefore questionable. Increasing temperatures or less oxygen lead to higher valence band maxima. Films deposited at temperatures above 200 °C are only weakly influenced by the oxygen content in the process atmosphere.

Variation of the In3d_{5/2} binding energy and the valence band maximum are set into correlation in Fig. 6.14. Deposition temperature is indicated by the marker color and oxygen content of the process atmosphere by its size. The black line indicates a slope of one, i.e. parallel shifting core levels and valence band maxima. Overall a good agreement between the line and the measurements can be seen. All data points, which show a feature close to the valence band onset are highlighted by the gray background. Only exception is the sample deposited at 600 °C, which is highlighted but does not show the band gap emission. A different correlation between core level binding energy and $E_F - E_{VBM}$ is therefore an effect of the altered shape of the valence band onset. Furthermore, it is eye-catching that the majority of all measurements are located around the same energies.

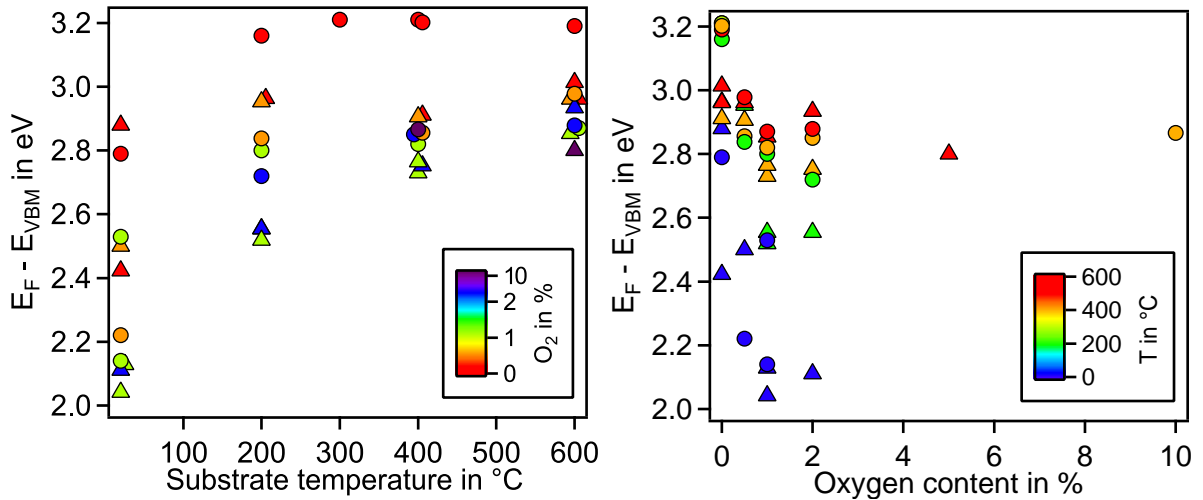


Figure 6.13: Ti:In₂O₃ valence band position plotted over the substrate temperature (left) or oxygen content (right) of process atmosphere. Colors indicate oxygen content or substrate temperature according to the scales. Triangles and circles represent samples with dopant concentrations of 2 mol% and 5 mol%.

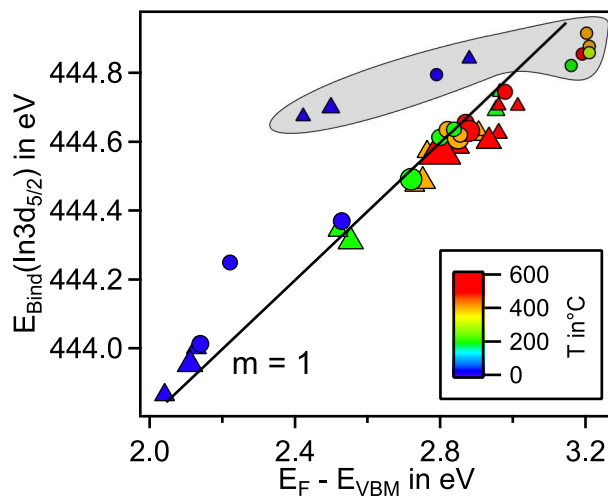


Figure 6.14: In3d_{5/2} binding energy plotted over Ti:In₂O₃ valence band position. Colors indicate the substrate temperature according to the scale, marker size the oxygen content during deposition. Triangles and circles represent samples with dopant concentrations of 2 mol% and 5 mol%. The black line represents a slope of one. Samples, which show a specific state close to the valence band maximum, are indicated by the gray background.

XP spectroscopy of the Ti:In₂O₃ thin films show that core level shape and binding energies as well as position of the valence band maximum behave as expected based on the Hall carrier concentration and observations made on other dopants. Lowest and highest values for $E_F - E_{VBM}$ were observed for 2 mol% and 5 mol%, respectively. Nevertheless, the dopant concentration in the target has a rather weak effect on the binding energies. Titanium at the surface of films deposited at 600 °C or in a process atmosphere which contains oxygen is present in a 4+ oxidation state. Lower temperatures and pure argon lead to the presence of a feature in the band gap and a second component in the Ti2p spectrum, which likely is correlated to Ti³⁺ and will be discussed in Sec. 6.4.3. Ti segregation at the

surface is found for increasing temperature and decreasing oxygen content in the process atmosphere. Some samples show a feature close to $E_F - E_{\text{VBM}}$, which will be discussed in more detail after presenting the UP spectra in the next section.

6.4.2 Ultraviolet Photoelectron Spectroscopy and Surface Potentials

UP spectra of 2 mol% and 5 mol% doped $\text{Ti:In}_2\text{O}_3$ thin films deposited at different substrate temperatures or oxygen content are shown in Fig. 6.15 - Fig. 6.17. Only the regions where either the secondary electron cutoff or the valence band maximum can be found are displayed. All spectra were scaled for matching maximum intensities in each region. In the subwindows the band gap state and the Fermi edge are shown. Values of the ionization potential and the work function as obtained from the latter spectra are presented in Fig. 6.18 and Fig. 6.19. The effect of the deposition conditions on the valence band maxima and latter surface potentials will be investigated. In addition, $E_F - E_{\text{VBM}}$ obtained from UPS and from previously discussed XPS will be compared.

As seen in Fig. 6.15, temperatures up to 400 °C hardly alter the shape or position of the valence band maximum in 5 mol% samples. No significant variation of $E_F - E_{\text{VBM}}$ coincides with the findings from XPS measurements. A changing slope can be observed for the film deposited at 600 °C. This is in contrast to the XPS measurements where a different slope was found for the sample deposited at room temperature. The evolution of the pre-edge emission is consistent with XPS. The feature close to the valence band maximum observed for the 600 °C sample is related to the satellite line of the UV source. The position of the secondary electron cut off shows a rather small variation up to 400 °C followed by a shift of about 0.3 eV. This may indicate changes at the surface to happen at 600 °C.

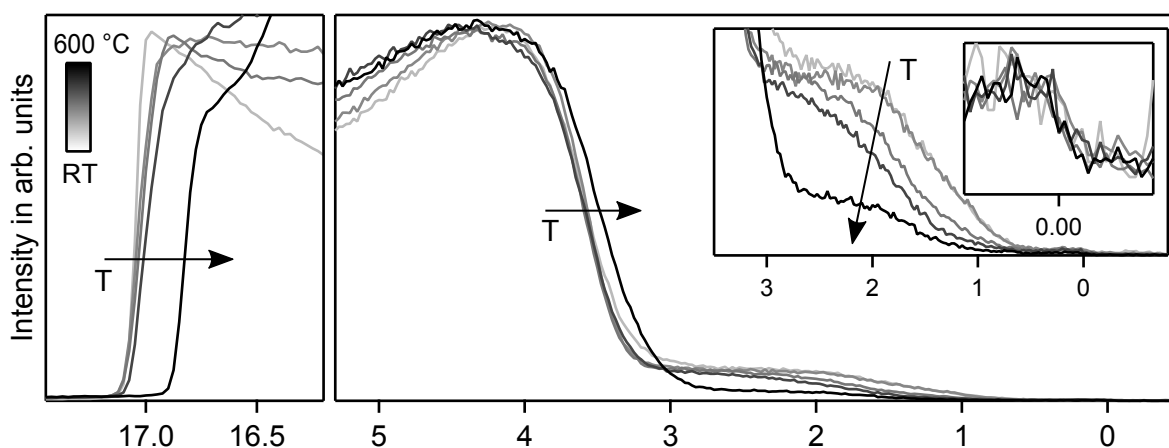


Figure 6.15: UP spectra of 5 mol% $\text{Ti:In}_2\text{O}_3$ samples deposited in argon at substrate temperatures of 20 °C, 200 °C, 300 °C, 400 °C and 600 °C. Different levels of gray indicate the deposition temperature.

The temperature series for the 2 mol% doped $\text{Ti:In}_2\text{O}_3$ films (Fig. 6.16) shows similar effects as observed for the higher doping concentration. Likewise to the XPS measurements the slope of the valence band onset does get steeper when room temperature is exceeded and a variation in $E_F - E_{\text{VBM}}$ can be seen. The pre-edge feature changes and remains in the

same shape for 200 °C and above. Similar E_{SEC} values are measured for the two low and the two high temperatures. Both sets differ by about 0.2 eV.

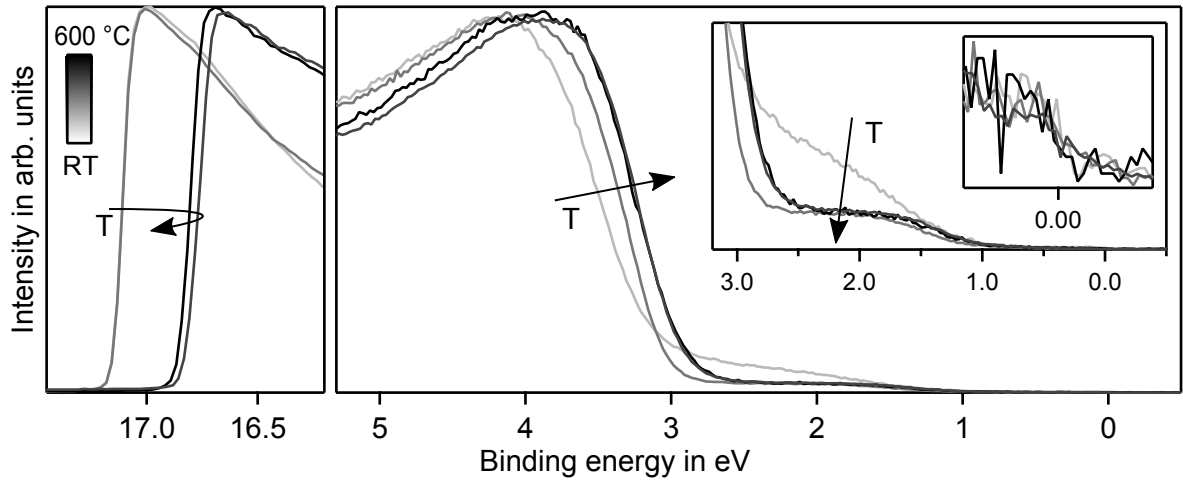


Figure 6.16: UP spectra of 2 mol% Ti:In₂O₃ samples deposited in argon at substrate temperatures of 20 °C, 200 °C, 400 °C and 600 °C. Different levels of gray indicate the deposition temperature.

The effect on $E_F - E_{\text{VBM}}$ when oxygen is added to a deposition at 400 °C as shown in Fig. 6.17 is the same when UPS and XPS measurements are compared. A huge initial shift is followed by constant values. A monotonous shift of E_{SEC} towards lower binding energies with increasing oxygen content can be seen.

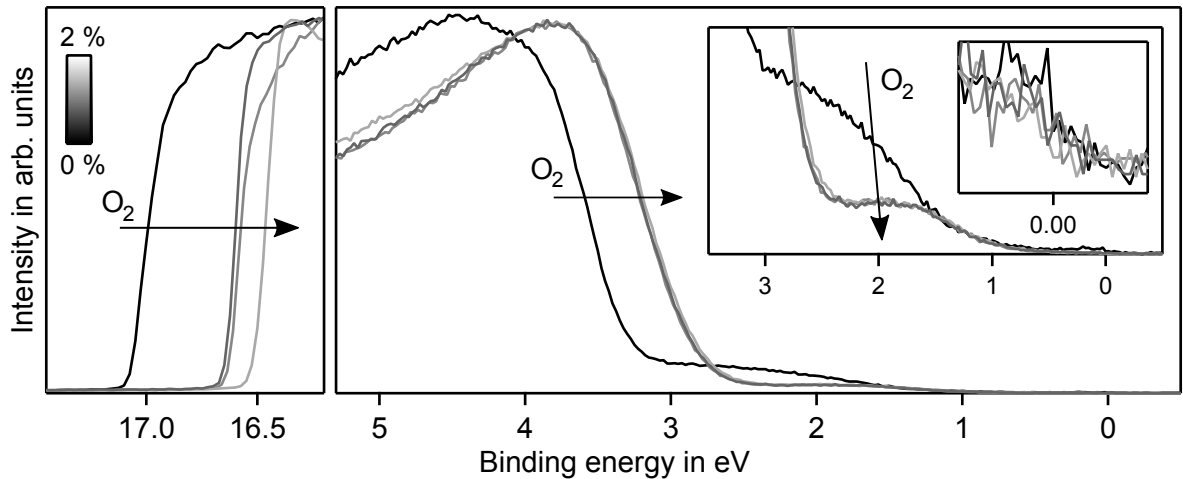


Figure 6.17: UP spectra of 5 mol% Ti:In₂O₃ samples deposited at 400 °C in 0%, 0.5%, 1% or 2% oxygen containing atmosphere. Different levels of gray indicate the amount of oxygen in process atmosphere.

Ionization potentials and work functions of all Ti:In₂O₃ thin films are shown in Fig. 6.18 and Fig. 6.19. They are plotted either versus deposition temperature or oxygen content. The other parameter is indicated by the marker color according to the given scale. Values for the ionization potential lie in between 7.1 eV and 7.7 eV, for the work function between 4.2 eV and 5.4 eV. Both surface potentials are therefore in the range of what is reported for doped In₂O₃ [32].

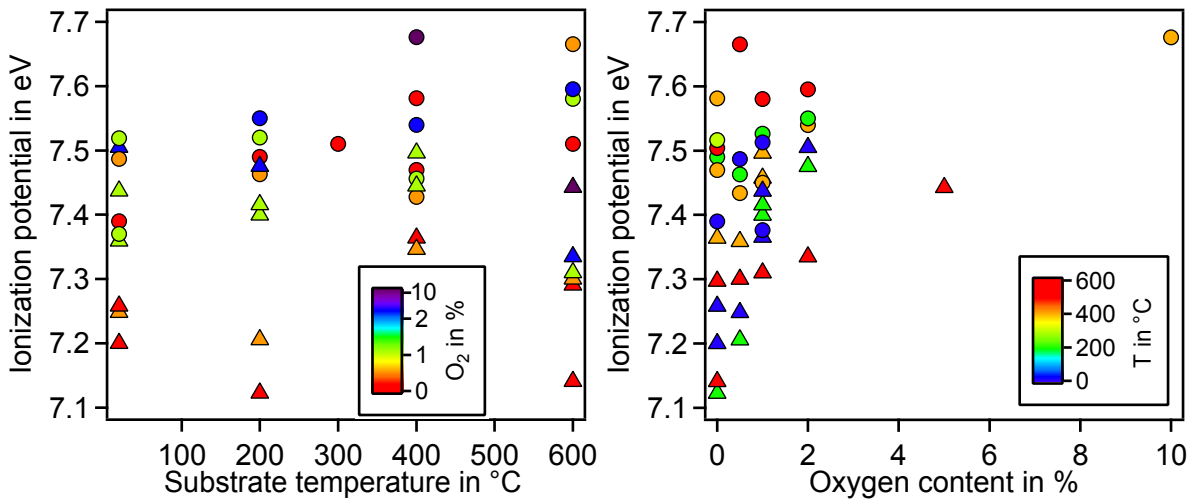


Figure 6.18: Ionization potential plotted over substrate temperature (left) and oxygen content of process atmosphere (right) for 2 mol% (triangles) and 5 mol% (circles) doped Ti:In₂O₃ films. The colors indicate oxygen content of the process atmosphere or substrate temperature respectively.

The substrate temperature has only a minor influence on the ionization potentials. Higher values are observed for increasing oxygen content. Looking at the distribution of the markers it is obvious that a lower doping concentration leads to lower ionization potentials.

Since the work functions show a larger variation, trends are more clear as for the ionization potentials. In this case both, temperature and oxygen content, have an effect. While higher temperatures lead to decreasing work functions increasing oxygen content has an opposite influence. No significant difference can be observed between the two doping concentrations.

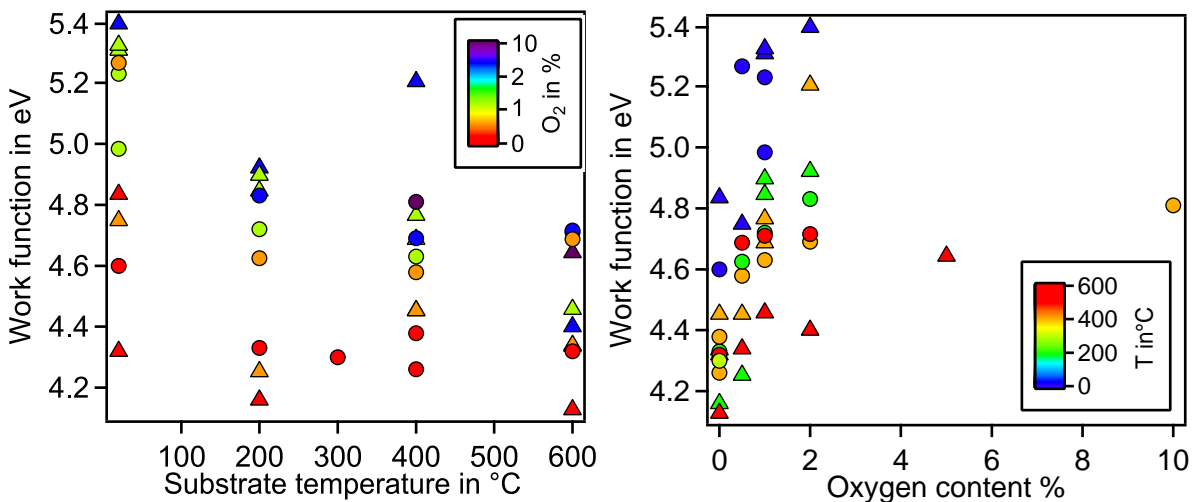


Figure 6.19: Work function plotted over substrate temperature (left) and oxygen content of process atmosphere (right) for 2 mol% (triangles) and 5 mol% (circles) doped Mo:In₂O₃ films. The colors indicate oxygen content of the process atmosphere or substrate temperature respectively.

The ionization potentials and work functions of the 5 mol% doped samples plotted over the Ti concentration at the surface are shown in Fig. 6.20. An increasing I_p is observed for a higher Ti concentration while the work function does not show a systematic variation. Work functions for the room temperature samples are significantly higher than the others, which however is related to a deviating slope of the valence band onset, since ϕ_{XPS} is shown (see Sec. 4.3).

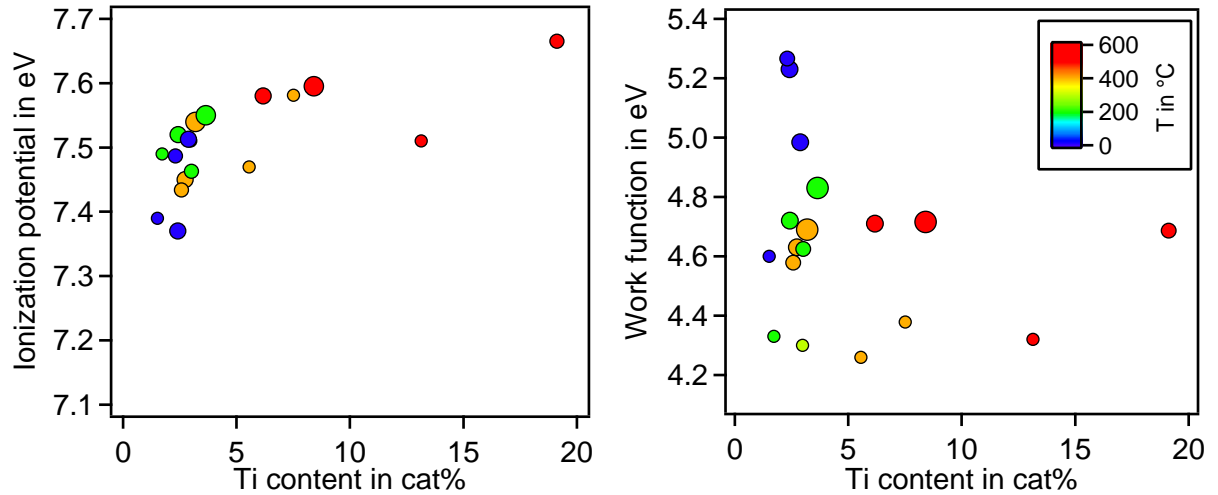


Figure 6.20: Ionization potential (left) or work function (right) plotted over Titanium cat% in the nominally 5 mol% doped films. The colors indicate substrate temperature and marker size the oxygen content during deposition.

Observations considering the valence band maximum made by XPS and UPS are very similar. Matching values for $E_F - E_{VBM}$ are found except for samples deposited at room temperature. Latter values determined by XPS are approximately 0.4 eV lower as compared to UPS. The deposition temperature has only a minor effect on I_p while it is more significantly affected by the oxygen content or titanium concentration in the film and at the surface. Lower Ti contents lead to lower values of I_p . A decreasing work function is found with increasing temperature and less oxygen in the process atmosphere. No systematic effect of the dopant concentration can be seen.

6.4.3 Titanium Band Gap State

An emission close to the valence band onset was observed in photoelectron spectra of some Ti:In₂O₃ thin films. It appears for both dopant concentrations even though the conditions for its presence and its shape are different. For a doping concentration of 5 mol% temperatures below 600 °C and reducing conditions are required. While room temperature and an oxygen content of 0.5 % or below lead to its observation for 2 mol% doped Ti:In₂O₃ thin films. It looks similar to band tailing of the valence band maximum as seen for Sn:In₂O₃ thin films deposited under reducing conditions in the latter case. The origin of those tails could, however, not be clarified [37]. For a higher doping concentration it resembles more to a discrete emission as seen for Mo:In₂O₃ thin films, which will be discussed in the following.

Band gap states are a commonly observed feature in TiO_2 [184, 185]. Occupied $\text{Ti}3d$ states or Ti^{3+} interstitials are made responsible for their observation. The Ti^{3+} oxidation state should then also be visible in the Ti core level spectra. To investigate the presence of a second titanium oxidation state, Ti2p spectra of two films, one with and one without the band gap states, were inspected more closely. Spectra of films deposited at 400°C or 600°C in argon were selected, representing samples with and without the feature respectively. The Ti2p emissions are shown in Fig. 6.9. As specified before, the background subtraction for the Ti2p core level is rather ambiguous. For the measurements shown here it was carried out in two steps. At first the In 3d satellite structure, which can be seen in Fig. 6.8 in gray, was scaled, shifted and then subtracted from the Ti2p spectrum followed by a Shirley background subtraction. The results for both films after normalization are shown in Fig. 6.21.

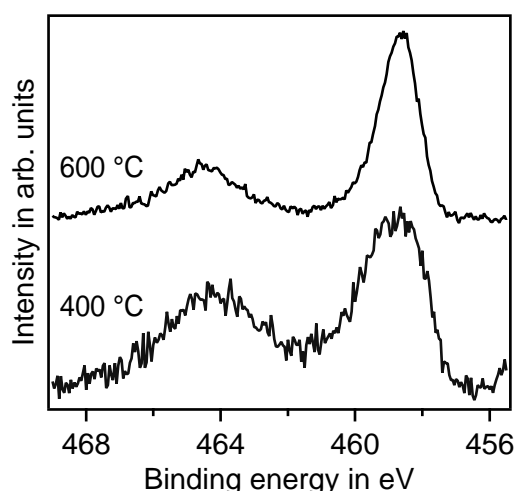


Figure 6.21: Ti2p core level spectra of films deposited in Ar at either 400°C or 600°C after background subtraction. The spectra were normalized for matching $\text{Ti}2p_{3/2}$ components.

Looking at the two spectra it is obvious that the FWHM of both $\text{Ti}2p_{3/2}$ emissions is significantly different. A much sharper peak is observed for the film deposited at 600°C as compared to the lower temperature. Considering the spectra of the other samples shown in Fig. 6.9 and Fig. 6.11, it can be seen that all films showing the band gap state possess a broader $\text{Ti}2p_{3/2}$ emission. The larger FWHM of the $\text{Ti}2p_{3/2}$ peak suggests, that it is composed of two components and therefore the presence of a second titanium oxidation state. A difference in binding energy of 1.7 eV is reported for Ti^{4+} and Ti^{3+} core levels [186], which is significantly more than the separation of the components found here. The presence of Ti^{3+} at the surface of some of the $\text{Ti}:\text{In}_2\text{O}_3$ thin films is nevertheless a possible explanation for the broadening of the $\text{Ti}2p_{3/2}$ peak and fits very well to the presence of the band gap emission. It can however not be proven with absolute certainty.

Fang *et al.* [99] carried out density functional theory calculations for the electronic structure of 6.25 at% doped $\text{Ti}:\text{In}_2\text{O}_3$. Similar to In_2O_3 , the valence band maximum is dominated by O 2p and a minor fraction of In 5p states. The conduction band consists of In 5s and strongly localized Ti3d states. The Fermi level is found to be roughly 3 eV above the valence band maximum and only slightly below the Ti3d bands. Based on this all tita-

mium ions should be present as Ti^{4+} and no band gap states originating from the $\text{Ti}:\text{In}_2\text{O}_3$ would be expected.

The latter DFT calculations are not able to predict charge carrier localization though [187]. For other metal oxides, however, localization of charge carriers due to interaction with lattice distortions were found to have a significant impact on the electronic structure [187–189]. The formation of those so-called polarons reduces the free energy of a carrier. Kweon *et al.* [187] could show that including carrier localization in the DFT calculations leads to the appearance of polaron states inside the band gap of BiVO_4 . Carriers with a high effective mass increase the probability for the formation of polarons. Considering the energetic position and low dispersion of the Ti3d bands [99], Ti^{3+} polaron states in the band gap of $\text{Ti}:\text{In}_2\text{O}_3$ seem conceivable. The simultaneous appearance of a band gap state and Ti^{3+} in the Ti2p photoelectron spectra could be explained by the formation of polaron states. At the bottom line, the $\text{Ti}^{3+/4+}$ charge transfer point can be expected to be found at lower energies as discussed in Ref. [99].

The deposition conditions required for the existence of Ti^{3+} do not lead to a conclusive explanation. It is plausible that addition of oxygen to the process atmosphere leads to a suppression. A decreasing intensity of the gap state with increasing temperature, i.e. nominally more reducing conditions, is puzzling. Since the Ti segregation increases with increasing substrate temperature, the formation of a TiO_2 phase at the surface can explain this observation, however.

The hypothesis of Ti^{3+} polaron states, i.e. the $\text{Ti}^{3+/4+}$ charge transfer point being in the here accessible energy range, can explain the presence of the discrete valence band states as observed for some of $\text{Ti}:\text{In}_2\text{O}_3$ thin films. Based on the observations made here no final proof can be given, though.

6.5 Summary

- $\text{Ti}:\text{In}_2\text{O}_3$ thin films were grown on glass by rf magnetron sputtering from 2 mol% and 5 mol% doped targets. The deposition conditions, i.e. substrate temperature and oxygen content of the process atmosphere affect the performance similar to In_2O_3 doped with other elements.
- XRD measurements show that the films consist of a single phase and confirm a bixbyite structure. A correlation between texture and oxygen content of the deposition atmosphere is indicated. In contrast to In_2O_3 thin films a (100) texture is found under reducing conditions, transitioning to (211) when oxygen is added to the deposition atmosphere.
- Based on conductivity and Hall-effect measurements the influence of the dopant concentration on the charge carrier mobility is much stronger pronounced as on the charge carrier concentration. Mobilities of up to $105 \text{ cm}^2 (\text{Vs})^{-1}$ are measured for 2 mol% $\text{Ti}:\text{In}_2\text{O}_3$ thin films. This exceeds the limits postulated by the In_2O_3 single crystal model but is comparable to values obtained for H- or Zr-doped In_2O_3 . The mobility measured for most of the 5 mol% $\text{Ti}:\text{In}_2\text{O}_3$ samples deposited at 600°C diminishes to almost zero. Overall carrier concentration and mobility are increasing

with increasing substrate temperature while the addition of oxygen has an opposing effect.

- Transmission and reflection spectra show features similar to the previously discussed Mo:In₂O₃. Burstein-Moss shift and free carrier absorption provide an explanation for the variation of the absorption onset in the UV and for the reflection in the NIR. A good agreement between measured and modeled spectra could be achieved. Qualitatively, the evolution of the optical band gap and plasma frequency go along with the carrier concentration and $E_F - E_{\text{VBM}}$. The conflict of $\mu_{\text{Hall}} > \mu_{\text{Opt}}$ is found once again.
- XPS measurements show parallel shifting core levels and valence band maxima with the exception of a view room temperature films. The observed shift goes in hand with the variation of the carrier concentration. Evaluation of the Ti2p core level emission is more complicated as compared to Mo3d due to its lower atomic sensitivity factor and an overlap with In3d satellites. The binding energy of its most dominant component indicates Ti to be mainly found in a 4+ oxidation state. Some films show an emission close to the valence band maximum going with the broadening of the Ti2p peak. Latter might be explained by a Ti³⁺ polaron state. Due to previously mentioned reasons, a quantitative evaluation of the Ti concentration at the surface could be carried out only for 5 mol% doped samples. An increasing Ti surface concentration is found for reducing conditions. Dopant segregation follows similar trends as observed for Sn:In₂O₃. While the ionization potentials are affected by the dopant concentration in the target and at the surface, no systematic effect is found for the work function. As it could be expected based on the surface potentials measured on TiO₂ [184] no extraordinarily high values as found for Mo:In₂O₃ were measured.

7 Doped Indium Oxide - A Comparison

The experimental results on Mo and Ti doped In_2O_3 presented so far will be discussed in this chapter in a general context, also considering results for other dopant elements.

7.1 Optical Properties

Optical properties of $\text{Mo:In}_2\text{O}_3$ and $\text{Ti:In}_2\text{O}_3$ thin films were discussed in Sec. 5.3 and Sec. 6.3 on the basis of transmission and reflection spectra. A qualitative description was followed by a comparison of parameters obtained from the dielectric functions via a fitting procedure. For this purpose, spectroscopic ellipsometry measurements were taken into account as well. Significant influence of the deposition parameters was found for both dopant elements. While carrier concentrations determined by Hall-effect measurements match well with optically obtained ones, a rather poor agreement was found for the mobility.

Transmittance and reflectance of Sn, Zr, Ge, Mo and Ti doped In_2O_3 thin films are shown in Fig. 7.1. The electronic properties of the samples are given in Tab. 7.1. Films with a conductivity similar to 5000 Scm^{-1} were selected.

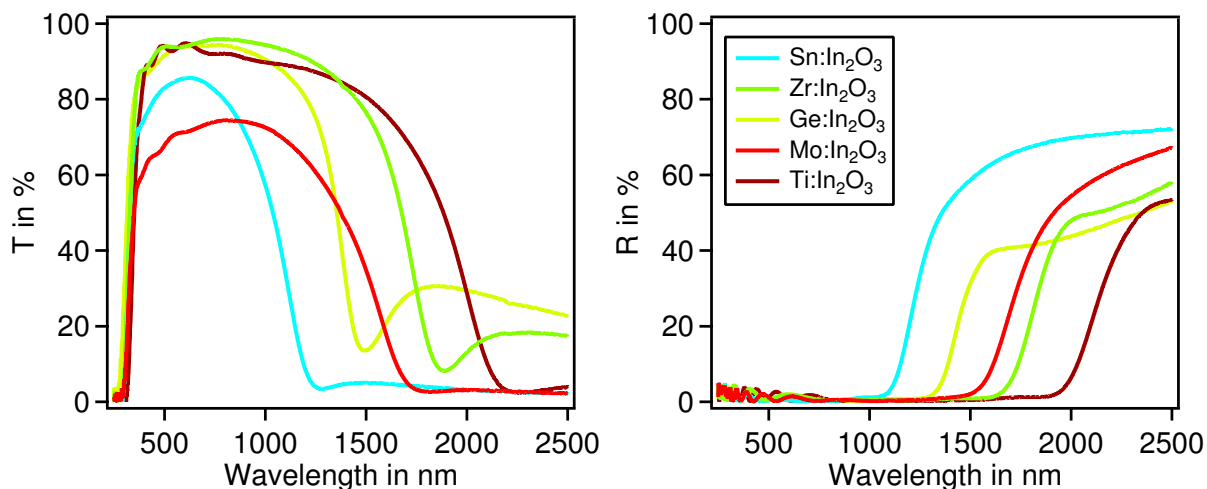


Figure 7.1: Transmittance and reflectance of 10 wt% $\text{Sn:In}_2\text{O}_3$, 2 wt% $\text{Zr:In}_2\text{O}_3$, 2 wt% $\text{Ge:In}_2\text{O}_3$, 5 mol% $\text{Mo:In}_2\text{O}_3$ and 2 mol% $\text{Ti:In}_2\text{O}_3$ thin films on fused-silica or soda-lime glass. Measurements were carried out at an incident angle of 60° using p polarized light. Electronic properties are given in Tab. 7.1.

All spectra show basically the same features: absorption in the UV, transmission in the VIS and adjacent NIR and reflection in the NIR region. Depending on the carrier concentration, absorption and reflection onsets are located at different wavelengths. The Burstein-Moss effect can explain the former [112, 113] while the Drude model, describing the correlation between free carrier absorption or plasma frequency and the carrier concentration, the latter [48]. Comparing the carrier concentrations given in Tab. 7.1 and the maximum transmission as seen in Fig. 7.1, it is obvious that the carrier concentration not

Table 7.1: Conductivity, carrier mobility and concentration of differently doped In_2O_3 thin films determined by conductivity Hall-effect measurements. Properties of the samples shown in Fig. 7.1 are presented.

material	dopant concentration	σ_{hall} in Scm^{-1}	μ_{hall} in $\text{cm}^2\text{V}^{-1}\text{s}^{-1}$	n_{hall} in 10^{20}cm^{-3}
Sn: In_2O_3	10 wt%	4830	26.2	11.5
Zr: In_2O_3	2 wt%	5113	74.10	4.31
Ge: In_2O_3	2 wt%	5356	57.1	5.86
Mo: In_2O_3	5 mol%	5180	55.1	5.71
Ti: In_2O_3	2 mol%	5114	101	2.98

necessarily determines the film transmittance, opposite to what has been stated elsewhere [64, 147].

Optical spectra of all available dopant elements were simulated to investigate whether the model applied here leads to a better match between optical and Hall-effect data. Transmission, reflection and SE spectra were fitted simultaneously in order to obtain the film thickness, carrier concentration and mobility. The model chosen for the simulation is well established in literature [89, 148, 149]. Even though a reasonable agreement between measured and simulated spectra can be obtained, some of the parameters extracted from the simulations differ significantly from the values obtained by other means. Only samples with carrier concentrations above $2 \times 10^{20} \text{cm}^{-3}$ were considered. For lower concentrations, the free carrier absorption is not occurring inside the measurement range, leading to no meaningful results of the Drude term.

The optically and electrically determined carrier concentrations and mobilities, n_{opt} and n_{Hall} and μ_{opt} and μ_{Hall} are compared in Fig. 7.2. Simulations were carried out assuming a constant effective electron mass of 0.3. The resulting values are shown as open symbols. Colored symbols indicate values obtained after adjustment to a carrier concentration dependent effective mass [148]. After this correction, coinciding carrier concentrations are found for both methods. This holds true independent on the dopant element and concentration. In contrast, mobilities differ quite significantly. The mobilities vary between $0 - 100 \text{cm}^2 (\text{Vs})^{-1}$ or $20 - 64 \text{cm}^2 (\text{Vs})^{-1}$ for the Hall-effect and optical measurements, respectively. No correlation between both is found. Fujiwara *et al.* [148] reported a rather similar behavior. A difference between both mobilities indeed is plausible due to the fact that the paths electrons have to travel in DC Hall-effect or optical measurements is very different [89, 148]. Since grain boundaries are not expected to affect optically determined mobilities, μ_{opt} exceeding μ_{Hall} would fit in. Even though this holds true for some of the samples, the majority show the opposite behavior.

Spectra of samples showing either low or high Hall mobility can both be simulated adequately by the applied model. Examples for both are shown in Fig. 7.3. T, R, SE measurements and their simulations are displayed. Arrows in Fig. 7.2 point towards the samples chosen for the comparison. A Mo: In_2O_3 and a Ti: In_2O_3 thin film were selected.

Independent on dopant element, measured and simulated spectra match very well. It is known that a good fit of optical spectra can also be achieved by physically unreasonable

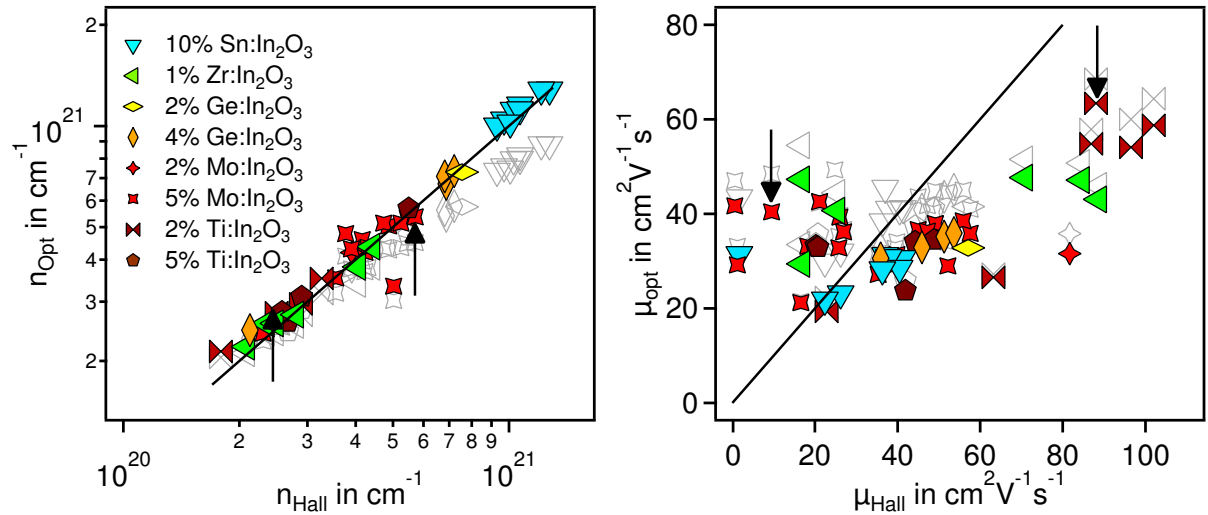


Figure 7.2: Comparison of carrier concentration and mobility as determined by simulation of optical spectra and conductivity Hall-effect measurements. Grey symbols represent values of n_{Opt} and μ_{Opt} which were calculated based on a fixed effective electron mass of 0.3. A non-constant electron mass was assumed for the colored symbols [148]. Black lines go through the origin and possess a slope of 1. Arrows point towards the samples displayed in Fig. 7.3.

parameters [81]. Simultaneously analyzing different measurements as done here should, however, reduce this uncertainty.

Koida *et al.* [149] reported a good agreement between optical and electrical carrier mobilities for H: In_2O_3 . Thin films with similar electronic properties as compared to this study were analyzed in latter article. One significant difference is, however, that measurements over a wavelength region from $1.7 \mu\text{m}$ to $30 \mu\text{m}$ were considered. This suggests, that the energy range investigated in this work may not be sufficient to correctly determine carrier mobilities from optical measurements.

Optical characterization methods are an important tool considering the properties of TCOs. They potentially can be used for a simple determination of transparency windows or a more complex spectrum analysis revealing the dielectric function of a material and other physical properties. The latter particularly promises access to a variety of parameters based on rather simple measurements. Great care has to be taken though when choosing the optical model and starting conditions for the simulations and especially when selecting the energy range which is analyzed.

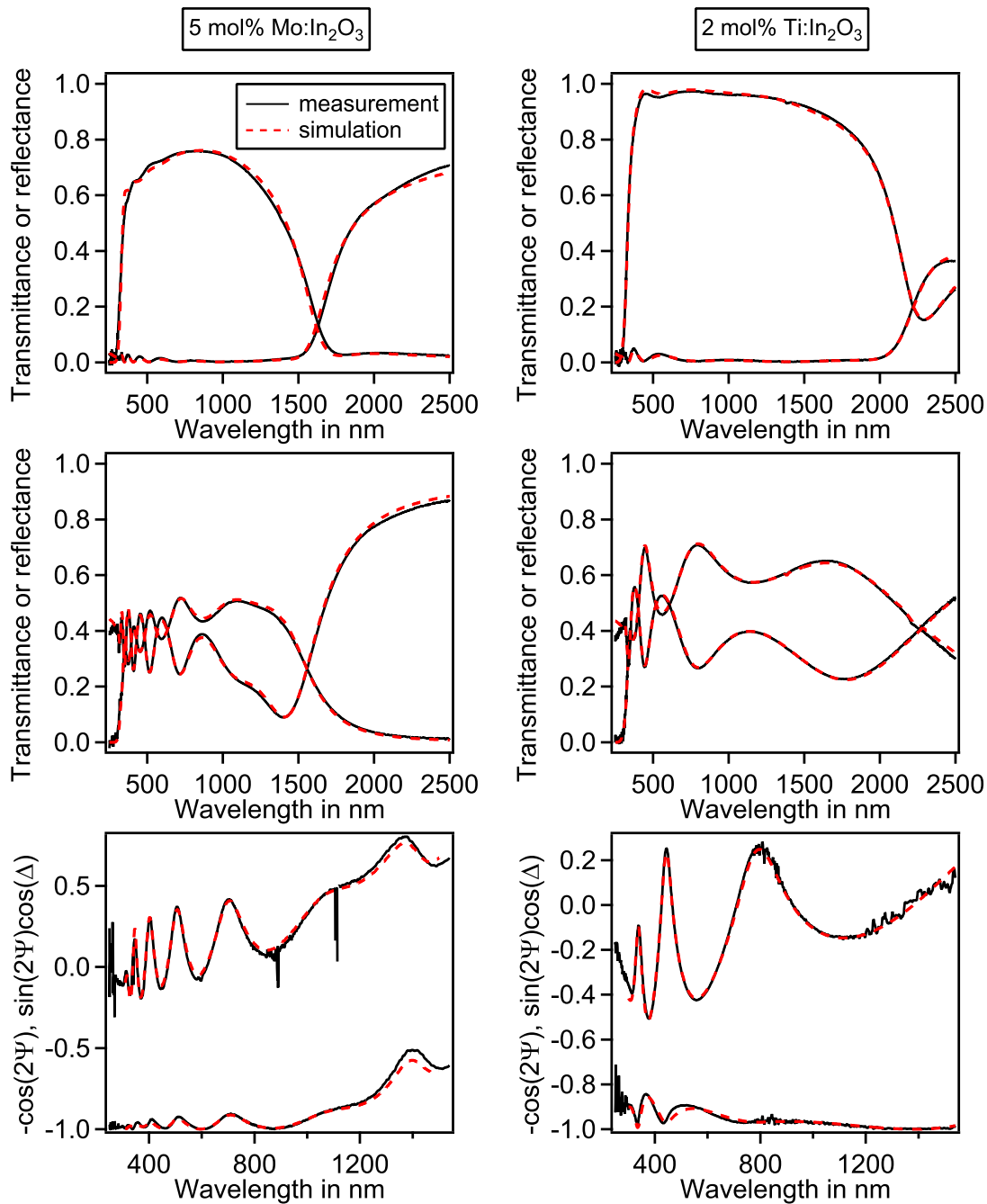


Figure 7.3: Transmittance, reflectance and spectroscopic ellipsometry spectra of 5 mol% Mo:In₂O₃ and 2 mol% Ti:In₂O₃ thin films on the left and on the right respectively. All measurements were carried out at an incident angle of 60°. P polarized light was used for transmission and reflection measurements shown at the top and s polarized light for the spectra in the middle. Simulated spectra, using the model described in Sec. 3.1.5, are displayed as well.

7.2 Surface Potentials

7.2.1 Summary of Observations

The variation of the surface potentials of Mo:In₂O₃ and Ti:In₂O₃ thin films with the deposition conditions was presented in Sec. 5.4.4 and Sec. 6.4.2. Data obtained in the framework of this thesis as well as data collected by other members of the research group will be discussed in this section. A comparison between undoped, Sn-, Zr-, Ge-, Mo- and Ge-doped In₂O₃ thin films is carried out.

The graphs displayed in Fig. 7.4 show the work function plotted over $E_F - E_{VBM}$ for the different materials. Solid lines possessing a slope of -1 indicate constant ionization potentials with values as annotated.

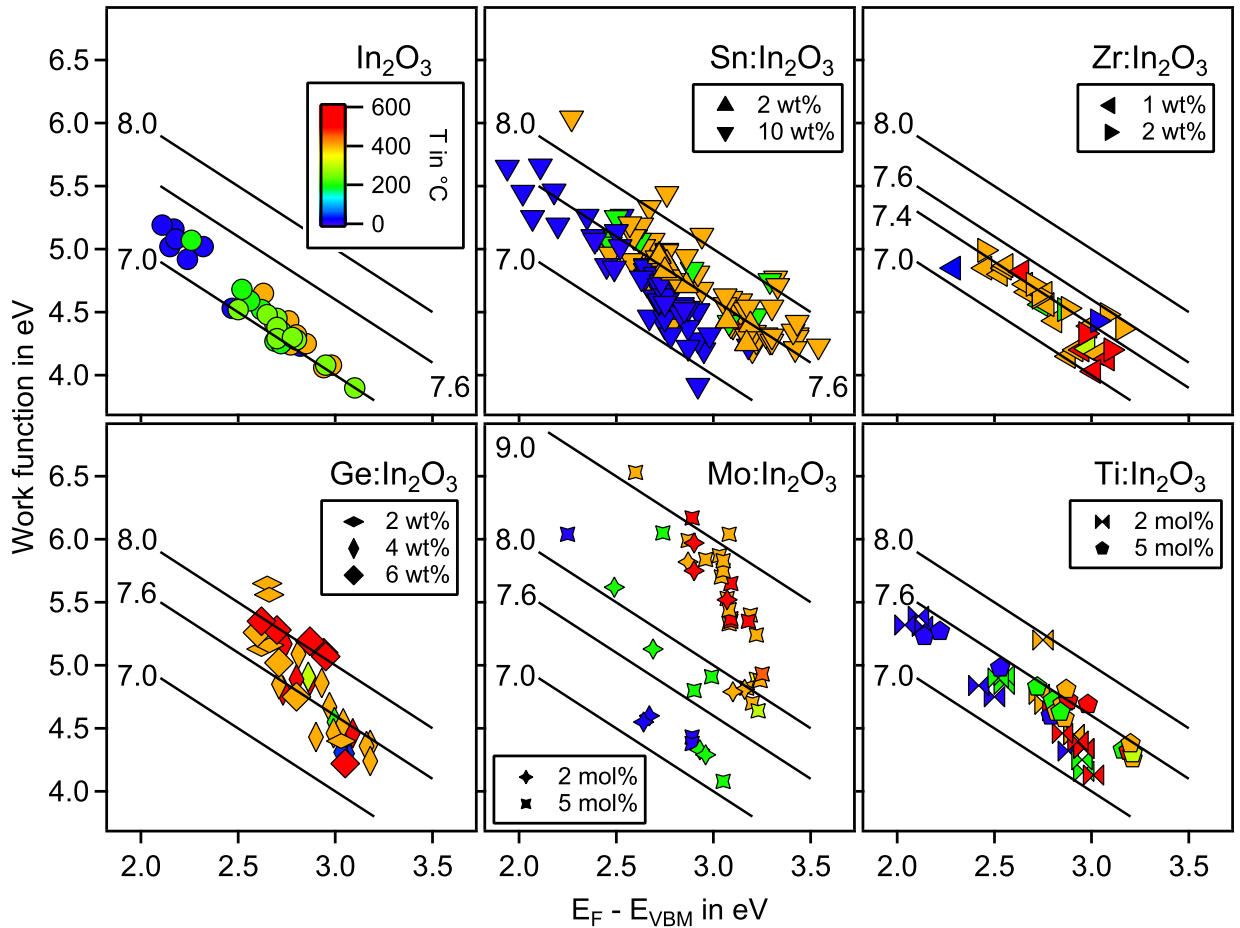


Figure 7.4: Work function plotted over $E_F - E_{VBM}$ for different dopants. Solid lines with the slope of one indicate constant ionization potentials. Deposition temperatures are indicated by the marker color according to the given scale.

The ionization potentials of the undoped In₂O₃ thin films shown here range from 6.9 eV to 7.4 eV. Klein *et al.* [32] report values of ≈ 7.1 eV to be mostly found for polycrystalline films, which tend to increase towards ≈ 7.6 eV for oxidizing conditions. Simulations predict the surface termination and orientation to influence the surface dipole [7]. Different

surfaces and terminations are expected to possess varying surface energies, which are influenced by the oxygen chemical potential of the environment. Growth conditions can therefore be selected to stabilize certain surfaces leading to a preferential film orientation. Epitaxial films grown by Hohmann *et al.* [29] confirm the latter assumptions. They either show ionization potentials of 7.0 eV for (111) or 7.7 eV for (100) oriented thin films, which can be stabilized by growth in reducing or oxidizing conditions, respectively.

The surface orientation is expected to influence the ionization potential of doped In_2O_3 samples as well. Besides the oxygen chemical potential, the dopant itself is expected to have an effect on the stability of different surface phases. Simulations for $\text{Sn}:\text{In}_2\text{O}_3$ indeed showed changing surface stability with changing Sn concentration [7]. Different correlations between texture and deposition conditions may therefore be a result of doping. Furthermore, dopant segregation is considered to have a significant effect on the surface potentials. Both effects were thoroughly investigated on the example of $\text{Sn}:\text{In}_2\text{O}_3$, which will be the starting point before discussing other dopants.

As seen in Fig. 7.4 the majority of Sn doped thin films possess an ionization potential of about 7.6 eV [27, 28, 35, 41, 190]. Nevertheless, some samples show values below 7 eV or above 8 eV. Surface orientation will be discussed before taking a closer look on dopant segregation.

Samples deposited at room temperature and varying pressure of the process atmosphere show a transition from a (111) to a (100) texture when going from 1 Pa to 5 Pa [33]. In this case, a correlation between film texture and ionization potential is found. (100) textured films possess ionization potentials of ≈ 7.6 eV while a preferential (111) orientation leads to $I_p = 7.0$ eV [29, 33].

In contrast to the latter observation, the ionization potential of epitaxial $\text{Sn}:\text{In}_2\text{O}_3$ thin films grown on YSZ single crystals at substrate temperatures of 400 °C is found to be independent on the film orientation. Values of 7.6 eV and 7.8 eV were determined when grown under reducing or oxidizing conditions respectively [27]. Atomic force and scanning electron microscopy revealed faceting of the (100) oriented films forming (111) surfaces. No differences in the surface potentials are reasonable considering that in both cases the same surface orientation was measured.

The deposition conditions influence the preferential orientation of polycrystalline thin films [15, 27, 33, 38]. Parameters to control the texture of rf magnetron sputtered In_2O_3 films, however, were found to be rather inconsistent [15, 38]. Plasma excitation by pulsed DC, i.e. pulsed DC magnetron sputtering (pDCms), proved to be a suitable tool to adjust the texture of $\text{Sn}:\text{In}_2\text{O}_3$ thin films grown on amorphous substrates. A variation of oxygen content or pressure of the deposition atmosphere results in strongly (100) or (111) textured thin films. Nevertheless, (111) facets were found in this work for all (100) textured films, even for room temperature depositions.

Based on the latter observations, the stability of the (111) compared to the (100) surface is increased by adding Sn as a dopant, leading to the formation of (111) facets on (100) oriented films. Neither the epitaxial nor the textured films grown by pDCms are therefore suitable to comment on the orientation dependence of I_p of $\text{Sn}:\text{In}_2\text{O}_3$ films. Because of the

findings on room temperature samples deposited by rf sputtering, orientation dependence of the surface dipole in Sn:In₂O₃ is still plausible.

Comparing the ionization potentials of (111) oriented Sn:In₂O₃ films grown at room temperature by rfms to ones deposited by pDCMs or at 400 °C, a difference of about 0.7 eV is found. While former samples show values of ≈ 7.0 eV, similar to undoped In₂O₃ (111) surfaces, I_p of the latter films amounts to about 7.7 eV, which is much higher as expected based on simulations [7] or experimental results on undoped In₂O₃ [29]. Dopant segregation and the formation of a SnO_x layer at the surface are possible explanations and will be discussed in the following.

Dopant segregation was already mentioned to be an important aspect for Sn:In₂O₃. It may lead to a gain or loss in surface energy depending on the surface orientation and termination [7]. Based on calculations, energy is gained for (100) while (110) and (111) surfaces are hardly affected. It has been reported that the Sn concentration depends on the surface Fermi level position i.e. the overall charge carrier concentration [15, 41]. This observation cannot be explained by a simple reduction of the surface tension by dopant segregation. Enhanced Sn surface concentration is found for reducing conditions, i.e. high $E_F - E_{VBM}$, which in turn goes with a high carrier concentrations [15]. This leads to the conclusion that the solubility of Sn decreases under reducing conditions. One mechanism to reduce the bulk Sn concentration is segregation of the dopant to grain boundaries or the sample surface.

For an explanation, the defect formation in Sn:In₂O₃, which was introduced in Sec. 2.4.2, has to be considered. A decreasing formation energy of oxygen interstitials is found for high Fermi energies i.e. high Sn concentrations [36]. Latter defects are responsible for the compensation of effective Sn dopant by the formation of neutral $(2\text{Sn}_{\text{In}}^{\bullet}\text{O}_i^{\prime\prime})^x$ defect associates [20, 21, 36, 70]. The Fermi energy is therefore determined by the concentration of Sn in the lattice and the compensating oxygen interstitials. Reducing conditions or treatments, as required for a high $E_F - E_{VBM}$ in Sn:In₂O₃, go with the removal of oxygen interstitials. The loss of the latter species can then be compensated by removal of Sn from the lattice e.g. by segregation to grain boundaries or surfaces [15]. A further explanation based on the free energy of formation of dopant defects will be discussed later.

Deposition temperatures above room temperature usually lead to an increased Sn surface concentration and a mostly invariant I_p . The segregation of Sn at the surface is a plausible explanation for this observation. Strongly oxidizing post deposition treatments of Sn:In₂O₃ films as exposure to ozone, oxygen plasma or annealing in oxygen containing atmospheres elevates I_p up and above 8.0 eV [27, 32, 190]. High ionization potentials are then a result of the formation of peroxide species at the surface [29].

Surface potentials of Zr:In₂O₃ thin films were investigated by Wardenga in the framework of a master thesis [191]. 1 wt% and 2 wt% doped Zr:In₂O₃ thin films tend to show ionization potentials of 7.4 eV. At high Fermi energies, slightly decreasing values of I_p are found for 1 mol% samples. The Zr content at the surface increases with both temperature and oxygen content in the process atmosphere. Here it is not possible to conclude on a correlation between Zr content and I_p . Since insufficient XRD data are available for this material, no comment can be made on a possible orientation dependence.

Hoyer *et al.* [35] carried out an in depth investigation of the surface potentials and dopant segregation of germanium doped In_2O_3 thin films in her Master thesis. The $\text{Ge}:\text{In}_2\text{O}_3$ samples show an average I_p of $\approx 7.7\text{ eV}$, which is decreasing with increasing Fermi energy. Since the film orientation is hardly affected by the deposition conditions, it can be ruled out as influencing parameter. A strong variation of the surface germanium concentration with the deposition conditions indicates significant dopant segregation. In contrast to the observations made on $\text{Sn}:\text{In}_2\text{O}_3$, an enhanced dopant concentration is found for oxidizing conditions. High ionization potentials and Ge surface concentrations are both observed for oxidizing deposition conditions. A correlation between the latter is therefore suggested. The formation of a GeO_2 surface layer may be an explanation for the values similar to 8 eV under oxidizing conditions.

The determination of surface potentials of $\text{Mo}:\text{In}_2\text{O}_3$ thin films was presented in Sec. 5.4.4. In comparison to the other dopants, the largest variation in I_p is found. Values in the range between 7.0 eV and 9.0 eV were measured. No difference is found for the different dopant concentrations investigated in this work. The dependence of the Mo surface concentration is alike to $\text{Ge}:\text{In}_2\text{O}_3$ thin films, except that the maximum concentration is reached at 400°C . A clear correlation between Mo segregation and ionization potential is found. I_p increases up to a surface Mo content of about $8\text{ at}\%$ followed by constant values. At similar substrate temperatures, oxidizing conditions lead to higher I_p values as compared to reducing conditions. The I_p found for a molybdenum oxide thin film grown on $\text{Sn}:\text{In}_2\text{O}_3$ amounts to 9.6 eV . Other surface potentials for MoO_3 can be found in Tab. 9.1. The formation of a MoO_3 surface layer can therefore explain the exceptionally high ionization potentials of high temperature films deposited with oxygen. Since I_p and Mo surface concentrations are little affected by temperatures above 400°C , it can be assumed that a potential surface layer is fully developed and no further effect on the surface dipole is obtained. Based on the available XRD data in this work no conclusion can be drawn considering a correlation between texture and I_p . The presence of MoO_3 could, however, be confirmed for a sample deposited at 600°C .

In Sec. 6.4.2 the surface potentials of $\text{Ti}:\text{In}_2\text{O}_3$ thin films were presented. The correlation between ϕ and $E_F - E_{\text{VBM}}$ is shown in Fig. 7.4. Most of the samples possess ionization potentials of about 7.5 eV while $\approx 7.1\text{ eV}$ and $\approx 7.7\text{ eV}$ are the lowest and highest measured values. The Ti surface concentration was quantified for $5\text{ mol}\%$ doped samples and shows a behavior similar to $\text{Sn}:\text{In}_2\text{O}_3$, i.e. reducing conditions lead to stronger segregation. For the $5\text{ mol}\%$ doped films a slight increase in I_p is observed with increasing Ti concentration at the surface. The variation amounts to 0.3 eV . No systematic variation of I_p with $E_F - E_{\text{VBM}}$ can be seen for higher dopant concentrations while decreasing ionization potentials with increasing Fermi energy are found for the $2\text{ mol}\%$ thin films. Single and polycrystalline anatase or rutile samples possess ionization potentials between 7.4 eV and 7.9 eV , which depends strongly on the preparation and surface treatment [184]. Since ionization potentials observed for $\text{Ti}:\text{In}_2\text{O}_3$ are similar to the ones of other doped In_2O_3 as well as to TiO_2 , no clear conclusion concerning possible titanium oxide surface layers can be drawn. The XRD patterns shown in Sec. 6.1 hint on the film texture to be influenced by the deposition conditions. Due to the lack of more data a correlation between I_p and the film texture cannot be commented on.

After comparing the ionization potentials of differently doped In_2O_3 thin films, it is obvious that the measured values are highly dopant specific. I_p of the doped films is limited on the low side by the values measured for In_2O_3 . Depending on the dopant, much higher values may be obtained. Orientation dependence was found for epitaxial In_2O_3 films but cannot be confirmed for $\text{Sn}:\text{In}_2\text{O}_3$, which, however, might be explained by the formation of (111) facets. Room temperature $\text{Sn}:\text{In}_2\text{O}_3$ samples seem to show a correlation. Due to limited XRD data for the other dopants no comment on the orientation dependence of I_p can be made here.

The major effect on the I_p seems to have its origin in surface segregation of the dopant. While an increasing surface concentration of Sn and Ti is observed under reducing conditions, elevated temperatures and oxygen in the deposition atmosphere favor dopant segregation of Ge and Mo. A significantly increased dopant concentration at the surface may result in the formation of a surface oxide layer. Considering that Sn and Ti segregation is stronger under reducing deposition conditions, reduced surfaces, containing Sn^{2+} and Ti^{3+} seem plausible [35]. Oxidizing conditions, as required for stronger dopant segregation in the case of $\text{Ge}:\text{In}_2\text{O}_3$ and $\text{Mo}:\text{In}_2\text{O}_3$ may promote the formation of stoichiometric or oxidized surfaces. The exceptionally high ionization potentials found for $\text{Mo}:\text{In}_2\text{O}_3$ fit quite well to the values of MoO_3 . A lower ionization potential, most likely similar to SnO_2 , is expected for GeO_2 . Good agreement of the measured values point towards the formation of a GeO_2 surface layer [35].

7.2.2 Influence of Dopant Segregation

Surface dopant segregation seems to be decisive for the surface potentials of doped In_2O_3 . Possible parameters influencing the segregation will be discussed in the following. An attempt at clarifying the reasons why either reducing or oxidizing conditions lead to enhanced dopant surface segregation will be made.

It is assumed that the dopant may either be incorporated in the In_2O_3 lattice as substitutional defect D_{In}^\bullet or form an oxide layer at the surface DO_2^{seg} . Since the absolute amount of dopant in a sample must be maintained, the following reaction equation can be used to describe the equilibrium between dopant in the sample and at the surface [46]:



This equation is valid for oxidizing conditions. For reducing conditions, the formation of monoxides is more likely. Independent on the conditions, the free energy of formation of the substitutional defect and of the dopant oxide can be assumed to determine dopant segregation.

Standard molar Gibbs free energies of formation for the possible oxides are given in literature [192] and are shown in Tab. 7.2. A higher absolute value of $\Delta_f G^0$ indicates a higher stability of the oxide. The formation of the segregated phase is therefore more favorable with increasing absolute value $\Delta_f G^0$.

Table 7.2: Standard molar Gibbs free energy of formation given for different oxides[192].

Compound	$\Delta_f G^0$ in kJ/mol	Compound	$\Delta_f G^0$ in kJ/mol
In ₂ O ₃	-830.7	InO	n.a.
SnO ₂	-515.8	SnO	-251.9
GeO ₂	-521.4	GeO	-237.2
ZrO ₂	-1042.8		
MoO ₃	-668.0	MoO ₂	-553.0
TiO ₂	-888.8	TiO	-495.0

The Gibbs free energy for the formation of defects ΔG_D must be calculated and is only available in the case of Sn:In₂O₃ and Mo:In₂O₃ [3, 26]. It is therefore not possible to directly compare oxide and defect formation energies of all dopants. ΔG_D can be described by Eq. 7.2 in the case of In₂O₃ [22, 24, 193–196]:

$$\Delta G_D = G_{\text{def}} - G_{\text{host}} - \Delta n_{\text{In}} \mu_{\text{In}} - \Delta n_{\text{O}} \mu_{\text{O}} + q (E_{\text{VBM}} + E_{\text{F}}) \quad (7.2)$$

with G_{def} and G_{host} being the free energy of a defective and an ideal supercell, Δn_i the change of atoms i from the ideal to the defective system, μ_i the chemical potentials and q the charge of the defect. The Gibbs free energy of formation of a defect changes with the chemical potential of indium and oxygen and in case of a charged defect based on the Fermi level position.

An other way to express the free energy of formation of a defect is shown in Eq. 7.3 [22]:

$$\Delta G_D = \Delta H_D - T \Delta S_D + p \Delta V_D \quad (7.3)$$

with the formation enthalpy ΔH_D , the formation entropy ΔS_D and formation volume ΔV_D . Since the formation enthalpy ΔH_D has the strongest contribution to ΔG_D , the following approximation is commonly made: $\Delta G_D \approx \Delta H_D$ ($T = 0$ K). For different dopant elements, it is nevertheless important to consider the formation volume, which is strongly correlated to the ionic radii of the dopant elements compared to the native In_{In}^x [196, 197]. A large difference between $r_{i,eff}(D^{4+})$ and $r_{i,eff}(In^{3+})$ requires a stronger lattice distortion to be compensated, which is energetically unfavorable [99, 193]. The effective ionic radii of all relevant elements are given in Tab. 2.1.

The defect formation energy ΔG_D can be used to calculate the equilibrium defect concentration c_{def} [195, 198]:

$$c_{\text{def}} = c_{\text{sites}} \exp\left(-\frac{\Delta G_D}{k_b T}\right) \quad (7.4)$$

Since ΔG_D is a function of $E_F - E_{VBM}$ and the defect formation volume, c_{def} will be as well. On the one hand, a larger difference in ionic radii leads to a lower equilibrium defect concentration. On the other hand, ΔG_D increases with increasing Fermi energy in the case of positively charged defects as D_{In}^\bullet . The solubility of the dopant therefore is expected to decrease with increasing ΔV_D and with increasing $E_F - E_{VBM}$.

The transition from a positive to negative defect formation energy is critical for the stability of a material. Defect concentrations would exceed the concentration of lattice sites for negative ΔG_D . It is important to differentiate between intrinsic and extrinsic defects. For intrinsic defects such as oxygen vacancies, a negative formation energy would result in the destabilization of the material. Energy would be gained by the formation of defects and the material is thermodynamically unstable [195, 199, 200]. A negative formation energy of extrinsic defects as D_{In}^\bullet does not necessarily lead to a destabilization. In the case of a limited dopant supply, it is energetically favorable to integrate all of the available dopants. Whether all of the dopant will be dissolved in the host crystal depends on the existence and stability of other ternary compounds or phases [193].

Dopant defect and oxide formation so far were discussed as competing mechanisms, which determine dopant segregation. While the defect formation volume and $\Delta_f G^0$ of a surface oxide layer are both fixed by the choice of dopant element, ΔG_D still depends on the electrochemical potential in the sample. The first two parameters should allow for a first guess on how strong dopant segregation is to be expected. ΔG_D depends on $E_F - E_{VBM}$ independent on the dopant, therefore a similar effect on the segregation is expected upon variation of the latter for any D_{In}^\bullet .

In Fig. 7.5, $\Delta_f G^0$ is plotted over $\Delta r_{i,eff}$, which is the difference in the effective ionic radii of In_{In} and D_{In}^\bullet . Segregation is expected to be more significant when either one or both energies are large. No clear tendency, which of the latter energies is dominating the segregation can be identified. $\Delta_f G^0$ of ZrO_2 is by far the largest but $r_{i,eff}(Zr^{4+})$ matches very well to $r_{i,eff}(In^{3+})$. This compares to the absence of strong dopant segregation for $Zr:In_2O_3$. The oxides formed by Sn and Ge possess similar formation energies while their ionic radii are significantly different. For both, an increased dopant concentration at the surface was found. $r_{i,eff}(Mo^{4+})$ is only slightly smaller than $r_{i,eff}(Sn^{4+})$ whereas $r_{i,eff}(Mo^{6+})$ differs more significantly. Both have a higher $\Delta_f G^0$, $Mo:In_2O_3$ still shows strong surface segregation. TiO_2 forms the second most stable oxide and possesses a rather large $\Delta r_{i,eff}$ and $\Delta_f G^0$ and a strong dopant segregation could be seen. While oxidizing conditions were required for enhanced dopant segregation in case of $Ge:In_2O_3$ and $Mo:In_2O_3$, it's the opposite for $Sn:In_2O_3$ and $Ti:In_2O_3$.

The reason why either reducing or oxidizing conditions lead to enhanced dopant segregation is not clear yet. Based on Eq. 7.2 a dependence of the Gibbs free formation energy of dopant defects on the Fermi level is obvious. Higher values of ΔG_D result in a lower equilibrium dopant concentration (Eq. 7.4) or a shift of the chemical equilibrium (Eq. 7.1) towards DO_2^{seg} . This means a stronger segregation would be expected for a higher $E_F - E_{VBM}$, i.e. reducing conditions, independent on the dopant element.

Only for $Sn:In_2O_3$ thin films, a clear correlation between relative Sn content at the surface and $E_F - E_{VBM}$ was found in the expected manner [41]. Higher Sn surface con-

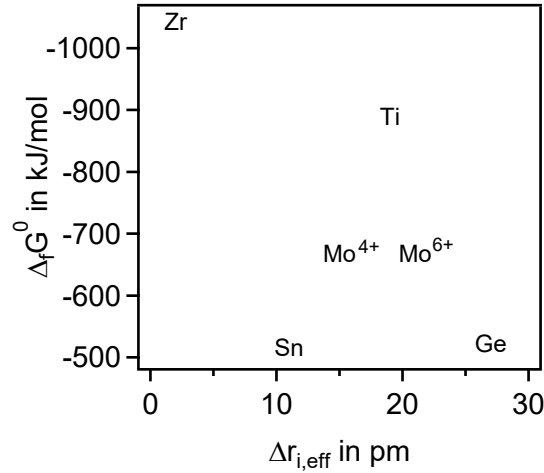


Figure 7.5: Standard molar Gibbs free energy of formation for the binary dopant oxides [192] plotted over the difference in ionic radii $\Delta r_{i,eff} = r_{i,eff}(\text{In}^{3+}) - r_{i,eff}(\text{D}^{4+})$ [68].

centrations are achieved under reducing condition, i.e. higher $E_F - E_{VBM}$. Calculations by Lany *et al.* [3] which predict such a behavior were confirmed by XPS measurements [41]. This observation was previously explained based on the competing defect concentrations of $\text{Sn}_{\text{In}}^\bullet$ and $(2\text{Sn}_{\text{In}}^\bullet \text{O}_i'')^x$ [15, 35]. An opposing correlation between $E_F - E_{VBM}$ and the Ge surface concentration was found for Ge: In_2O_3 thin films [35]. Oxidizing conditions lead to enhanced Ge segregation.

It has to be considered that the discussion so far assumes a sample to be in thermodynamic equilibrium. Since magnetron sputtering is a non-equilibrium deposition method, it is likely that as-deposited films are not in equilibrium. For Sn: In_2O_3 thin films, however, temperature and atmosphere dependent Hall effect as well as high pressure XPS measurements showed a reversibility of the charge carrier concentration or Fermi energy, respectively [15, 29, 39, 41]. Latter samples therefore can be assumed to be in thermodynamic equilibrium and the dopant solubility obeys the expected Fermi level dependence. Similar experiments were carried out for Ge: In_2O_3 samples. The charge carrier concentration proved not to be reversible. Therefore it is reasonable to assume that latter films are not in thermodynamic equilibrium and former rules are not applicable.

While SnO_2 and GeO_2 possess a very similar free energy of formation, the effective ionic radius of Ge^{4+} is significantly smaller than that of Sn^{4+} . Due to the large $\Delta r_{i,eff}$, a stronger distortion of the Ge: In_2O_3 lattice is expected, reducing the diffusion of the dopant significantly [197]. Based on this assumption, the following hypothesis may explain enhanced dopant segregation under oxidizing conditions. Additional oxygen in the deposition atmosphere leads to a stronger bombardment of the sample with highly energetic oxygen ions, which eventually increases the concentration of O_i'' . It is reasonable to assume that the lattice distortion introduced by doping with germanium is reduced by the incorporation of oxygen interstitials. A reduced stress state of the lattice is likely to result in a faster diffusion.

This explanation seems plausible when following requirements are met: (i) doped In_2O_3 thin films are not in thermodynamic equilibrium after the deposition; (ii) the dopant con-

centration in the sample is larger than the equilibrium solubility; (iii) diffusion is hindered due to the lattice distortion introduced by a large ΔV_D ; (iv) incorporation of O_i'' leads to a lattice relaxation and increased diffusivity.

Above given model is suitable to explain segregation in Sn:In₂O₃ films under reducing conditions and in Ge:In₂O₃ films under oxidizing conditions. When Mo:In₂O₃ and Ti:In₂O₃ samples are considered it nevertheless seems to have its limits. The order of the effective ionic radii is as follows: $Sn^{4+} > Mo^{4+} > Ti^{4+} > Ge^{4+}$. Enhanced dopant segregation under reducing or oxidizing conditions for Ti:In₂O₃ or Mo:In₂O₃ samples, respectively, is therefore unexpected. No final conclusion can be drawn here.

7.2.3 Summary

Surface potentials of doped and undoped In₂O₃ thin films were discussed in this section. The deposition conditions always have a strong impact on $E_F - E_{VBM}$ and ϕ while the variation of the surface dipole or I_p strongly depends on the dopant element. Post deposition treatments sometimes are necessary to affect the ionization potential. The lower limit in I_p of about 7.0 eV is defined by undoped In₂O₃. Highest values of 9.0 eV were found for Mo:In₂O₃. Dopant segregation to the surface and presumably the formation of a dopant oxide layer DO_2^{seg} strongly influences the surface dipole.

A hypothesis explaining enhanced dopant segregation for either reducing or oxidizing conditions was given. Only samples being in thermodynamic equilibrium are expected to follow a Fermi level dependence as predicted by Eq. 7.2. Large ΔV_D are assumed to reduce dopant diffusion, hindering a sample to reach thermodynamic equilibrium. The diffusivity can be increased by the incorporation of oxygen interstitials, leading to enhanced dopant segregation under oxidizing conditions. When the effective ionic radii of the dopants investigated here are compared, this model is not fully supported. Since it is based on a sample being in thermodynamic equilibrium or not, the latter fact has to be investigated in more detail. Temperature and atmosphere dependent conductivity and Hall effect measurements are a suitable starting point. Reversible carrier concentrations confirm thermodynamic equilibrium in Sn:In₂O₃ thin films [15, 39]. Such experiments can take up to several weeks and have not been conducted in this work. Temperature and atmosphere dependent conductivity and Hall effect measurements carried out for Ge:In₂O₃ lead to opposite observations. Relaxation times allowed in these experiments were maybe too short for establishing thermodynamic equilibrium in the sample. It is therefore required to repeat latter experiments to be able to judge whether the foundation of this hypothesis is reasonable.

7.3 Carrier Concentration

The influence of the deposition conditions on the carrier concentration in Mo:In₂O₃ and Ti:In₂O₃ thin films was discussed in Sec. 5.2 and Sec. 6.2. Similar to other dopants, the oxygen chemical potential, being defined by the amount of oxygen in the deposition atmosphere, was found to significantly affect n . Substrate temperature is important for the film crystallinity and dopant segregation, therefore influencing the carrier concentration

as well. While the donor concentration influences n , the correlation is not necessarily uniform.

Carrier concentrations of various doped and undoped In_2O_3 thin films are shown in Fig. 7.6. Data measured by former members of the research group, and those collected in the framework of this thesis are shown. The nominal dopant concentration of the films, which is based on the dopant concentration in the target as specified by the manufacturer, is the theoretical limit for n . Black lines indicate the latter values. Nominal dopant concentrations in the target and resulting carrier concentrations are given in Tab. 9.2.

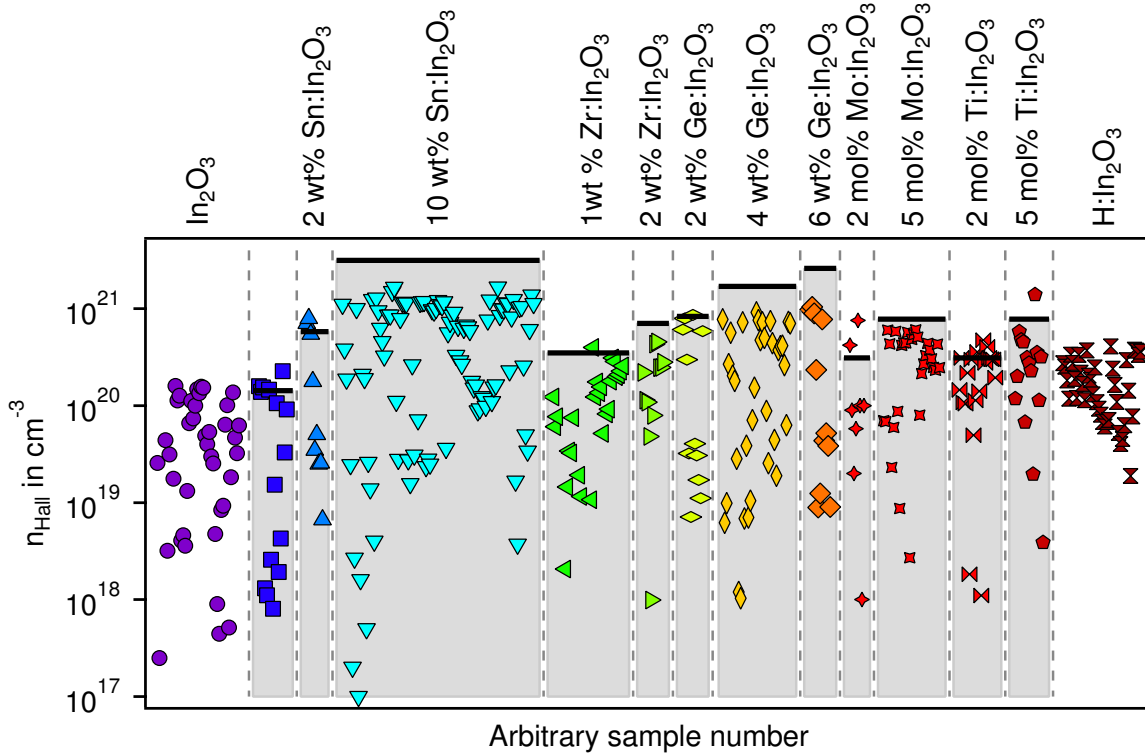


Figure 7.6: Hall carrier concentration of differently doped In_2O_3 thin films. The gray bars indicate the theoretically possible carrier concentration based on the nominal dopant concentration in the sputter targets.

The films show carrier concentrations varying by several orders of magnitude for every dopant. Different substrate temperatures and oxygen content of the atmosphere during the deposition are the reason for this large diversity. The maximum in n is related to the dopant species and concentration. It is questionable whether the highest carrier concentrations measured for 2 mol% Mo: In_2O_3 and 5 mol% Ti: In_2O_3 should be taken into account. In comparison to the other data points they seem unrealistically high.

Before discussing the doping limits in detail, an equation describing the total carrier concentration will be introduced. The total carrier concentration in doped In_2O_3 is determined by a variety of parameters. Eq. 7.5 summarizes the most relevant ones.

$$n = [D] - [A_{\text{intr}}^-] - [D^0] - [\text{Cat}_{\text{cat}}^-] - [D^{\text{seg}}] \quad (7.5)$$

[D] is the nominal concentration of donor dopants, $[A_{\text{intr}}^-]$ the concentration of intrinsic acceptors, $[D^0]$ of neutral dopants, $[\text{Cat}_{\text{cat}}^-]$ of negatively charged host cations and $[D^{\text{seg}}]$ of segregated dopants.

[D] is given by the amount of extrinsic donors in the film. Intrinsic donors as $V_{\text{O}}^{\bullet\bullet}$ hardly contribute due to their comparably low concentration and therefore can be neglected [21, 67]. The nominal concentration of donor dopants is assumed to be equal to the dopant concentration in the target as specified by the manufacturer.

$[A_{\text{intr}}^-]$ is assumed to resemble the concentration of oxygen interstitials. As explained in Sec. 2.4.1, these are the dominating intrinsic acceptor defect in Sn:In₂O₃ and explain the oxygen dependence of the carrier concentration. Since a similar influence of oxygen is observed for all other dopants, O_i'' is assumed as dominating intrinsic acceptor in doped In₂O₃ in general [3, 20]. Other intrinsic acceptor defects are indium vacancies V_{In}''' , which are expected to be of minor importance though.

$[D^0]$ depends on the charge transfer point in relation to the Fermi energy. Charge transfer points are defined as the energy level for the transition from donor to neutral or acceptor state [189]. Above this energy, dopant states will be charged at the expense of free carriers.

$[\text{Cat}_{\text{cat}}^-]$ depends, similar to the latter mechanism, on charge transfer points. The difference is that a valence change of the host cations i.e. In_{In} are considered this time. A limitation of the Fermi energy due to this effect could be shown for iron oxide [189].

$[D^{\text{seg}}]$ specifies the concentration of inactive, segregated dopants, which is not incorporated in the lattice on appropriate donor sites. For high dopant concentrations, phase separation may even occur, as was reported for Sn:In₂O₃ [33, 41].

The above given processes describe possible mechanisms, exhibiting doping limits in In₂O₃. From Fig. 7.6 it can be seen that those limits or the doping efficiency, i.e. the total carrier concentration as compared to the nominal dopant concentration, vary with dopant species and concentration. Highest n is obtained for Sn:In₂O₃ followed by Ge:In₂O₃, Mo:In₂O₃ and Ti:In₂O₃, both with similar values and finally Zr:In₂O₃. The exceptionally high carrier concentrations measured for few 2 mol% Mo:In₂O₃ and 5 mol% Ti:In₂O₃ are most likely not attributed to real carrier concentrations and will therefore be neglected.

The diagrams shown in Fig. 7.7 will be used to discuss each of the mentioned processes. To explain self compensation, i.e. the formation of intrinsic defects, and dopant segregation the defect formation energy in dependence of the Fermi energy has to be considered. Energy band diagrams shown in the middle and on the right illustrate charge transfer and valence change. The mechanisms will be discussed separately before a final remark is made.

7.3.1 Doping Limit by Intrinsic Defects: Self-Compensation

As can be seen in Fig. 7.7, formation energies of charged defects depend on the Fermi energy [22, 36, 193]. Intrinsic defect and charge carrier concentration therefore are correlated [33]. The formation energy of O_i'' and V_{In}''' in In₂O₃ is decreasing with increasing

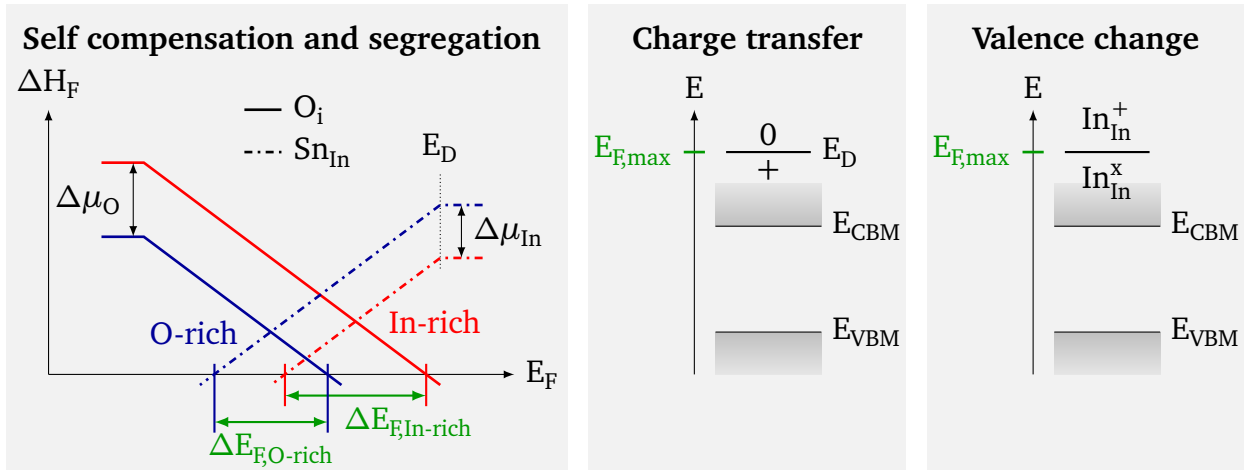


Figure 7.7: Schematic representation of the Fermi energy limiting mechanisms in doped In_2O_3 on the basis of [33]. Formation enthalpies of O_i and Sn_{In} in dependence of the Fermi energy, for O- and In-rich conditions are given on the left. The limits in E_F , as well as the defect energy E_D are annotated. An illustration for charge transfer and valence change is given by the schematic band diagrams in the middle and on the right.

$E_F - E_{\text{VBM}}$ due to their negative charge. This resembles an increasing concentration of intrinsic acceptors [200]. The Fermi energy reaches its limit when the formation energy of intrinsic acceptor defects approaches zero. Any additional donor beyond this point is compensated by the formation of an acceptor state. This mechanism is called self-compensation and reported to be the limiting process for the carrier concentration in donor-doped In_2O_3 [33, 200]

The formation energy of oxygen interstitials commonly approaches zero for lower values of $E_F - E_{\text{VBM}}$ as compared to the one of indium vacancies [3, 22]. It is therefore sufficient to focus on O_i'' . Fermi energies for which the formation energy of latter defect is zero are shown in Tab. 7.3. They were calculated for doped and undoped In_2O_3 , under In- and O-rich conditions. Comparing the values for both conditions, self-compensation is expected to start at much higher energies under reducing conditions. Highest carrier concentrations obtained for reducing conditions confirm latter point. The absolute limit for the Fermi energy due to self-compensation is nevertheless much higher as its experimentally determined maximum.

Table 7.3: Fermi energies for which defect formation energies of O_i'' in doped and undoped In_2O_3 approach zero. Values are given in eV. ^a Only formation energies for V_{In} were available in [26], latter are given.

material	In-rich	O-rich	Ref.
In_2O_3	4.1	2.2	[22]
$\text{Sn}:\text{In}_2\text{O}_3$	4.4	3	[3]
$\text{Sn}:\text{In}_2\text{O}_3/\text{Mo}:\text{In}_2\text{O}_3$	≈ 9.89	≈ 5.16	[26] ^a

Formation energies of each defect type are calculated separately (Eq. 7.3). If association energies of the defects are neglected, all formation energies but the ones for the dopant

defect itself are independent on the dopant element [3, 22, 26]. Based on this, identical values for $E_F - E_{\text{VBM}}$ should be expected for all dopant elements. Since the formation energies of the dopant defects and the density of states may differ for each dopant element, slight variations in the carrier concentrations can still be expected. For increasing dopant concentration, association energies of the defects gain importance [22]. Dopant dependent differences in formation energies are therefore plausible but cannot be evaluated here.

In Sec. 7.2, the effective ionic radius of the dopant element and the correlated defect formation volume was mentioned. Smaller ionic radii as compared to the native In^{3+} lead to a stronger lattice distortion, which in turn may decrease the formation energy of O_i'' . A dopant element and concentration dependent O_i'' formation energy further indicates dopant specific limits for $E_F - E_{\text{VBM}}$. The most simple consideration is a decreasing formation energy with decreasing ionic radius. In this case, self-compensation would be expected to start at lower $E_F - E_{\text{VBM}}$ resulting in a lower maximum carrier concentration. Comparing the ionic radii given in Sec. 2.4 to the maximum carrier concentration this can not be confirmed, though.

7.3.2 Doping Limit by Charge Transfer Points

The energy level of the dopant E_D , i.e. its transition point from a donor to a neutral or acceptor state and vice versa can limit the carrier concentration in doped semiconductors as well [189, 201]. It is indicated on the left side of Fig. 7.7 and a schematic band diagram suitable to describe this mechanism in doped In_2O_3 is shown in the middle. Raising the Fermi energy beyond the donor level would result in charge transfer to this state, counteracting an increase in Fermi energy. To comment on whether charge transfer points of the dopant elements limit the carrier concentration in doped In_2O_3 , those energies will be estimated and compared to experimental results.

Charge transfer points either can be calculated [26, 201] or, since this mechanism goes with a change of the dopant oxidation state, evaluated based on redox potentials. The electrochemical series references redox-reactions to the standard hydrogen electrode (SHE), which in turn can be used to assess the transition points relative to the vacuum level [192]. Eq. 7.6 can be used to do the transfer between both energy scales [202]:

$$E_{\text{phys}} = -(E_{\text{SHE}} + 4.44 \text{ eV}) \quad (7.6)$$

An energy of 0 eV relative to the vacuum level (E_{phys}) is equal to -4.44 eV on the SHE scale (E_{SHE}). Tab. 7.4 gives an overview for the relevant standard reduction potentials, if available. In some cases a comparison to other references is given to estimate the potentials for missing reactions.

The variation in work function defines the variation of the Fermi energy with respect to the vacuum level. For easy comparison, the charge transfer points and the experimentally accessible range of the Fermi energy are visualized in Fig. 7.8 for In and all dopants.

Table 7.4: Redox reactions and corresponding reduction potentials vs. the standard hydrogen electrode E^0 (if not explicitly annotated) or the vacuum level E_{phys} [192]. ^a E vs. SCE from [203], ^b vs. silver-silver chloride [Ag-AgCl(0.1 N)] reference electrode in molten, equimolar KCl-NaCl salt, taken from [204].

Reaction	E^0 in V	E_{phys} in eV
In		
$\text{In}^{4+/2+}$	+0.015	-4.455
$\text{In}^+ + e^- \rightleftharpoons \text{In}$	-0.14	-4.3
$\text{In}^{2+} + e^- \rightleftharpoons \text{In}^+$	-0.40	-4.04
$\text{In}^{3+} + e^- \rightleftharpoons \text{In}^{2+}$	-0.49	-3.95
$\text{In}^{3+} + 2e^- \rightleftharpoons \text{In}^+$	-0.443	-3.997
$\text{In}^{3+} + 3e^- \rightleftharpoons \text{In}$	-0.3382	-4.1018
Sn		
$\text{Sn}^{2+} + 2e^- \rightleftharpoons \text{Sn}$	-0.1375	-4.3025
$\text{Sn}^{4+} + 2e^- \rightleftharpoons \text{Sn}^{2+}$	+0.151	-4.591
Zr		
$\text{Zr}^{4+} + 4e^- \rightleftharpoons \text{Zr}$	-1.45	-2.99
Ge		
$\text{Ge}^{2+} + 2e^- \rightleftharpoons \text{Ge}$	+0.24	-4.68
$\text{Ge}^{4+} + 4e^- \rightleftharpoons \text{Ge}$	+0.124	-4.564
$\text{Ge}^{4+} + 2e^- \rightleftharpoons \text{Ge}^{2+}$	+0.00	-4.4
Mo		
$\text{Mo}^{3+} + 3e^- \rightleftharpoons \text{Mo}$	-0.200	-4.24
$(\text{Mo}^{6+} + e^- \rightleftharpoons \text{Mo}^{5+})$	(+0.43)	-4.87
^a $\text{Mo}^{6+} + e^- \rightleftharpoons \text{Mo}^{5+}$	+1.0	
^a $\text{Mo}^{5+} + e^- \rightleftharpoons \text{Mo}^{4+}$	-0.1	
^a $\text{Mo}^{4+} + e^- \rightleftharpoons \text{Mo}^{3+}$	-0.7	
Ti		
$\text{Ti}^{2+} + 2e^- \rightleftharpoons \text{Ti}$	-1.630	-2.81
$\text{Ti}^{3+} + e^- \rightleftharpoons \text{Ti}^{2+}$	-0.9	-3.54
$\text{Ti}^{3+} + 3e^- \rightleftharpoons \text{Ti}$	-1.37	-3.07
^b $\text{Ti}^{4+} + e^- \rightleftharpoons \text{Ti}^{3+}$	-0.37	
^b $\text{Ti}^{3+} + e^- \rightleftharpoons \text{Ti}^{2+}$	-1.0	

In the case of Sn:In₂O₃ and Ge:In₂O₃, the relevant standard reduction potentials of the donor/acceptor transition are known. It can be seen that the position of the charge transfer point is inside of the accessible Fermi energy range for both dopants. A location towards the top is noticeable.

Only the 4+ /0 transfer point was found for zirconium. No other stable oxidation states are expected, though. A large difference of the Fermi level position and the charge transfer point is expected for Zr:In₂O₃.

Standard reduction potentials could not be found for all relevant donor/neutral, donor/acceptor levels and dopants. To comment on whether charge transfer points

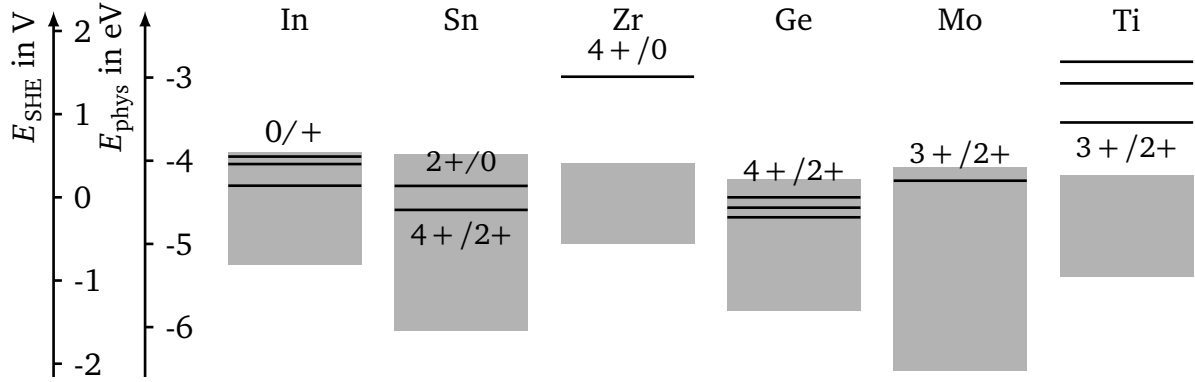


Figure 7.8: Valence change energy for In or charge transfer points for each dopant are given either vs. E_{SHE} or vacuum energy. Values are taken from Tab. 7.4. The accessible range in Fermi energy is represented by the gray squares. Latter limits were determined by the highest and lowest work function measured for the different materials.

limit the Fermi energy in those cases, further considerations have to be made. Reduction/oxidation does not necessarily follow a consecutive order from highest to lowest oxidation state. For assumptions regarding the relevant charge transfer levels of molybdenum and titanium references dealing with electrochemical studies of latter have to be included.

Pennisi [203] determined the average half cell reaction potentials of molybdic acid at a graphite electrode in sulfuric acid. The voltages vs. saturated calomel electrode were found to change from 1.0V to $-0.7V$ for the reactions: $Mo^{6+} + e^- \rightleftharpoons Mo^{5+}$; $Mo^{5+} + e^- \rightleftharpoons Mo^{4+}$; $Mo^{4+} + e^- \rightleftharpoons Mo^{3+}$. The electrochemical reduction of Ti^{4+} , as well carried out in KCl-NaCl melt, lead to reactions in following order [204]: $Ti^{4+} + e^- \rightleftharpoons Ti^{3+}$; $Ti^{3+} + e^- \rightleftharpoons Ti^{2+}$; $Ti^{2+} + 2e^- \rightleftharpoons Ti(\text{Pt alloy})$; $Ti^{2+} + 2e^- \rightleftharpoons Ti(\text{pure})$. Complex formation or other processes, which stabilize otherwise unfavorable species will not be considered in the following.

Including latter studies into the picture of standard reduction potentials, following estimations can be made: the charge transfer point for $Mo:In_2O_3$ and $Ti:In_2O_3$, i.e. Mo^{4+}/Mo^{3+} and Ti^{4+}/Ti^{3+} , are expected close to $E_{F,max}$. A similar image as for $Sn:In_2O_3$ and $Ge:In_2O_3$ is drawn.

When comparing the highest Fermi energies in In_2O_3 to the dopant dependent charge transfer points, estimated from standard reduction potentials, donor/neutral or donor/acceptor transitions are found close to the highest accessible Fermi energy in each material. The only exception is given by $Zr:In_2O_3$, with the transfer level far above $E_{F,max}$.

A second approach is based on the calculation of the donor transition levels. As before, data is rather scarce. Swallow *et al.* [26] calculated the 0/+1 transition level for Sn_{In} and Mo_{In} , obtaining values of 0.85 eV and 0.64 eV above the conduction band minimum. In combination with the band gap, which was calculated to be 2.63 eV, transfer points are expected at 3.48 eV and 3.27 eV above the valence band maximum. These values for $Sn:In_2O_3$ and $Mo:In_2O_3$ fit very well to the highest $E_F - E_{VBM}$ measured by XPS of 3.54 eV and 3.24 eV respectively.

Simulations for Ti:In₂O₃, carried out by Raebiger *et al.* [201], lead to a Ti³⁺/Ti⁴⁺ transition energy of 2.70 eV with respect to the valence band maximum. According to the latter article this results in a position of 0.7 eV below the conduction band minimum, i.e. the Fermi energy being limited inside the band gap. The band gap used in this work of 3.4 eV overestimates the fundamental band gap and is closer to what is expected for the optical band gap of thin films. The transition level is still found below the conduction band minimum even when a more realistic band gap of 2.9 eV is assumed. Measurements on Ti:In₂O₃ thin films, carried out in this work, lead to a maximum $E_F - E_{\text{VBM}}$ value of 3.2 eV, which is significantly higher as predicted by Raebiger *et al.* [201]. Since the samples with a high Fermi energy show the presence of Ti³⁺ states according to the experiment, the Ti³⁺/Ti⁴⁺ charge transfer point is a plausible limit for the in Ti:In₂O₃. The mismatch in calculated and experimentally determined Fermi energy as well as an over-estimated fundamental band gap, raise the question of the accuracy of the conducted calculations.

It is reasonable to assume that the Fermi energy and therefore the charge carrier concentration is limited by donor/neutral or donor/acceptor transitions. The approaches taken here, i.e. a comparison to standard reduction potentials and calculated values, support this assumption. The only exception is made by Zr:In₂O₃. No clear conclusion can be drawn though because of a lack of reliable data. Standard reduction potentials are determined in solution and may significantly differ in a solid. Calculations carried out by Swallow *et al.* [26] are very close to experimental results. Latter therefore suggest the described limitation of the Fermi energy.

The energies for the valence changes of In, being the host cation, are given in Tab. 7.4 and Fig. 7.8. The mechanism is comparable to the charge transfer of the dopant ions. The schematic band diagrams shown for both mechanisms in Fig. 7.7 are therefore similar. The Fermi energy range displayed in Fig. 7.8 is based on the work functions measured for In₂O₃. Similar to most of the dopants, the charge transfer of the host cation to form an acceptor is positioned close to the highest accessible Fermi energy.

7.3.3 Doping Limit by Dopant Segregation

Dopant segregation was discussed in Sec. 7.2 to have a significant effect on the surface dipole of doped In₂O₃ thin films. The formation of dopant oxide layers at the surface is an explanation for the exceptionally high ionization potentials for some of the materials. At high dopant concentrations phase separation, was also reported to occur in Sn:In₂O₃ [33, 41, 205]. Considering that dopants become inactive when not incorporated in the lattice on appropriate sites [33, 61], a correlation between dopant segregation and carrier concentration or $E_F - E_{\text{VBM}}$ is plausible. In Sec. 7.2 the segregation behavior was pointed out to be specific for each dopant element. Before comparing the different dopant elements, a look will be taken on the segregation behavior in the extensively studied Sn:In₂O₃ [15, 41, 206].

Sn⁴⁺ usually is incorporated as substitutional defect on an In³⁺ lattice site [9, 67, 205]. If compensating defects as O_i^{''} are not considered, each Sn donates one electron [33, 200]. Dopants bound in a secondary phase or a surface oxide layer do not count to the electron donors. Hall-effect measurements at high temperatures further indicate Sn segregation

to the grain boundaries [29]. Especially here, Sn might be present as Sn^{2+} forming an acceptor state and therefore acting as electron trap [15].

The defect formation energy of $\text{Sn}_{\text{In}}^{\bullet}$ increases with increasing Fermi energy due to its positive charge. Latter dependence is shown on the left in Fig. 7.7. According to Eq. 7.4, the solubility of a defect decreases with increasing formation energy. A lower Sn concentration and therefore an enhanced segregation is expected for increasing Fermi energy. Depending on the correlation between the O_i'' and $\text{Sn}_{\text{In}}^{\bullet}$ formation energies, segregation may further be enhanced to compensate for the lack of O_i'' at high Fermi energies and reducing conditions as was discussed before.

A comparison between the dopant surface- and Hall carrier concentration is shown for Sn, Ge, Mo and Ti as dopant elements in Fig. 7.9. The surface concentration is given in cat% as determined by XPS. For $\text{Zr}:\text{In}_2\text{O}_3$ and 2 mol% doped $\text{Ti}:\text{In}_2\text{O}_3$ thin films no data for the surface concentration are available. Measurements carried out in this work were added to the data points published for $\text{Sn}:\text{In}_2\text{O}_3$ by Frischbier *et al.* [15].

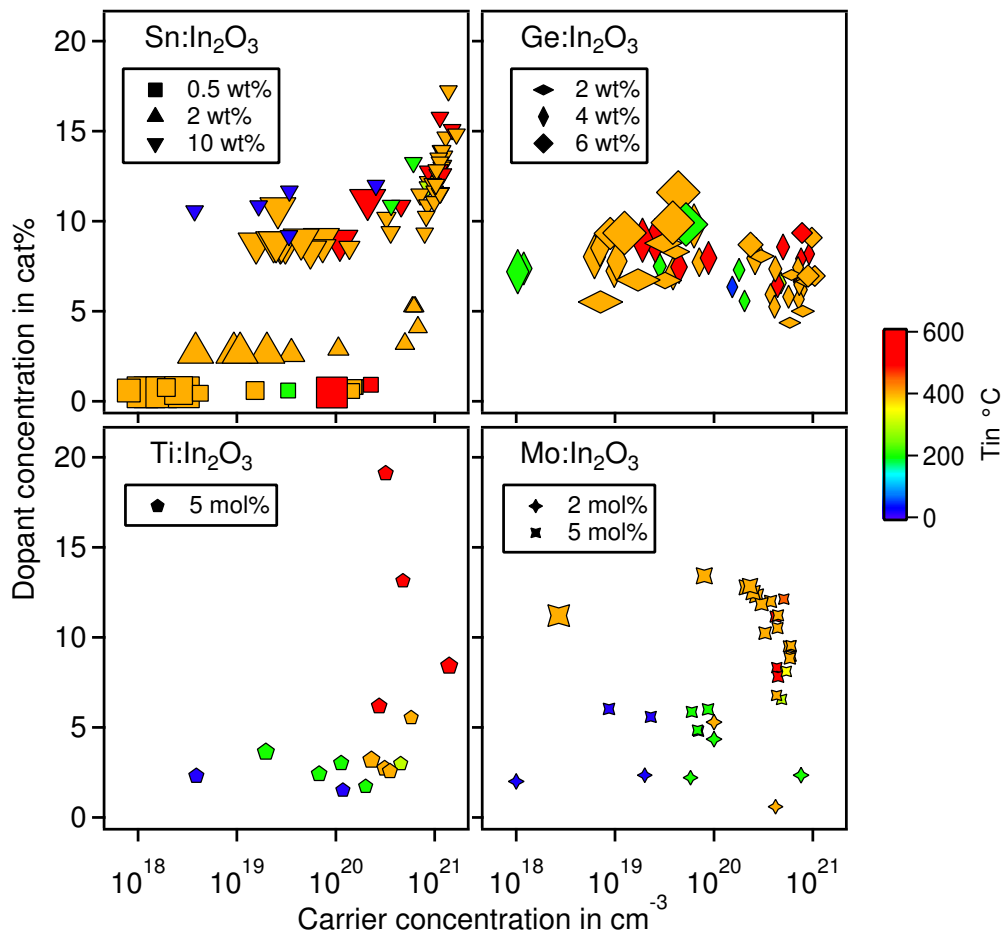


Figure 7.9: Dopant concentration at the surface, as determined by XPS, plotted over the Hall carrier concentration. Dopant element and nominal concentration is specified in each graph. Marker color and size indicate deposition temperature or oxygen content in the deposition atmosphere.

Depending on the Sn concentration in the target, different surface concentrations are measured. Enhanced Sn segregation can be seen for increasing carrier concentration, i.e. reducing deposition conditions [15]. Nominal dopant concentrations of 2 wt% and 10 wt% are required for latter observation. The highest carrier concentration measured for 0.5 wt% doped films is one order of magnitude below the absolute maximum observed in Sn:In₂O₃. This means the dopant surface concentration starts to increase when n is approaching its absolute limit. As previously explained an increasing Fermi energy is counteracted by the formation of O_i''. If the abundance of oxygen is restricted, the concentration of O_i' is restricted as well. Under reducing conditions, increasing $E_F - E_{\text{VBM}}$ therefore is compensated by the exclusion of Sn donors from the lattice, i.e. by segregation to the surface and to the grain boundaries [35]. Vice versa, addition of oxygen results in a reduction of the carrier and of the dopant surface concentration.

The segregation behavior of Ti in In₂O₃ is similar to Sn. An increasing Ti surface concentration with increasing carrier concentration therefore match the expectations.

While the surface concentration in Sn:In₂O₃ and Mo:In₂O₃ thin films clearly corresponds to the nominal dopant concentration in the target, the Ge concentration at the surface of Ge:In₂O₃ thin films does not depend on the Ge concentration in the target. Similarly, the maximum carrier concentration in Sn:In₂O₃ and Mo:In₂O₃ thin films is affected by the nominal dopant concentration in the target, while hardly any variation can be seen in Fig. 7.6 for Ge:In₂O₃. Overall, the differences in the Ge surface concentration are rather weak. Highest values are found between $10^{19} - 10^{20} \text{ cm}^{-3}$ when significant amounts of oxygen are added to the deposition atmosphere. Those observations fit to the reports of enhanced segregation under oxidizing conditions [35].

Mo:In₂O₃ thin films were previously discussed to show a segregation behavior more similar to Ge:In₂O₃. A much stronger variation of $[D^{\text{seg}}]$ can be seen in Fig. 7.9, though, both with nominal Mo concentration as well as with carrier concentration. As it is discussed in Sec. 5.4.2, temperatures above 200 °C are required for Mo to become mobile and highest carrier concentrations are measured around 400 °C in 5 mol% doped films. Enhanced dopant segregation as found for high carrier concentrations is therefore plausible. The addition of oxygen, however, further increases the Mo surface concentration, while decreasing the carrier concentration. Mo segregation is therefore promoted by oxidizing conditions and not dependent on the carrier concentration.

A correlation between dopant segregation and Hall carrier concentration is not given for all materials. Dopant surface concentration in Ge:In₂O₃ and Mo:In₂O₃ thin films is highest when oxygen is added during the deposition, therefore at intermediate carrier concentrations. In the case of Sn:In₂O₃ and Ti:In₂O₃, the highest carrier concentrations are measured for highest dopant surface concentrations. Only here dopant segregation could therefore be a limiting factor.

7.3.4 Summary

Mechanisms possibly limiting the carrier concentration in doped In₂O₃ were discussed in this section. Self compensation, charge transfer, valence change and dopant segregation

were considered. Comparing the experimentally accessible range in Fermi energy to the limit defined by the formation of intrinsic acceptor defects, self compensation can likely be excluded. Based on the estimation of the valence change point of In_{In}^x and the charge transfer points of the dopant elements a rather good agreement to the experimentally determined limits in Fermi energy is found. The only exception is given by $\text{Zr}:\text{In}_2\text{O}_3$. For $\text{Sn}:\text{In}_2\text{O}_3$ and $\text{Ti}:\text{In}_2\text{O}_3$ an increasing dopant surface concentration goes with increasing carrier concentration. No definite conclusion on the limiting mechanism can be drawn here. It may as well be defined by the dopant element itself.

7.4 Carrier Mobility

The influence of the deposition conditions on the carrier mobility in $\text{Mo}:\text{In}_2\text{O}_3$ and $\text{Ti}:\text{In}_2\text{O}_3$ was illustrated in Sec. 5.2 and Sec. 6.2. Both dopants were expected to yield mobilities exceeding values calculated for undoped In_2O_3 and $\text{Sn}:\text{In}_2\text{O}_3$ single crystals [26, 65]. While this holds true for $\text{Ti}:\text{In}_2\text{O}_3$, mobilities measured on $\text{Mo}:\text{In}_2\text{O}_3$ in this work stay in the boundaries of the calculated limits [17]. For both dopants, a strong decline in mobility was found when deposited at 600°C . Results of this work will be compared to previous research carried out in this group and literature. Mobilities for In_2O_3 thin films doped with a variety of elements and concentrations are plotted over the carrier concentration in Fig. 7.10. The modeled limit in mobility and values measured for single crystals are shown as well [17].

A brief account about the theoretical mobility limits in $\text{Sn}:\text{In}_2\text{O}_3$ will be given at first [17]. Since this model is made for single crystalline samples, grain boundaries are not considered as scattering centers, but polar optical phonons, acoustic deformation potentials and fully ionized impurities are. $\text{Sn}_{\text{In}}^\bullet$ is assumed as ionized impurity. All dopants are expected to be ionized. Taking oxygen vacancies or interstitials into account would result in a lower mobility due to a higher charge [17, 207]. Scattering at polar optical phonons limits the mobility at low carrier concentrations while it is ionized impurity scattering at high concentrations. The model shows a reasonable agreement with experimental data for epitaxial and single crystalline In_2O_3 and $\text{Sn}:\text{In}_2\text{O}_3$ except for carrier concentrations around 10^{20} cm^{-3} . In this region, the measured mobilities are significantly underestimated by the model. Preissler *et al.* [17] assume that the screening of optical phonons by free charge carriers is underestimated in their model. The reason for this discrepancy nevertheless is not fully understood yet [15].

In Fig. 7.10 it can be seen that all polycrystalline films show a large decrease of mobility for decreasing carrier concentrations, which can be explained by grain boundary scattering [13, 15, 29]. Depending on dopant element and concentration, maximum mobilities match quite well to the single crystal model when high carrier concentrations are considered. This can not be confirmed for hydrogen, zirconium or titanium doped films. One of the unintentionally doped samples even shows exceeding mobilities.

Coinciding mobilities at high carrier concentration of the measured polycrystalline films and the single crystal model imply vanishing influence of grain boundaries [15]. Decreasing barrier heights with increasing $E_F - E_{\text{VBM}}$, i.e. higher carrier concentrations and better screening of trapped charges at the grain boundaries explain latter observation.

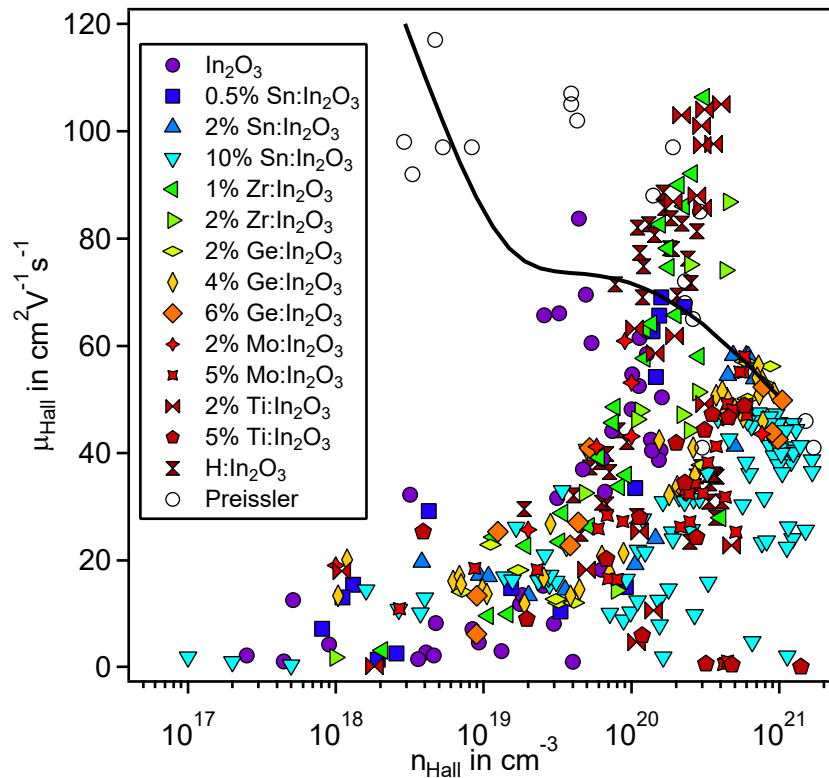


Figure 7.10: Hall carrier mobility plotted over the logarithm of the Hall carrier concentration of doped In_2O_3 thin films. Colored markers represent samples prepared and measured by members of the research group, open circles data for In_2O_3 and $\text{Sn:In}_2\text{O}_3$ single crystals or epitaxial thin films [17]. Variation of the deposition conditions, i.e. deposition temperature and oxygen content, leads to the diversity of electronic properties for a single dopant type and concentration. The solid black line indicates the theoretical mobility limit, calculated for $\text{Sn:In}_2\text{O}_3$ single crystals [17].

Grain boundary barrier heights, mobility limits and the influence of the dopant element onto the latter will be discussed in the following.

7.4.1 Grain Boundary Barriers

Frischbier *et al.* [15] determined grain boundary potential barrier heights of differently doped In_2O_3 films. For $\text{Sn:In}_2\text{O}_3$ the barrier is found to increase with Sn concentration. Zr and unintentionally doped In_2O_3 show intermediate grain boundary barriers while lowest values are obtained with hydrogen as dopant.

No determinations of the barrier heights are available for $\text{Ge:In}_2\text{O}_3$, $\text{Mo:In}_2\text{O}_3$ or $\text{Ti:In}_2\text{O}_3$ films. A comparison to the other dopants will therefore be used for the assessment. $\text{Ge:In}_2\text{O}_3$ films show slightly higher mobilities as compared to 10 wt% $\text{Sn:In}_2\text{O}_3$ at high carrier concentrations [35]. Slightly lower grain boundary barriers are therefore expected. It has to be noted, that the Ge concentration investigated in latter work does not significantly affect the mobility. Measurements of 2 mol% and 5 mol% $\text{Mo:In}_2\text{O}_3$ thin films match rather well to 0.5 wt% and 2 wt% $\text{Sn:In}_2\text{O}_3$ thin films respectively. Mobilities measured for 5 mol% $\text{Ti:In}_2\text{O}_3$ films agree with 5 mol% $\text{Mo:In}_2\text{O}_3$ thin films while a lower Ti

concentration yields very high values, matching Zr as dopant. Comparable barrier heights to the already calculated ones are therefore expected.

Increasing doping concentration evidently leads to higher grain boundary barriers in the case of Sn:In₂O₃, Mo:In₂O₃ and Ti:In₂O₃. Furthermore, the mobility in all three materials is found to decrease to almost zero when deposited at 600 °C. Ge:In₂O₃ thin films on the opposite site neither show a concentration dependent mobility nor very low mobilities when deposited at high temperatures.

Dopant segregation at the grain boundaries was reported to be a likely reason for the behavior observed in Sn:In₂O₃ [15]. As discussed, enhanced Sn segregation is found under reducing conditions. Reduced SnO₂ surfaces in turn are known to exhibit Sn²⁺ [32]. Latter may therefore also be present at Sn:In₂O₃ grain boundaries forming acceptor states. Those electron traps at the grain boundaries would lead to particularly high barriers [15]. Since Mössbauer spectroscopy only gives evidence for Sn⁴⁺ in Sn:In₂O₃, other oxidation states are therefore questionable [48, 61, 70, 71]. Minor amounts at the surfaces or grain boundaries may, however, not be detected.

Since increasing segregation of Ti is as well observed under reducing conditions for Ti:In₂O₃ thin films, the theory of trap states at the grain boundaries could be applied as well. In contrast to the findings on SnO₂, no Ti²⁺ could be found under reducing conditions even for TiO₂ [184]. Therefore it is questionable as well whether Ti trap states are suitable to explain high grain boundary barriers.

Germanium segregation does not seem to negatively affect the mobility, which is probably related to segregation of Ge⁴⁺ occurring under oxidizing conditions [35]. In contrast to Sn²⁺, no trap states are expected to be formed. Based on the discussion for Sn:In₂O₃ and Ti:In₂O₃ the question about the importance of trap states at the grain boundaries remains. Segregation of molybdenum tends to increase for similar conditions as for Ge:In₂O₃. A correlation between dopant concentration and mobility is nevertheless found. The very low mobility of samples deposited at 600 °C may be related to the formation of MoO₃ as reported in Sec. 5.1.

All of those four dopant elements show significant segregation, even though promoted under different conditions. For both Sn:In₂O₃ and Ti:In₂O₃ reducing conditions could theoretically lead to the formation of dopant acceptor states at the grain boundaries. The existence of the 2+ oxidation state in latter materials is questionable though. No significant influence of the dopant concentration as well as the otherwise observed vanishing mobility in films deposited at 600 °C can be observed for Ge:In₂O₃. Both effects are found for Mo:In₂O₃ thin films, showing similar segregation behavior as Ge:In₂O₃. The reason for the difference in grain boundary barriers is thus not clear.

7.4.2 Mobility Limit

Maximum mobilities measured for Mo:In₂O₃ thin films prepared in this work are much lower as compared to values found in literature [16, 26, 142]. Depending on the deposition method, mobilities of up to 149 cm²V⁻¹s⁻¹ are reported. While the highest mobilities were obtained by spray pyrolysis, 99 cm²V⁻¹s⁻¹ have also been reached by RF

co-sputtering [143]. The improvement of the mobility with lower dopant concentration observed here and regarding that higher mobility values are obtained for even lower concentrations indicate that 2 mol% Mo:In₂O₃ targets still lead to over-doped films. Similar to H, Ti and Zr doped In₂O₃, those high mobilities are found for carrier concentrations around approximately $2 \times 10^{20} \text{ cm}^{-3}$. So far there is no definite explanation for mobilities exceeding expectations for single crystalline material.

For Zr:In₂O₃ a correlation to the high permittivity of ZrO₂ was mentioned to increase the mobility due to its impact on ionized impurity scattering [15, 17, 208]. Looking at titanium and molybdenum oxide, both showing a high permittivity, latter explanation may still hold true [192]. High mobilities in H:In₂O₃ thin films must have another reason.

Bhachu *et al.* [16] investigate high mobilities in Mo:In₂O₃ and suggest the energetic position and hybridization of the Mo donor states as explanation. The Mo4d donor states are found to be localized and positioned above the conduction band minimum [26]. Since they hardly show any hybridization with the states forming the conduction band minimum, latter do not represent electronic defects or scattering centers. For Sn:In₂O₃, in contrast, Sn5s states are reported to be positioned between O2p and In5s states and to show a strong hybridization with the conduction band minimum [26, 99]. This results in a perturbation of the dispersion and an increased effective mass.

Band structures calculated for Ti:In₂O₃ and Zr:In₂O₃ can as well be found in literature [99, 209]. Similar to Mo:In₂O₃, donor states are found to be strongly localized and positioned well above the conduction band minimum in both cases. Since no hybridization between donor and valence band forming states occurs, high mobilities in latter materials can be explained.

Even though a high permittivity of the dopant oxide or absence of hybridization of the dopant states and the states forming the conduction band minimum are able to explain a high mobility in comparison to Sn:In₂O₃, both fail to explain the discrepancy between the single crystal model and measurements on polycrystalline thin films exceeding the latter limits. The fact that mobilities beyond the theoretical limit are measured for hydrogen and a few of the unintentionally doped In₂O₃ films points to another explanation. The question is raised if the latter observations are indeed dopant specific or whether mobilities in In₂O₃ exceeding the single crystal model can be achieved independent on the dopant. The measurements for Ge:In₂O₃, Mo:In₂O₃ and Sn:In₂O₃ thin films presented here do not show this behavior. Since for Mo:In₂O₃ very high mobilities were reported [16, 26] it is suggested that the ideal deposition conditions or methods were not applied in this work.

The previous discussion finally implies short comings considering the model proposed by Preissler *et al.* [17]. The authors fit their theoretical model to Hall-effect and Seebeck measurements of epitaxial In₂O₃ and Sn:In₂O₃ thin films. Since only Sn_{In}[•] is assumed as ionized impurity, it is based on a strictly linear dependence of the carrier concentration on the Sn_{In}[•] concentration. A more realistic correlation between electron concentration, defect concentration or Fermi energy in dependence of [Sn_{In}] is shown in Fig. 7.11 [33]. As discussed in Sec. 2.4.2 the concentration of compensating O_i^{''} can be neglected up to a certain Sn content. Beyond this doping level nevertheless, the carrier concentration starts to deviate from the [Sn_{In}]. It is questionable whether the assumptions made so far are an

adequate representation of the electronic properties in doped In_2O_3 thin films. Revisiting the calculations would be advisable.

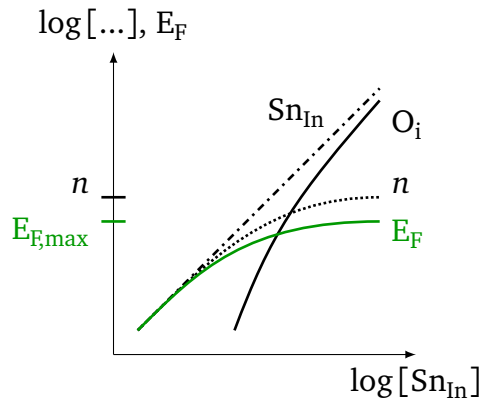


Figure 7.11: Course of the defect concentration, charge carrier concentration or Fermi energy plotted over the $\text{Sn}_{\text{In}}^{\bullet}$ concentration in $\text{Sn}:\text{In}_2\text{O}_3$, based on [33].

As extensively discussed, the mobility depends on the carrier concentration, which in turn can be tuned by adjusting the deposition conditions. It turns out, however, that this method, may not be the best choice when it comes to tracking $\mu(n)$. Besides a variation in carrier concentration the microstructure and dopant segregation are affected, which influence μ as well [15].

Hunka [210] followed a different approach with the goal of electrically tuning the carrier concentration. A sample structure, in imitation of Brichzin *et al.* [211], consisting of a $10 \times 10 \times 0.5 \text{ mm}^3$ yttria stabilized zirconia (YSZ) single crystal and both faces coated with $\text{Sn}:\text{In}_2\text{O}_3$ thin films was chosen. Since YSZ is an oxygen ion conductor, the oxygen concentration in both $\text{Sn}:\text{In}_2\text{O}_3$ electrodes is controllable by a voltage bias. The homemade, high temperature conductivity and Hall-effect setup [38, 39] was modified to accommodate measurements with the described sample structure. The carrier concentration in $\text{Sn}:\text{In}_2\text{O}_3$ could be changed by more than three orders of magnitude and carrier mobility followed the expected behavior by showing a maximum close to $2 \times 10^{20} \text{ cm}^{-3}$. On the cathodic side the film could even be reduced until metallic In was formed. Challenges considering the measurement setup and oxygen exchange with the environment nevertheless did not allow for a final conclusion. Still, latter experiments were successful in terms of giving a proof of concept.

Mobilities measured for H, Ti or Zr doped In_2O_3 thin films significantly exceed the calculations for single crystals. Even though there are explanations suitable for some dopants, it is questionable whether the reason is not simply due to short comings in the theoretical model. Calculations based on more complex assumptions considering the dominant defects and scattering centers are necessary to make final remarks. Different methods to control the carrier concentration should be considered as well.



8 Conclusion And Future Outlook

The goal of this work was to extend the knowledge concerning the optical, electronic and surface properties of doped In_2O_3 thin films and get new insight into fundamental features of this material class. The characteristics were intensively studied for rf magnetron sputtered $\text{Mo}:\text{In}_2\text{O}_3$ and $\text{Ti}:\text{In}_2\text{O}_3$ thin films by means of transmission and reflection spectroscopy, spectroscopic ellipsometry, conductivity and Hall-effect as well as photoelectron spectroscopy measurements. By setting these new results into perspective with previously obtained ones [35, 37–39] existing and new models considering defect chemistry and the effect of different dopants on the physical properties of In_2O_3 were discussed.

$\text{Mo}:\text{In}_2\text{O}_3$ and $\text{Ti}:\text{In}_2\text{O}_3$

The 2 mol% and 5 mol% Mo and Ti doped In_2O_3 thin films studied in this work show a bixbyite structure with a lattice parameter close to undoped In_2O_3 . A variation of the lattice parameter with deposition conditions could be seen but cannot be assigned to a dopant effect or as a result of extrinsic strain induced during sample preparation. The substrate temperature and the oxygen content in the process atmosphere have a similar influence on the physical properties as observed for other dopants. Reducing conditions, i.e. high temperature and pure Ar, lead to a high carrier concentration while increasing oxygen chemical potential leads to a reduction. This fact emphasizes the importance of oxygen related defects in In_2O_3 . A compensation of free charge carriers by interstitial oxygen ions or oxygen defect clusters is expected. The carrier concentration determined by conductivity and Hall-effect measurements scale reasonably well with the ones obtained via simulation of the optical spectra. A good agreement between n_{Hall} and n_{Opt} and poor agreement between μ_{Hall} and μ_{Opt} was found though, which probably is correlated to the optical measurement not extending far enough in the IR. Expectations for Hall mobilities exceeding the single crystal model [17] were fulfilled for $\text{Ti}:\text{In}_2\text{O}_3$ with a maximum value of $105 \text{ cm}^2 (\text{Vs})^{-1}$. For $\text{Mo}:\text{In}_2\text{O}_3$ in contrast, the values measured here remain well in the boundaries of the model and stay behind the mobilities reported in literature [16]. It is suggested that the doping concentration investigated in this work was too high for the ideal performance. Samples of both materials deposited at 600°C showed a very strong reduction of the mobility $< 1 \text{ cm}^2 (\text{Vs})^{-1}$.

Photoelectron spectroscopy revealed Ti to be in a +4 oxidation state in most of the samples. States close to $E_F - E_{\text{VBM}}$ and broadening of the Ti2p emission, attributed to the presence of Ti^{3+} , were observed for films with a high Fermi level. The $\text{Ti}^{4+}/\text{Ti}^{3+}$ charge transfer point may therefore limit the Fermi energy in $\text{Ti}:\text{In}_2\text{O}_3$. For the $\text{Mo}:\text{In}_2\text{O}_3$ samples up to three Mo core level emissions can be distinguished, the intensity changing with deposition conditions. The high binding energy component is doubtlessly attributed to Mo^{6+} , while it is not certain whether the other two are correlated to Mo^{5+} and Mo^{4+} or to Mo^{4+} and a screened component. An emission close to $E_F - E_{\text{VBM}}$ was observed as well, scaling with the intensity of the two components of lower binding energy. It can be explained by occupied Mo4d states which means a lower oxidation state than 6+. A variation in dopant concentration at the surface with deposition conditions was observed

for both elements. Enhanced dopant surface segregation is found for Ti:In₂O₃ as well as for Sn:In₂O₃ when deposited in reducing conditions while oxidizing conditions lead to a similar effect in the case of Mo:In₂O₃ and Ge:In₂O₃. For the first two materials, a higher Fermi energy results in stronger dopant segregation while this is not the case for Ge and Mo. The surface potentials measured for Ti:In₂O₃ fit well in the range as reported for Sn:In₂O₃. Exceptionally high ionization potentials were found for some of the Mo:In₂O₃ films with up to 9.1 eV. Those high values are correlated with strong surface segregation and therefore very likely to the formation of a MoO₃ oxide layer.

Simulation of Optical Spectra

In an attempt to go beyond a qualitative analysis of optical measurements, simulations of the spectra based on a model for the dielectric susceptibility were carried out. Transmission, reflection and spectroscopic ellipsometry spectra were measured and simultaneously fitted. P and s polarized light and incident angles of 60° were employed for best sensitivity. Independent on the dopant element, measurements and simulations agree reasonably well. Amongst others, the applied model allows to extract the film thickness, optical band gap, carrier concentration and carrier mobility. The optically determined film thickness was close to the one obtained by profilometry and even showed a better consistency with the deposition parameters. The initial assumptions to model the optical band gap of In₂O₃ are known to be physically not accurate for doped In₂O₃. The extracted values are considerably underestimated. It nevertheless leads to a good fit and reproduces the variation in the optical band gap with the carrier concentration very well. The optical carrier concentration and mobility are either connected to the plasma frequency or the damping term when the extended Drude model is applied. In an attempt to assure the extraction of meaningful Drude parameters, samples were preselected to show the free carrier absorption well below 2500 nm, i.e. in the accessible measurement range. A non-linear correlation between n_{Hall} and n_{opt} can be removed by assuming the electron effective mass to be a function of the Hall carrier concentration [148]. Hall mobilities poorly agree with the ones from the extended Drude model. Independent on the dopant element μ_{opt} was found to be rather constant over a wide range of μ_{Hall} . This may be reasonable for the region of $\mu_{opt} > \mu_{Hall}$ but not over the whole range as seen here. One possible explanation is that, based on the accessible measurement range in combination with the sample properties, the damping coefficient required for μ_{opt} cannot be reliably determined. Nevertheless wrong starting conditions or physically unreasonable parameter ranges cannot be excluded.

The simulation of optical spectra is a tool offering a high potential to access a variety of parameters based on uncomplicated measurements. It still proved to be rather challenging and the question whether the optical model or measurement range are appropriate to analyze the thin films prepared here remains open. It would be advisable to include optical measurements extending further into the IR. Spectroscopic ellipsometry over a wavelength range from 1.7 μm to 30 μm resulted in an improved agreement at least for H:In₂O₃ which are not included in this study [14, 149].

Dopant Segregation

By setting the results for Mo:In₂O₃ and Ti:In₂O₃ thin films in relation with other dopant elements, segregation once more turns out to be decisive for several physical properties of doped In₂O₃. Surface dipole, carrier concentration and mobility seem to be strongly affected. For almost all of the dopant elements, an increasing surface concentration under certain conditions is observed. Only exception is Zr:In₂O₃ which, however, can be explained by a combination of low concentration and low ASF making segregation hard to observe. It is plausible that dopant segregation at the surface eventually leads to the formation of a dopant oxide layer, which will strongly affect the surface dipole. Regarding grain boundaries as surfaces illustrates the effect on the carrier mobility by altering the grain boundary barrier height. Since segregation reduces the effective dopant concentration in the material a correlation to the carrier concentration is evident, too.

The connection between Fermi energy and segregation, which has been reported for Sn:In₂O₃, was explained by defect chemistry, i.e. the Fermi level dependence of defect formation energies. A similar argumentation can be applied to Ti:In₂O₃ since segregation occurs under reducing conditions as well. Such considerations are, however, not applicable to Ge:In₂O₃ and Mo:In₂O₃ thin films. Increasing dopant surface concentration was found for oxidizing conditions in those cases. The formation energy of the dopant oxide and the defect formation volume were discussed as driving force for segregation. It was suspected that the exclusion of the dopant from the In₂O₃ lattice is energetically favorable when either the dopant oxide has a high absolute free energy or the dopant defects a high defect formation volume. By comparing these parameters to the segregation behavior of all dopant elements, the hypothesis could not be confirmed though. Another model is based on whether the thin films reach an equilibrium in concentration of the dopant after deposition. In Sn:In₂O₃ thin films, segregation can be reversibly altered by changing from oxidizing to reducing annealing conditions [39]. Therefore they seem to be in thermodynamic equilibrium and the dopant concentration follows the Fermi energy as predicted based on defect chemistry. This in turn suggests that as deposited Ge:In₂O₃ and Mo:In₂O₃ films do not reach the dopant concentration, which is thermodynamically stable. The defect formation volume is suspected to influence this behavior by retarding dopant diffusion due to the accompanying lattice distortion. The ionic radius of both Ge and Mo are smaller compared to that of In, the incorporation of oxygen into the lattice may therefore counteract this effect and thereby enable segregation. Since the ionic radius of Ti is in between the one of Mo and Ge but nevertheless shows a behavior similar to Sn latter theory cannot be confirmed however.

The question why enhanced dopant segregation may be observed for either oxidizing or reducing conditions still can not be answered. Thermodynamic and defect equilibrium concentration nevertheless seem to remain a key. Extensive relaxation measurements, as carried out for In₂O₃ and Sn:In₂O₃ [39], are advisable to further investigate this behavior.

Limits in Carrier Concentration and Mobility

As previously reported, similar dopant concentrations of different elements do result in varying charge carrier concentrations and mobilities. The question of a dopant specific limit and possible reasons are still not answered. One objective therefore was to gain more insight into the basic causes.

In an attempt to explain the deviation between the nominal dopant concentration and resulting charge carrier concentration, following effects were discussed as carrier reducing mechanisms: self compensation, charge transfer of the dopant element, valence transfer of In and dopant segregation. Based on calculations for the formation energy of intrinsic acceptor defects such as oxygen interstitials and indium vacancies, self compensation is not expected to be limiting. To estimate valence change and charge transfer points, standard reduction potentials or DFT calculations were considered. Except for Zr:In₂O₃, valence change and charge transfer points match rather well with the highest experimentally determined Fermi energies in each material. A limitation due to this mechanisms is therefore likely. A correlation between the charge carrier concentration and dopant segregation evident in the case of Sn:In₂O₃ and Ti:In₂O₃ indicates that dopant segregation also contributes to the limit of n in this material, indicating that dopant segregation must be better understood.

Possible reasons for dopant element specific mobilities were discussed. The role of the dopant oxide having a high permittivity in improving the mobility is not certain but seems to be of minor importance considering that hydrogen doping similarly yield very high mobilities. Hybridization between dopant and conduction band minimum forming states was suggested to be important by affecting the mobility due to perturbation of the electronic states. Based on this, high mobilities are expected for Mo, Ti and Zr and exclude Sn as high mobility dopant. Experiments carried out here nevertheless show a strong influence on nominal dopant concentration and segregation promoting deposition conditions. Dopant element and concentration dependent grain boundary barriers could be shown to significantly affect the carrier mobilities [15]. It is plausible to explain increased grain boundary barrier heights under reducing conditions due to segregated acceptor species such as Sn²⁺, O_i'', V_{In}''' or Sn_{In}[•]. Oxidizing conditions may lead to a dopant oxide layer enhancing grain boundary barrier heights. Neither of the latter theories, however, can doubtlessly be confirmed.

Carrier mobilities of doped In₂O₃ predicted by a model for single crystals being exceeded by Hall effect measurement is still under discussion. A deviation due to screening of optical phonons being underestimated was suggested by Preissler *et al.* [17]. In this work, it was proposed that the inclusion of O_i'' as additional scattering center may lead to a different understanding. Consequently high mobility should be possible with all dopants, if segregation can be suppressed.

A prove could be given by showing that Sn:In₂O₃ thin films can exceed the modeled mobilities as well. Deposition conditions for Sn:In₂O₃ thin films, yielding carrier concentration in the range of interest, already allow for evident dopant segregation. One approach might be co-sputtering with a metallic Sn target. Motivation for latter is to achieve

sufficiently reducing deposition conditions without going to substrate temperatures, which allow for significant Sn diffusion and therefore segregation at grain boundaries.



References

- [1] H. Hosono, J. Kim, Y. Toda, T. Kamiya, and S. Watanabe, "Transparent amorphous oxide semiconductors for organic electronics: Application to inverted OLEDs," *Proceedings of the National Academy of Sciences*, vol. 114, no. 2, pp. 233–238, 2017.
- [2] T. Minami, "New n-type transparent conducting oxides," *Mrs Bulletin*, vol. 25, no. 8, pp. 38–44, 2000.
- [3] S. Lany and A. Zunger, "Dopability, intrinsic conductivity, and nonstoichiometry of transparent conducting oxides," *Phys Rev Lett*, vol. 98, no. 4, p. 045501, 2007.
- [4] K. Ellmer and R. Mientus, "Carrier transport in polycrystalline transparent conductive oxides: A comparative study of zinc oxide and indium oxide," *Thin Solid Films*, vol. 516, no. 14, pp. 4620–4627, 2008.
- [5] T. Koida and M. Kondo, "Comparative studies of transparent conductive Ti-, Zr-, and Sn-doped In_2O_3 using a combinatorial approach," *Journal of Applied Physics*, vol. 101, no. 6, 2007.
- [6] P. Erhart, A. Klein, R. G. Egdell, and K. Albe, "Band structure of indium oxide: Indirect versus direct band gap," *Physical Review B*, vol. 75, no. 15, 2007.
- [7] P. Ágoston and K. Albe, "Thermodynamic stability, stoichiometry, and electronic structure of bcc- In_2O_3 surfaces," *Physical Review B*, vol. 84, no. 4, p. 045311, 2011.
- [8] D. S. Ginley and C. Bright, "Transparent Conducting Oxides," *MRS Bulletin*, vol. 25 [8], no. 8, pp. 15–18, 2000.
- [9] R. Groth, "Untersuchungen an halbleitenden Indiumoxydschichten," *physica status solidi (b)*, vol. 14, no. 1, pp. 69–75, 1966.
- [10] Y. Yoshida, T. A. Gessert, C. L. Perkins, and T. J. Coutts, "Development of radio-frequency magnetron sputtered indium molybdenum oxide," *Journal of Vacuum Science & Technology A: Vacuum, Surfaces, and Films*, vol. 21, no. 4, pp. 1092–1097, 2003.
- [11] Y. Abe and N. Ishiyama, "Titanium-doped indium oxide films prepared by d.c. magnetron sputtering using ceramic target," *Journal of Materials Science*, vol. 41, no. 22, pp. 7580–7584, 2006.
- [12] N. Koch, "Organic electronic devices and their functional interfaces," *Chemphyschem*, vol. 8, no. 10, pp. 1438–55, 2007.
- [13] K. Ellmer and R. Mientus, "Carrier transport in polycrystalline ITO and $\text{ZnO}:\text{Al}$ II: The influence of grain barriers and boundaries," *Thin Solid Films*, vol. 516, no. 17, pp. 5829–5835, 2008.
- [14] T. Koida, Y. Ueno, and H. Shibata, " In_2O_3 -Based Transparent Conducting Oxide Films with High Electron Mobility Fabricated at Low Process Temperatures," *Physica Status Solidi a-Applications and Materials Science*, vol. 215, no. 7, 2018.

-
- [15] M. V. Frischbier, H. F. Wardenga, M. Weidner, O. Bierwagen, J. Jia, Y. Shigesato, and A. Klein, "Influence of dopant species and concentration on grain boundary scattering in degenerately doped In_2O_3 thin films," *Thin Solid Films*, vol. 614, pp. 62–68, 2016.
- [16] D. S. Bhachu, D. O. Scanlon, G. Sankar, T. D. Veal, R. G. Egdell, G. Cibin, A. J. Dent, C. E. Knapp, C. J. Carmalt, and I. P. Parkin, "Origin of High Mobility in Molybdenum-Doped Indium Oxide," *Chemistry of Materials*, vol. 27, no. 8, pp. 2788–2796, 2015.
- [17] N. Preissler, O. Bierwagen, A. T. Ramu, and J. S. Speck, "Electrical transport, electrothermal transport, and effective electron mass in single-crystalline In_2O_3 films," *Physical Review B*, vol. 88, no. 8, 2013.
- [18] "<https://www.nrel.gov/grid/solar-resource/spectra-am1.5.html>."
- [19] S. Lany and A. Zunger, "Assessment of correction methods for the band-gap problem and for finite-size effects in supercell defect calculations: Case studies for ZnO and GaAs," *Physical Review B*, vol. 78, no. 23, 2008.
- [20] G. B. Gonzalez, T. O. Mason, J. P. Quintana, O. Warschkow, D. E. Ellis, J. H. Hwang, J. P. Hodges, and J. D. Jorgensen, "Defect structure studies of bulk and nano-indium-tin oxide," *Journal of Applied Physics*, vol. 96, no. 7, pp. 3912–3920, 2004.
- [21] G. Frank and H. Köstlin, "Electrical-Properties and Defect Model of Tin-Doped Indium Oxide Layers," *Applied Physics a-Materials Science & Processing*, vol. 27, no. 4, pp. 197–206, 1982.
- [22] P. Ágoston, P. Erhart, A. Klein, and K. Albe, "Geometry, electronic structure and thermodynamic stability of intrinsic point defects in indium oxide," *J. Phys. Condens Matter*, vol. 21, no. 45, p. 455801, 2009.
- [23] J. de Wit, "Structural aspects and defect chemistry in In_2O_3 ," *Journal of Solid State Chemistry*, vol. 20, p. 143, 1977.
- [24] A. Zunger, "Practical doping principles," *Applied Physics Letters*, vol. 83, no. 1, pp. 57–59, 2003.
- [25] K. Ellmer, A. Klein, and B. Rech, *Transparent Conductive Zinc Oxide Basics and Applications in Thin Film Solar Cells*. Springer Series in Materials Science, Berlin, Heidelberg: Springer Berlin Heidelberg, 2008.
- [26] J. E. N. Swallow, B. A. D. Williamson, S. Sathasivam, M. Birkett, T. J. Featherstone, P. A. E. Murgatroyd, H. J. Edwards, Z. W. Lebens-Higgins, D. A. Duncan, M. Farnworth, P. Warren, N. Peng, T.-L. Lee, L. F. J. Piper, A. Regoutz, C. J. Carmalt, I. P. Parkin, V. R. Dhanak, D. O. Scanlon, and T. D. Veal, "Resonant doping for high mobility transparent conductors: the case of Mo-doped In_2O_3 ," *Materials Horizons*, 2019.
- [27] A. Hubmann, D. Dietz, J. Brötz, and A. Klein, "Interface Behaviour and Work Function Modification of Self-Assembled Monolayers on Sn-Doped In_2O_3 ," *Surfaces*, vol. 2, no. 2, pp. 241–256, 2019.

-
- [28] S. P. Harvey, T. O. Mason, C. Körber, Y. Gassenbauer, and A. Klein, "Evidence for surface dipole modifications in In_2O_3 -based transparent conductors," *Applied Physics Letters*, vol. 92, no. 25, p. 252106, 2008.
- [29] M. V. Hohmann, P. Agoston, A. Wachau, T. J. M. Bayer, J. Brotz, K. Albe, and A. Klein, "Orientation dependent ionization potential of In_2O_3 : a natural source for inhomogeneous barrier formation at electrode interfaces in organic electronics," *Journal of Physics-Condensed Matter*, vol. 23, no. 33, 2011.
- [30] T. Kugler, W. R. Salaneck, H. Rost, and A. B. Holmes, "Polymer band alignment at the interface with indium tin oxide: consequences for light emitting devices," *Chemical Physics Letters*, vol. 310, no. 5-6, pp. 391–396, 1999.
- [31] H. Ishii, K. Sugiyama, E. Ito, and K. Seki, "Energy Level Alignment and Interfacial Electronic Structures at Organic/Metal and Organic/Organic Interfaces," *Advanced Materials*, vol. 11, no. 8, pp. 605–625, 1999.
- [32] A. Klein, C. Körber, A. Wachau, F. Säuberlich, Y. Gassenbauer, R. Schafranek, S. P. Harvey, and T. O. Mason, "Surface potentials of magnetron sputtered transparent conducting oxides," *Thin Solid Films*, vol. 518, no. 4, pp. 1197–1203, 2009.
- [33] A. Klein, "Transparent Conducting Oxides: Electronic Structure-Property Relationship from Photoelectron Spectroscopy with in situ Sample Preparation," *Journal of the American Ceramic Society*, vol. 96, no. 2, p. 331–345, 2012.
- [34] P. W. Tasker, "Stability of Ionic Crystal Surfaces," *Journal of Physics C-Solid State Physics*, vol. 12, no. 22, pp. 4977–4984, 1979.
- [35] K. L. Hoyer, A. H. Hubmann, and A. Klein, "Influence of dopant segregation on the work function and electrical properties of Ge-doped in comparison to Sn-doped In_2O_3 thin films," *physica status solidi (a)*, 2016.
- [36] P. Ágoston, C. Körber, A. Klein, M. J. Puska, R. M. Nieminen, and K. Albe, "Limits for n-type doping in In_2O_3 and SnO_2 : A theoretical approach by first-principles calculations using hybrid-functional methodology," *Journal of Applied Physics*, vol. 108, no. 5, p. 053511, 2010.
- [37] Y. Gassenbauer, *Untersuchung der elektronischen und chemischen Oberflächeneigenschaften von Zinn-dotiertem Indiumoxid im Hinblick auf die Funktion in organischen Leuchtdioden*. Ph.d. thesis, Technische Universität Darmstadt, 2007.
- [38] A. Wachau, *Sauerstoffaustausch polykristalliner kathodenzerstäubter Indiumoxid-Dünnschichten*. Ph.d. thesis, Technische Universität Darmstadt, 2014.
- [39] M. Frischbier, *Die elektrischen Eigenschaften von Indiumoxid-Dünnschichten: in-situ Hall-Effekt-Messungen zur Aufklärung des Einflusses von Punktdefekten und Korngrenzen*. Thesis, Technische Universität Darmstadt, 2015.
- [40] G. K. Deyu, *Defect modulation doping for transparent conducting oxide materials*. Thesis, Technische Universität Darmstadt, 2020.

-
- [41] Y. Gassenbauer, R. Schafraneck, A. Klein, S. Zafeiratos, M. Hävecker, A. Knop-Gericke, and R. Schlögl, "Surface states, surface potentials, and segregation at surfaces of tin-doped In_2O_3 ," *Physical Review B*, vol. 73, no. 24, 2006.
- [42] F. Fuchs and F. Bechstedt, "Indium-oxide polymorphs from first principles: Quasi-particle electronic states," *Physical Review B*, vol. 77, no. 15, 2008.
- [43] I. Hamberg and C. G. Granqvist, "Evaporated Sn-doped In_2O_3 films: Basic optical properties and applications to energy-efficient windows," *Journal of Applied Physics*, vol. 60, no. 11, pp. R123–R160, 1986.
- [44] M. Marezio, "Refinement of the crystal structure of In_2O_3 at two wavelengths," *Acta Crystallographica*, vol. 20, no. 6, pp. 723–728, 1966.
- [45] F. P. Sabino, R. Besse, L. N. Oliveira, S.-H. Wei, and J. L. F. Da Silva, "Origin of and tuning the optical and fundamental band gaps in transparent conducting oxides: The case of M_2O_3 ($\text{M}=\text{Al}, \text{Ga}, \text{In}$)," *Physical Review B*, vol. 92, no. 20, 2015.
- [46] A. Walsh, J. L. F. Da Silva, S. H. Wei, C. Körber, A. Klein, L. F. J. Piper, A. DeMasi, K. E. Smith, G. Panaccione, P. Torelli, D. J. Payne, A. Bourlange, and R. G. Egdell, "Nature of the band gap of In_2O_3 revealed by first-principles calculations and x-ray spectroscopy," *Physical Review Letters*, vol. 100, no. 16, 2008.
- [47] R. L. Weiher and R. P. Ley, "Optical Properties of Indium Oxide," *Journal of Applied Physics*, vol. 37, no. 1, pp. 299–302, 1966.
- [48] H. Köstlin, R. Jost, and W. Lems, "Optical and Electrical Properties of Doped In_2O_3 Films," *Physica Status Solidi a-Applied Research*, vol. 29, no. 1, pp. 87–93, 1975.
- [49] K. Irmscher, M. Naumann, M. Pietsch, Z. Galazka, R. Uecker, T. Schulz, R. Schewski, M. Albrecht, and R. Fornari, "On the nature and temperature dependence of the fundamental band gap of In_2O_3 ," *physica status solidi (a)*, vol. 211, no. 1, pp. 54–58, 2014.
- [50] F. P. Sabino, L. N. Oliveira, S. H. Wei, and J. L. F. Da Silva, "Optical and fundamental band gaps disparity in transparent conducting oxides: new findings for the In_2O_3 and SnO_2 systems," *Journal of Physics-Condensed Matter*, vol. 29, no. 8, 2017.
- [51] P. D. C. King, T. D. Veal, F. Fuchs, C. Y. Wang, D. J. Payne, A. Bourlange, H. Zhang, G. R. Bell, V. Cimalla, O. Ambacher, R. G. Egdell, F. Bechstedt, and C. F. McConville, "Band gap, electronic structure, and surface electron accumulation of cubic and rhombohedral In_2O_3 ," *Physical Review B*, vol. 79, no. 20, 2009.
- [52] C. Körber, V. Krishnakumar, A. Klein, G. Panaccione, P. Torelli, A. Walsh, J. L. F. Da Silva, S. H. Wei, R. G. Egdell, and D. J. Payne, "Electronic structure of In_2O_3 and Sn-doped In_2O_3 by hard x-ray photoemission spectroscopy," *Physical Review B*, vol. 81, no. 16, 2010.
- [53] L. F. J. Piper, A. DeMasi, S. W. Cho, K. E. Smith, F. Fuchs, F. Bechstedt, C. Körber, A. Klein, D. J. Payne, and R. G. Egdell, "Electronic structure of In_2O_3 from resonant x-ray emission spectroscopy," *Applied Physics Letters*, vol. 94, no. 2, 2009.

-
- [54] A. J. Morris and B. Monserrat, "Optical absorption driven by dynamical symmetry breaking in indium oxide," *Physical Review B*, vol. 98, no. 16, 2018.
- [55] A. Walsh and C. R. A. Catlow, "Structure, stability and work functions of the low index surfaces of pure indium oxide and Sn-doped indium oxide (ITO) from density functional theory," *Journal of Materials Chemistry*, vol. 20, no. 46, p. 10438, 2010.
- [56] J. E. Medvedeva and C. L. Hettiarachchi, "Tuning the properties of complex transparent conducting oxides: Role of crystal symmetry, chemical composition, and carrier generation," *Physical Review B*, vol. 81, no. 12, 2010.
- [57] G. Rupprecht, "Untersuchungen Der Elektrischen Und Lichtelektrischen Leitfähigkeit Dunner Indiumoxydschichten," *Zeitschrift Fur Physik*, vol. 139, no. 5, pp. 504–517, 1954.
- [58] R. L. Weiher, "Electrical Properties of Single Crystals of Indium Oxide," *Journal of Applied Physics*, vol. 33, no. 9, pp. 2834–2839, 1962.
- [59] J. H. W. De Wit, G. Van Unen, and M. Lahey, "Electron concentration and mobility in In_2O_3 ," *Journal of Physics and Chemistry of Solids*, vol. 38, no. 8, pp. 819–824, 1977.
- [60] J. C. C. Fan, F. J. Bachner, and G. H. Foley, "Effect of O_2 Pressure during Deposition on Properties of Rf-Sputtered Sn-Doped In_2O_3 Films," *Applied Physics Letters*, vol. 31, no. 11, pp. 773–775, 1977.
- [61] N. Nadaud, N. Lequeux, M. Nanot, J. Jove, and T. Roisnel, "Structural studies of tin-doped indium oxide (ITO) and $\text{In}_4\text{Sn}_3\text{O}_{12}$," *Journal of Solid State Chemistry*, vol. 135, no. 1, pp. 140–148, 1998.
- [62] Y. Meng, X.-l. Yang, H.-x. Chen, J. Shen, Y.-m. Jiang, Z.-j. Zhang, and Z.-y. Hua, "Molybdenum-doped indium oxide transparent conductive thin films," *Journal of Vacuum Science and Technology A: Vacuum, Surfaces, and Films*, vol. 20, no. 1, pp. 288–290, 2002.
- [63] Y.-H. Shin, H.-K. Kim, and S.-I. Na, "Effect of MoO_3 doping power on the electrical, optical, and structural properties of MoO_3 -doped In_2O_3 anodes for organic solar cells," *Journal of Vacuum Science & Technology A: Vacuum, Surfaces, and Films*, vol. 30, no. 6, p. 061507, 2012.
- [64] S.-Y. Sun, J.-L. Huang, and D.-F. Lii, "Properties of Indium Molybdenum Oxide Films Fabricated Via High-Density Plasma Evaporation at Room Temperature," *Journal of Materials Research*, vol. 20, no. 01, pp. 247–255, 2005.
- [65] M. F. A. M. van Hest, M. S. Dabney, J. D. Perkins, D. S. Ginley, and M. P. Taylor, "Titanium-doped indium oxide: A high-mobility transparent conductor," *Applied Physics Letters*, vol. 87, no. 3, p. 032111, 2005.
- [66] L. Vegard, "Die Konstitution der Mischkristalle und die Raumfüllung der Atome," *Zeitschrift für Physik*, vol. 5, no. 1, pp. 17–26, 1921.

-
- [67] J. H. Hwang, D. D. Edwards, D. R. Kammler, and T. O. Mason, "Point defects and electrical properties of Sn-doped In-based transparent conducting oxides," *Solid State Ionics*, vol. 129, no. 1-4, pp. 135–144, 2000.
- [68] R. D. Shannon, "Revised Effective Ionic-Radii and Systematic Studies of Interatomic Distances in Halides and Chalcogenides," *Acta Crystallographica Section A*, vol. 32, no. Sep1, pp. 751–767, 1976.
- [69] G. Frank, H. Köstlin, and A. Rabenau, "X-Ray and Optical Measurements in the In_2O_3 - SnO_2 System," *Physica Status Solidi a-Applied Research*, vol. 52, no. 1, pp. 231–238, 1979.
- [70] N. Yamada, I. Yasui, Y. Shigesato, H. Li, Y. Ujihira, and K. Nomura, "Doping Mechanisms of Sn in In_2O_3 Powder Studied Using ^{119}Sn Mössbauer Spectroscopy and X-Ray Diffraction," *Japanese Journal of Applied Physics*, vol. 38, no. Part 1, No. 5A, pp. 2856–2862, 1999.
- [71] Y. Shigesato, S. Takaki, and T. Haranou, "Crystallinity and electrical properties of tin-doped indium oxide films deposited by DC magnetron sputtering," *Applied Surface Science*, vol. 48-49, pp. 269–275, 1991.
- [72] H. Ibach, H.; Lüth, *Festkörperphysik*. Springer, Berlin, Heidelberg, 2009.
- [73] H. K. Müller, "Electrical and Optical Properties of Sputtered In_2O_3 Films. I. Electrical Properties and Intrinsic Absorption," *Physica Status Solidi*, vol. 27, no. 2, p. 723, 1968.
- [74] H. K. Müller, "Electrical and Optical Properties of Sputtered In_2O_3 Films. II. Optical Properties in near Infrared," *Physica Status Solidi*, vol. 27, no. 2, p. 733, 1968.
- [75] R. Clanget, "Ionized impurity scattering in degenerate In_2O_3 ," *Applied physics*, vol. 2, no. 5, pp. 247–256, 1973.
- [76] J. R. Bellingham, W. A. Phillips, and C. J. Adkins, "Intrinsic Performance Limits in Transparent Conducting Oxides," *Journal of Materials Science Letters*, vol. 11, no. 5, pp. 263–265, 1992.
- [77] K. Ellmer, "Resistivity of polycrystalline zinc oxide films: current status and physical limit," *Journal of Physics D*, vol. 34, no. 21, pp. 3097–3108, 2001.
- [78] J. Y. W. Seto, "Electrical Properties of Polycrystalline Silicon Films," *Journal of Applied Physics*, vol. 46, no. 12, pp. 5247–5254, 1975.
- [79] M. Weidner, *Fermi Level Determination in Tin Oxide by Photoelectron Spectroscopy*. Thesis, Technische Universität Darmstadt, 2015.
- [80] O. Stenzel and M. Ohlídal, *Optical Characterization of Thin Solid Films*. Springer Series in Surface Sciences, Springer-Verlag GmbH, 2018.
- [81] R. J. Mendelsberg, G. Garcia, and D. J. Milliron, "Extracting reliable electronic properties from transmission spectra of indium tin oxide thin films and nanocrystal films by careful application of the Drude theory," *Journal of Applied Physics*, vol. 111, no. 6, p. 063515, 2012.

-
- [82] R. A. Synowicki, "Spectroscopic ellipsometry characterization of indium tin oxide film microstructure and optical constants," *Thin Solid Films*, vol. 313, pp. 394–397, 1998.
- [83] G. L. Tan, M. F. Lemon, and R. H. French, "Optical properties and London dispersion forces of amorphous silica determined by vacuum ultraviolet spectroscopy and spectroscopic ellipsometry," *Journal of the American Ceramic Society*, vol. 86, no. 11, pp. 1885–1892, 2003.
- [84] R. A. Synowicki, B. D. Johs, and A. C. Martin, "Optical properties of soda-lime float glass from spectroscopic ellipsometry," *Thin Solid Films*, vol. 519, no. 9, pp. 2907–2913, 2011.
- [85] W. G. Driscoll and W. Vaughan, *Handbook of Optics*. New York: McGraw-Hill, 1978.
- [86] H. G. Tompkins and E. A. Irene, *Handbook of Ellipsometry*. Norwich, NY: William Andrew Publishing, 2005.
- [87] O. Stenzel, *Das Dünnschichtspektrum ein Zugang von den Grundlagen zur Spezialliteratur*. Berlin, Germany: Akademie Verlag, 1996.
- [88] A. Röseler, *Infrared Spectroscopic Ellipsometry*. Akademie-Verlag Berlin, 1990.
- [89] D. Mergel and Z. Qiao, "Dielectric modelling of optical spectra of thin $\text{In}_2\text{O}_3:\text{Sn}$ films," *Journal of Physics D-Applied Physics*, vol. 35, no. 8, pp. 794–801, 2002.
- [90] D. G. Avery, "An Improved Method for Measurements of Optical Constants by Reflection," *Proceedings of the Physical Society of London Section B*, vol. 65, no. 390, pp. 425–428, 1952.
- [91] S. P. F. Humphreys-Owen, "Comparison of Reflection Methods for Measuring Optical Constants without Polarimetric Analysis, and Proposal for New Methods based on the Brewster Angle," *Proceedings of the Physical Society*, vol. 77, no. 5, p. 949, 1961.
- [92] S. G. Tomlin, "Optical reflection and transmission formulae for thin films," *Journal of Physics D: Applied Physics*, vol. 1, no. 12, p. 1667, 1968.
- [93] R. F. Miller, A. J. Taylor, and L. S. Julien, "The optimum angle of incidence for determining optical constants from reflectance measurements," *Journal of Physics D: Applied Physics*, vol. 3, no. 12, p. 1957, 1970.
- [94] R. F. Miller and A. J. Taylor, "Optical Constants of Thin Films by an Optimized Reflection Ratio Method," *Journal of Physics D-Applied Physics*, vol. 4, no. 9, p. 1419, 1971.
- [95] S. K. O'Leary, S. R. Johnson, and P. K. Lim, "The relationship between the distribution of electronic states and the optical absorption spectrum of an amorphous semiconductor: An empirical analysis," *Journal of Applied Physics*, vol. 82, no. 7, pp. 3334–3340, 1997.
- [96] A. Solieman and M. A. Aegerter, "Modeling of optical and electrical properties of $\text{In}_2\text{O}_3:\text{Sn}$ coatings made by various techniques," *Thin Solid Films*, vol. 502, no. 1-2, pp. 205–211, 2006.

-
- [97] C. C. Kim, J. W. Garland, H. Abad, and P. M. Raccach, "Modeling the Optical Dielectric Function of Semiconductors - Extension of the Critical-Point Parabolic-Band Approximation," *Physical Review B*, vol. 45, no. 20, pp. 11749–11767, 1992.
- [98] W. Steinman, "Optical Plasma Resonances in Solids," *Physica Status Solidi*, vol. 28, no. 2, p. 437, 1968.
- [99] H. Fang, M. Hegde, P. Yin, and P. V. Radovanovic, "Tuning Plasmon Resonance of In₂O₃ Nanocrystals throughout the Mid-Infrared Region by Competition between Electron Activation and Trapping," *Chemistry of Materials*, vol. 29, no. 11, pp. 4970–4979, 2017.
- [100] J. Tauc, R. Grigorovici, and A. Vancu, "Optical Properties and Electronic Structure of Amorphous Germanium," *Physica Status Solidi*, vol. 15, no. 2, pp. 627–637, 1966.
- [101] A. Bhardwaj, B. K. Gupta, A. Raza, A. K. Sharma, and O. P. Agnihotri, "Fluorine-Doped SnO₂ Films for Solar-Cell Application," *Solar Cells*, vol. 5, no. 1, pp. 39–49, 1981.
- [102] F. Demichelis, G. Kaniadakis, A. Tagliaferro, and E. Tresso, "New Approach to Optical Analysis of Absorbing Thin Solid Films," *Applied Optics*, vol. 26, no. 9, pp. 1737–1740, 1987.
- [103] A. Dolgonos, T. O. Mason, and K. R. Poeppelmeier, "Direct optical band gap measurement in polycrystalline semiconductors: A critical look at the Tauc method," *Journal of Solid State Chemistry*, vol. 240, pp. 43–48, 2016.
- [104] J. I. Pankove, *Optical Processes in Semiconductors*. New York: Dover, 1975.
- [105] H. Kim, C. M. Gilmore, A. Pique, J. S. Horwitz, H. Mattoussi, H. Murata, Z. H. Kafafi, and D. B. Chrisey, "Electrical, optical, and structural properties of indium-tin-oxide thin films for organic light-emitting devices," *Journal of Applied Physics*, vol. 86, no. 11, pp. 6451–6461, 1999.
- [106] F. Ruske, M. Wimmer, G. Köppel, A. Pflug, and B. Rech, "Optical characterization of high mobility polycrystalline zno:al films," in *SPIE OPTO*, vol. 8263, p. 13, SPIE, 2012.
- [107] O. S. Heavens, *Optical properties of thin solid films*. London: Butterworths Scientific Publications, 1955.
- [108] R. E. Denton, R. D. Campbell, and S. G. Tomlin, "The determination of the optical constants of thin films from measurements of reflectance and transmittance at normal incidence," *Journal of Physics D: Applied Physics*, vol. 5, no. 4, p. 852, 1972.
- [109] Q. H. Wu, "Extraction of Extinction Coefficient of Weak Absorbing Thin-Films from Special Absorption," *Journal of Physics D-Applied Physics*, vol. 22, no. 9, pp. 1384–1385, 1989.
- [110] M. Thirumoorthi and J. Thomas Joseph Prakash, "Structure, optical and electrical properties of indium tin oxide ultra thin films prepared by jet nebulizer spray pyrolysis technique," *Journal of Asian Ceramic Societies*, vol. 4, no. 1, pp. 124–132, 2016.

-
- [111] R. Kitamura, L. Pilon, and M. Jonasz, "Optical constants of silica glass from extreme ultraviolet to far infrared at near room temperature," *Applied Optics*, vol. 46, no. 33, pp. 8118–8133, 2007.
- [112] E. Burstein, "Anomalous Optical Absorption Limit in InSb," *Physical Review*, vol. 93, no. 3, pp. 632–633, 1954.
- [113] T. S. Moss, "The Interpretation of the Properties of Indium Antimonide," *Proceedings of the Physical Society of London Section B*, vol. 67, no. 418, pp. 775–782, 1954.
- [114] L. Gupta, A. Mansingh, and P. K. Srivastava, "Band-Gap Narrowing and the Band-Structure of Tin-Doped Indium Oxide-Films," *Thin Solid Films*, vol. 176, no. 1, pp. 33–44, 1989.
- [115] L. J. Meng and M. P. dos Santos, "Properties of indium tin oxide films prepared by rf reactive magnetron sputtering at different substrate temperature," *Thin Solid Films*, vol. 322, no. 1-2, pp. 56–62, 1998.
- [116] S. Hüfner, *Photoelectron Spectroscopy*, vol. 3. Springer-Verlag Berlin Heidelberg, 2003.
- [117] A. Klein, T. Mayer, A. Thissen, and W. Jaegermann, "Photoelectron Spectroscopy in Materials Science and Physical Chemistry: Analysis of Composition, Chemical Bonding and Electronic Structure of Surfaces and Interfaces," *Bunsenmagazin*, vol. 10, pp. 124–139, 2008.
- [118] J. Moulder, W. Stickle, P. Sobol, and K. Bomben, *Handbook of X-ray Photoelectron Spectroscopy*. Eden Prairie: Physical Electronics, Inc., 1995.
- [119] J. J. Yeh and I. Lindau, "Atomic Subshell Photoionization Cross-Sections and Asymmetry Parameters - 1 Less-Than-or-Equal-to Z Less-Than-or-Equal-to 103," *Atomic Data and Nuclear Data Tables*, vol. 32, no. 1, pp. 1–155, 1985.
- [120] D. M. Mattox, *Handbook of Physical Vapor Deposition (PVD) Processing (Second Edition)*. 2010.
- [121] R. Maissel, L. I. Glang, *Handbook of thin film technology*. 1970.
- [122] K. Ellmer, "Magnetron sputtering of transparent conductive zinc oxide: relation between the sputtering parameters and the electronic properties," *Journal of Physics D: Applied Physics*, vol. 33, no. 4, pp. R17–R32, 2000.
- [123] R. A. Synowicki, "Suppression of backside reflections from transparent substrates," *physica status solidi (c)*, vol. 5, no. 5, pp. 1085–1088, 2008.
- [124] M. Lederer, *Untersuchung von Molybdän-dotiertem Indiumoxid*. B.sc. thesis, Technische Universität Darmstadt, 2017.
- [125] G. Andersson and A. Magneli, "On the Crystal Structure of Molybdenum Trioxide," *Acta Chemica Scandinavica*, vol. 4, no. 5, pp. 793–797, 1950.

-
- [126] E. M. McCarron, D. M. Thomas, and J. C. Calabrese, "Hexagonal Molybdates: Crystal-Structure of $(\text{Na}\cdot\text{H}_2\text{O})\text{Mo}_{5.33}[\text{H}_{4.5}]_{0.67}\text{O}_{18}$," *Inorganic Chemistry*, vol. 26, no. 3, pp. 370–373, 1987.
- [127] E. Elangovan, A. Marques, F. M. B. Fernandes, R. Martins, and E. Fortunato, "Preliminary studies on molybdenum-doped indium oxide thin films deposited by radio-frequency magnetron sputtering at room temperature," *Thin Solid Films*, vol. 515, no. 13, pp. 5512–5518, 2007.
- [128] R. K. Gupta, K. Ghosh, S. R. Mishra, and P. K. Kahol, "Structural, optical and electrical characterization of highly conducting Mo-doped In_2O_3 thin films," *Applied Surface Science*, vol. 254, no. 13, pp. 4018–4023, 2007.
- [129] X. F. Li, W. N. Miao, Q. Zhang, L. Huang, Z. J. Zhang, and Z. Y. Hua, "Preparation of molybdenum-doped indium oxide thin films using reactive direct-current magnetron sputtering," *Journal of Materials Research*, vol. 20, no. 6, pp. 1404–1408, 2005.
- [130] C. Warm Singh, Y. Yoshida, D. W. Readey, C. W. Teplin, J. D. Perkins, P. A. Parilla, L. M. Gedvilas, B. M. Keyes, and D. S. Ginley, "High-mobility transparent conducting Mo-doped In_2O_3 thin films by pulsed laser deposition," *Journal of Applied Physics*, vol. 95, no. 7, p. 3831, 2004.
- [131] L. Spieß, *Moderne Röntgenbeugung Röntgendiffraktometrie für Materialwissenschaftler, Physiker und Chemiker*. Wiesbaden: Vieweg + Teubner, 2., überarb. u. erw. Aufl. ed., 2009.
- [132] F. M. D'Heurle and J. M. E. Harper, "Note on the Origin of Intrinsic Stresses in Films Deposited Via Evaporation and Sputtering," *Thin Solid Films*, vol. 171, no. 1, pp. 81–92, 1989.
- [133] M. Birkholz, *Thin film analysis by X-ray scattering*. Weinheim: Wiley-VCH, 2006.
- [134] G. B. Gonzalez, "Investigating the Defect Structures in Transparent Conducting Oxides Using X-ray and Neutron Scattering Techniques," *Materials (Basel)*, vol. 5, no. 5, pp. 818–850, 2012.
- [135] R. Roy, D. K. Agrawal, and H. A. McKinstry, "Very Low Thermal Expansion Coefficient Materials," *Annual Review of Materials Science*, vol. 19, no. 1, pp. 59–81, 1989.
- [136] R. Kleinhempel, G. Kaune, M. Herrmann, H. Kupfer, W. Hoyer, and F. Richter, "Properties of ITO films prepared by reactive magnetron sputtering," *Microchimica Acta*, vol. 156, no. 1-2, pp. 61–67, 2006.
- [137] D. Mergel and Z. Qiao, "Correlation of lattice distortion with optical and electrical properties of $\text{In}_2\text{O}_3:\text{Sn}$ films," *Journal of Applied Physics*, vol. 95, no. 10, pp. 5608–5615, 2004.
- [138] S.-Y. Sun, J.-L. Huang, and D.-F. Lii, "Effects of oxygen contents on the electrical and optical properties of indium molybdenum oxide films fabricated by high density

plasma evaporation,” *Journal of Vacuum Science & Technology A: Vacuum, Surfaces, and Films*, vol. 22, no. 4, pp. 1235–1241, 2004.

- [139] E. Elangovan, G. Gonçalves, R. Martins, and E. Fortunato, “RF sputtered wide work function indium molybdenum oxide thin films for solar cell applications,” *Solar Energy*, vol. 83, no. 5, pp. 726–731, 2009.
- [140] M. F. A. M. van Hest, M. S. Dabney, J. D. Perkins, and D. S. Ginley, “High-mobility molybdenum doped indium oxide,” *Thin Solid Films*, vol. 496, no. 1, pp. 70–74, 2006.
- [141] S. Catalán, L. Álvarez-Fraga, E. Salas, R. Ramírez-Jiménez, A. Rodríguez-Palomo, A. de Andrés, and C. Prieto, “Charge mobility increase in indium-molybdenum oxide thin films by hydrogen doping,” *Applied Surface Science*, vol. 386, pp. 427–433, 2016.
- [142] N. Yamada, M. Yamada, H. Toyama, R. Ino, X. Cao, Y. Yamaguchi, and Y. Ni-nomiya, “High-throughput optimization of near-infrared-transparent Mo-doped In_2O_3 thin films with high conductivity by combined use of atmospheric-pressure mist chemical-vapor deposition and sputtering,” *Thin Solid Films*, vol. 626, pp. 46–54, 2017.
- [143] N. Yamada, T. Tatejima, H. Ishizaki, and T. Nakada, “Effects of Postdeposition Annealing on Electrical Properties of Mo-Doped Indium Oxide (IMO) Thin Films Deposited by RF Magnetron Cosputtering,” *Japanese Journal of Applied Physics*, vol. 45, no. No. 44, pp. L1179–L1182, 2006.
- [144] S. Parthiban, E. Elangovan, K. Ramamurthi, R. Martins, and E. Fortunato, “Investigations on high visible to near infrared transparent and high mobility Mo doped In_2O_3 thin films prepared by spray pyrolysis technique,” *Solar Energy Materials and Solar Cells*, vol. 94, no. 3, pp. 406–412, 2010.
- [145] R. K. Gupta, K. Ghosh, R. Patel, and P. K. Kahol, “Effect of thickness on optoelectrical properties of Mo-doped indium oxide films,” *Applied Surface Science*, vol. 255, no. 5, pp. 3046–3048, 2008.
- [146] T. Koida and M. Kondo, “Improved near-infrared transparency in sputtered In_2O_3 -based transparent conductive oxide thin films by Zr-doping,” *Journal of Applied Physics*, vol. 101, no. 6, p. 063705, 2007.
- [147] A. L. Dawar and J. C. Joshi, “Semiconducting transparent thin films: their properties and applications,” *Journal of Materials Science*, vol. 19, no. 1, pp. 1–23, 1984.
- [148] H. Fujiwara and M. Kondo, “Effects of carrier concentration on the dielectric function of $\text{ZnO}:\text{Ga}$ and $\text{In}_2\text{O}_3:\text{Sn}$ studied by spectroscopic ellipsometry: Analysis of free-carrier and band-edge absorption,” *Physical Review B*, vol. 71, no. 7, 2005.
- [149] T. Koida, M. Kondo, K. Tsutsumi, A. Sakaguchi, M. Suzuki, and H. Fujiwara, “Hydrogen-doped In_2O_3 transparent conducting oxide films prepared by solid-phase crystallization method,” *Journal of Applied Physics*, vol. 107, no. 3, 2010.

-
- [150] Y. Gassenbauer and A. Klein, "Electronic and chemical properties of tin-doped indium oxide (ITO) surfaces and ITO/ZnPc interfaces studied in-situ by photoelectron spectroscopy," *Journal of Physical Chemistry B*, vol. 110, no. 10, pp. 4793–4801, 2006.
- [151] D. O. Scanlon, G. W. Watson, D. J. Payne, G. R. Atkinson, R. G. Egdell, and D. S. L. Law, "Theoretical and Experimental Study of the Electronic Structures of MoO₃ and MoO₂," *Journal of Physical Chemistry C*, vol. 114, no. 10, pp. 4636–4645, 2010.
- [152] B. Brox and I. Olefjord, "Esca Studies of MoO₂ and MoO₃," *Surface and Interface Analysis*, vol. 13, no. 1, pp. 3–6, 1988.
- [153] J. Baltrusaitis, B. Mendoza-Sanchez, V. Fernandez, R. Veenstra, N. Dukstiene, A. Roberts, and N. Fairley, "Generalized molybdenum oxide surface chemical state XPS determination via informed amorphous sample model," *Applied Surface Science*, vol. 326, pp. 151–161, 2015.
- [154] C. R. Clayton and Y. C. Lu, "Electrochemical and XPS Evidence of the Aqueous Formation of Mo₂O₅," *Surface and Interface Analysis*, vol. 14, no. 1-2, pp. 66–70, 1989.
- [155] N. A. Dhas and A. Gedanken, "Characterization of sonochemically prepared unsupported and silica-supported nanostructured pentavalent molybdenum oxide," *Journal of Physical Chemistry B*, vol. 101, no. 46, pp. 9495–9503, 1997.
- [156] M. T. Greiner, L. Chai, M. G. Helander, W.-M. Tang, and Z.-H. Lu, "Transition Metal Oxide Work Functions: The Influence of Cation Oxidation State and Oxygen Vacancies," *Advanced Functional Materials*, vol. 22, no. 21, pp. 4557–4568, 2012.
- [157] R. Kleyna, H. Mex, M. Voss, D. Borgmann, L. Viscido, and J. M. Heras, "Modification of MoO₃ surfaces by vapour-deposited cobalt atoms," *Surface Science*, vol. 433, pp. 723–727, 1999.
- [158] M. Probst, M. Voss, R. Denecke, L. Viscido, J. M. Heras, D. Borgmann, and H. P. Steinruck, "Electron spectroscopic studies of vapor-deposited Co layers on MoO₃ surfaces," *Journal of Electron Spectroscopy and Related Phenomena*, vol. 114, pp. 539–544, 2001.
- [159] W. E. Swartz and D. M. Hercules, "X-Ray Photoelectron Spectroscopy of Molybdenum Compounds - Use of Esca in Quantitative Analysis," *Analytical Chemistry*, vol. 43, no. 13, p. 1774, 1971.
- [160] O. Y. Khyzhun, T. Strunskus, and Y. M. Solonin, "XES, XPS and NEXAFS studies of the electronic structure of cubic MoO_{1.9} and H_{1.63}MoO₃ thick films," *Journal of Alloys and Compounds*, vol. 366, no. 1-2, pp. 54–60, 2004.
- [161] L. Brewer and R. H. Lamoreaux, "The Mo-O system (Molybdenum-Oxygen)," *Journal of Phase Equilibria*, vol. 1, no. 2, pp. 85–89, 1980.
- [162] O. Y. Khyzhun, V. L. Bekenev, and Y. M. Solonin, "Electronic structure of face-centred cubic MoO₂: A comparative study by the full potential linearized augmented plane

wave method, X-ray emission spectroscopy and X-ray photoelectron spectroscopy,” *Journal of Alloys and Compounds*, vol. 459, no. 1-2, pp. 22–28, 2008.

- [163] M. Morales-Luna, S. A. Tomás, M. A. Arvizu, M. Pérez-González, and E. Campos-Gonzalez, “The evolution of the Mo 5+ oxidation state in the thermochromic effect of MoO₃ thin films deposited by rf magnetron sputtering,” *Journal of Alloys and Compounds*, vol. 722, pp. 938–945, 2017.
- [164] R. T. White, E. S. Thibau, and Z. H. Lu, “Interface Structure of MoO₃ on Organic Semiconductors,” *Sci Rep*, vol. 6, p. 21109, 2016.
- [165] C. McGuinness, C. B. Stagarescu, P. J. Ryan, J. E. Downes, D. Fu, K. E. Smith, and R. G. Egdell, “Influence of shallow core-level hybridization on the electronic structure of post-transition-metal oxides studied using soft X-ray emission and absorption,” *Physical Review B*, vol. 68, no. 16, 2003.
- [166] H. Odaka, S. Iwata, N. Taga, S. Ohnishi, Y. Kaneta, and Y. Shigesato, “Study on electronic structure and optoelectronic properties of indium oxide by first-principles calculations,” *Japanese Journal of Applied Physics Part 1-Regular Papers Brief Communications & Review Papers*, vol. 36, no. 9a, pp. 5551–5554, 1997.
- [167] J. E. Medvedeva, “Magnetically mediated transparent conductors: In₂O₃ doped with Mo,” *Phys Rev Lett*, vol. 97, no. 8, p. 086401, 2006.
- [168] E. A. Kraut, R. W. Grant, J. R. Waldrop, and S. P. Kowalczyk, “Semiconductor Core-Level to Valence-Band Maximum Binding-Energy Differences - Precise Determination by X-Ray Photoelectron-Spectroscopy,” *Physical Review B*, vol. 28, no. 4, pp. 1965–1977, 1983.
- [169] A. Klein, “Electronic properties of In₂O₃ surfaces,” *Applied Physics Letters*, vol. 77, no. 13, pp. 2009–2011, 2000.
- [170] W. H. E. Schwarz, “The Full Story of the Electron Configurations of the Transition Elements,” *Journal of Chemical Education*, vol. 87, no. 4, pp. 444–448, 2010.
- [171] K. Kanai, K. Koizumi, S. Ouchi, Y. Tsukamoto, K. Sakanoue, Y. Ouchi, and K. Seki, “Electronic structure of anode interface with molybdenum oxide buffer layer,” *Organic Electronics*, vol. 11, no. 2, pp. 188–194, 2010.
- [172] R. Tokarz-Sobieraj, K. Hermann, M. Witko, A. Blume, G. Mestl, and R. Schlogl, “Properties of oxygen sites at the MoO₃(010) surface: density functional theory cluster studies and photoemission experiments,” *Surface Science*, vol. 489, no. 1-3, pp. 107–125, 2001.
- [173] Irfan, H. Ding, Y. Gao, C. Small, D. Y. Kim, J. Subbiah, and F. So, “Energy level evolution of air and oxygen exposed molybdenum trioxide films,” *Applied Physics Letters*, vol. 96, no. 24, 2010.
- [174] R. P. Burns, G. Demaria, J. Drowart, and R. T. Grimley, “Mass Spectrometric Investigation of the Sublimation of Molybdenum Dioxide,” *Journal of Chemical Physics*, vol. 32, no. 5, pp. 1363–1366, 1960.

-
- [175] P. E. Blackburn, *The Vapor Pressure of Molybdenum Oxides and Tungsten Oxides*. Thesis, Ohio State University, 1954.
- [176] P. E. Blackburn, M. Hoch, and H. L. Johnston, "The Vaporization of Molybdenum and Tungsten Oxides," *Journal of Physical Chemistry*, vol. 62, no. 7, pp. 769–773, 1958.
- [177] U.S. National Institute of Standards, "<http://www.nist.gov/srd/nist71.cfm>."
- [178] R. K. Gupta, K. Ghosh, S. R. Mishra, and P. K. Kahol, "High mobility Ti-doped In₂O₃ transparent conductive thin films," *Materials Letters*, vol. 62, no. 6-7, pp. 1033–1035, 2008.
- [179] R. K. Gupta, K. Ghosh, S. R. Mishra, and P. K. Kahol, "Opto-electrical properties of Ti-doped In₂O₃ thin films grown by pulsed laser deposition," *Applied Surface Science*, vol. 253, no. 24, pp. 9422–9425, 2007.
- [180] H. Jong-Hyun, J. Ki-Young, K. Dong-Joo, L. Don-Kyu, and S. Youl-Moon, "Fabrication of Titanium-Doped Indium Oxide Films for Dye-Sensitized Solar Cell Application Using Reactive RF Magnetron Sputter Method," *IEEE Transactions on Plasma Science*, vol. 37, no. 8, pp. 1586–1592, 2009.
- [181] A. Chaoumead, H. Park, B. Joo, D. Kwak, M. Park, and Y. Sung, "Structural and Electrical Properties of Titanium-Doped Indium Oxide Films Deposited by RF Sputtering," *Energy Procedia*, vol. 34, pp. 572–581, 2013.
- [182] D.-J. Kim, B.-s. Kim, and H.-K. Kim, "Effect of thickness and substrate temperature on the properties of transparent Ti-doped In₂O₃ films grown by direct current magnetron sputtering," *Thin Solid Films*, vol. 547, pp. 225–229, 2013.
- [183] B. Grew, J. W. Bowers, F. Lisco, N. Arnou, J. M. Walls, and H. M. Upadhyaya, "High Mobility Titanium-doped Indium Oxide for Use in Tandem Solar Cells Deposited via Pulsed DC Magnetron Sputtering," *Energy Procedia*, vol. 60, pp. 148–155, 2014.
- [184] S. Kashiwaya, J. Morasch, V. Streibel, T. Toupance, W. Jaegermann, and A. Klein, "The Work Function of TiO₂," *Surfaces*, vol. 1, no. 1, pp. 73–89, 2018.
- [185] P. Reckers, M. Dimamay, J. Klett, S. Trost, K. Zilberberg, T. Riedl, B. A. Parkinson, J. Brötz, W. Jaegermann, and T. Mayer, "Deep and Shallow TiO₂ Gap States on Cleaved Anatase Single Crystal (101) Surfaces, Nanocrystalline Anatase Films, and ALD Titania Ante and Post Annealing," *The Journal of Physical Chemistry C*, vol. 119, no. 18, pp. 9890–9898, 2015.
- [186] M. J. Jackman, A. G. Thomas, and C. Muryn, "Photoelectron Spectroscopy Study of Stoichiometric and Reduced Anatase TiO₂(101) Surfaces: The Effect of Subsurface Defects on Water Adsorption at Near-Ambient Pressures," *The Journal of Physical Chemistry C*, vol. 119, no. 24, pp. 13682–13690, 2015.
- [187] K. E. Kweon, G. S. Hwang, J. Kim, S. Kim, and S. Kim, "Electron small polarons and their transport in bismuth vanadate: a first principles study," *Phys Chem Chem Phys*, vol. 17, no. 1, pp. 256–60, 2015.

-
- [188] A. J. Rettie, W. D. Chemelewski, D. Emin, and C. B. Mullins, “Unravelling Small-Polaron Transport in Metal Oxide Photoelectrodes,” *J Phys Chem Lett*, vol. 7, no. 3, pp. 471–9, 2016.
- [189] C. Lohaus, A. Klein, and W. Jaegermann, “Limitation of Fermi level shifts by polaron defect states in hematite photoelectrodes,” *Nature Communications*, vol. 9, no. 1, p. 4309, 2018.
- [190] A. Klein, C. Körber, A. Wachau, F. Säuberlich, Y. Gassenbauer, S. P. Harvey, D. E. Proffit, and T. O. Mason, “Transparent Conducting Oxides for Photovoltaics: Manipulation of Fermi Level, Work Function and Energy Band Alignment,” *Materials (Basel)*, vol. 3, no. 11, pp. 4892–4914, 2010.
- [191] H. Wardenga, *Characterization of Zr and H doped In₂O₃ films deposited by radio frequency magnetron sputtering*. M. Sc., Technische Universität Darmstadt, 2013.
- [192] D. R. Lide, *CRC Handbook of Chemistry and Physics, Internet Version 2005*. Boca Raton, FL: CRC Press, 2005.
- [193] J. E. N. Swallow, B. A. D. Williamson, T. J. Whittles, M. Birkett, T. J. Featherstone, N. Peng, A. Abbott, M. Farnworth, K. J. Cheetham, P. Warren, D. O. Scanlon, V. R. Dhanak, and T. D. Veal, “Self-Compensation in Transparent Conducting F-Doped SnO₂,” *Advanced Functional Materials*, vol. 28, no. 4, 2018.
- [194] S. B. Zhang, S. H. Wei, and A. Zunger, “Intrinsic n-type versus p-type doping asymmetry and the defect physics of ZnO,” *Physical Review B*, vol. 63, no. 7, 2001.
- [195] C. Freysoldt, B. Grabowski, T. Hickel, J. Neugebauer, G. Kresse, A. Janotti, and C. G. Van de Walle, “First-principles calculations for point defects in solids,” *Reviews of Modern Physics*, vol. 86, no. 1, pp. 253–305, 2014.
- [196] P. Erhart, K. Albe, and A. Klein, “First-principles study of intrinsic point defects in ZnO: Role of band structure, volume relaxation, and finite-size effects,” *Physical Review B*, vol. 73, no. 20, 2006.
- [197] S. A. Centoni, B. Sadigh, G. H. Gilmer, T. J. Lenosky, T. Diaz de la Rubia, and C. B. Musgrave, “First-principles calculation of intrinsic defect formation volumes in silicon,” *Physical Review B*, vol. 72, no. 19, 2005.
- [198] A. Janotti and C. G. Van de Walle, “Native point defects in ZnO,” *Physical Review B*, vol. 76, no. 16, 2007.
- [199] S. Bajaj, H. Wang, J. W. Doak, C. Wolverton, and G. Jeffrey Snyder, “Calculation of dopant solubilities and phase diagrams of X–Pb–Se (X = Br, Na) limited to defects with localized charge,” *Journal of Materials Chemistry C*, vol. 4, no. 9, pp. 1769–1775, 2016.
- [200] A. Gassmann, S. V. Yampolskii, A. Klein, K. Albe, N. Vilbrandt, O. Pekkola, Y. A. Genenko, M. Rehahn, and H. von Seggern, “Study of electrical fatigue by defect engineering in organic light-emitting diodes,” *Materials Science and Engineering: B*, vol. 192, pp. 26–51, 2015.

-
- [201] H. Raebiger, S. Lany, and A. Zunger, "Electronic structure, donor and acceptor transitions, and magnetism of 3d impurities in In_2O_3 and ZnO ," *Physical Review B*, vol. 79, no. 16, 2009.
- [202] S. Trasati, "The absolute electrode potential: an explanatory note (Recommendations 1986)," *Journal of Electroanalytical Chemistry and Interfacial Electrochemistry*, vol. 209, no. 2, pp. 417–428, 1986.
- [203] P. Pennisi, *A Study of Molybdenum Redox Couples*. Thesis, The University of New South Wales, 1995.
- [204] C. Guang-Sen, M. Okido, and T. Oki, "Electrochemical studies of titanium ions (Ti^{4+}) in equimolar KCl-NaCl molten salts with 1 wt K_2TiF_6 ," *Electrochimica Acta*, vol. 32, no. 11, pp. 1637–1642, 1987.
- [205] O. Bierwagen, "Indium oxide - a transparent, wide-band gap semiconductor for (opto)electronic applications," *Semiconductor Science and Technology*, vol. 30, no. 2, 2015.
- [206] S. P. Harvey, T. O. Mason, Y. Gassenbauer, R. Schafrank, and A. Klein, "Surface versus bulk electronic/defect structures of transparent conducting oxides: I. Indium oxide and ITO," *Journal of Physics D: Applied Physics*, vol. 39, no. 18, pp. 3959–3968, 2006.
- [207] R. Bel Hadj Tahar, T. Ban, Y. Ohya, and Y. Takahashi, "Tin doped indium oxide thin films: Electrical properties," *Journal of Applied Physics*, vol. 83, no. 5, pp. 2631–2645, 1998.
- [208] T. A. Gessert, Y. Yoshida, C. C. Fesenmaier, and T. J. Coutts, "Sputtered In_2O_3 and ITO thin films containing zirconium," *Journal of Applied Physics*, vol. 105, no. 8, 2009.
- [209] E. Aydin, M. De Bastiani, X. Yang, M. Sajjad, F. Aljamaan, Y. Smirnov, M. N. Hedhili, W. Liu, T. G. Allen, L. Xu, E. Van Kerschaver, M. Morales-Masis, U. Schwingenschlöggl, and S. De Wolf, "Zr-Doped Indium Oxide (IZRO) Transparent Electrodes for Perovskite-Based Tandem Solar Cells," *Advanced Functional Materials*, vol. 29, no. 25, 2019.
- [210] J. Hunka, *Aufbau und Anwendung einer Vorrichtung zur elektrischen Modifizierung der Sauerstoffkonzentration in ITO*. M.sc. thesis, Technische Universität Darmstadt, 2018.
- [211] V. Brichzin, J. Fleig, H. U. Habermeier, G. Cristiani, and J. Maier, "The geometry dependence of the polarization resistance of Sr-doped LaMnO_3 microelectrodes on yttria-stabilized zirconia," *Solid State Ionics*, vol. 152-153, pp. 499–507, 2002.

9 Appendix

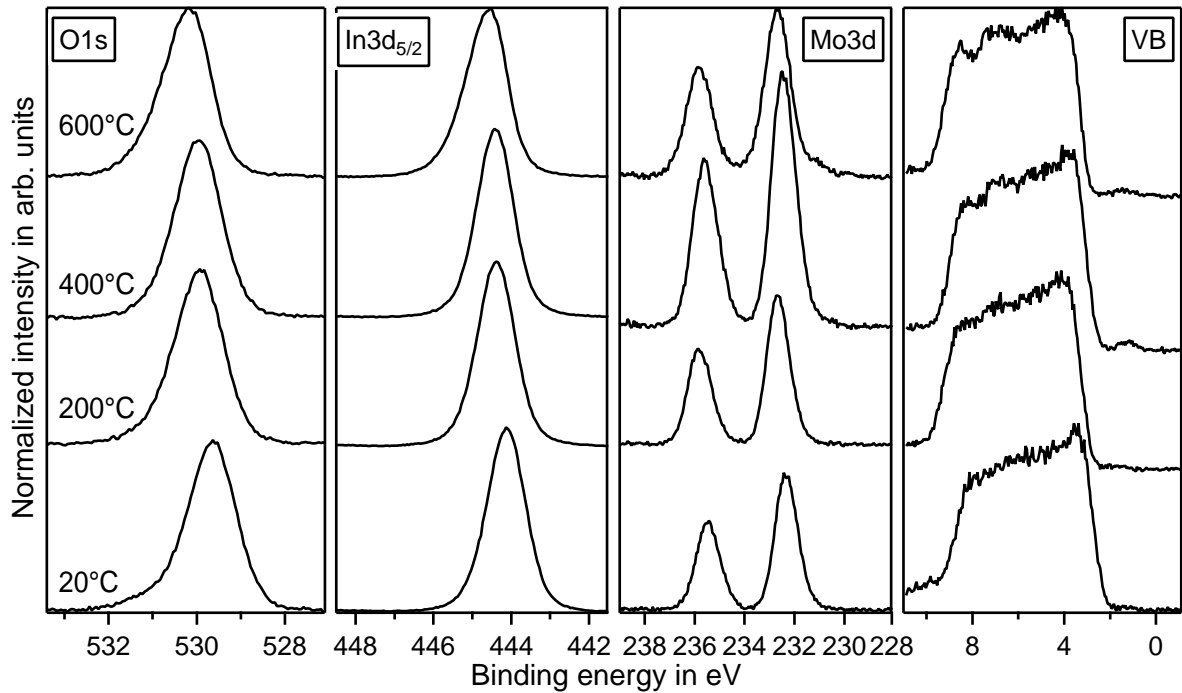


Figure 9.1: XPS O1s, In3d_{5/2}, Mo3d core level spectra and valence band region of 5 mol% Mo:In₂O₃ thin films on glass. Films were deposited at various temperatures in a process atmosphere containing 10% O₂. All spectra are normalized to the overall weighted area.

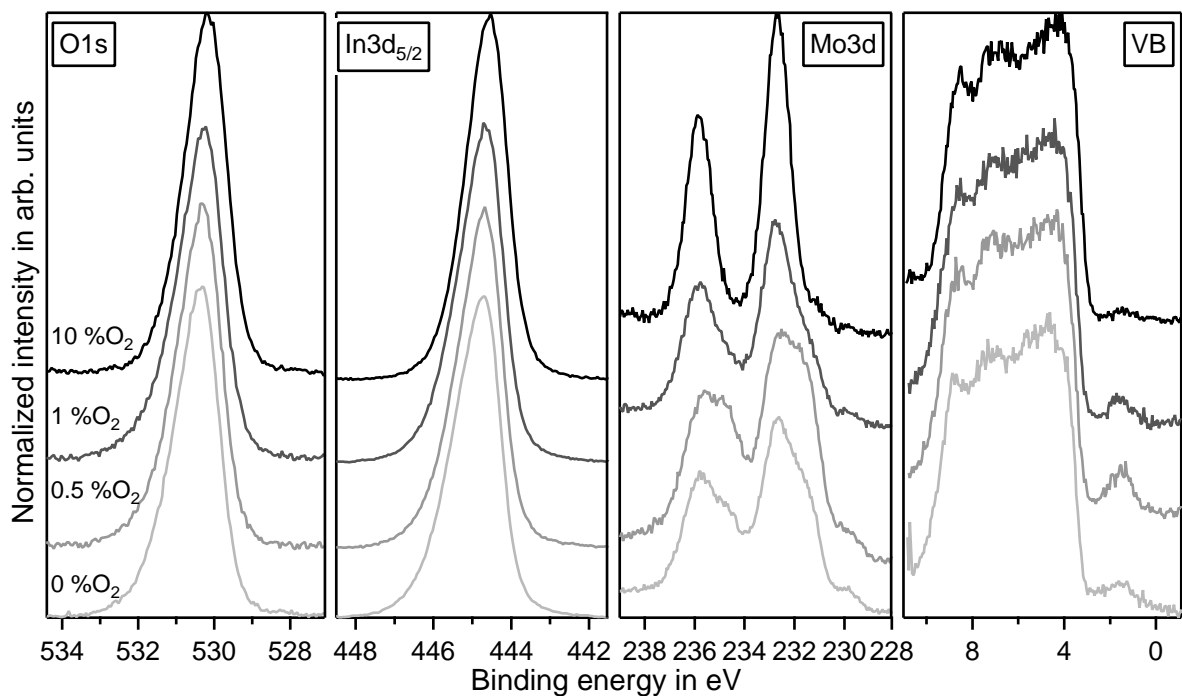


Figure 9.2: XPS O1s, In3d_{5/2}, Mo3d core level spectra and valence band region of 5 mol% Mo:In₂O₃ thin films on glass. Films were deposited at 600°C in process atmospheres containing different oxygen contents. All spectra are normalized to the overall weighted area.

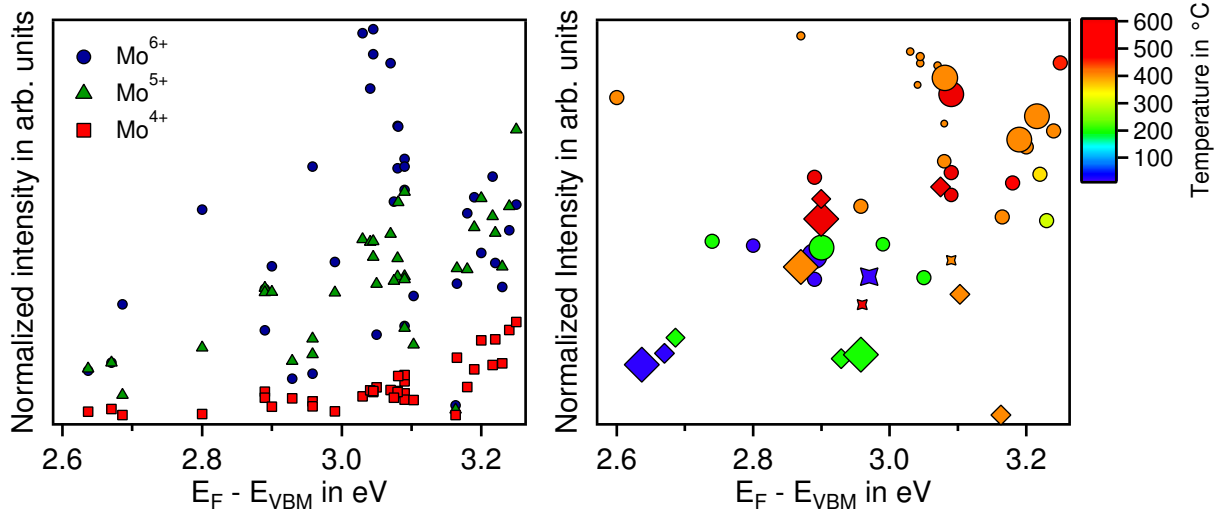


Figure 9.3: Intensity of components forming Mo3d peak as obtained from fit on left and integrated peak area of Mo3d emission on right plotted over XPS valence band maximum. Intensities were normalized to overall peak area. The substrate temperature in the right graph according to color scale and marker size determines oxygen content.

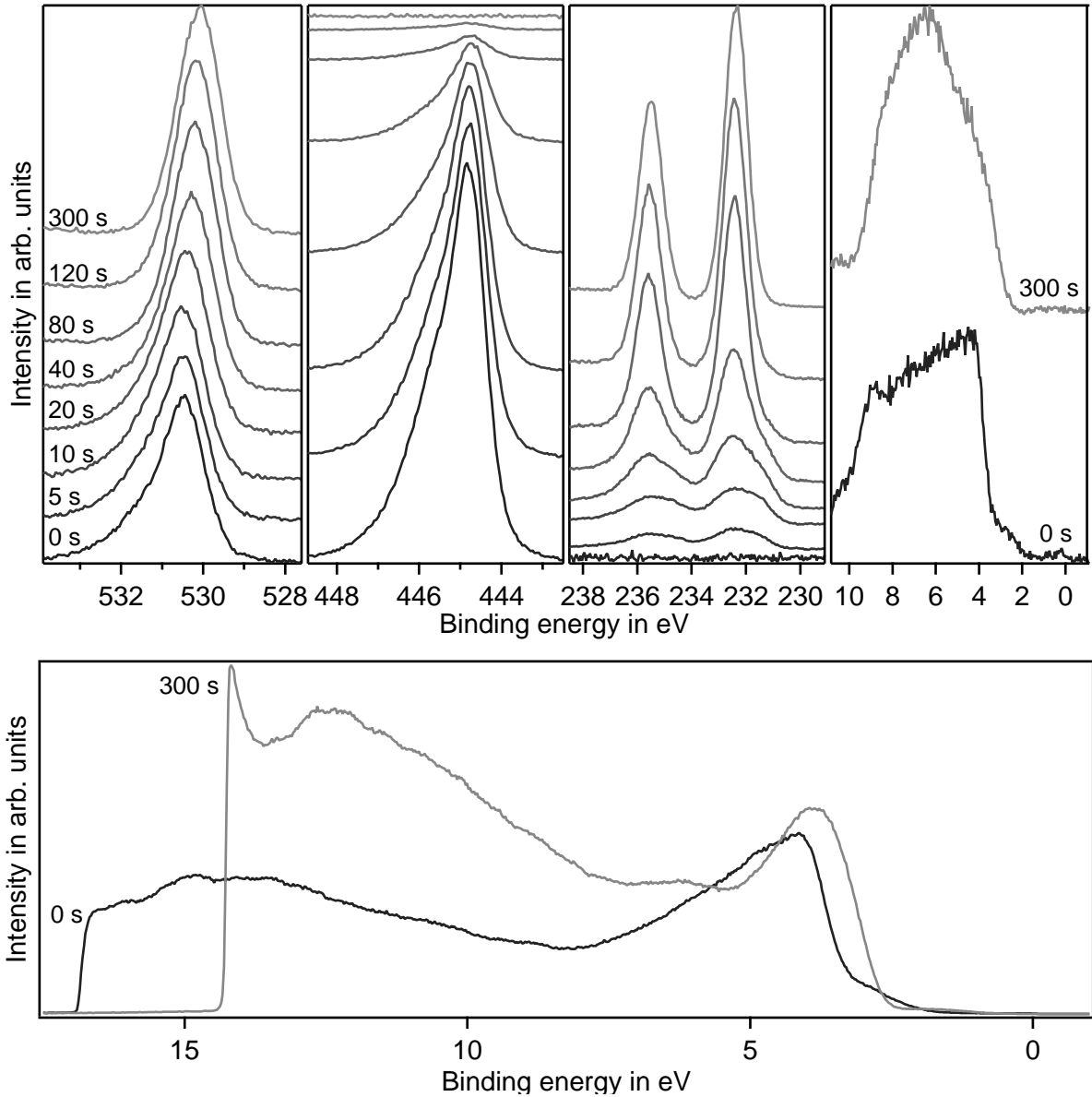


Figure 9.4: XP and UP spectra obtained during an interface experiment of MoO₃ on ITO. 10wt% Sn:In₂O₃ was deposited on glass using standard conditions. MoO₃ powder was thermally evaporated from a homemade effusion cell at a crucible temperature of 600 °C. Deposition time is given in the graphs. Deposition rate of MoO₃ is 0.1 nm/s.

Table 9.1: Surface potentials of thick ITO and thick MoO₃ from interface experiment shown in Fig. 9.4. Values are given in eV. ϕ and I_p were calculated using Eq. 4.2-Eq. 4.3

	$E_{VBM}-E_F$ (XPS)	$E_{VBM}-E_F$ (UPS)	ϕ (XPS)	ϕ (UPS)	I_p
Sn:In ₂ O ₃	3.3	3.2	4.3	4.4	7.6
MoO ₃	2.6	2.7	7.0	7.0	9.6

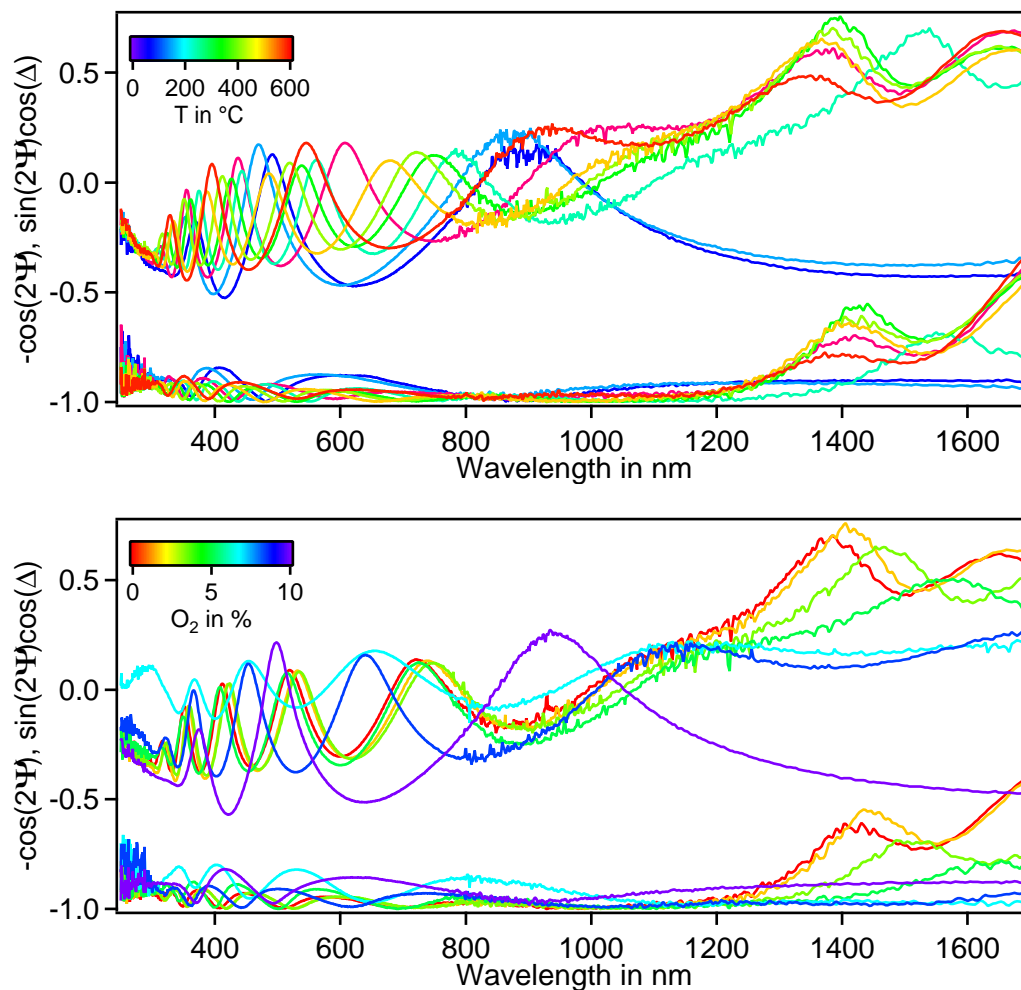


Figure 9.5: Spectrometric ellipsometry measurements of samples deposited at varying temperature in pure argon atmosphere (top) or at different oxygen content at a substrate temperature of 400 °C (bottom). The Fourier coefficients are plotted versus the wavelength.

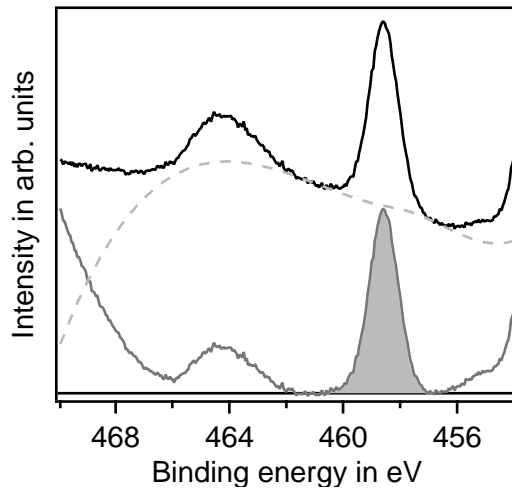


Figure 9.6: Example for approximation of background for $Ti2p_{3/2}$ emission. Measured spectrum is shown as a black solid line. Gray dashed line indicates the spline used as background. Corrected spectrum is shown at the bottom, used area for the quantification of the titanium content is displayed gray.

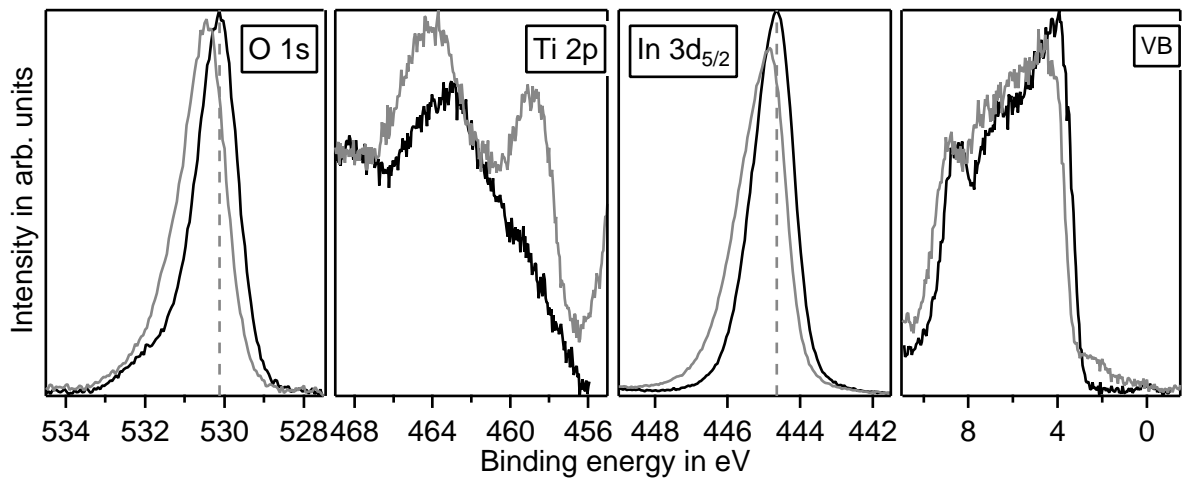


Figure 9.7: $Ti:In_2O_3$ 2 mol% and 5 mol%, deposited in pure Argon at $400^\circ C$.

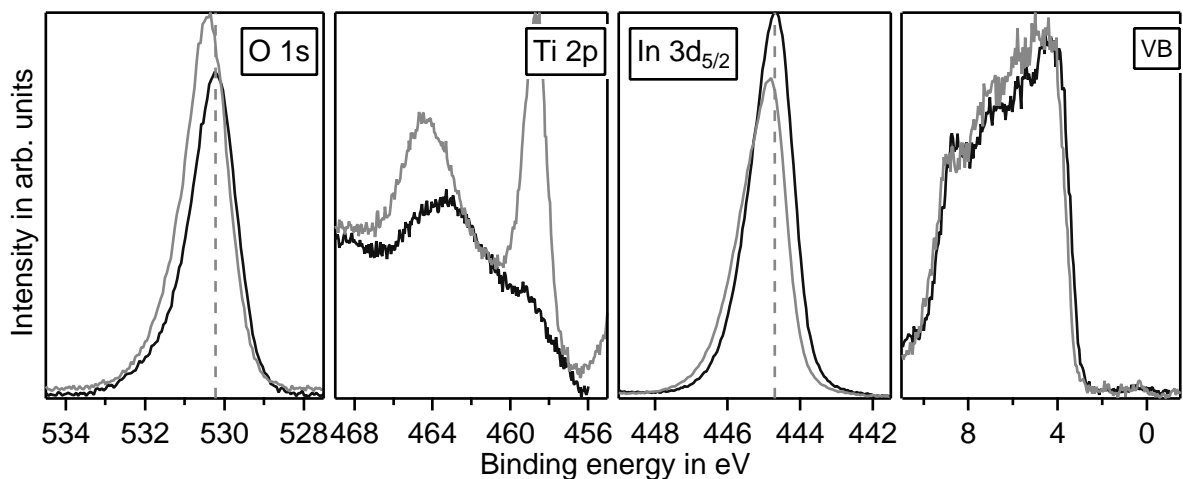


Figure 9.8: $Ti:In_2O_3$ 2 mol% and 5 mol%, deposited in pure Argon at $600^\circ C$.

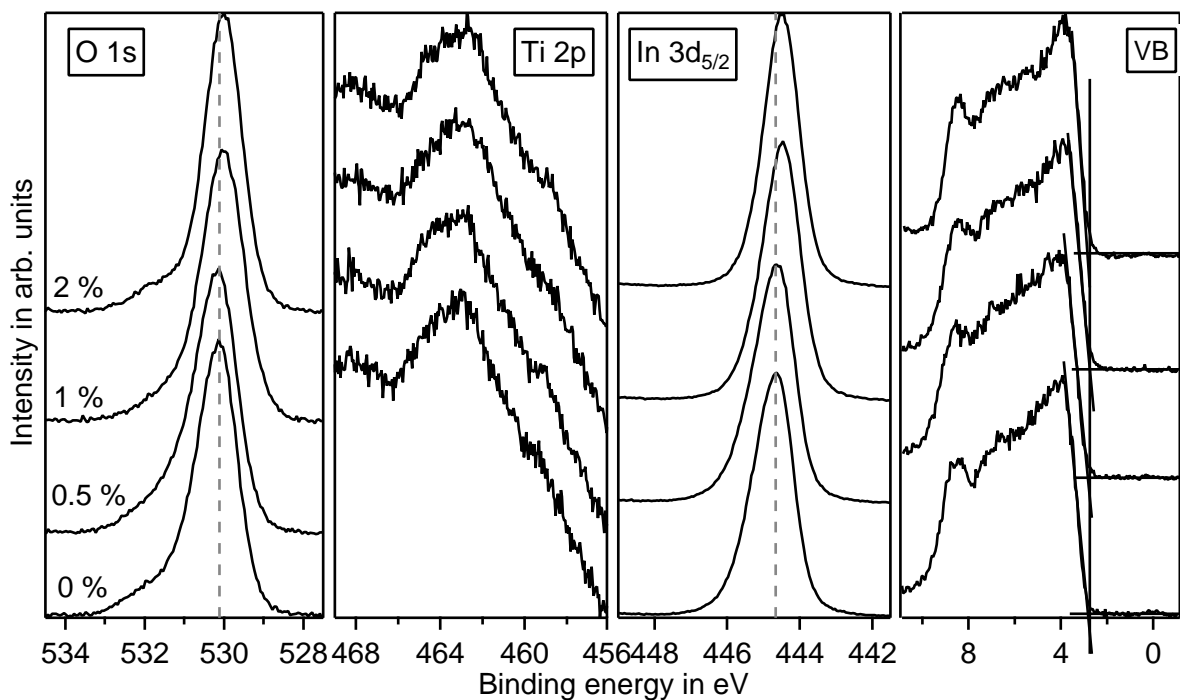


Figure 9.9: Ti:In₂O₃ 2 mol, deposited under various oxygen partial pressures at substrate temperature of 400 °C.

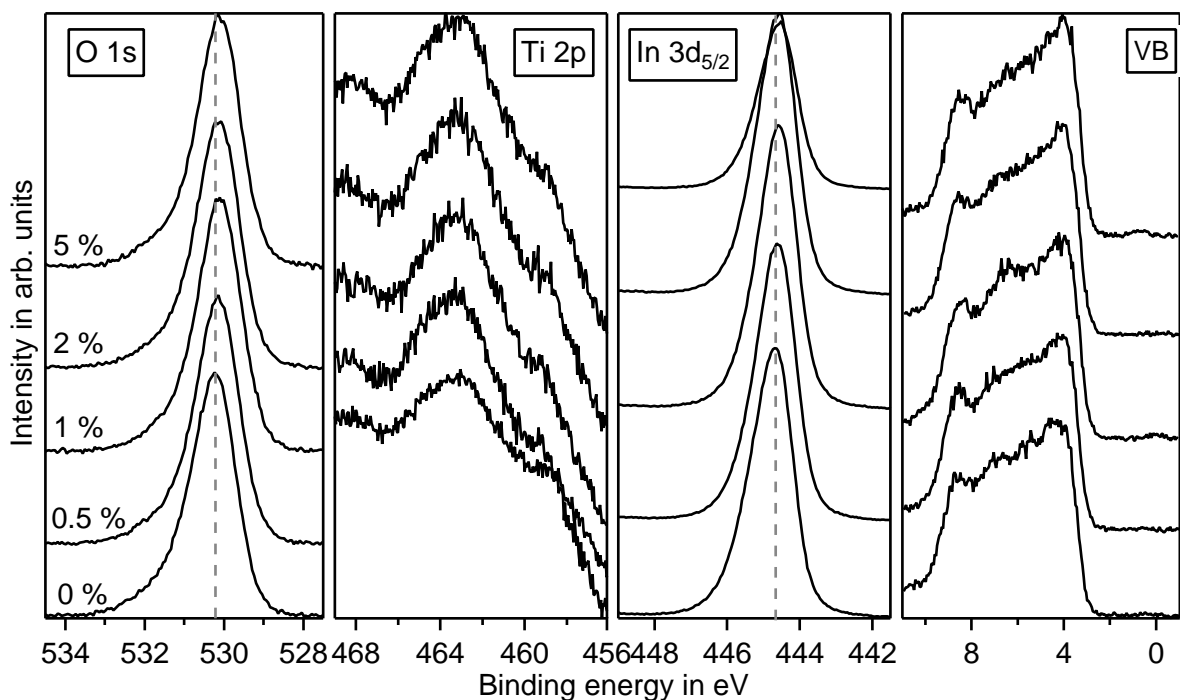


Figure 9.10: Ti:In₂O₃ 2 mol, deposited under various oxygen partial pressures at substrate temperature of 600 °C.

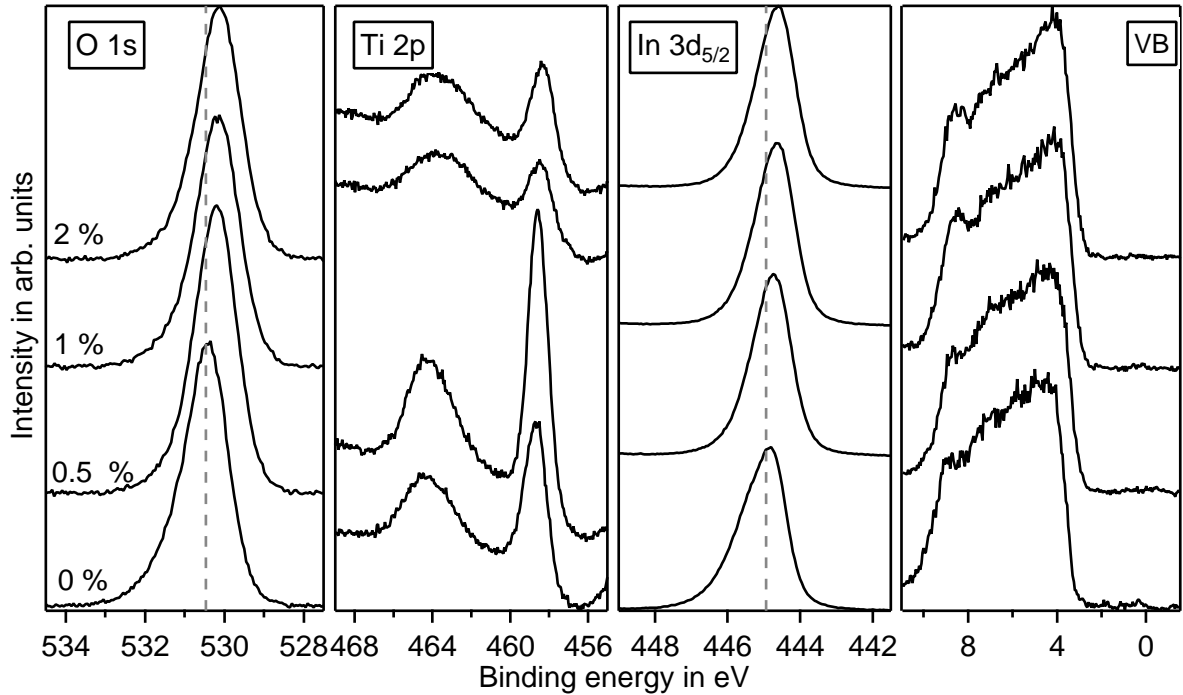


Figure 9.11: Ti:In₂O₃ 5 mol, deposited under various oxygen partial pressures at substrate temperature of 600 °C.

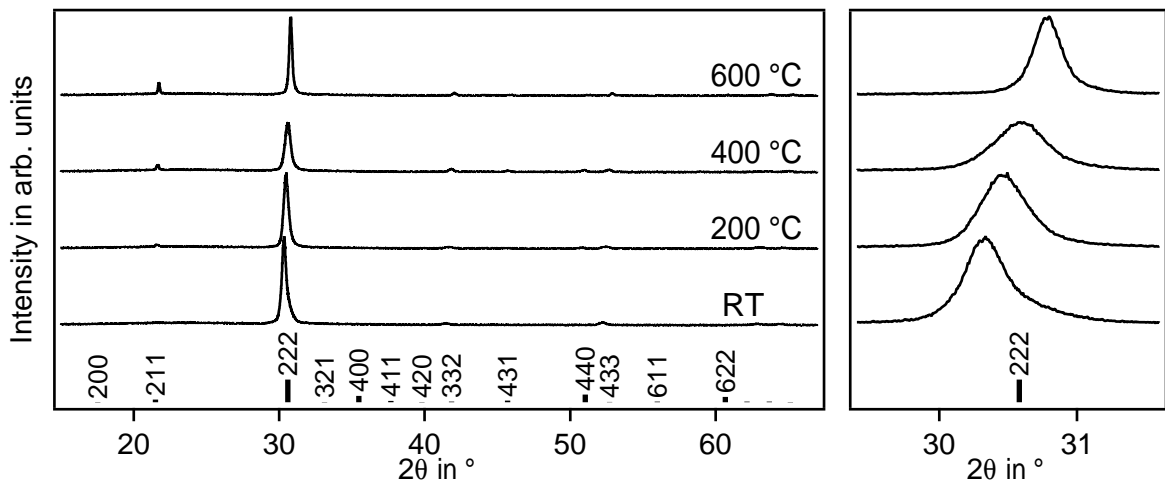


Figure 9.12: $\theta/2\theta$ X-Ray diffraction patterns of In₂O₃ deposited on glass at different substrate temperatures. The region around the (222) reflection is shown magnified on the right. Pure Ar atmosphere, pressure of 0.5 Pa, substrate-to-target distance of 10 cm. Reference spectrum for In₂O₃ powder ICDD 00-006-0416.

Table 9.2: Target composition according to manufacturer specifications. A mixture of In_2O_3 and either SnO_2 , ZrO_2 , GeO_2 , MoO_3 or TiO_2 powder was used. mol% and wt% consider either molar or weight fraction of the powders used for sintering. cat% specifies the fraction of dopant and In, at% the fraction of dopant, In and O. cat% is calculated based on the wt% and used for the determination of at%. The carrier concentration n is calculated based on the assumption of a doping efficiency of 100 %.

Dopant	wt%	mol%	at%	cat%	n in 10^{20}cm^{-1}
Sn	0.5	0.92	0.18	0.46	1.44
	2	3.62	0.75	1.85	5.81
	10	17.0	3.93	9.28	30.6
Zr	1	2.23	0.45	1.13	3.53
	2	4.44	0.91	2.25	7.10
Ge	2	5.14	1.07	2.64	8.34
	4	9.95	2.16	5.24	16.8
	6	14.5	3.28	7.81	25.5
Mo	1.05	2	0.40	1.01	3.17
	2.66	5	1.04	2.56	8.12
Ti	0.58	2	0.40	1.01	3.17
	1.49	5	1.04	2.56	8.12

Veröffentlichungen und Konferenzbeiträge

Veröffentlichungen

A. H. Hubmann, S. Li, S. Zhukov, S. H. von Seggern, und A. Klein. "Polarisation dependence of Schottky barrier heights at ferroelectric BaTiO₃ / RuO₂ interfaces: influence of substrate orientation and quality," *Journal of Physics D: Applied Physics*, vol. 49, no. 29, 2016

K. L. Hoyer, **A. H. Hubmann** und A. Klein, "Influence of dopant segregation on the work function and electrical properties of Ge-doped in comparison to Sn-doped In₂O₃ thin films," *Physica Status Solidi (a)*, p. 1-8, 2016.

A. H. Hubmann, D. Dietz, J. Brötz, A. Klein, "Interface Behaviour and Work Function Modification of Self-Assembled Monolayers on Sn-Doped In₂O₃," *Surfaces*, vol. 2, no. 2, p. 241-256, 2019

Konferenzbeiträge

European Materials Research Society

Lille (Frankreich), 2016

Electrical and surface properties of Ge-doped In₂O₃ thin films - *Poster-Präsentation*

6 th International Symposium on Transparent Conducting Materials

Platanias (Griechenland), 2016

Does the dopant influence the texture of magnetron sputtered In₂O₃ thin films? - *Poster-Präsentation*

European Materials Research Society

Straßburg (Frankreich), 2017

Work function modification of epitaxial ITO by organic monolayers: Influence of surface orientation and treatment - *Poster-Präsentation*

7 th International Symposium on Transparent Conducting Materials

Platanias (Griechenland), 2018

Assessing the conductivity limits and scattering processes of doped In₂O₃ thin films by electrically tuning the carrier concentration – preliminary results - *Vortrag*

Betreute Arbeiten

K. L. Hoyer

Untersuchung von GeO_2 dotierten In_2O_3 -Schichten
Master-Thesis, 2016

J. Philipp

Herstellung von Zinkoxid Schottky-Dioden durch Magnetron-Kathodenzerstäubung
Bachelor-Thesis, 2016

B. Huang

Study on Temperature Dependent Current-Voltage Measurements of Sn- and Ge-doped
 In_2O_3 Thin Films
Advanced Research Lab, 2016

M. Lederer

Untersuchung von Molybdän-dotiertem Indiumoxid
Bachelor-Thesis, 2017

J. Hunka

Aufbau und Anwendung einer Vorrichtung zur elektrischen Modifizierung der Sauerstoff-
konzentration in ITO
Master-Thesis, 2018

Lebenslauf

Andreas Hilarius Hubmann

Berufliche Laufbahn

- 04/2020 - heute Prozessingenieur für Dünneschichten, Heraeus Holding GmbH, Nexsensos
- 07/2015 - 02/2019 Wissenschaftlicher Mitarbeiter an der Technischen Universität Darmstadt im Fachgebiet Materialwissenschaft, Fachbereich Elektronenstruktur von Materialien
- 07/2011 - 09/2011 Praktikum im Internationalen technischen Entwicklungszentrum, Adam Opel AG in Rüsselsheim zur Untersuchung der Entstehung von Verformungsmartensit in austenitischen Stählen bei Zugbelastung

Ausbildung

- 07/2015 - heute Dissertation an der Technischen Universität Darmstadt im Fachgebiet Materialwissenschaft, Fachbereich Elektronenstruktur von Materialien, betreut durch Prof. Andreas Klein
- 10/2012 - 04/2015 Master of Science materials science (Gesamtnote 1,04)
Technische Universität Darmstadt
Masterthesis mit dem Titel „Investigation of the Polarization Behavior of BaTiO₃ Single Crystals“, betreut durch Prof. Andreas Klein (Note 1,0)
- 11/2013 - 02/2014 Forschungspraktikum an der Oregon State University, USA
School of Electrical Engineering and Computer Science
Herstellung und Charakterisierung von Dünnschicht Transistoren auf Basis von amorphen Oxid-Halbleitern betreut durch Prof. John F. Wager
- 10/2009 - 09/2012 Bachelor of Science Materialwissenschaft (Gesamtnote 1,58)
Technische Universität Darmstadt
Bachelorthesis mit dem Titel „Untersuchung der Schottky-Barriere an den BaTiO₃/RuO₂-Grenzflächen in Abhängigkeit der dielektrischen Polarisierung und kristallographischen Orientierung“, betreut durch Prof. Andreas Klein (Note 1,0)
- 06/2009 Abitur Immanuel-Kant-Schule, Rüsselsheim (Note 1,8)



Danksagung

Zuerst möchte ich mich bei Andreas Klein dafür bedanken, das Potential als Doktorand in mir gesehen und mir die Möglichkeit in der ESM Gruppe zu promovieren gegeben zu haben. Das Vertrauen und die Freiheit sich in den Grenzen eines Projektes nach links und rechts umzuschauen, hat mich sicherlich herausgefordert, aber mir auch vieles über Wissenschaft, Arbeit in der Forschung und nicht zuletzt über meine eigenen Stärken und Schwächen gelehrt. Danke dafür, dass Du immer zur Verfügung gestanden hast, um wissenschaftliche Unsicherheiten aus dem Weg zu räumen und vor allem um neue Inspiration zu verleihen.

Ich bedanke mich bei Prof. Karsten Albe für die Erstellung des zweiten Gutachtens zu meiner Arbeit und bei den Professoren Jörg Schneider und Ralph Krupke für das Eintreten als Prüfer.

Allen Kolleginnen und Kollegen der ESM oder OF Gruppe möchte ich dafür danken, die Uni zu mehr als nur einem Arbeitsplatz gemacht zu haben. Die Zusammenarbeit im Labor, das Teilen von Freude und/oder Leid an der Arbeit und weit darüber hinausgehende Gespräche beim gemeinsamen Kaffee waren ein wichtiger Bestandteil für mich.

Ich bedanke mich bei meiner Familie und allen Freundinnen und Freunden, die mich stets unterstützt haben den Weg bis hier her zu finden. Ob es nun von Anfang an, ab einem späteren Zeitpunkt, bis hier her, oder nur ein Stück war, waren es auch Eure Worte und Taten, die mich so weit gebracht haben.